

**SPACE-BASED DOPPLER LIDAR SAMPLING STRATEGIES --
ALGORITHM DEVELOPMENT AND SIMULATED
OBSERVATION EXPERIMENTS**

Final Report
Under
NASA Contract NAS8-38559

Covering the Period
June 27, 1990 to December 1, 1993

Submitted by

Simpson Weather Associates, Inc.
809 E. Jefferson Street
Charlottesville, VA 22902

1 December 1993

TABLE OF CONTENTS

	PAGE
1.0 Introduction.....	1
2.0 LAWS Simulations for the OSSEs.....	1
3.0 LAWS Trade Studies.....	2
4.0 Ground-Based Efforts.....	3
5.0 GLOBE Data in HDF Format.....	3
APPENDIX A: LAWS SIMULATION MODEL (GLOBAL VERSION).....	A-1
APPENDIX B: 1992 OBSERVING SYSTEM SIMULATION EXPERIMENTS....	B-1
APPENDIX C: 1991 OBSERVING SYSTEM SIMULATION EXPERIMENTS....	C-1
APPENDIX D: GROUND-BASED DOPPLER LIDAR STUDIES.....	D-1
APPENDIX E: ADDITIONAL STUDIES.....	E-1
APPENDIX F: HDF FORMAT FOR GLOBE DATA.....	F-1
APPENDIX G: CONFERENCE PRESENTATIONS AND PAPERS.....	G-1
REFERENCES.....	R-1

SUMMARY

1.0 Introduction

Simpson Weather Associates, Inc. (SWA) has been funded, under contract NAS8-38559, to research the feasibility and optimum functionality of the NASA proposed space-based Doppler lidar, the Laser Atmospheric Wind Sounder (LAWS), to measure global winds in the earth's troposphere. SWA has developed a LAWS Simulation Model (LSM) to evaluate the potential impacts of LAWS measurements on the prediction skills of current climate and forecast models and to address critical LAWS design issues such as orbit selection, scanning patterns, and power budgets. This final report covers the period from June 27, 1990 to December 1, 1993, where SWA's efforts were largely concentrated on addressing the impacts of several orbit configurations on LAWS global coverage, measurement accuracy, wind information, trade studies and ground based Doppler lidar data processing. A complete technical write up of the LSM is included in Appendix A. Following is a brief overview of the contract activities.

2.0 LAWS Simulations for the OSSEs

In the first year of this contract, SWA was tasked to conduct a series of LAWS simulations to address the selection of orbit (altitude and inclination) and system design criteria for LAWS (see Appendix C.). The European Center for Medium Range Weather Forecasting (ECMWF) provided 25 days of sequentially consistent atmospheric fields referred to as the Nature Run. The global LAWS Simulation Model (LSMg) was run for several sets of five Nature Run days for several orbits. The simulated lidar data sets, i.e., Line-of-Sight (LOS) and horizontal components, were given to the ongoing Observing System Simulation Experiments (OSSE) being run at NASA/Goddard Space Flight Center (GSFC) (Atlas and Emmitt, 1991) and Florida State University (FSU) (Krishnamurti et al., 1991; Rohaly and Krishnamurti, 1993). The initial set of LAWS OSSEs were designed to bracket the performance of LAWS. The first series of LAWS simulations were considered to be "perfect" LAWS measurements (i.e., the best any optical wind sensor could do with 10^9 shots in 5 years). Only opaque clouds and terrain obscurations prevented LAWS from making a measurement at a pressure level. The second series of LAWS simulations were considered to be more "realistic" by incorporating the effects of variables such as aerosol backscatter, molecular attenuation, the presence of cirrus clouds and atmospheric turbulence in the calculations of the horizontal wind components. As these experiments were being run, the choice of orbit configuration was refined. Table 1 summarizes the LAWS orbital configurations that were simulated in 1990-1991 period.

Table 1. LAWS Orbital Configuration Experiments for 1991

System Configuration	Orbit	Simulation
20 JOULE/1.50 M	98 DEG 705 KM	PERFECT
20 JOULE/1.50 M	98 DEG 450 KM	PERFECT
20 JOULE/1.50 M	55 DEG 450 KM	PERFECT
20 JOULE/1.50 M	98 DEG 525 KM	PERFECT
20 JOULE/1.50 M	55 DEG 575 KM	PERFECT
20 JOULE/1.50 M	55 DEG 575 KM	REALISTIC
20 JOULE/1.50 M	98 DEG 525 KM	REALISTIC

In the second year of our contract, SWA was tasked to upgrade the LSMg to support the new ECMWF T106 (~ 100x100 km grid) Nature Run data, incorporate aerosol information from the NASA Global Backscatter Experiment (GLOBE) and incorporate the Slingo cloud prediction model (see Appendix A.). A series of realistic LAWS simulations were performed in cooperation with the OSSE efforts ongoing at GSFC and FSU (see Appendix B) to address the performance of LAWS under various system configurations ranging from a low power LAWS to the "full up" LAWS. Table 2 lists the LAWS system configurations that were simulated in 1992-1993 period.

Table 2. LAWS System Configuration Experiments

System Configuration	Orbit	Simulation
20 JOULE/1.50 M	98 DEG 525 KM	5 days
5 JOULE/0.75 M	98 DEG 525 KM	5 days
.1 JOULE/0.50 M	98 DEG 200 KM	5 days
.2 JOULE/0.60 M	98 DEG 300 KM	5 days
2. JOULE/0.75 M	98 DEG 300 KM	3 hours

3.0 Trade Studies

Prior to generating extended (several days) LAWS simulated data sets for use in OSSEs, an engineering version (developed with SWA R&D funds) of the LSM was used to define optimal system and sub-system parameters within specified technological or resource constraints. The system trade studies included the specification of:

- the optimal nadir scan angle for a conically scanned lidar;
- the optimal pattern of sampling for both conically scanned and multi-telescoped unscanned systems;

- the optimal combination of energy/pulse and pulse repetition frequency for a given platform power budget; and
- the optimal management of lidar shots given fixed laser-lifetimes and platform resources.

Since the trade studies were normally against some reference atmosphere, SWA developed a new LAWS Baseline Atmosphere Model (BAM) to be used for LAWS trade studies to NASA/Marshall Space Flight Center (MSFC) (Wood and Emmitt, 1990; Wood and Emmitt, 1991). BAM gives the probability of a given aerosol backscatter as a function of altitude. The presence of thin cirrus clouds and molecular attenuation is also available in the model. The original backscatter profile was based on GLOBE data. The new version has added an expected maritime backscatter profile based on the LAWS Science Team's research.

4.0 Ground-Based Studies

The development of an optimal design for a space-based lidar wind sounder has been an iterative process as the science community provides better data and product generation algorithms to the LAWS system simulation/impact studies. Without a space-based heritage, the Doppler lidar programs have had to rely on ground-based and airborne experience to provide some sense of the reasonableness of model simulations. As part of this effort, SWA developed a series of computer tools to process and analyze NASA/MSFC ground-based Doppler lidar polypulse-pair and single shot data. Appendix D describes the models and a series of ground-based experiments in system stability, accuracy versus SNR, winds from cirrus decks, single shot pairing and detailed error analyses.

5.0 GLOBE Data in HDF Format

The GLOBE database project involves the development of a system for archiving, distributing and retrieving aerosol data obtained from seven different sites. Over the past several months, the archival strategy was completed for one site (GSFC) with the goal of developing a storage format that could be generalized to data from all sites. The Hierarchical Database Format (HDF) routines called from C programs were used to archive the data. The use of HDF allowed data and meta-data to be stored in the same HDF file. This strategy will make it possible in the future to distribute GLOBE database project files to interested users through the DAACs or the Earth Observing System Data Information System (EOSDIS).

APPENDIX A LAWS SIMULATION MODEL (GLOBAL VERSION)

1.0 Introduction

The LAWS Simulation Model (LSMg) simulates a space-based Doppler lidar wind sounder providing global or regional three-dimensional simulated lidar winds and corresponding errors. The major modules of the LSMg include the platform, orbit, scanner, atmospheric library, line of sight, horizontal wind component and error models.

1.1 Past and Current LSM Applications

Over the past 8 years, NASA has supported SWA to develop LAWS Simulation Models that evaluate the potential impact of direct global wind observations on global climate models and current forecast models (GCM and regional scale). Under previous contracts, SWA developed two basic algorithms for use with simulated Doppler lidar wind profilers (Emmitt and Wood, 1988). A Shot Management Algorithm (SMA) controls timing and placement of lidar pulses and a Multi-Paired Algorithm (MPA) extracts horizontal wind components from the lidar radial velocity observations. These algorithms evolved into a fully integrated 'top to bottom' LAWS Simulation Model (Emmitt et al., 1990) that modeled the platform, orbit, scanner, signal processor along with an atmospheric library that incorporated the effects of atmospheric aerosols, water vapor, clouds, terrain and atmospheric turbulence. SWA used the LSM to address key LAWS issues and trades such as global coverage, accuracy and representativeness of LAWS measurements, data density, signal strength, cloud obscuration and temporal resolution.

Under the current contract, the LSM has evolved into a set of computer models that is schematically depicted in Fig. A.1. The current LAWS Simulation Model (LSMg) was designed to address questions ranging from the feasibility and optimal functionality of a space-based Doppler lidar system to the impact of global winds observations on the predictive ability of GCM forecast models. The LSMg assesses the impact of global winds by providing simulated lidar winds to institutions such as NASA/GSFC and FSU for Observing System Simulation Experiments (OSSEs) as described in Fig. A.2 (Atlas and Emmitt, 1991; Krishnamurti et al., 1991; Rohaly and Krishnamurti, 1993).

1.2 LAWS Simulation Model Inputs and Outputs

A new methodology for using SWA's LAWS Simulation Model (LSMg) to provide simulated LAWS winds and errors to OSSEs was introduced in this contract. Due to the cost of OSSEs and the growing need to expedite the turn around time for impact assessment, the LSMg was recoded. The LSMg was redesigned to run

on the NASA/GSFC CRAY YMP. The LSMg operates via three data file: an operations data file (LSMINP), an orbital coverage data set (COVDAT) and a Global Atmospheric Data Set (GADS). The LSMg operational inputs are read in from LSMINP that define the LAWS simulation run, system configuration, orbital parameters and laser wavelength. Current system and platform configurations are discussed in Section A2.0. A COVDAT file contains satellite and shot locations for a given orbit and scanner configuration and is discussed in Section A3.0. The LSMg shot management algorithms are discussed in Section A4.0. The GADS file contains ECMWF T106 nature run profiles, aerosol and water vapor optical properties, clouds and terrain and is discussed in Section A5.0. Signal processing models are discussed in Section A6.0. The LSMg provides three output files; level 1 LAWS products (LEVEL1), level 2 LAWS products (LEVEL2) and a performance matrix (MATRIX). The level 1 products are defined as simulated lidar line-of-sight winds and associated signal processing variables (Section A7.0). The level 2 products are defined as simulated lidar horizontal wind components and associated observational errors (Section A8.0). The performance display model and graphic algorithms are discussed in Section A9.0.

2.0 System Configurations

The LSMg supports a broad range of laser/optic system configurations. Table A.1 lists the primary parameters used in the LSMg.

Table A.1. System Configuration Parameters

LASER WAVELENGTH (μm)
TRANSMITTED ENERGY (Joules)
TELESCOPE DIAMETER (m)
NADIR SCAN ANGLE (DEG)
PULSE REPETITION FREQUENCY
OPTICAL EFFICIENCY
DETECTOR QUANTUM EFFICIENCY
HETERDYNE MIXING EFFICIENCY
PULSE DURATION

3.0 The Orbit/Scanner Model

The Orbit model provides the satellite latitude and longitude and the inclination angle of the orbit as a function of orbital time. The orbit model solves an oblique spherical triangle algorithm to compute the satellites location. The model assumes a spherical earth. Figure A.3 demonstrates an example of a 13 hour LAWS coverage orbit.

Equation 3.1 gives the speed of the satellite as a function of satellite altitude.

$$V_{\text{sat}} = ((GM/((R_e + Z_s)/1000))^{1/2})/1E06 \quad (3.1)$$

where

V_{sat} (km/s)	satellite velocity
GM	Earth constant, 3.991e14
Z_s (km)	satellite altitude
R_e (km)	radius of earth.

The scanner models computes the latitude and longitude of each lidar shot as a function of atmospheric level and azimuth scan angle. The Eqs. 3.2-3.5 involve the nadir scan geometry angles and swath width, respectively, as shown in Fig. A.4.

$$\alpha = \pi - \text{SIN}^{-1}((Z_s + R_e)/(R_e \cdot \text{SIN}(\phi))) \quad (3.2)$$

$$\gamma = \pi - \phi - \alpha \quad (3.3)$$

$$\theta = \pi/2 - \phi - \gamma \quad (3.4)$$

$$\text{SW} = 2 \cdot \gamma/360 \cdot 2 \cdot \pi \cdot R_e \quad (3.5)$$

where

α (rad)	satellite to shot to center of the earth angle
π	a constant, 3.14159
Z_s (km)	satellite altitude
R_e (km)	radius of earth
ϕ (deg)	nadir scan angle
γ (rad)	satellite to earth's center to shot angle
θ (rad)	slant path elevation angle
SW (km)	swath distance.

The scanner model uses the longitude and latitude of the satellite and the azimuth scan angle of the laser along with the orbital parameters (satellite altitude and velocity, scanner period, etc.) to compute laser shot locations. The model uses an oblique spherical triangle algorithm (Kells, et al, 1940) that solves for a spherical triangle defined by the north pole, the position of the satellite and the position of the shot. The scanner model supports conical and fixed beam patterns as demonstrated in Fig. A.5. The conical scanner gives the latitude and longitude of the lidar shot and the azimuth scan angle for a counterclockwise scanning lidar. Figure A.6 shows the conical scanning geometry convention.

While conical scanning provides the best coverage/accuracy performance, the physical complexity of the large rotating telescope makes a set of fixed telescopes a reasonable alternative. The French BEST program proposed a quad-beam arrangement illustrated in Fig. A.7. The LSMg was upgraded to include a quad-beam simulation. The quad-beam scanner gives the latitude and longitude of the lidar shot for four telescopes with fixed azimuth and nadir look angles.

4.0 Shot Management

Unlike most passive sensors in space, active laser based systems have limited lifetimes (pulses) and are ultimately constrained by available platform power. Such conditions call for some form(s) of resource management that will optimize the number of useful observations and the potential impact on the primary mission objective - i.e., improved understanding of the global circulations and transports.

Management of the lidar pulses has become a core focus of research under this contract. The objectives of shot management include:

- 1) extend mission lifetime;
- 2) optimize within a scan distribution of shots to obtain best wind measurements; and
- 3) optimize global distribution of shots within an orbit to favor regions of high ageostrophic (i.e., tropics, jet streams, major mountain ranges, etc.).

To meet these objectives, seven modes of shot management have been defined (Table A.2). While the detailed options of scheduling lidar pulses are unlimited, the general sense of the management is to use a finite number of shots to achieve the best set of data for a given mission objective. For example, if the mission objective is to provide full global coverage every 12 hours, then a combination of modes 2 and 3 is in order. If the mission objective is to provide direct measurements of winds in regions of ageostrophic flows, then a combination of modes 4 and 5 may be proper. If the mission objective is to provide data preferentially in regions where a forecasting model is having difficulties, then mode 7 would be employed.

The LSM is designed to invoke modes 1 through 5. The most common mode combination is 2 plus 3. Mode 2 applies only to the conical scanner. Given the shot number in a no cosine modification scan (Eq. 3.6) and the rotation rate, the model computes a new scan azimuth angle (Eq. 3.7) to back out a new time for the shot (Eq. 3.8). Figure A.8 gives a comparison of

Table A.2 LAWS Shot Management Modes

MODE	DESCRIPTION	Ratio ¹
1	Constant PRF at 100% duty	1
2	Cosine modulation of PRF within a scan period	1
3	12-hour polar redundancy suppression	.7
4	Tropical enhanced	.7
5	Ageostrophic priority	.1-.5
6	Condition recognition (on board)	.7- 1
7	Condition recognition (up-linked)	.7- 1

Note 1: Ratio of shots taken per orbit for each mode compared to Mode 1.

the conical scan with and without the cosine modifier.

$$N_{\text{sh}} = \text{NINT}((T/(V_{\text{rot}}/\#_{\text{sh}}) - (\text{INT}(T/V_{\text{rot}}) \cdot \#_{\text{sh}})) \quad (3.6)$$

$$\text{IF } N_{\text{sh}} \geq 1 \text{ AND } N_{\text{sh}} \leq (0.5 \cdot \#_{\text{sh}})$$

$$\beta' = \text{COS}^{-1}(1.0 - (4 \cdot N_{\text{sh}})/((\#_{\text{sh}}/V_{\text{rot}}) \cdot V_{\text{rot}})) \quad (3.7)$$

$$\text{IF } N_{\text{sh}} \geq (0.5 \cdot \#_{\text{sh}}) \text{ AND } N_{\text{sh}} \leq \#_{\text{sh}}$$

$$\beta' = 2\pi - \text{COS}^{-1}((4 \cdot N_{\text{sh}})/((\#_{\text{sh}}/V_{\text{rot}}) \cdot V_{\text{rot}}) - 3) \quad (3.8)$$

$$\text{TIME} = V_{\text{rot}} \cdot \beta' / 2\pi + T$$

where

T	unmodified time,
T(s)	change in time between shots,
# _{sh}	number of shots in one scan,
N _{sh}	shot number in scan,
V _{sat} (km/s)	satellite velocity,
V _{rot} (s ⁻¹)	scanner rotation,
β' (deg)	modified azimuth scan angle,
TIME (s)	modified time.

5.0 Atmosphere Generator Model for the Global Atmospheric Data Set

The Atmosphere Generator Model (AGMg) creates Global Atmospheric Data Sets (GADS) that the LSMg uses to obtain atmospheric profiles as a function of latitude and longitude. Each profile contains an ECMWF T106 Nature Run profile, aerosol and water vapor optical properties, clouds and terrain. GADS is a direct access file created by using the T106 data in liaison with the LSMg optical property models, cloud models, and terrain data set. The spacial resolution of the data set is 111.11 km by 111.11 km and the temporal resolution is 3 hours. It contains 32,412 grid area profiles (records) per time period. A record's content is defined below.

Table A.3. GADS Record Content

-
- center of grid area latitude (deg)
 - center of grid area longitude (deg)
 - surface pressure (mb)
 - surface altitude (km)
 - cloud cover (0-1)
 - level index for base level above the terrain
 - tropopause height level index
 - surface temperature (k)
 - surface dewpoint temperature (k)
 - surface horizontal wind component U (m/s)
 - surface horizontal wind component V (m/s)
 - convective precip (mm/day)
 - height profile (m)
 - temperature profile (k)
 - relative humidity profile (%)
 - u horizontal wind profile (m/s)
 - v horizontal wind profile (m/s)
 - vertical velocity profile (pa/s)
 - cloud percentage profile (%)
 - integrated cloud percentage profile (%)
 - integrated cloud percentage profile as seen by LAWS (%)
 - incremental cloud amount (%)
 - layer index for a cirrus cloud
 - cloud type index
 - 0 - opaque cloud or no cloud
 - 1 - thick cirrus cloud
 - 2 - thin cirrus cloud
 - aerosol backscatter profile at 2.1 μm
 - aerosol backscatter profile at 9.11 μm
 - aerosol backscatter profile at 10.59 μm
 - molecular attenuation profile at 2.1 μm
 - molecular attenuation profile at 9.11 μm
 - molecular attenuation profile at 10.59 μm

- cloud backscatter profile
- cloud attenuation profile

The T106 profile data has data for the following pressure levels: 1013, 1000, 850, 700, 500, 400, 300, 250, 200, 150, 100, 70, 50, 30, 10 mb. Figures A.9-A.25 are global maps of the GADS on January 16, 1987, 0300Z, for temperature, relative humidity and horizontal wind components at the surface and at the 500 mb level.

5.1 Optical Property Models

The AGMg has several options for estimating aerosol backscatter and molecular (water vapor) attenuation coefficients. The first option uses AFGL optical property models (LOWTRAN 7) in conjunction with the ECMWF global circulation data sets. A second method uses Global Backscatter Experiment (GLOBE) data sets in conjunction with global circulation model data sets. A third option uses the baseline atmosphere median profiles (Wood and Emmitt, 1991) in conjunction with the global circulation model data sets.

5.1.1 AFGL Optical Property Models

The AGMg contains a "trimmed down" version of the LOWTRAN 7 aerosol models (Kneizys et al., 1983) and FASCODE (Gallery et al., 1983) molecular attenuation models. This algorithm coupled with a global data base of LOWTRAN inputs and ECMWF meteorological profiles provides aerosol backscatter and water vapor attenuation for the laser wavelengths, 9.11, 10.59 and 2.1 μm . The optical property's natural variability due to altitude, location, seasons, and meteorological conditions are taken into consideration in the model.

The AGMg optical property model reads in an input index from a FORTRAN direct access data file, OPTTOP. Each index is stored as a function of latitude and longitude (-90S to 90N for -180W to 180E) at a $1^\circ \times 1^\circ$ resolution. The index is used as a pointer for 5 pre-defined LOWTRAN inputs. The inputs are location profile model, haze model, coastal influence parameter, stratosphere model and upper atmosphere model. Given the ECMWF meteorological profile and shot location, the AGMg can estimate the optical properties as shown in Table A.4.

The OPTTOP data base is considered to be a baseline nominal data base. The model location index is a function of latitude. The haze model is a function of continent vs. desert vs. ocean location. The current version of the data set does not use the urban, ocean or fog models, but the data bases are stored in the AGMg for future upgrades. The coastal influence is a function of distance from a land mass (only three of the AFGL LOWTRAN options

Table A.4. Optical Property Model Options

Seasonal Models Location	Aerosol Haze Models	Coastal Influence Parameter	Stratospheric Model	Upper Atm. Model
Tropical	Rural 23 km vis	Open Ocean	Background Stratospheric	Normal Upper
Subtropical Summer	Rural 5 km vis	Midway to Continent	Moderate Aged Aerosol	Extreme Upper
Subtropical Winter	NAVY Maritime	Close to Continent	Moderate Fresh Aerosol	Volcanic to Normal
Midlatitude Summer	Ocean		High Aged Aerosol	Normal to Volcanic
Midlatitude Winter	Urban		High Fresh Aerosol	
Sub-Arctic Summer	Tropo-spheric		Extreme Aged Aerosol	
Sub-Arctic Winter	Desert		Extreme Fresh Aerosol	
U.S. Stndrd Summer	Fog 1			
U.S. Stndrd Winter	Fog 2			

are used). The stratosphere and upper atmosphere variables are set to clean background mode. Any variations to the computed baseline optical properties are made in the LSMg. For example, if one wanted to include a volcanic stratospheric dust level or an advection of maritime aerosols over Europe, one would use the LSMg to modify the baseline inputs as a function of latitude and longitude.

Given location and LOWTRAN pre-defined inputs along with the vertical profile of meteorological data from the ECMWF data set, the AGMg computes the scattering coefficient, backscatter phase function and the aerosol scaling parameter as a function of altitude. Aerosol backscatter is computed by Eq. 5.1 with consideration of aerosol natural variability due to local wind speed, temperature, relative humidity and standard visual range (Hanel, 1972). The AGMg computes the attenuation coefficient, shown in Eq. 5.2, from the molecular (water vapor) absorption, aerosol absorption, molecular scattering and aerosol scattering.

$$\beta_{\pi} = (\sigma_s \cdot P_{\pi} \cdot SCL) / 1000 \quad (5.1)$$

$$\alpha = \alpha_m + \sigma_m + (\alpha_a + \sigma_a) \cdot SCL + RAY \quad (5.2)$$

where

β_π ($\text{m}^{-1}\text{sr}^{-1}$)	aerosol backscatter coefficient
P_π (sr^{-1})	backscatter phase function
SCL	aerosol scaling function,
α (km^{-1})	attenuation coefficient
α_m (km^{-1})	molecular absorption coefficient
α_a (km^{-1})	aerosol absorption coefficient
σ_m (km^{-1})	molecular scattering coefficient
σ_s (km^{-1})	aerosol scattering coefficient
RAY (km^{-1})	Rayleigh scattering coefficient.

5.1.2 Aerosol Backscatter and Molecular Attenuation Distributions

Figures A.26-27 are illustrations of global distributions of aerosol backscatter coefficients at three levels for single time period of the ECMWF nature run. Below 850 mb, LOWTRAN/FASCODE is used to generate the backscatter. Above 850 mb to the tropopause, one of the three median GLOBE profiles is used, depending upon latitude and season, for backscatter. The three profiles obtained during GLOBE II were provided by Robert Menzies (Jet Propulsion Laboratory) and are shown in Fig. A28. Variability around the median values is slewed to variations in the relative humidity profiles provided by the ECMWF nature run. All the attenuation coefficients are computed from LOWTRAN/FASCODE models.

5.2 Cloud Model

The AGMg cloud model is based on the Slingo Cloud parameterization scheme (Slingo, 1987). The Slingo approach provides distinctions between high and mid-tropospheric stratiform clouds, convective clouds with and without anvil cirrus, low level clouds driven by weak vertical motion or inversion capped moist boundary layers.

5.2.1 Convective cloud

The convective cloud is inferred from 3 hour integrated precipitable water from the T106 meteorological profiles. A critical threshold value of 0.14 mm/day must be met for a convective cloud to be present. If the threshold is met, the convective cloud base amount is empirically derived. A restrictive limit of 80% is set for the convective cloud amount.

$$cc = 0.2473 + 0.1258 * cppt \quad (5.3)$$

where

cc is the base layer convective cloud amount (%)
 cppt is the integrated precipitable water (mm/day).

The top of the convective cloud layer is a function of the base layer convective cloud amount and the tropopause height. The cloud top is limited at the tropopause.

$$cc_{top} = (cc + 0.2) * TH \quad (5.4)$$

where

cc_{top} is the convective cloud top (km)
 cc is the base layer convective cloud amount (%)
 TH is the tropopause height (km).

The convective cloud coverage between cloud base and cloud top is defined as 25% of the base layer convective cloud amount.

If the top of the convective cloud is above the 400 mb layer and the integrated precipitable water more than 3.4 mm/day, then an anvil is defined. All anvil clouds are considered to be thick cirrus layers. The anvil cloud amount (%) is defined as

$$cc_{anv} = 2 (cc - 0.3) \quad (5.5)$$

5.2.2 High Non-Convective Clouds

All non-convective high clouds are derived as a function of relative humidity from the ECMWF T106 meteorological profile. A high layer cloud is only derived when the tropopause height is higher than the 400 mb layer. The AGMg evaluates the T106 relative humidity profile to find the highest value which is used to compute a relative humidity threshold.

$$RH_{thr} = (RH_{hgh} - 0.8) / (1.0 - 0.8) \quad (5.6)$$

where

RH_{thr} is the high relative humidity threshold (%)
 RH_{hgh} is the high relative humidity (%).

If the relative humidity threshold is greater than 0%, then high level cloud cover (%) is estimated as follows

$$HC = (RH_{thr})^2 \quad (5.7)$$

The cloud is considered to be thin cirrus. See Section A5.2.6 for discussion on how this percent high cloud is used to provide variability in cloud optical depths.

5.2.3 Middle Non-Convective Clouds

All non-convective middle clouds are derived as a function of relative humidity from the ECMWF T106 meteorological profile. If there was a convective cloud or a high layer cloud, the AGMg dries out the T106 relative humidity profile.

$$RH = RH * (1.0 - CC) \quad (5.8)$$

where

CC is either the convective or high layer cloud cover (%)

Like the high cloud algorithm, the AGMg finds the highest relative humidity in the profile and computes the relative humidity threshold (Eq. 5.6). If the relative humidity threshold is greater than 0%, then middle layer cloud cover (%) is estimated as follows

$$MC = HC + (RH_{thr})^2 \quad (5.9)$$

5.2.4 Low Non-Convective Clouds

The estimate of low level non-convective clouds is based upon two parameters: vertical velocity and potential temperature profile. From vertical velocity, the AGMg finds the layer with the largest negative vertical velocity and computes the critical relative humidity (Eq. 5.8) for the layer. If the vertical velocity is less than 0.1, the cloud cover is defined as

$$LC = (RH_{thr})^2 \quad (5.10a)$$

else

$$LC = (RH_{thr})^2 * (-10 * VV) \quad (5.10b)$$

where

VV (m/s) is the vertical velocity for the layer.

The potential temperature is used only if there was no cloud cover from the vertical velocity method. Potential temperature lapse rates are computed for every sublayer between 1000 mb and 700 mb as follows

$$\theta_{lr} = -6.67 * \Delta T / \Delta P \quad (5.11)$$

where

θ_{lr} is the potential temperature lapse rate
 ΔT is the change in temperature over the layer

ΔP is the change in pressure over the layer.

If the lapse rate is greater than zero, then the model tests upon relative humidity to compute the cloud cover. If the relative humidity is less than 60%, there is no cloud cover. If the relative humidity is greater than 60% and lower than the threshold relative humidity, then the cloud cover is

$$LC = \theta_{1r} * (1 - (RH_{thr} - RH)/(1 - RH_{thr})) \quad (5.12a)$$

else

$$LC = \theta_{1r} \quad (5.12b)$$

5.2.5 Global Statistics and Empirical Adjustments

We expect that clouds will be in the field-of-view (FOV) of LAWS 70-80% of the time. This estimate is based upon the recently reported analysis of two years of HIRS data (Menzel et al., 1992), the cirrus climatology derived from SAGE data by Woodbury and McCormick (1986) and the Nimbus-7 global cloud climatology (Stowe et al., 1989). Much of this cloud coverage is high cloud (above 400-500 mb) and is semi-transparent (~ 30-40%). Very thin or subvisual cirrus ($\tau < .07$) is not detected by HIRS or Nimbus-7 but may be occasionally represented in the SAGE observations. Thus, we conclude that the occurrence of very thin cirrus is clearly underestimated in current climatologies.

Of particular interest to the LAWS program are the semi-transparent and optically thin clouds since they provide strong returns without full extinction. When one considers that the statistics given above are, in most cases, exclusive - i.e., they do not provide a good representation of coincident clouds at different altitudes, it is very likely that there are many occasions when there are multi-layers of thin clouds underlaid by opaque clouds.

The ECMWF T106 Nature Run provides accumulated convective precipitation (based upon Kuo's scheme) and the total cloud coverage. Unfortunately, layer-by-layer information on cloud cover is not provided. We have developed a means to use the basic concepts within the Slingo scheme to reproduce the layer-by-layer cloud statistics that we need for LAWS simulations (see Section 5.2).

The distribution of clouds (over a 1 x 1 km area) based upon the ECMWF total cloud coverage as a function of latitude are shown in Figs. A.29 and A.30. While the total coverage is quite reasonable and compares well with the Nimbus-7 statistics, the amount of midlevel cloud forecast for the tropics is considerably less than the 30-40% reported using the satellite data. Conversations with the National Meteorological Center's (NMC)

personnel (Pan and Baker) suggest that this is an ongoing point for discussion and study with the modeling community suggesting that the interpretation of midlevel cloud in satellite imagery may be faulty.

For now, we do not attempt to force the model's clouds to fit the climatology. The resulting global coverage maps for a single time period (0300 GMT) are shown in Figs. A.31-A.34.

5.2.6 Cloud Optical Properties

All cloud backscatter values are preset in the AGMg to be $1e-06 \text{ m}^{-1} \text{ sr}^{-1}$. We believe this value is properly conservative, since recent midlayer cloud backscatter, measured with a lidar in the Antarctic, range from $1e-06$ to $1e-04 \text{ m}^{-1} \text{ sr}^{-1}$ (Del Guasta et al., 1993). Once a lidar shot gets a return from an opaque cloud, the shot is considered to be fully attenuated and is terminated. For cirrus cloud layers, we allow all the shots a finite probability to pass through to the next layer. The cirrus cloud attenuation model is a modified version of the analytical LOWTRAN cirrus algorithm (Kneizys, et al., 1983), where

$$\tau = e^{-0.14 * L^2} \quad (5.13)$$

where

τ is the cirrus transmittance
 L is the cirrus cloud thickness.

Since the AGMg is restricted to the coarse vertical resolution of the Nature Run, SWA uses the cirrus cloud percentage as a surrogate for cloud optical thickness.

The major assumption is that while the Slingo model derives a percent cirrus cloud coverage (i.e., 30%) from an average relative humidity within a grid volume, it is just as reasonable to interpret a thickness tendency from the same fields. Instead of using the percent coverage as literally meaning that 30% of the grid has cirrus cloud and 70% is totally cloud-free, the AGMg assumes that the whole grid area is covered by a cirrus cloud that has an optical thickness that scales to the percent coverage. The cirrus cloud attenuation is defined as

$$ci_{att} = 10^\alpha * (CLD_\% * 10)^2 \quad (5.14)$$

where

ci_{att} is the cirrus cloud attenuation
 α is the LOWTRAN cirrus attenuation coefficient for a 1 km thick layer
 $CLD_\%$ is the cirrus cloud percentage cover.

5.3 Atmospheric Turbulence Model

The LSMg has two options for estimating subgrid scale variance. The first method uses rawinsonde uncertainties (300 x 300 km area) as a function of altitude as sampling scale variance in the gridded area. The second method attempts to better represent the sampling scale turbulence on the ECMWF grid scale and to provide "realistic" variability in the winds based upon the mean wind field. The model represents the uncertainties by scaling them mean ECMWF wind speed by 20%. Using one day of the ECMWF data, we computed the global distribution of variance for 12 atmospheric pressure levels. Table A.4 compares the total global averages with the NMC OI rawinsonde profiles and suggest that the simulated variances are not unreasonable. Figures A.35-A.40 show the global U and V variances for 500 mb and 250 mb levels.

Table A.4. Comparison of the NMC rawinsonde variances and the global average variances obtained by the LSM using a 24-hour sample of ECMWF data.

P (mb)	NMC Old	NMC New	LSMg Global Average
1000	1.8	1.4	1.44
850	1.8	2.2	1.65
700	2.4	2.4	1.81
500	3.8	2.8	2.42
400	4.7	3.4	3.00
300	5.9	3.4	3.61
250	5.9	3.2	3.87
200	5.9	3.0	4.00
150	5.5	2.7	3.83
100	4.9	2.5	3.12
70	4.9	2.5	2.80
50	3.9	2.7	2.80

5.4 Terrain Model

The terrain data base is a 1° x 1° direct access data file (OPTTOP) contains, in addition to the LOWTRAN index inputs, land elevation (M) and sea depths (M) for the globe.

6.0 Signal Processing Models

The LSMg has the option to use the narrow band signal to noise model or a consensus curve algorithm for signal processing of the lidar signal.

6.1 Narrow Band Signal-to-Noise and Line-of-Sight Uncertainty Models

There are several signal-to-noise (SNR) equations that have been suggested for use with LAWS. The narrow band SNR equation (along with default values) that we use in the LSMg is:

$$\text{SNR}_N = \frac{\pi \cdot c \cdot \eta_1 \cdot \eta_2 \cdot \eta_3 \cdot \eta_4 \cdot J \cdot D^2 \cdot \tau \cdot \beta \cdot e^{-2 \int \alpha(r) dr}}{8 \cdot h_v \cdot (R^2 + (.25 \cdot D \cdot D/\lambda)^2)} \quad (6.1)$$

where

c = speed of light (m/s)
 η_1 = heterodyne quantum efficiency
 η_2 = optical efficiency
 η_3 = beam shape factor
 η_4 = truncation factor
 J = laser power (Joules)
 D = mirror diameter (m)
 τ = pulse length (sec)
 β = backscatter ($\text{m}^{-1} \text{sr}^{-1}$)
 e = 2 way attenuation
 h_v = photon energy (J)
 R = slant range (m)
 λ = laser wavelength (m)

As with the lidar SNR equation, there are several radial or LOS velocity error estimates, σ_r , that have been suggested for use with LAWS. While the Cramer-Rao Lower Bound may provide a limit to the extraction of a velocity estimate from a noisy signal, we have chosen the more conservative estimate based upon pulse pair autocorrelation processing of the Doppler signal. The following is derived from Eq. 6.22a in Doviak and Zrnic (1984).

$$\sigma_r = \frac{\lambda}{4\pi} \cdot \frac{f}{2t} \cdot .5 \quad (2 \pi^{1.5} W + 16 \pi^2 W^2 / \text{SNR}_w + 1 / \text{SNR}_w^2) \cdot .5 \quad (6.2)$$

where

λ = wavelength (m)
 V_{max} = maximum velocity measured
 f = sampling frequency = $2 \cdot V_{\text{max}} / \lambda$
 t = pulse duration (sec)
 W = normalized frequency spread of return signal (m/s)
 V_{bw} = uncertainty due to pulse bandwidth (m s^{-1})
 V_{atm} = uncertainty due to turbulent eddies and wind shear within the pulse volume
 SNR_w = $\sqrt{2\pi} W \text{SNR}_N$

6.2 Consensus Curves Model

Studies by Mike Hardesty and Barry Rye of NOAA have provided a general consensus algorithm used to simulate the processing of LAWS data.

The consensus algorithm computes wideband signal-to-noise (SNR_w) for each lidar shot along the slant path to a T106 nature run altitude as follows:

$$SNR_w = \left[\frac{\pi}{16 \cdot h \cdot R^2 \cdot V} \right] * [\eta_m \cdot \eta_o \cdot \eta_{qe}] * [E_T \cdot D^2] * [\tau^2 \beta] * \lambda^2 \quad (6.3)$$

$\Rightarrow 1.09 \times 10^{19}$

where

R	=	range
V	=	maximum wind window
η_m	=	mixing efficiency
η_o	=	optical transmission
η_{qe}	=	quantum efficiency
E_T	=	energy/pulse
D^2	=	area of primary
τ^2	=	two-way transmission
β	=	backscatter
λ^2	=	wavelength

The SNR_w is used to look up the probability of detection (POD) as shown in Fig. A.41a and the false alarm ratio (FAR) as shown in Fig. A.41b. The model uses the POD and the FAR to compute the probability of consensus as shown below

$$FARM = (FAR/100 * POD) / (1 - FAR/100) \quad (6.3)$$

$$CONS = POD + FARM$$

If the probability of consensus is greater than a random white noise value, the shot passes consensus. Once a shot passes consensus, the consensus algorithm test if the false alarm ratio is greater than a random white noise value. If true, then the shot is not a false alarm and the line-of-sight uncertainty is set to 0.5 m/s.

The measurement uncertainty for the observational error model is computed from Fig. A.41c (see Section 8.3).

7.0 Line-of-Sight Wind Products

If the lidar shot is not a false alarm, the LSMg computes the simulated line-of-sight wind velocity as

$$V_{los} = (U_{hwc} * \cos(\beta) + V_{hwc} * \sin(\beta)) * \cos(\theta) \quad (7.1) \\ + W_{vwc} * \sin(\theta) + LOS_{unc}$$

where

V_{los} is the line-of-sight wind velocity (m/s)
 U_{hwc} is the cross track wind velocity at the shot location (m/s)
 V_{hwc} is the along track wind velocity at the shot location (m/s)
 W_{vwc} is the vertical velocity at the shot location (m/s)
 θ is the elevation angle (radians)
 β is the azimuth scanning angle (radians)
 LOS_{unc} is the line-of-sight uncertainty (m/s).

The along track and cross track winds at the shot location are computed from the input GADS horizontal wind components, orbit inclination and the sampling scale uncertainties that are obtained by using a random Gaussian distribution around the GADS turbulence profiles. The line-of-sight uncertainty comes from the consensus algorithm.

If the lidar shot is a false alarm, the LSMg compute the line-of-sight wind velocity using a random white noise value and the velocity maximum window as shown below

$$V_{los} = (RD - 0.5) * 2 * V_{max} \quad (7.2)$$

where

V_{los} is the line-of-sight wind velocity (m/s)
 RD is a random value (0-1)
 V_{max} is the velocity maximum window.

The LSMg LEVEL1 output products are listed in Table A.5.

Table A.5. Line-of-Sight Wind Products (LEVEL1)

Global grid box index for the LOS wind
Latitude of the LOS wind (deg)
Longitude of the LOS wind (deg)
Altitude of the LOS wind (km)
Time of the LOS wind (s)
Azimuth scan of the LOS wind (deg)
Sampling scale uncertainty in U of the LOS wind (m/s)
Sampling scale uncertainty in V of the LOS wind (m/s)
Sampling scale uncertainty in W of the LOS wind (m/s)
Line-of-sight uncertainty of the LOS wind (m/s)
Simulated line of sight wind velocity (m/s)

8.0 Horizontal Wind Component Models

The LSM uses either the Multi-Paired Algorithm (MPA) or the least squares techniques to compute the U and V horizontal wind components.

8.1 Multi-Paired Algorithm (MPA)

The MPA matches forward and aft lidar line-of-sight wind velocities to compute weighted horizontal wind components. The MPA weights the winds by angular separation from orthogonality and by the distance between the lidar shots (Emmitt and Wood, 1988). The distance weight and angle weight are shown in Eqs. 8.1 and 8.2, respectively.

$$D_{wt} = 1 - (((\phi_a * \theta_c * \cos(\theta_a) - \phi_f * \theta_c * \cos(\theta_f))^2 + ((\theta_a + 90) * \theta_c - (\theta_f + 90) * \theta_c)^2)^{1/2}) / D \quad (8.1)$$

$$\alpha_{wt} = 1.0 - ((\pi/2 - (\beta_a - \beta_f)) * (2/\pi))^4 \quad (8.2)$$

where

α_{wt}	angle shot pair weight
D_{wt}	distance shot pair weight
θ_c (km/deg)	degrees to kilometers conversion factor at equator (111.11)
D (km)	diagonal distance across the grid area
ϕ_a (deg)	longitude of the aft shot
ϕ_f (deg)	longitude of the forward shot
θ_a (deg)	latitude of the aft shot
θ_f (deg)	latitude of the forward shot.

The U and V horizontal wind components are computed by Eqs. 8.3 and 8.4, respectively.

$$U = (VLOS_a / (\cos(\theta) * \cos(\beta_a)) - (VLOS_f * \tan(\beta_a)) / (\cos(\theta) * \sin(\beta_f))) / (1.0 - \tan(\beta_a) / \tan(\beta_f)) \quad (8.3)$$

$$V = (VLOS_a - U * \cos(\theta) * \cos(\beta_a)) / (\cos(\theta) * \sin(\beta_a)) \quad (8.4)$$

where

U (m/s)	U horizontal wind component
V (m/s)	V horizontal wind component
VLOS _a (m/s)	line-of-sight lidar wind for aft shot
VLOS _f (m/s)	line-of-sight lidar wind for forward shot
θ (deg)	elevation angle
β_a (deg)	scanner angle for aft shot
β_f (deg)	scanner angle for forward shot.

An analytical expression for the MPA Errors dependent upon shot separation was derived. The line-of-sight (LOS) velocities for two shots from different perspectives can be expressed as follows:

$$VLOS_1 = (U_1 \cos\phi_1 + V_1 \sin\phi_1) \cdot \sin\theta + W_1 \cos\theta + N_1 \quad (8.5)$$

$$VLOS_2 = (U_2 \cos\phi_2 + V_2 \sin\phi_2) \cdot \sin\theta + W_2 \cos\theta + N_2 \quad (8.6)$$

where:

$VLOS_i$	=	line-of-sight velocity for shot i
U_i	=	u component of the wind at location i
V_i	=	v component of the wind at location i
W_i	=	w component of the wind at location i
N_i	=	random noise
ϕ_i	=	azimuth for shot i from mathematic +x
θ	=	elevation angle from the nadir

Given the scarcity of shots, the following assumptions are made to solve for the horizontal wind components:

$$u_1 = u_2; v_1 = v_2; w_1 = w_2 = 0.0; \phi_2 = -\phi_1; N_1 = N_2 = 0$$

Thus:

$$VLOS_1 = (U \cdot \cos\phi_1 + V \sin\phi_2) \cdot \sin\theta \quad (8.7)$$

$$VLOS_2 = (U \cos\phi_2 + V \sin\phi_2) \cdot \sin\theta \quad (8.8)$$

To get two equations in two unknowns (u,v) we substitute $-\theta_1$ for θ_2 :

$$VLOS_1 = (u \cos\phi_1 + v \sin\phi_1) \cdot \sin\theta$$

$$VLOS_2 = (u \cos\phi_1 - v \sin\phi_1) \cdot \sin\theta$$

Solving for u:

$$VLOS_1 + VLOS_2 = 2 u \cos\phi_1 \cdot \sin\theta \quad (8.9)$$

$$u = (VLOS_1 + VLOS_2) / (2 \cos\phi_1 \sin\theta)$$

Solving for v:

$$VLOS_1 - VLOS_2 = 2 v \sin\phi_1 \cdot \sin\theta \quad (8.10)$$

$$v = (VLOS_1 - VLOS_2) / (2 \sin\phi_1 \sin\theta)$$

However, if U_2 , U_1 and V_2 , V_1 then we make the following substitution into Eq. 8.8:

$$U_2 = U_1 + u$$

$$V_2 = V_1 + v$$

$$VLOS_2 = (u \cos\phi_2 + v \sin\phi_2) \cdot \sin\theta + (u \cos\theta_2 + v \sin\theta_2) \cdot \sin\theta \quad (8.11)$$

$$= (u \cos\phi - v \sin\phi) \cdot \sin\theta + (u \cos\phi - v \sin\phi) \sin\theta$$

Solving for u and v using Eqs. 8.7 and 8.11:

$$u = (VLOS_1 + VLOS_2) / (2 \cos\phi \sin\theta) + \frac{\partial u}{2} - \frac{\partial v \tan\phi}{2}$$

$$v = (VLOS_1 - VLOS_2) / (2 \sin\phi \sin\theta) - \frac{\partial u}{2 \tan\phi} + \frac{\partial v}{2}$$

The correct u and v values would be $u + \frac{1}{2} u$ and $v + \frac{1}{2} v$. Therefore, the errors due to having different horizontal velocities at shot locations 1 and 2 are:

$$U_{\text{error}} = - \partial v \tan\phi / 2 \quad (8.12)$$

$$V_{\text{error}} = - \partial u / 2 \tan\phi \quad (8.13)$$

If u and v are statistically non-zero (i.e., related to some coherent structure) then there will be a residual error regardless of the number of shots used in the velocity estimates. With Eqs. 8.12 and 8.13 we can compute the average u and v errors for a given shot pair spacing. For example ($\phi_1 = 3010$):

$$\frac{du}{dx} = 10^{-5} \text{ s}^{-1}$$

$$u = du/dx \cdot x \quad (x \text{ is } x(u_2) - x(u_1))$$

$$\text{Let } x = 50 \text{ km} \quad u = .5 \text{ m/s}$$

$$u_{\text{error}} = 0$$

$$v_{\text{error}} = .43 \text{ m s}^{-1}$$

8.2 Least Squares Model

The least squares model performs a least squares fit to the lidar shots within a grid area to produce SNR weighted U and V horizontal wind components (Press et al., 1986).

8.3 Observational Errors

For a given number of lidar shots in a global grid area and at a one altitude, the LSMg computes the observational uncertainty in the global grid as follows

$$dn = 1 - \tan(\beta_f)/\tan(\beta_a) \quad (8.14)$$

$$u_{12} = \sigma_u^2 * (1/dn - .5)^2 \quad (8.15)$$

$$u_{22} = \sigma_v^2 * (\tan(\beta_f)/dn)^2 \quad (8.16)$$

$$u_{32} = \sigma_w^2 * (\tan(\phi)/\cos(\beta_f)/dn)^2 \quad (8.17)$$

$$u_{42} = 0 \quad (8.18)$$

$$u_{52} = \sigma_{los}^2 * (1/\cos(\phi)/\sin(\beta_a)*\tan(\beta_f)/dn)^2 + \sigma_{los}^2 * (1/\cos(\phi)/\cos(\beta_f)/dn)^2 \quad (8.19)$$

$$\sigma_u = (u_{12} + u_{22} + u_{32} + u_{42} + u_{52}) / (0.5 * nn) \quad (8.20)$$

$$\sigma_u = \text{sqrt}(\sigma_u) \quad (8.21)$$

where

nn	is the number of shots in the global grid,
ϕ	is the nadir scan angle (radians),
β_f	is the forward scan angle (radians),
β_a	is the aft scan angle (radians),
σ_u	is the cross track uncertainty (m/s),
σ_v	is the along track uncertainty (m/s),
σ_w	is the vertical velocity uncertainty (m/s),
σ_{los}	is the line-of-sight uncertainty (m/s),
σ_u	is the observational uncertainty (m/s).

9.0 Performance Display and Graphics Routines

Throughout the course of this contract, SWA has developed a series of graphics and display models for the LAWS simulations. The mapping algorithms allow the user to produce global (satellite view) or regional (mercator projection) graphics. The mapping models are the lidar shot location display, the lidar wind display model (plots input winds, output winds or both) and the T106/GADS color mapping model. A visual basic LAWS performance display model shown in Fig. A.42 was also developed which allows the user to plot line-of-sight and/or horizontal wind performance diagrams. The displays can be made for global performance or for a specific latitudinal band. The model has options for color or black and white.

FIGURE CAPTIONS

- Figure A.1: Block diagram for the LAWS Simulation Model (global version).
- Figure A.2: Schematic of the Observing System Simulation Experiments (OSSEs) for LAWS.
- Figure A.3: A 13-hour global coverage for LAWS at a 525 km orbit.
- Figure A.4: LAWS nadir scan geometry schematic.
- Figure A.5: Comparison of a conical (no modulation) and fixed beam (quad telescopes) scan patterns.
- Figure A.6: Conical scan geometry illustration.
- Figure A.7: Schematic configuration for a quad beam platform.
- Figure A.8: Comparison of conical scan with and without a cosine modification.
- Figure A.9: Global temperature color plot at the Prime Meridian for the Global Atmospheric Data Set (GADS) (January 21, 1980, 0600Z) at 1000 mb.
- Figure A.10: As for Fig. A.9 but for 500 mb.
- Figure A.11: Global temperature color plot at the International Dateline for the Global Atmospheric Data Set (GADS) (January 21, 1980, 0600Z) at 1000 mb.
- Figure A.12: As for Fig. A.11 but for 500 mb.
- Figure A.13: As for Fig. A.9 but for 250 mb.
- Figure A.14: As for Fig. A.11 but for 250 mb.
- Figure A.15: Global temperature color plot at the South Pole for the Global Atmospheric Data Set (GADS) (January 21, 1980, 0600Z) at 1000 mb.
- Figure A.16: Global relative humidity color plot at the Prime Meridian for the Global Atmospheric Data Set (GADS) (January 21, 1980, 0600Z) at 1000 mb.
- Figure A.17: As for Fig. A.16 but for the International Dateline.
- Figure A.18: As for Fig. A.16 but for 500 mb.

- Figure A.19: Global relative humidity color plot at the International Dateline for the Global Atmospheric Data Set (GADS) (January 21, 1980, 0600Z) at 500 mb.
- Figure A.20: Global relative humidity color plot at the Prime Meridian for the Global Atmospheric Data Set (GADS) (January 21, 1980, 0600Z) at 250 mb.
- Figure A.21: As for Fig. A.19 but for 250 mb.
- Figure A.22: Horizontal wind components, northeast of equatorial Prime Meridian, for the Global Atmospheric Data Set (GADS) (January 21, 1980, 0600Z) at 1000 mb.
- Figure A.23: Horizontal wind components, southeast of equatorial Prime Meridian, for the Global Atmospheric Data Sets (GADS) (January 21, 1980, 0600Z) at 1000 mb.
- Figure A.24: As for Fig. A.22 but for 500 mb.
- Figure A.25: As for Fig. A.23 but for 500 mb.
- Figure A.26: Global Atmospheric Data Set (GADS) aerosol backscatter for January 16, 1979, 0600Z at 850 mb.
- Figure A.27: As for Fig. A.26 but for 250 mb.
- Figure A.28: Median backscatter profiles from the Global Backscatter Experiment (GLOBE).
- Figure A.29: Low, middle and high integrated cloud amounts using the Slingo model with the January 16, 1979 GADS.
- Figure A.30: Comparison of the global average integrated cloud cover from the Slingo model to the GADS integrated cloud amount.
- Figure A.31: GADS low level integrated cloud amount for January 16, 1979, 0600Z.
- Figure A.32: As for Fig. A.31 but for midlevel integrated cloud amount.
- Figure A.33: As for Fig. A.31 but for high level integrated cloud amount.
- Figure A.34: GADS total integrated cloud cover for January 16, 1979, 0600Z.

Figure A.35: GADS u component variance for January 16, 1979, 0600Z at 850 mb.

Figure A.36: As for Fig. A.35 but for v component.

Figure A.37: As for Fig. A.35 but for 500 mb.

Figure A.38: As for Fig. A.36 but for 500 mb.

Figure A.39: As for Fig. A.35 but for 250 mb.

Figure A.40: As for Fig. A.36 but for 250 mb.

Figure A.41: LAWS simulation model consensus algorithm curves as a function of wideband signal-to-noise. The curves are probability of detection, false alarms and line-of-sight uncertainty errors.

Figure A.42: LAWS performance diagram model illustration.

LAWS SIMULATION MODEL (Global Version)

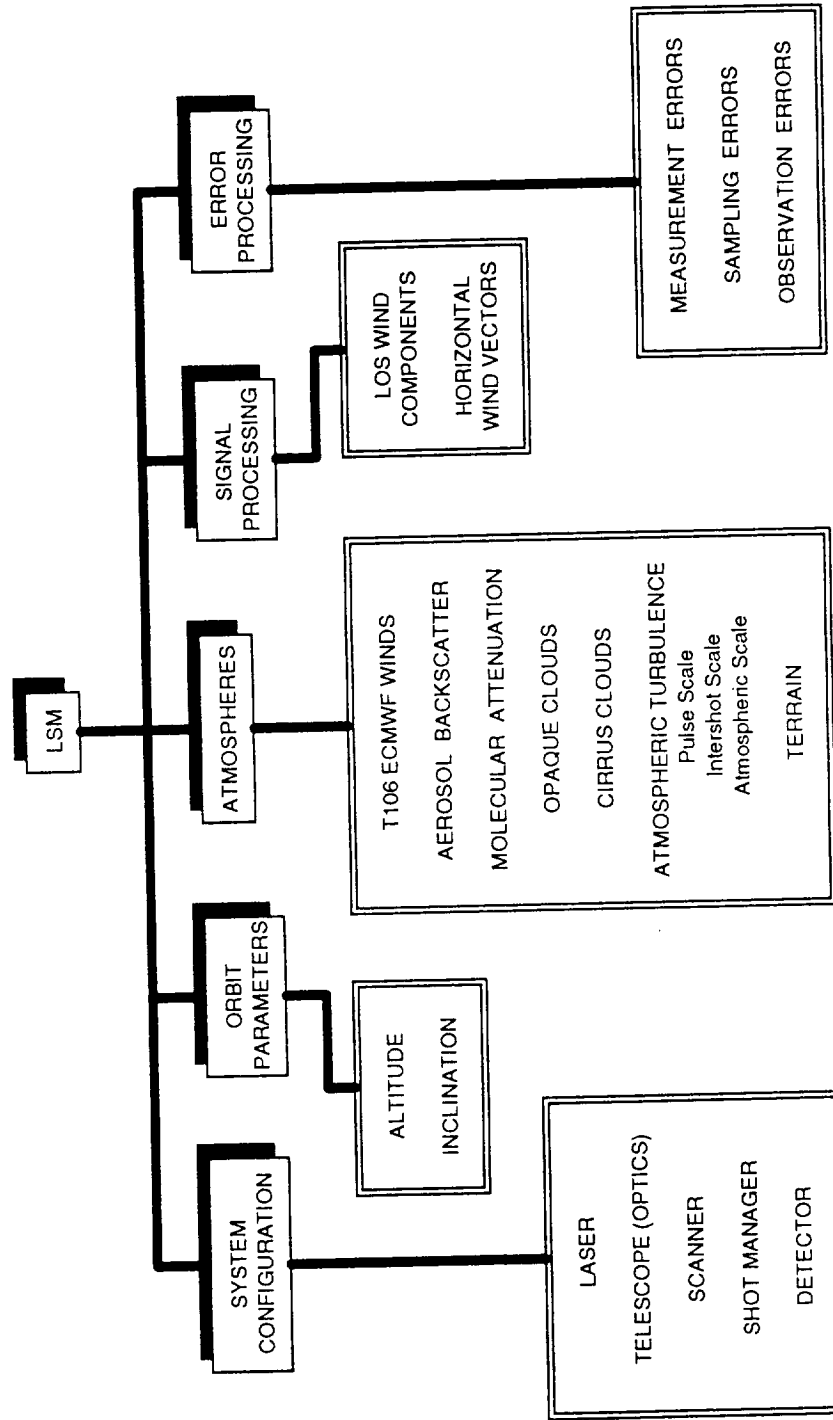


Figure A.1

THE OBSERVING SYSTEM SIMULATION EXPERIMENTS FOR LAWS

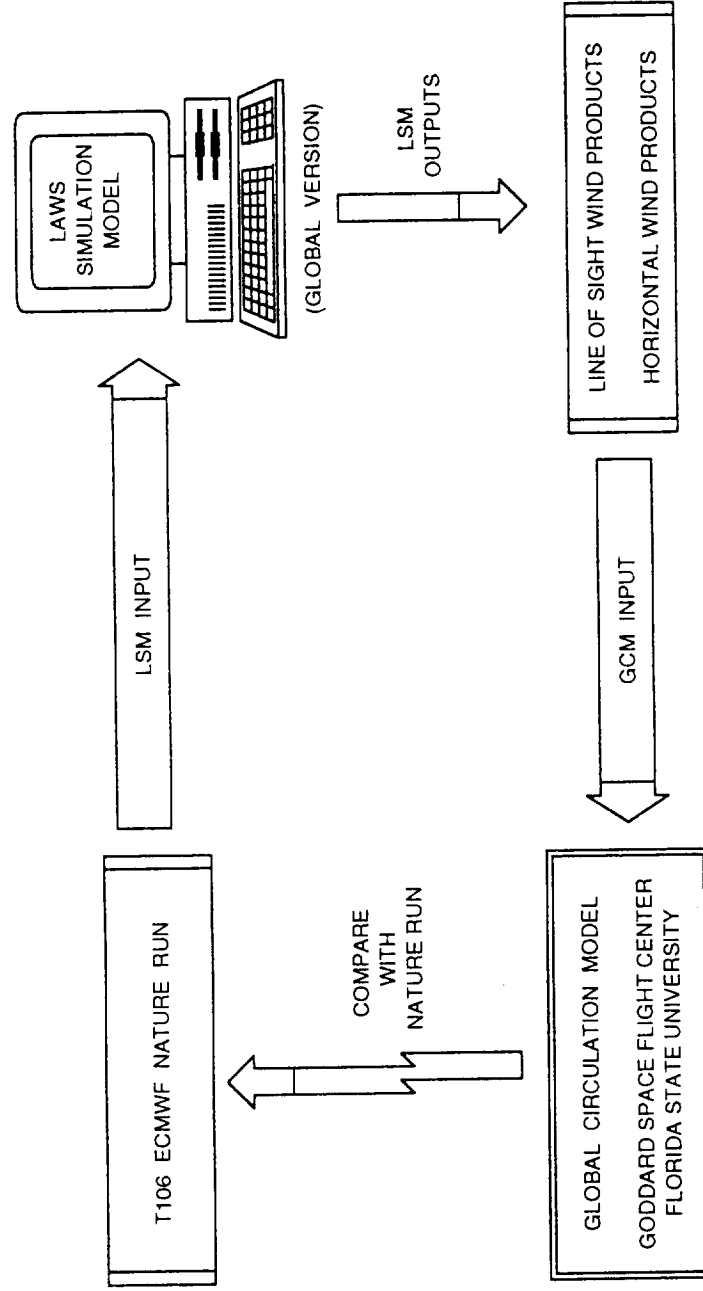


Figure A.2

LAWS 13 HOUR COVERAGE AT A 525 KM ORBIT

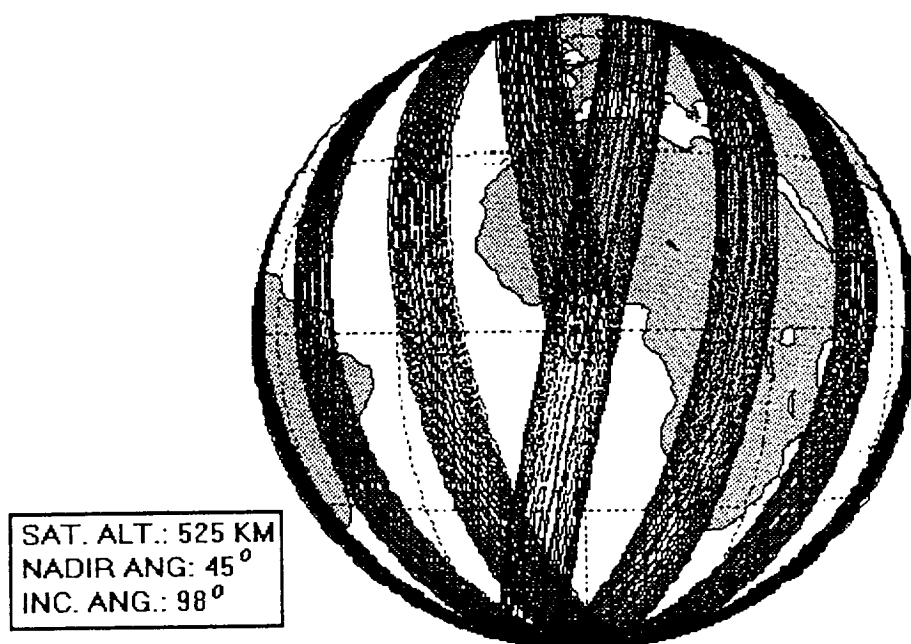
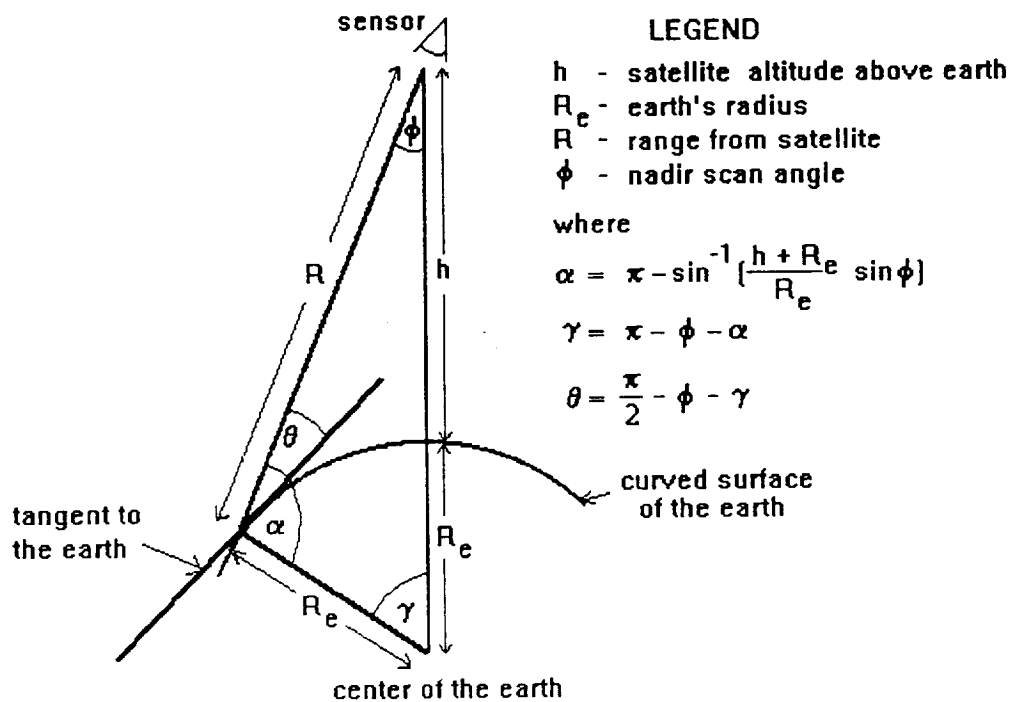


Figure A.3

LAWS NADIR SCAN GEOMETRY



LEGEND

- h - satellite altitude above earth
- R_e - earth's radius
- R - range from satellite
- ϕ - nadir scan angle

where

$$\alpha = \pi - \sin^{-1} \left(\frac{h + R_e}{R_e} \sin \phi \right)$$

$$\gamma = \pi - \phi - \alpha$$

$$\theta = \frac{\pi}{2} - \phi - \gamma$$

NOT DRAWN TO SCALE

Figure A.4

COMPARISON OF THE CONIC AND QUAD BEAM SCANNERS

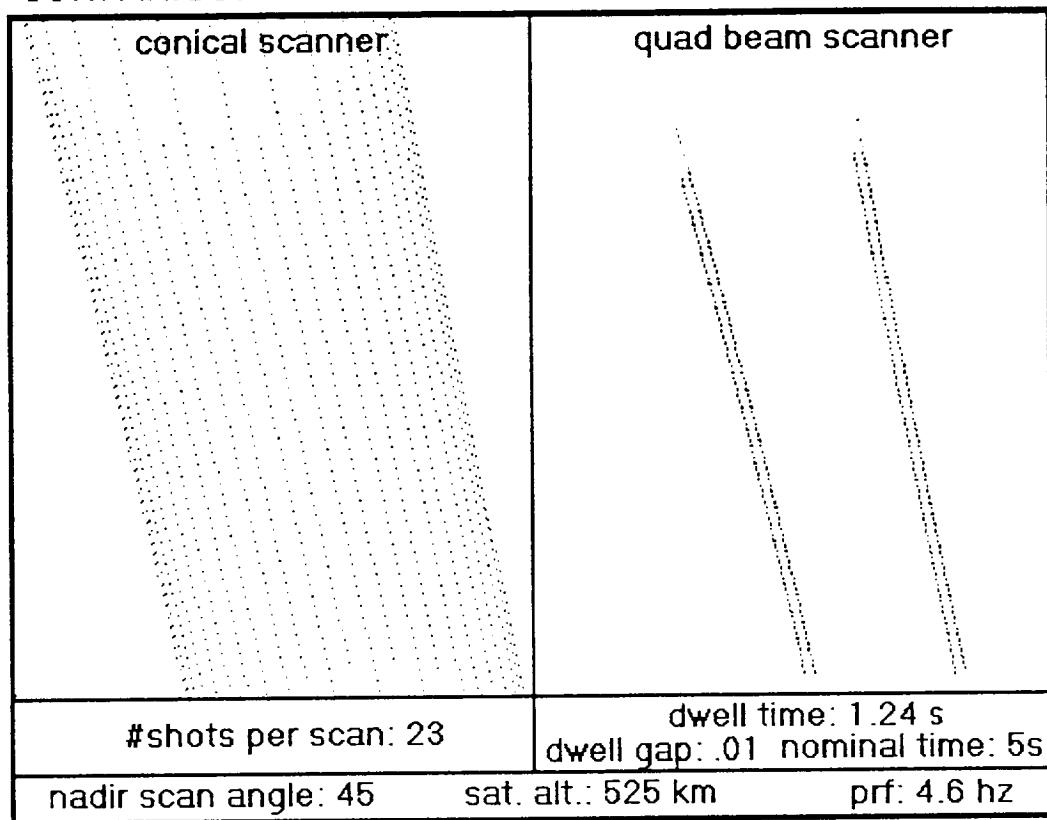


Figure A.5

CONICAL SCANNER GEOMETRY CONVENTION

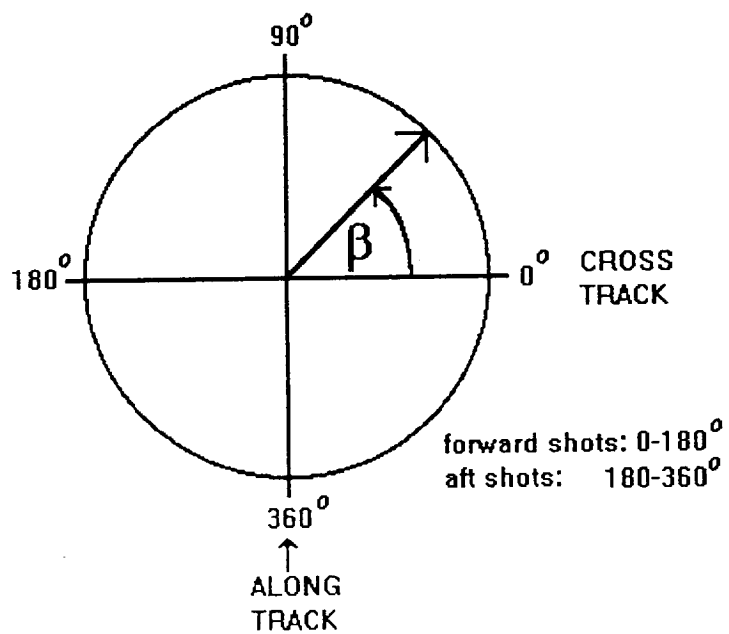


Figure A.6

Schematic Configuration of the Windmatic System on the BEST Platform

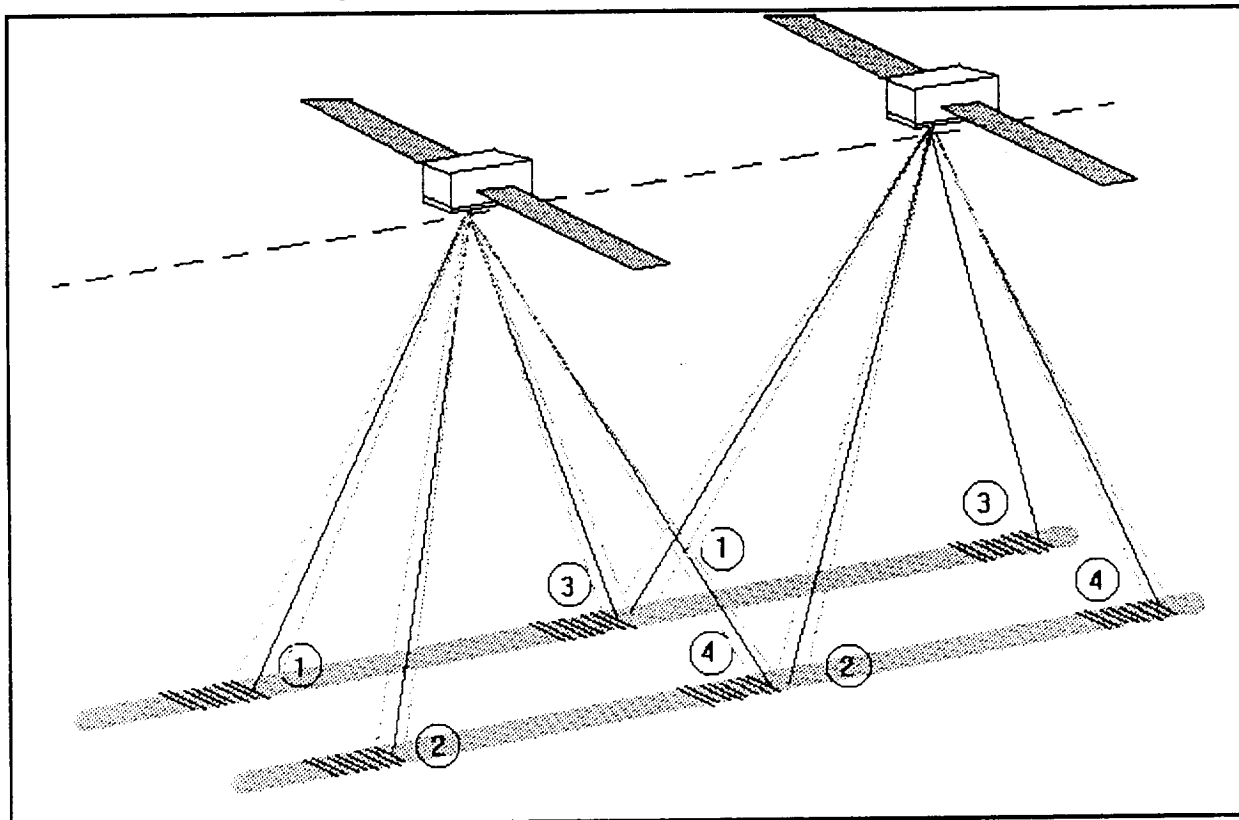


Figure A.7

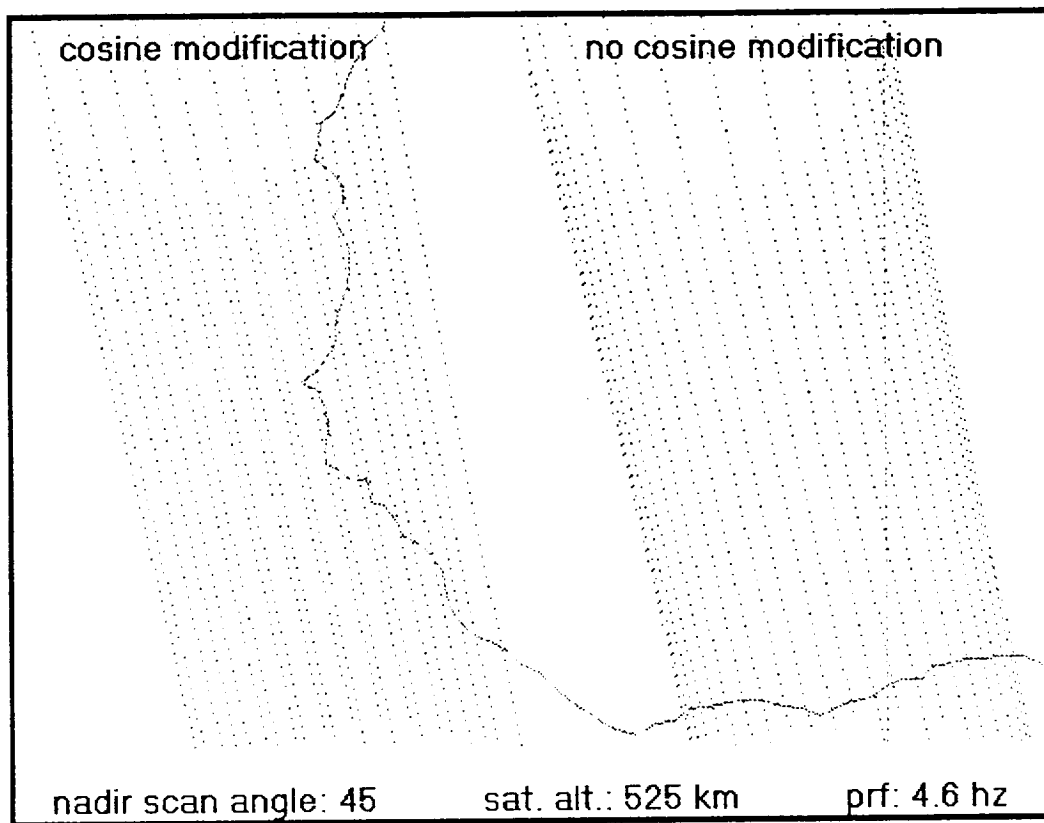


Figure A.8

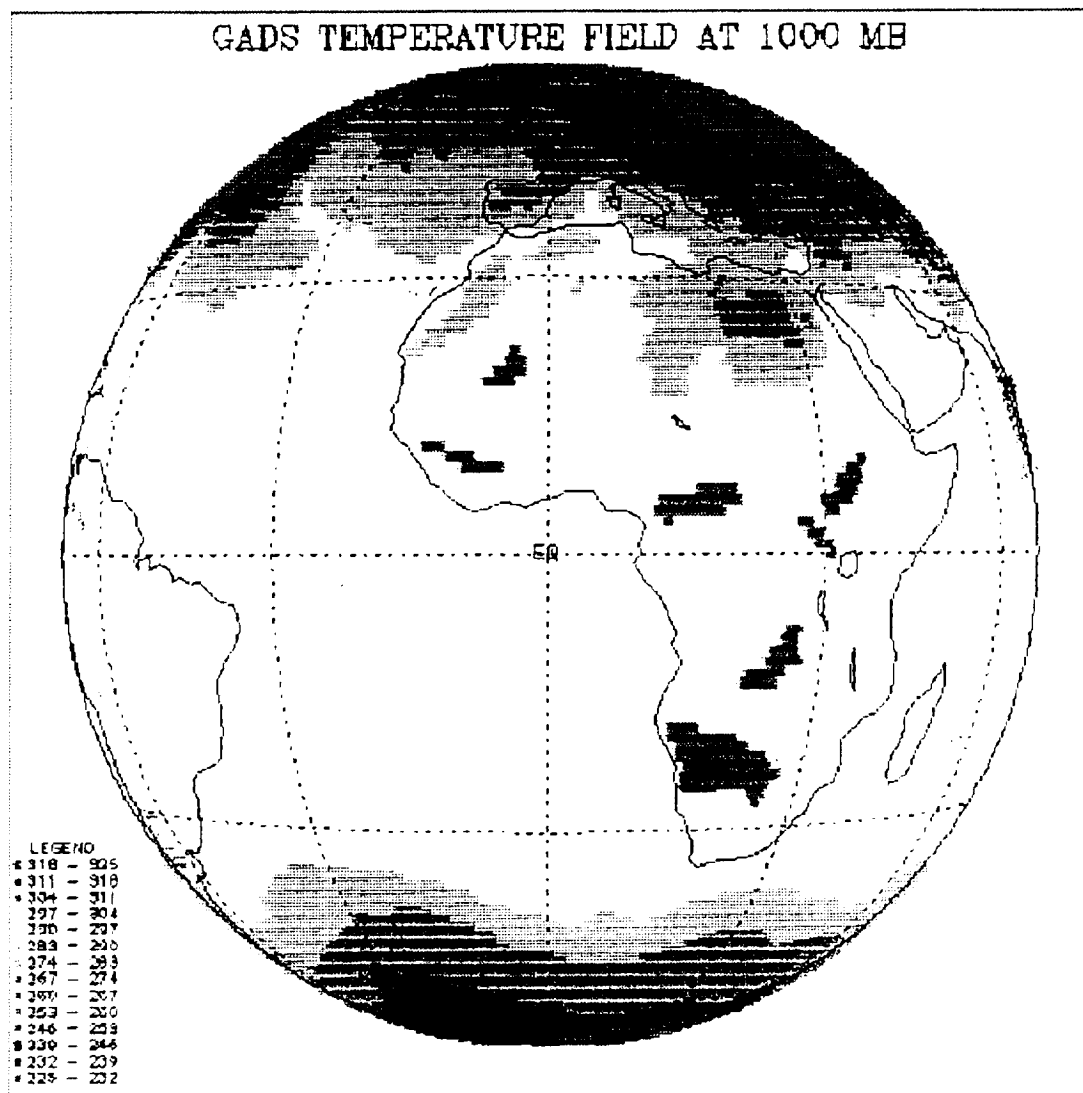


Figure A.9

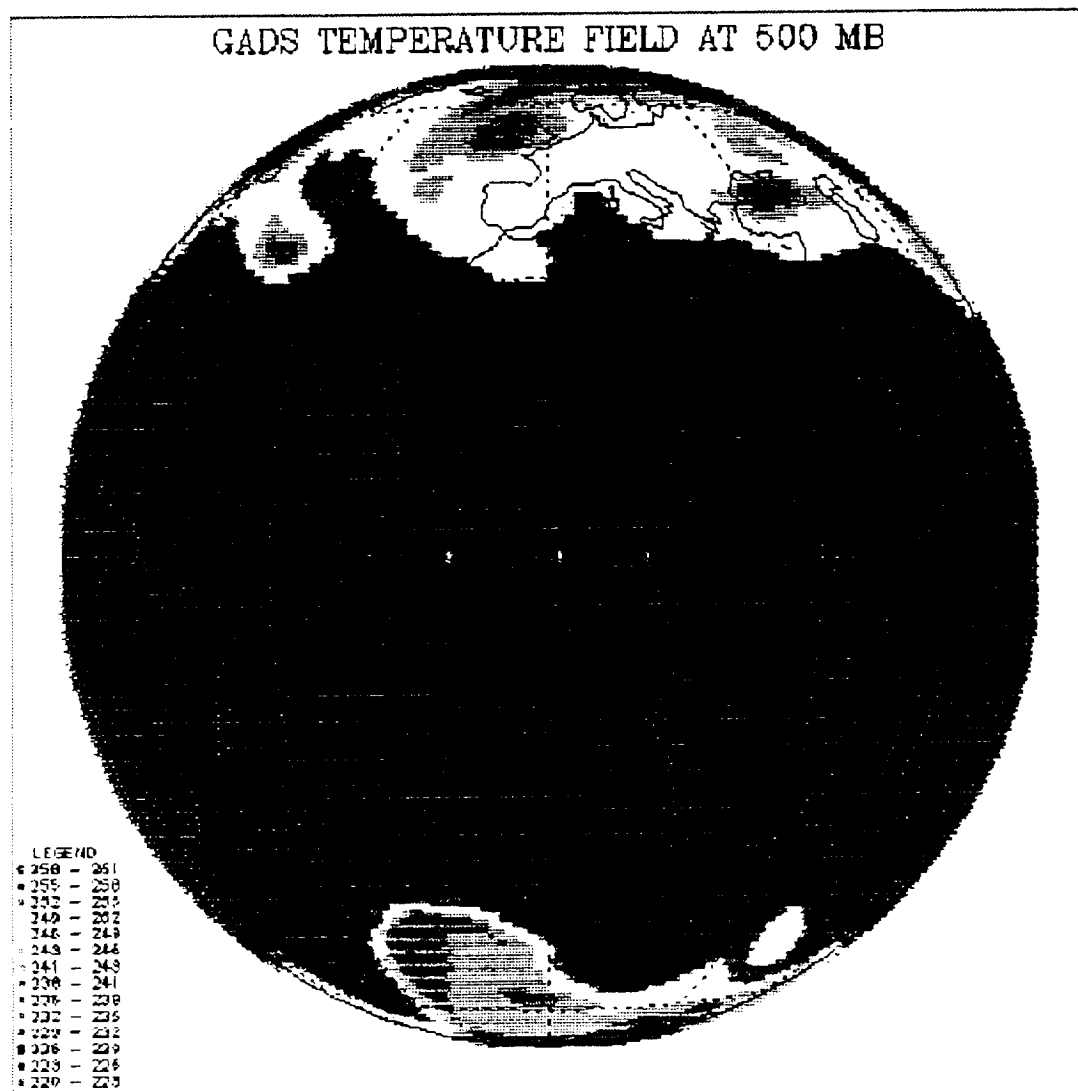


Figure A.10

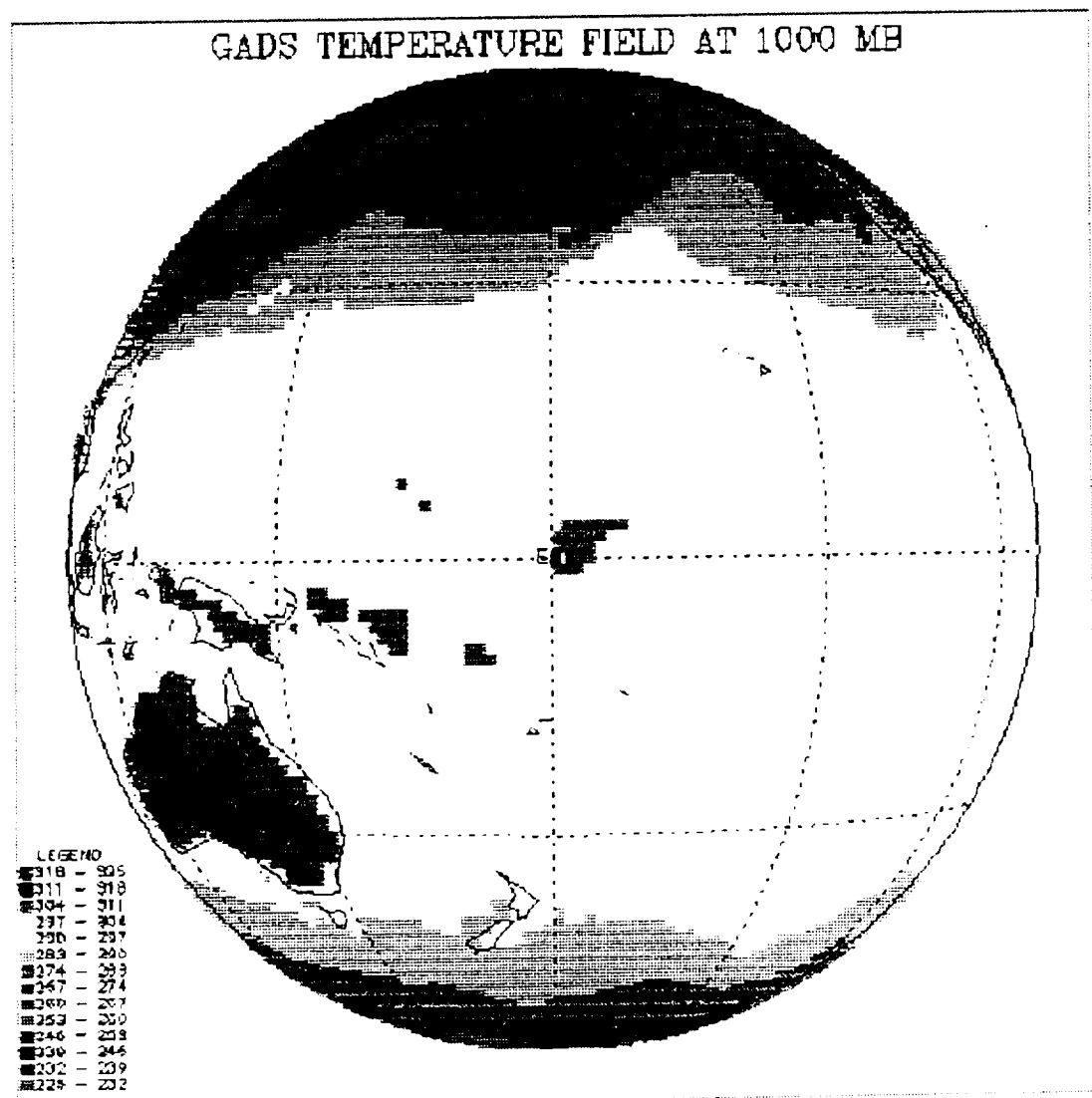


Figure A.11

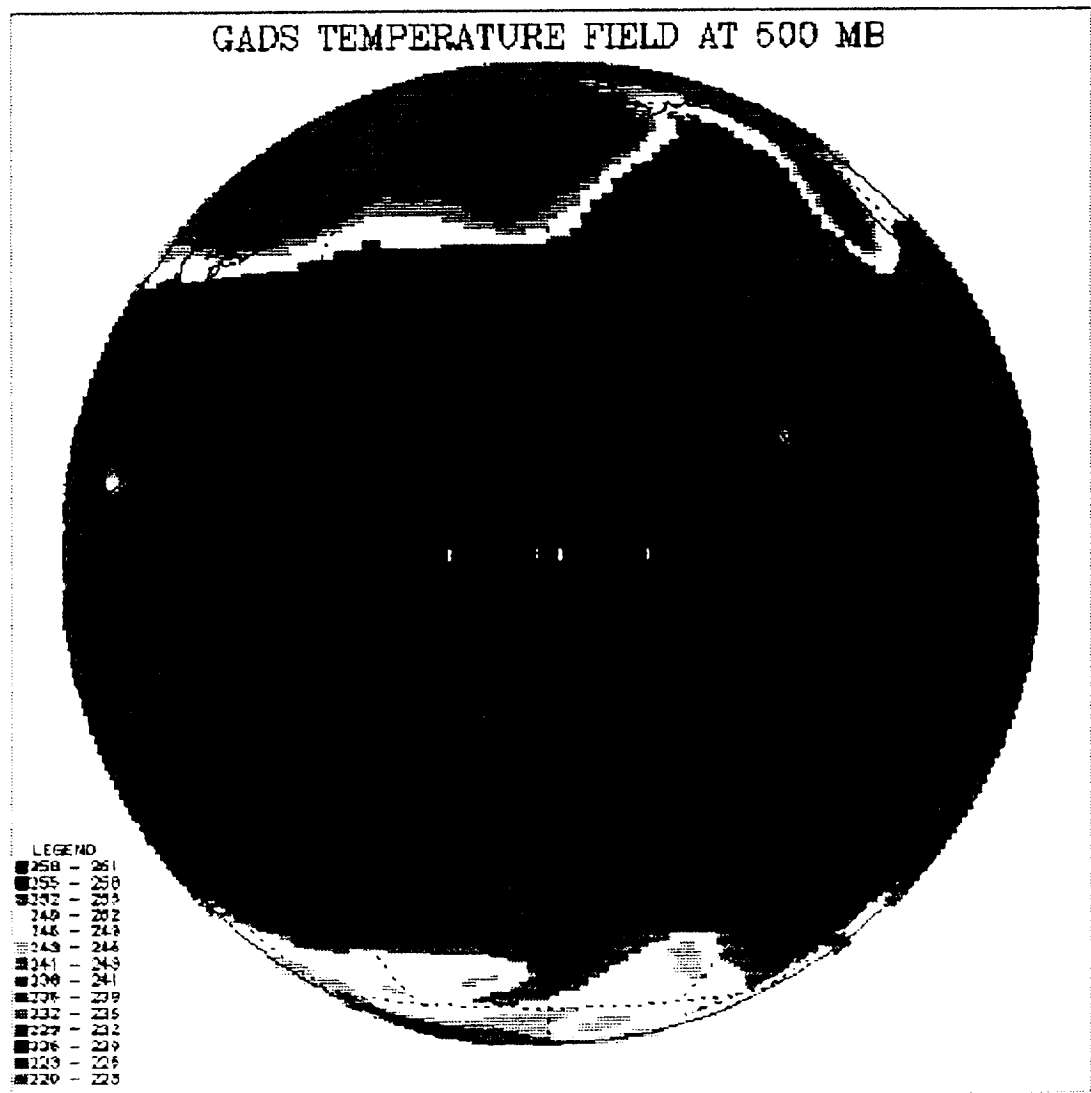


Figure A.12

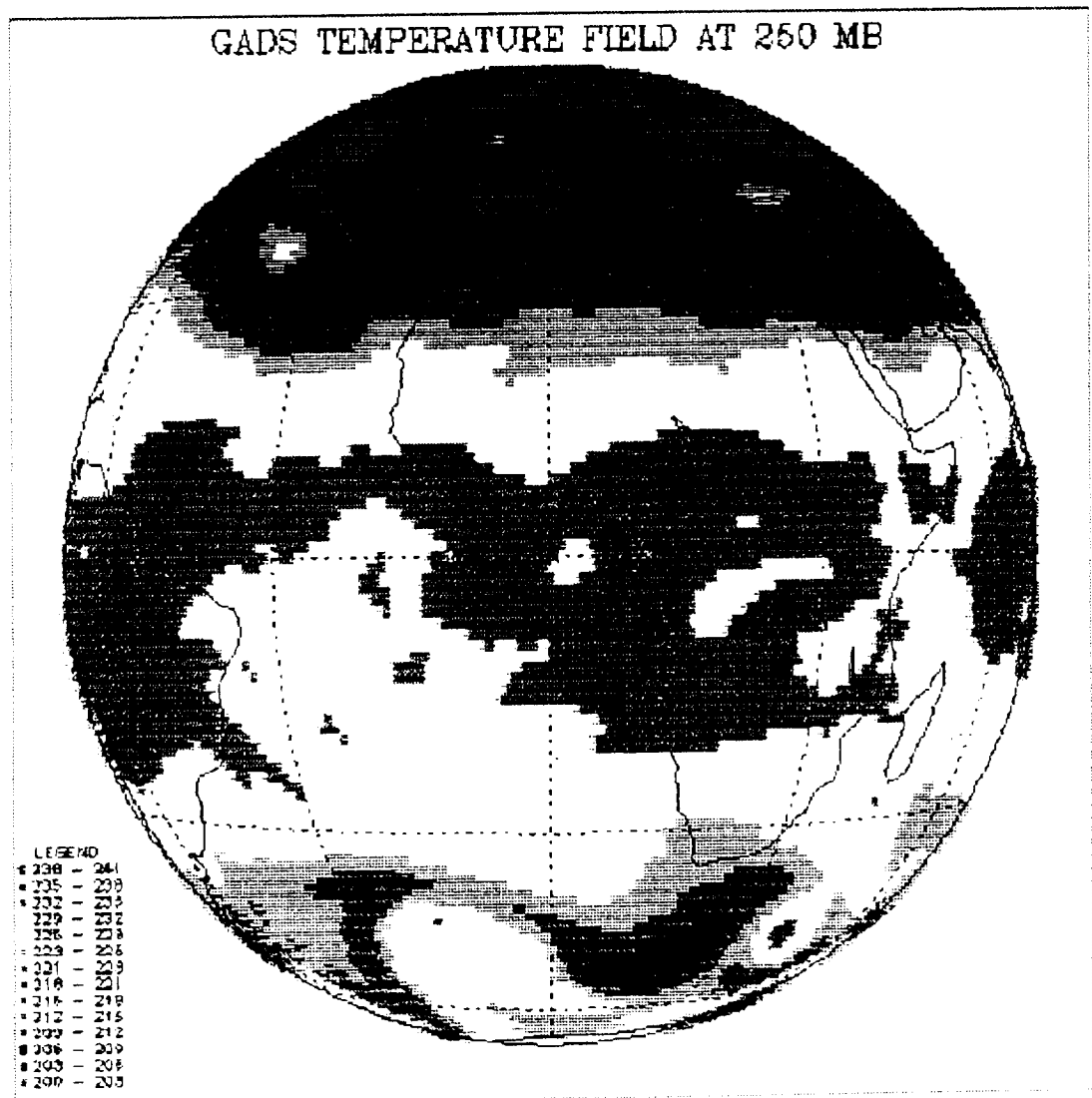


Figure A.13

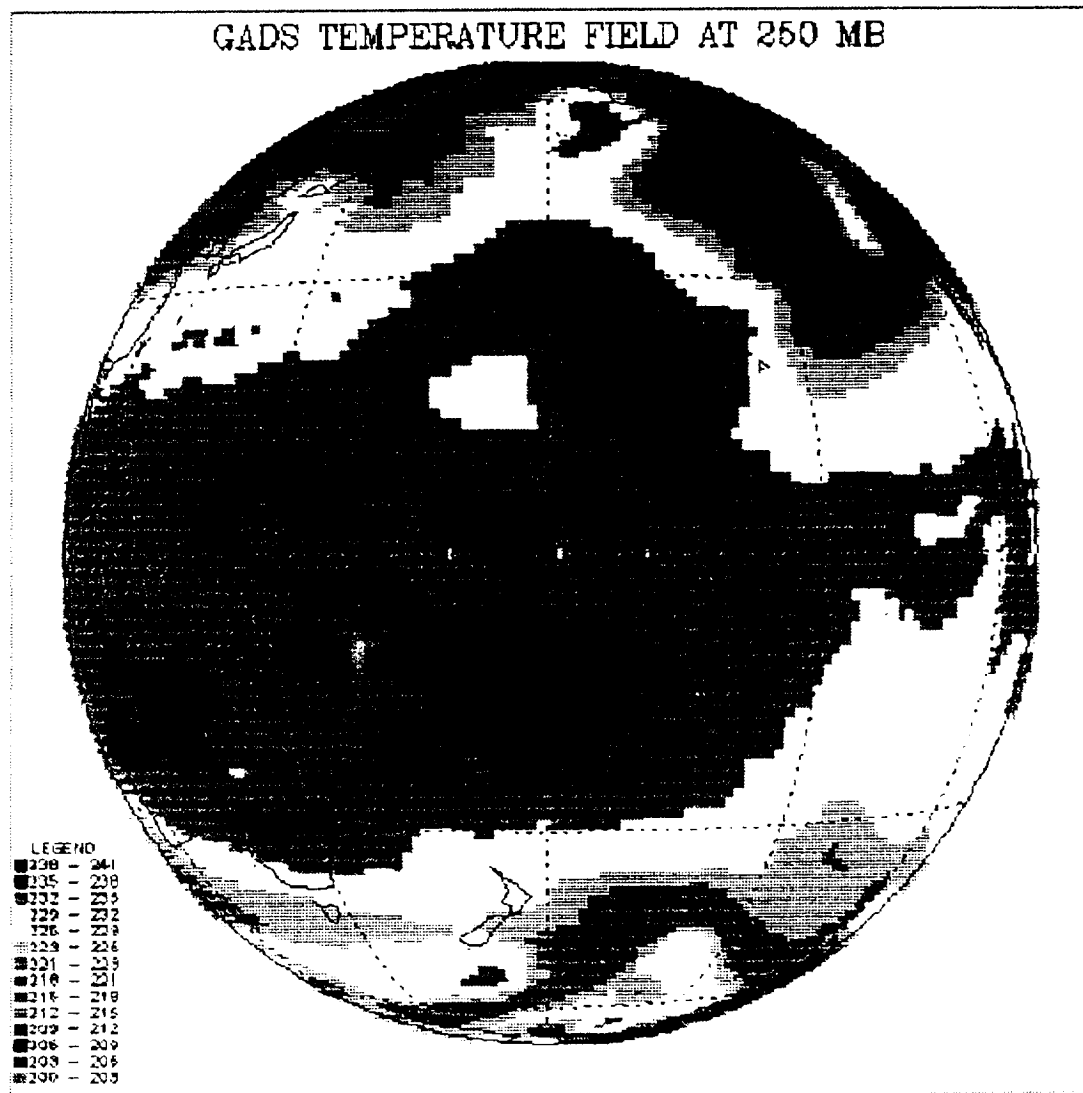


Figure A.14

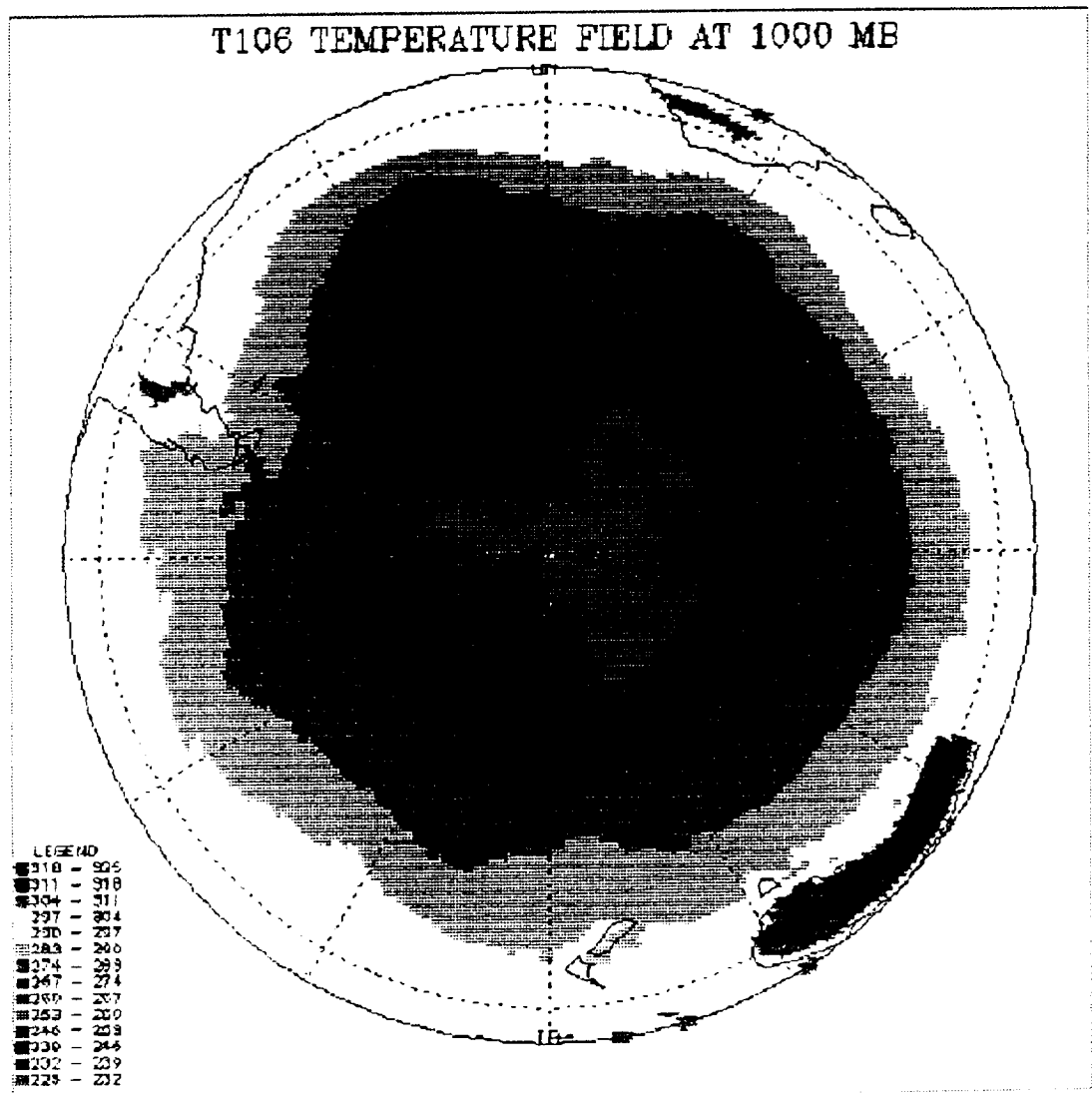


Figure A.15

GADS RELATIVE HUMIDITY FIELD AT 1000 MB

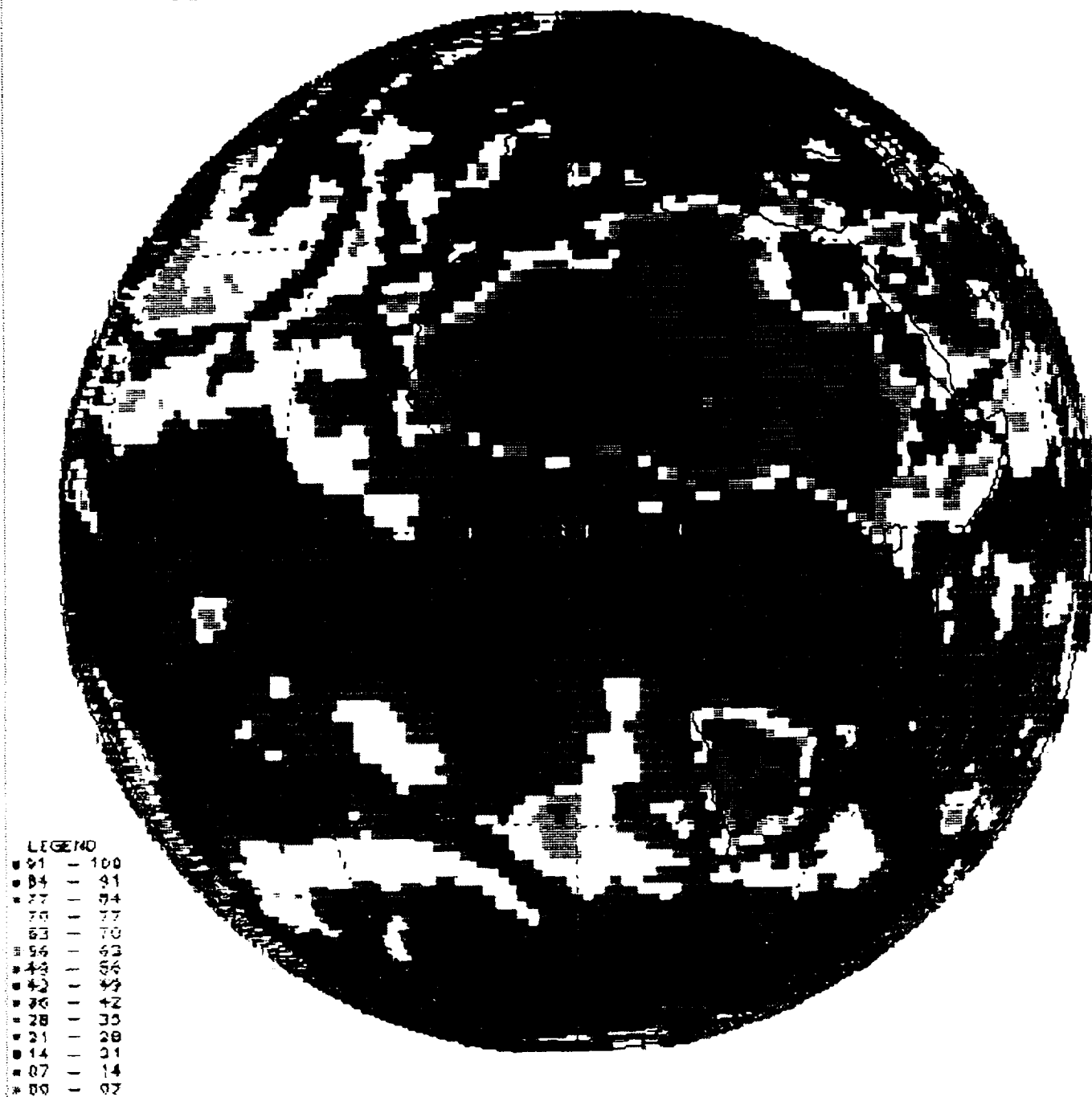


Figure A.16

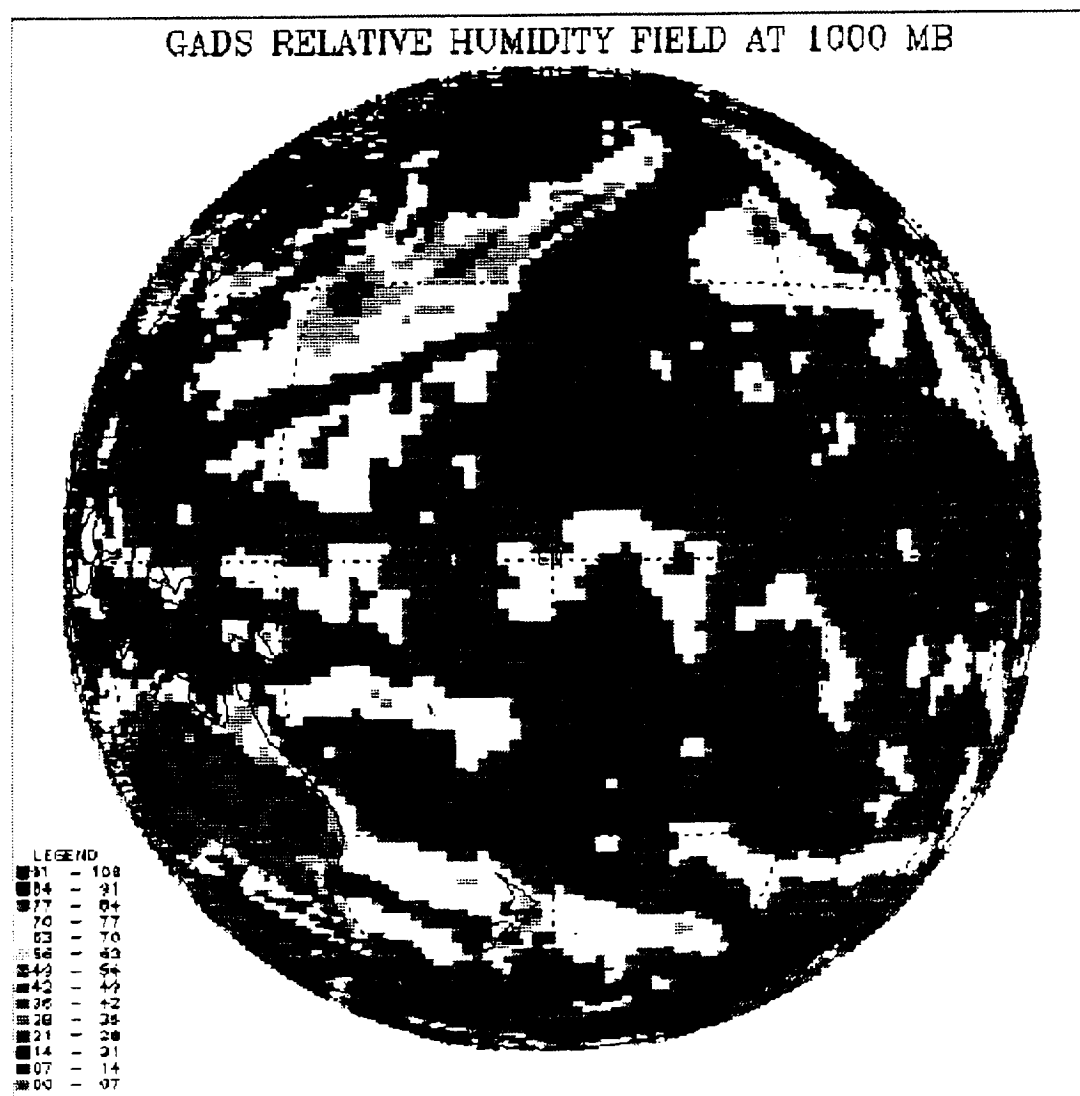


Figure A.17

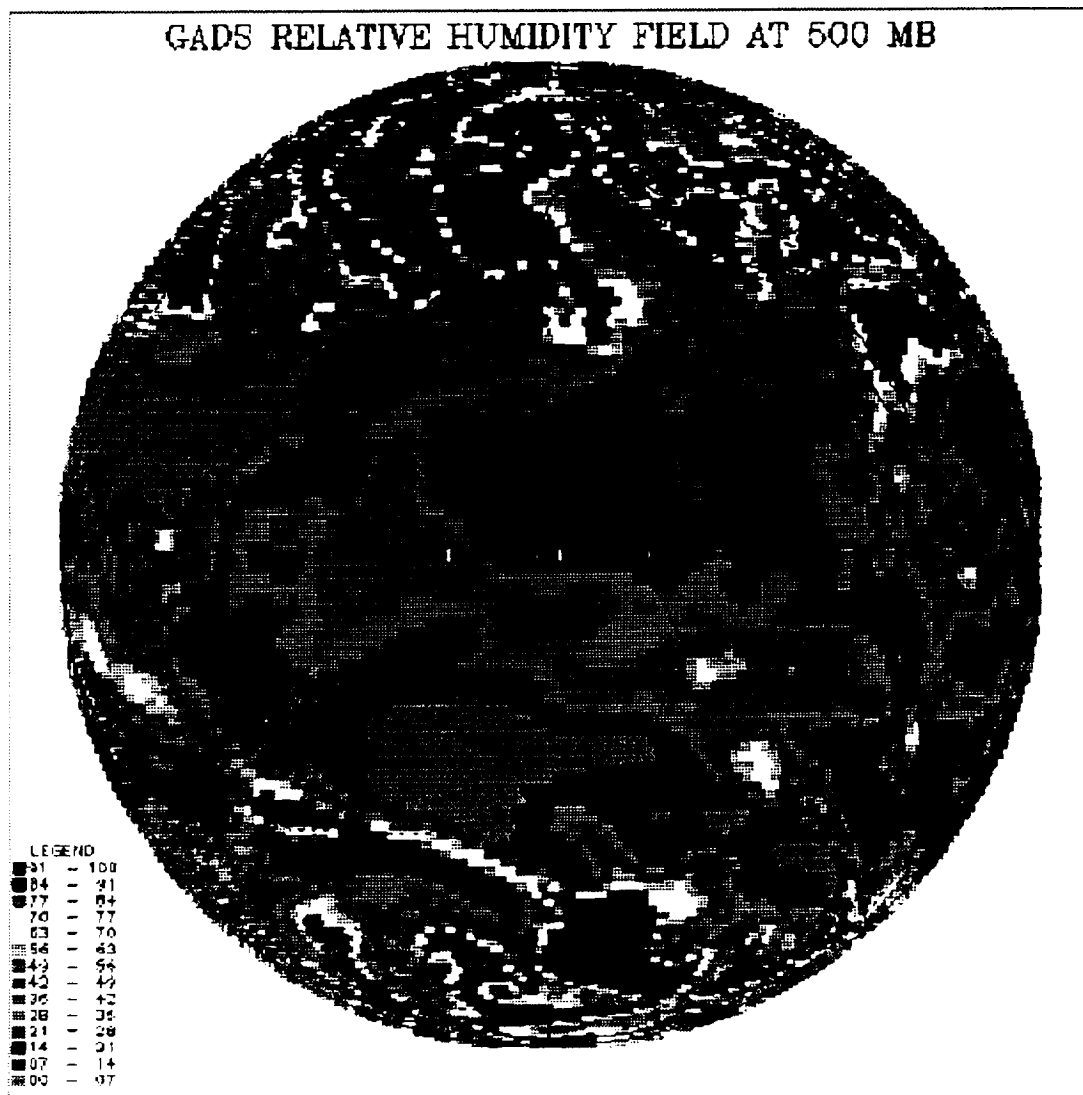


Figure A.18

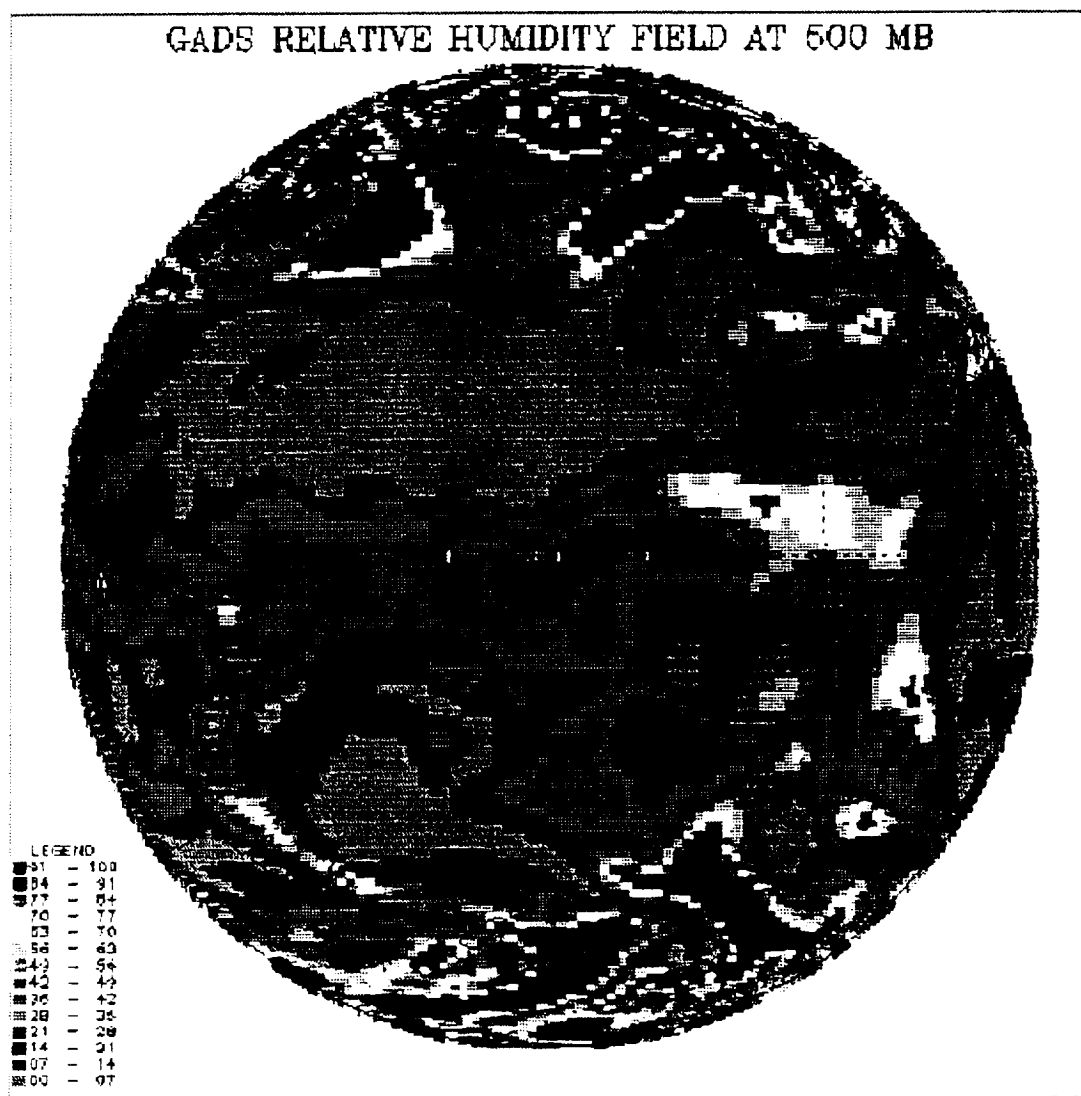


Figure A.19

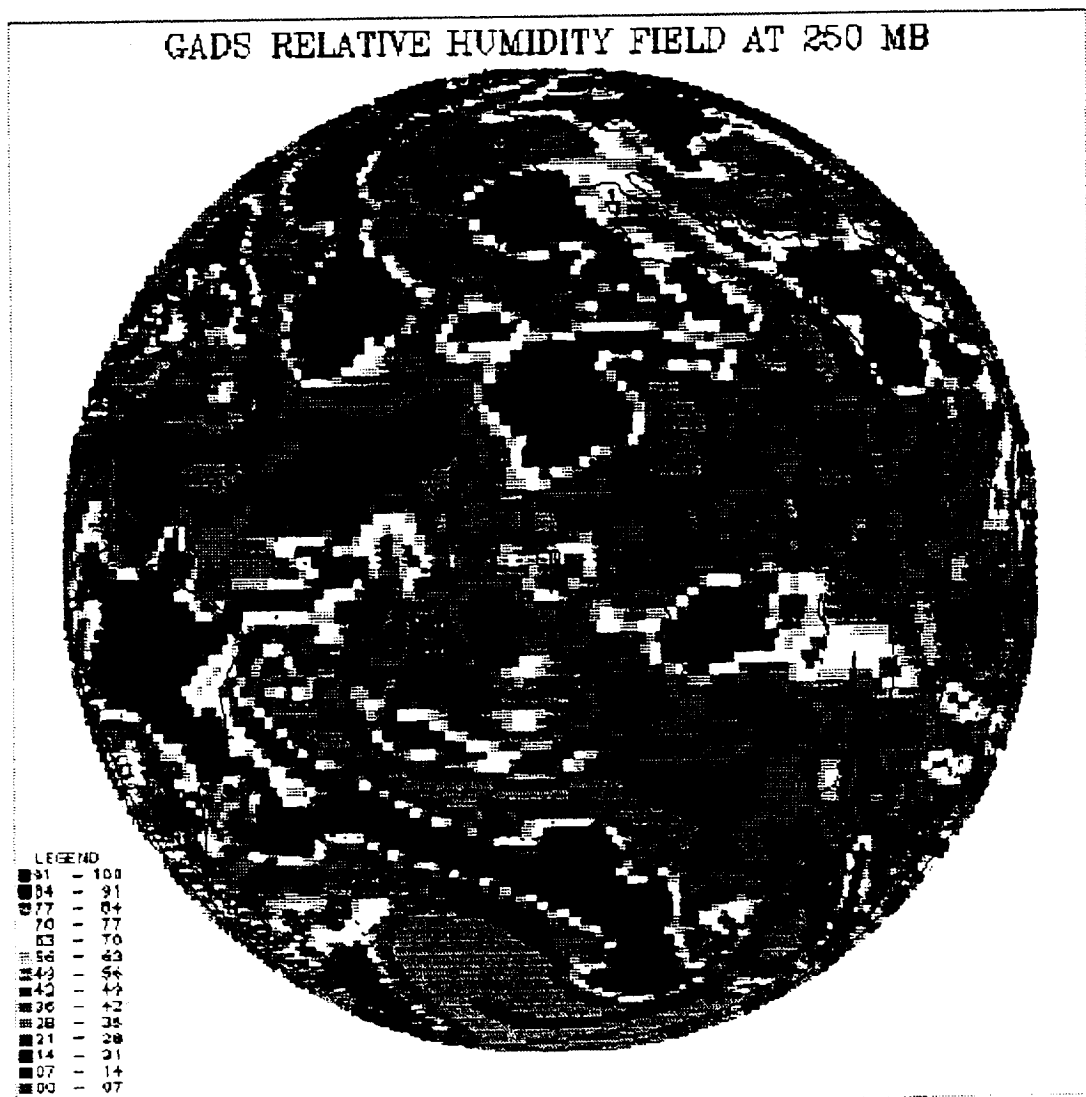


Figure A.20

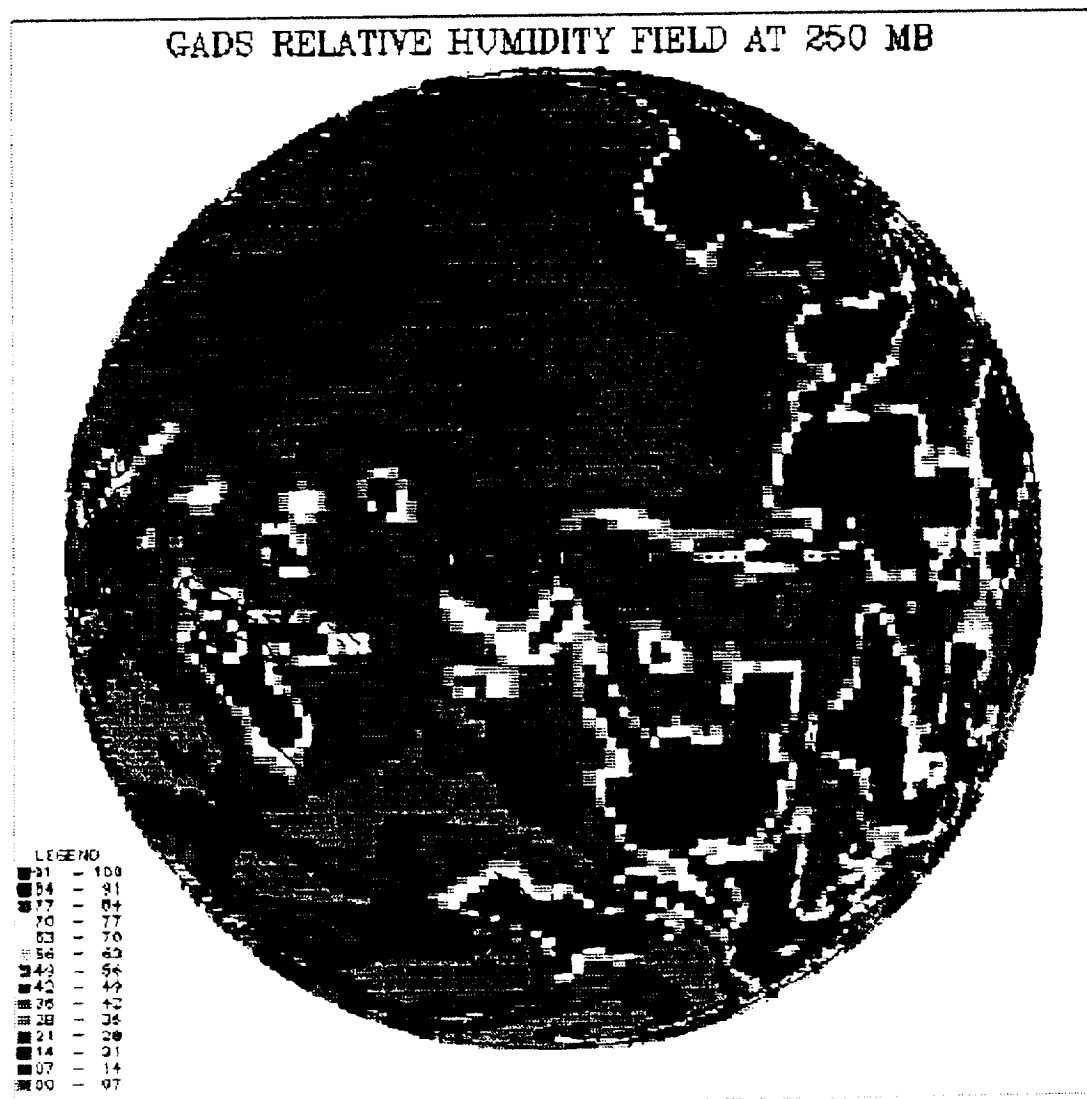


Figure A.21

GADS HORIZONTAL WIND FIELD AT 1000 MB

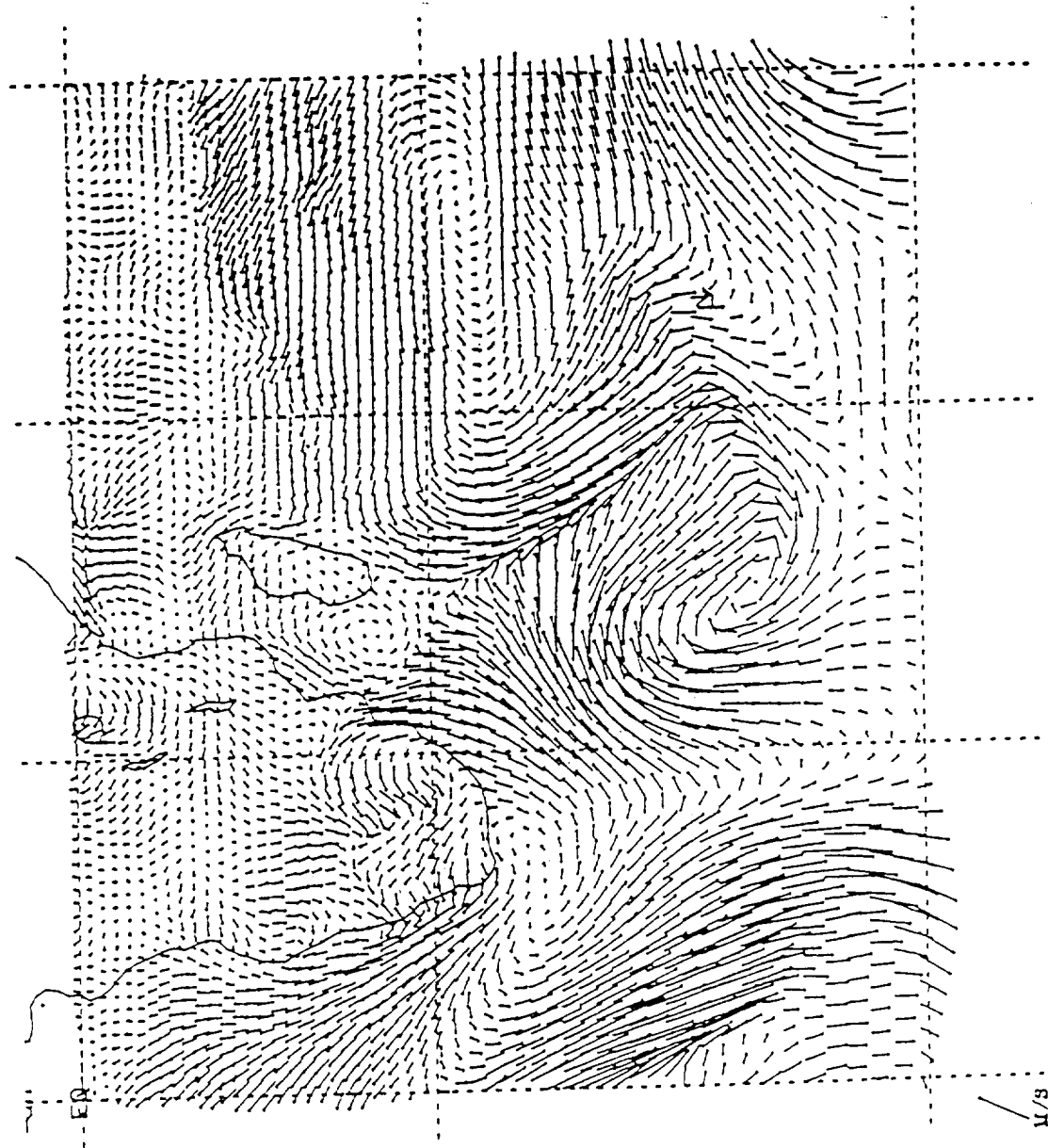


Figure A.22

GADS HORIZONTAL WIND FIELD AT 1000 MB

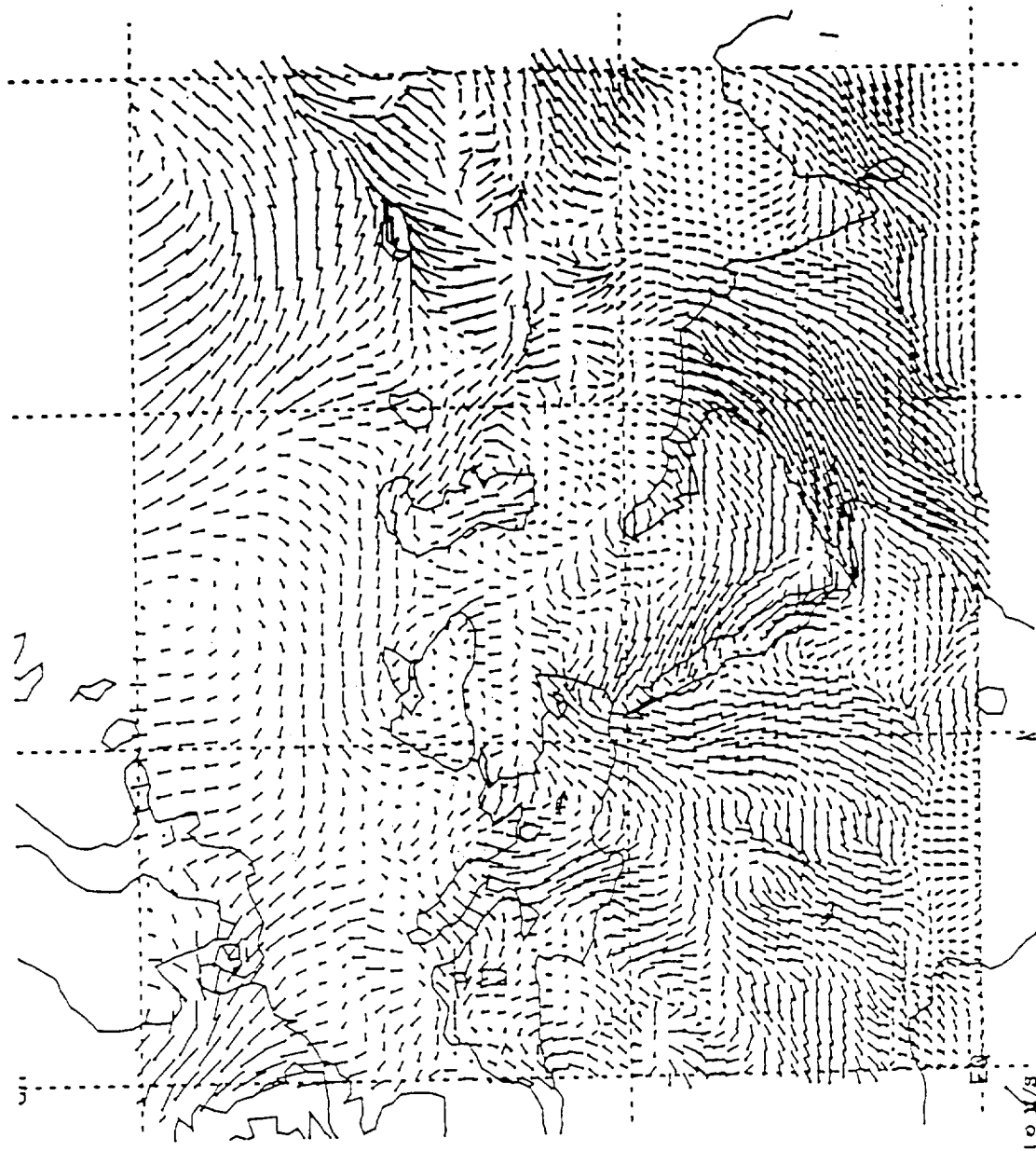


Figure A.23

GADS HORIZONTAL WIND FIELD AT 500 MB

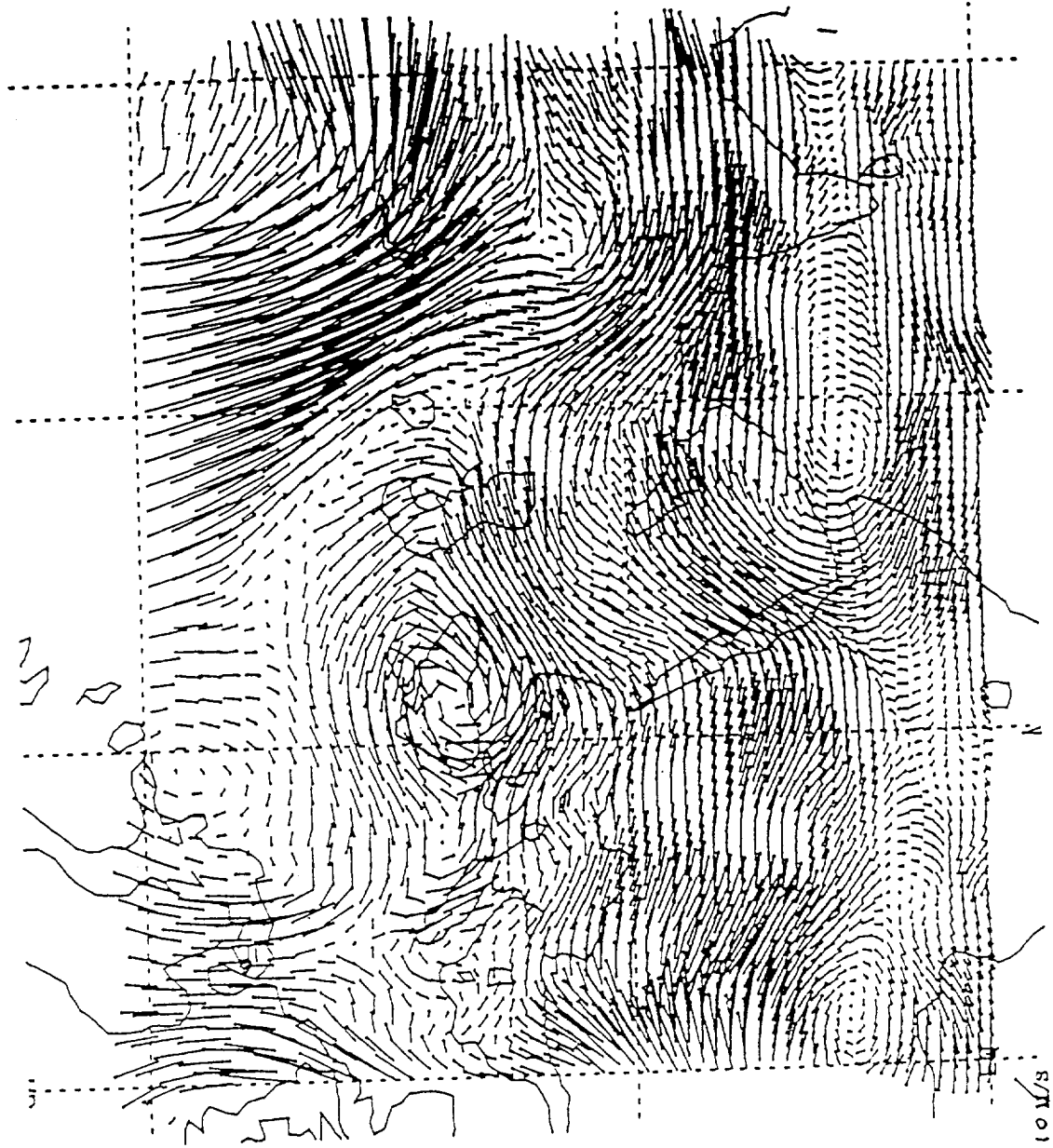


Figure A.24

GADS HORIZONTAL WIND FIELD AT 500 MB

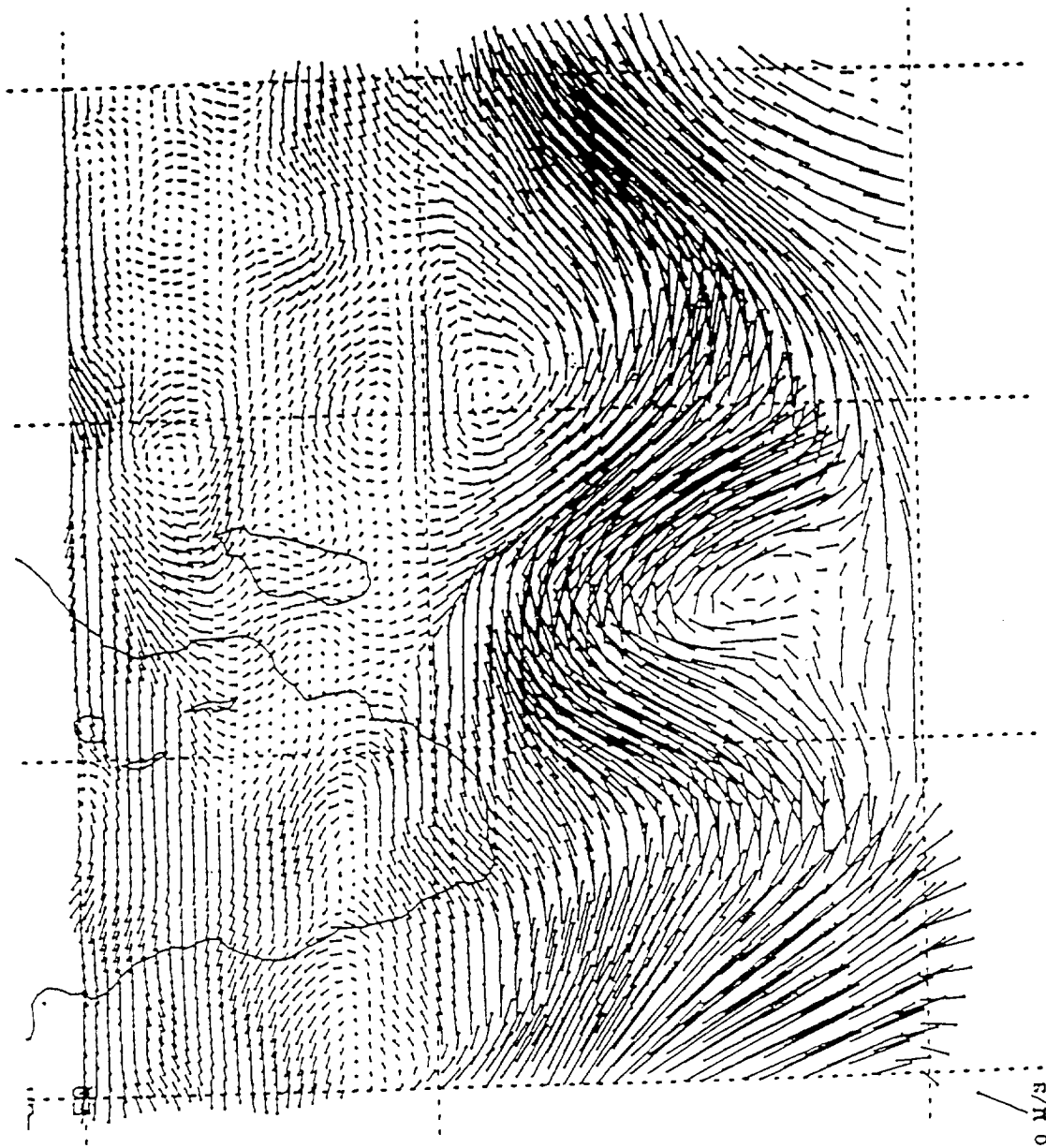


Figure A.25

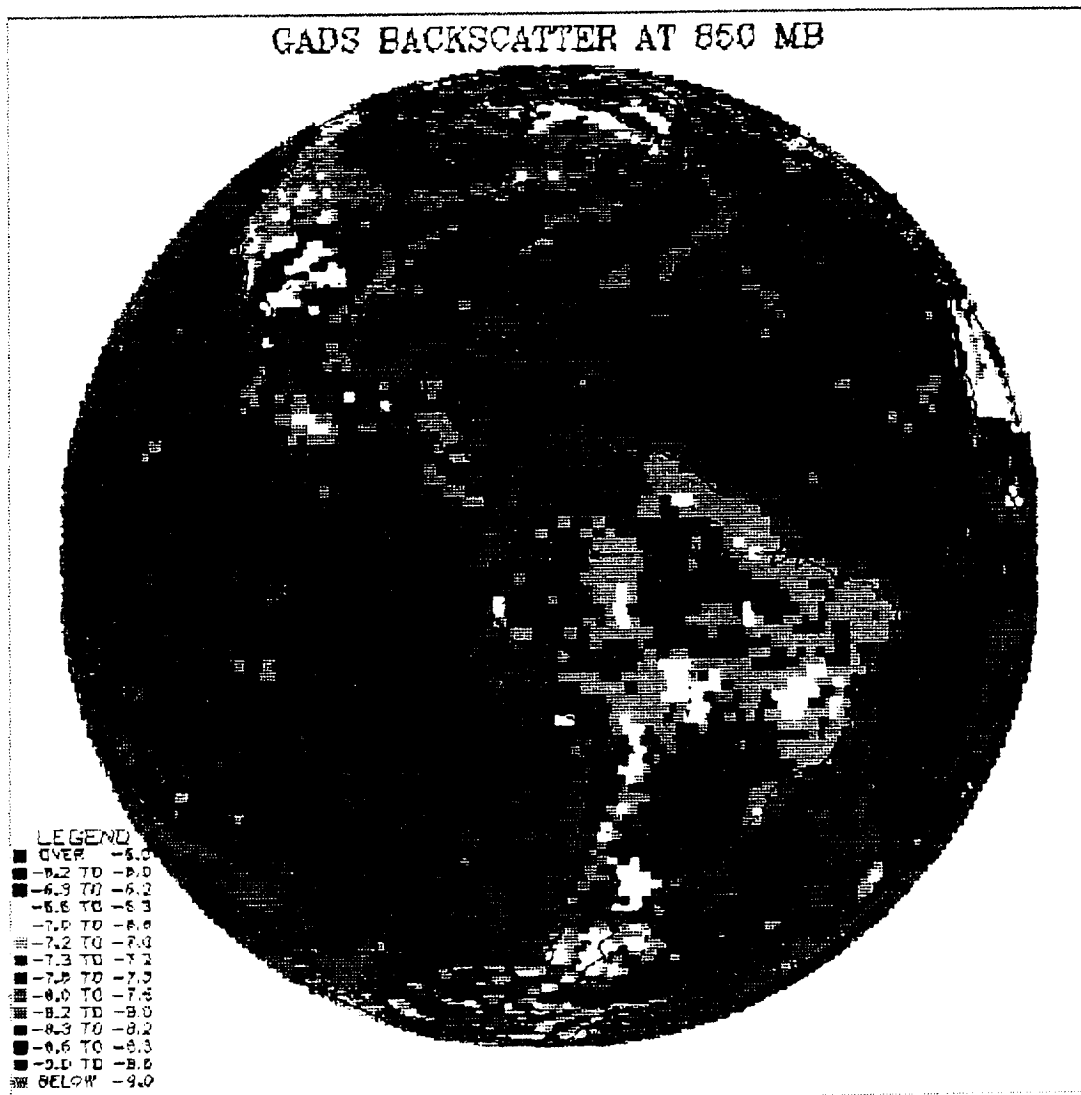


Figure A.26

GADS BACKSCATTER AT 250 MB

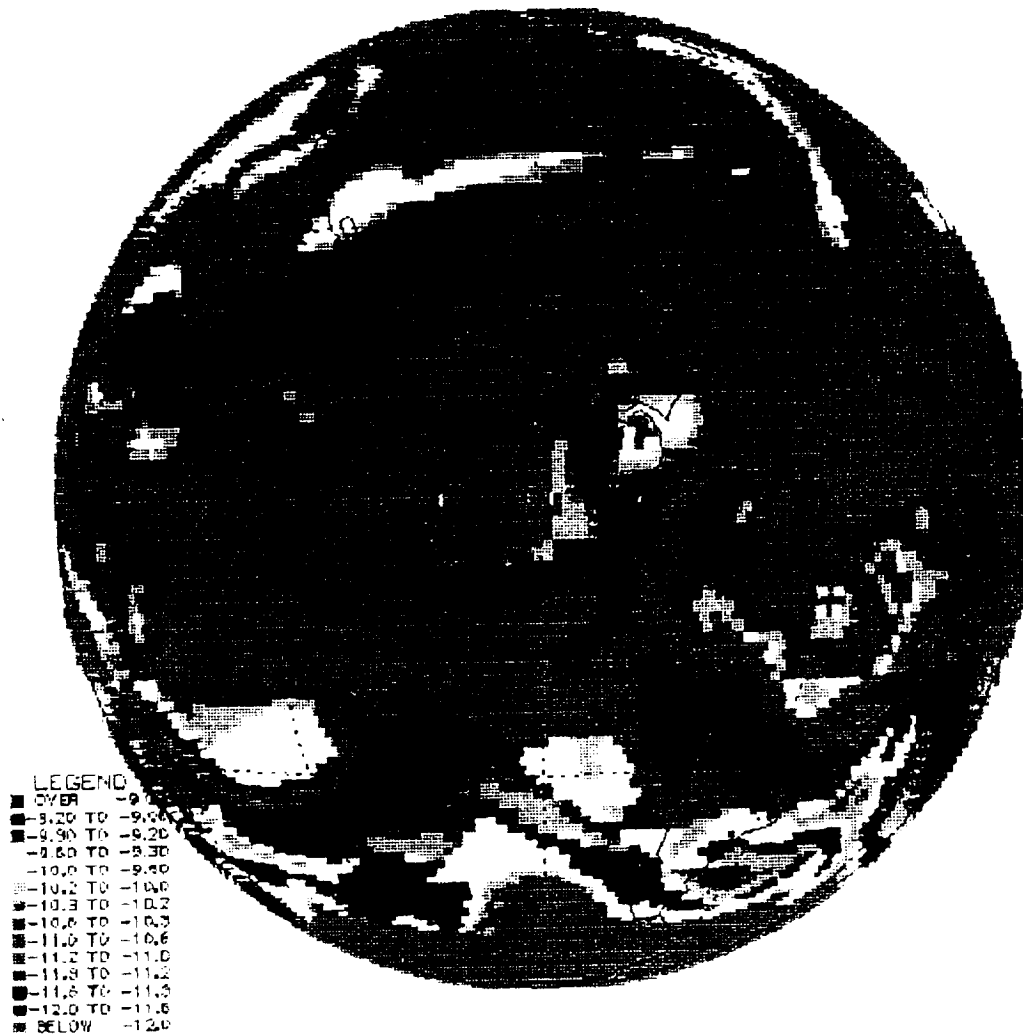


Figure A.27

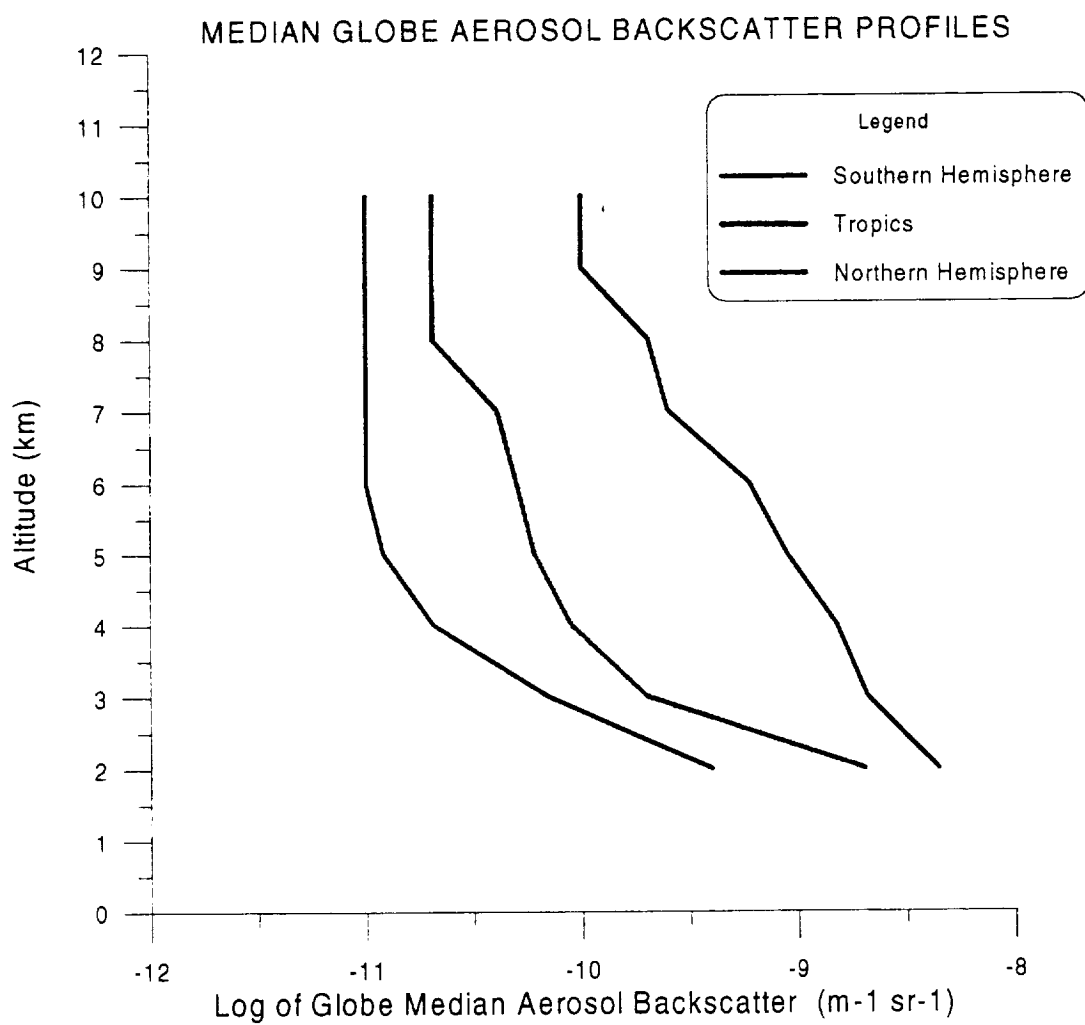
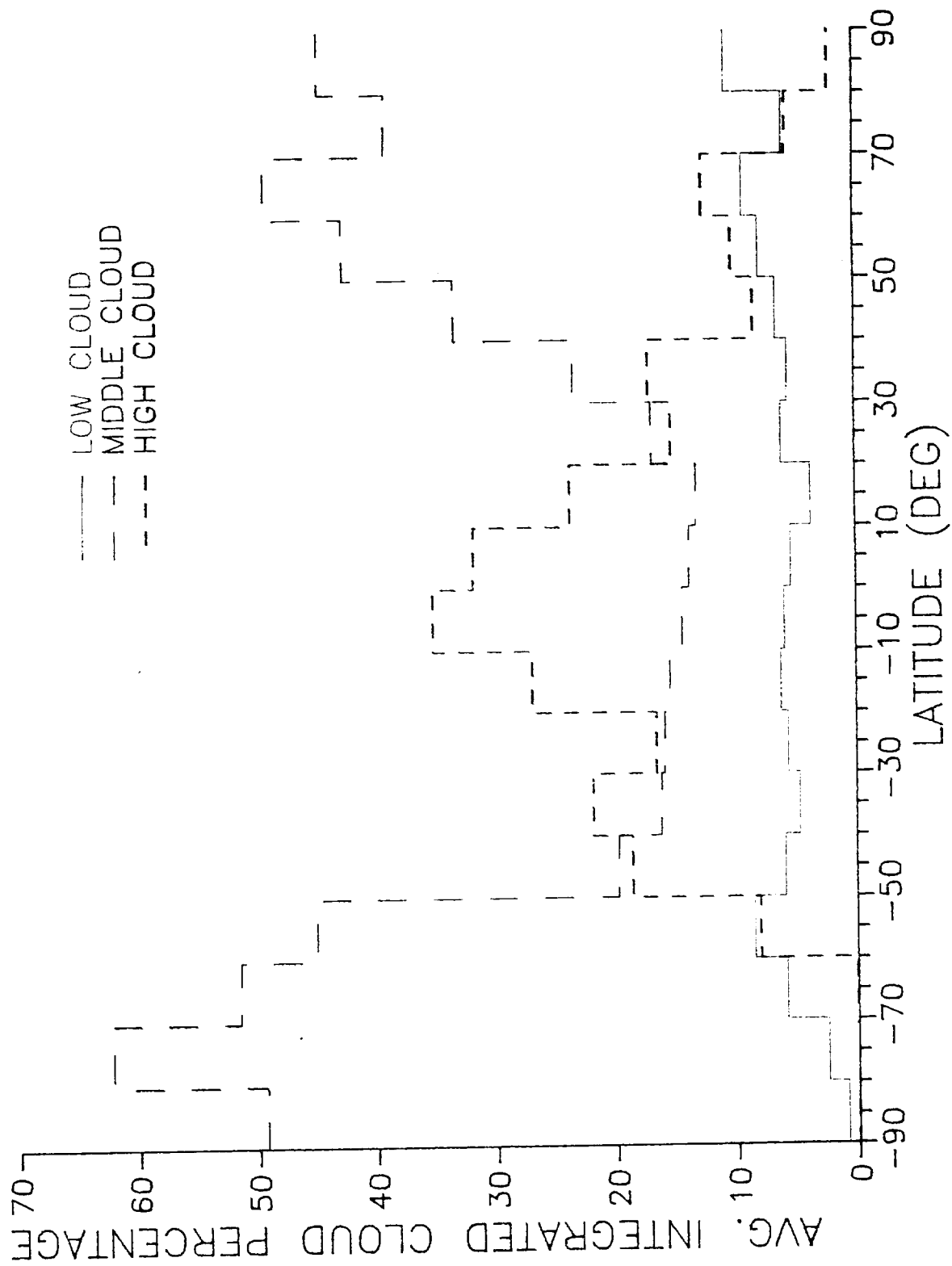


Figure A.28

LOW, MIDDLE, HIGH CLOUD AMOUNTS FOR 10 DEGREE LATITUDE BANDS



ONE DAY GLOBAL AVERAGE INTEGRATED CLOUD AMOUNTS FOR 10 DEGREE LATITUDE BANDS

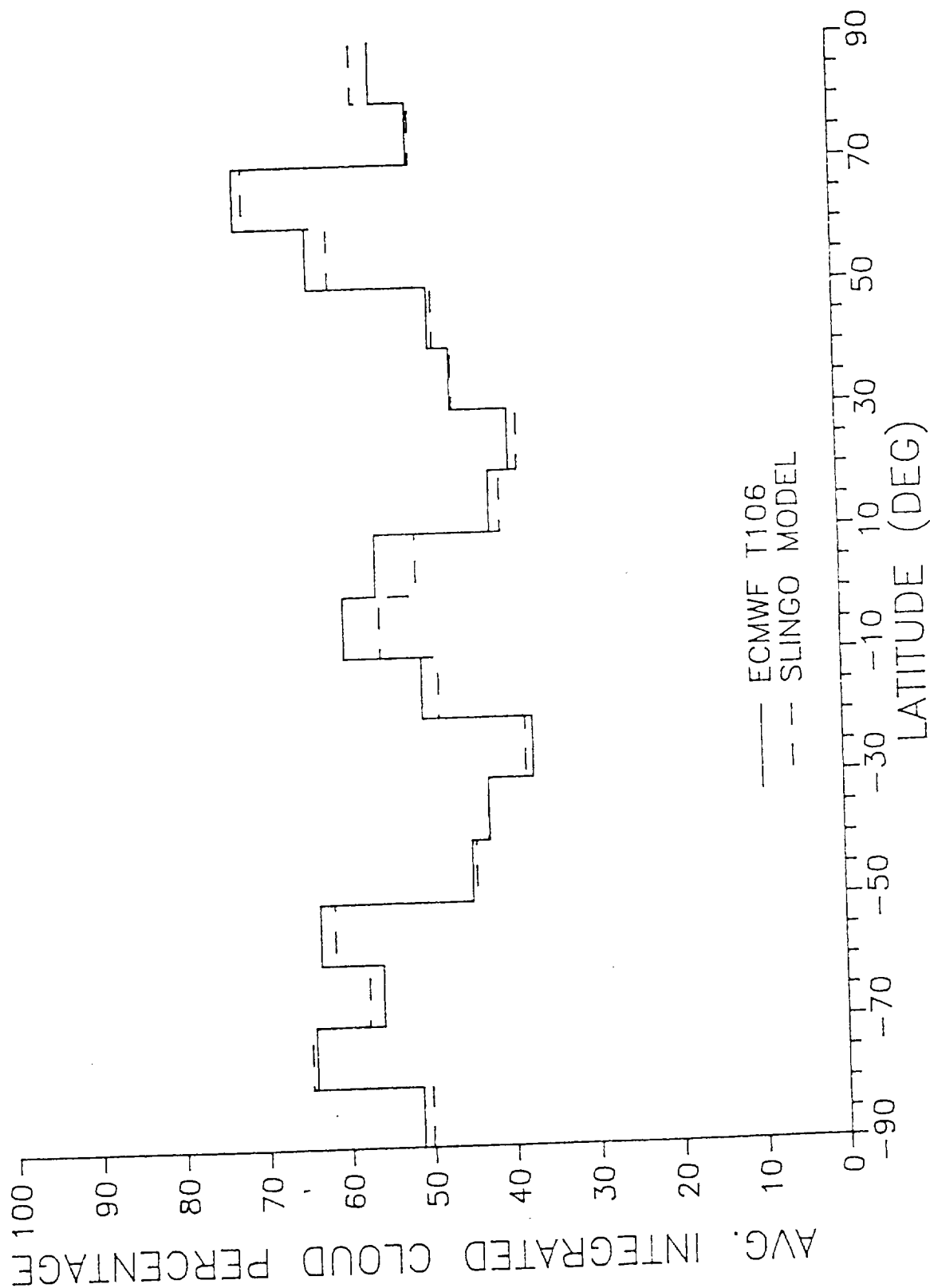


Figure A.30

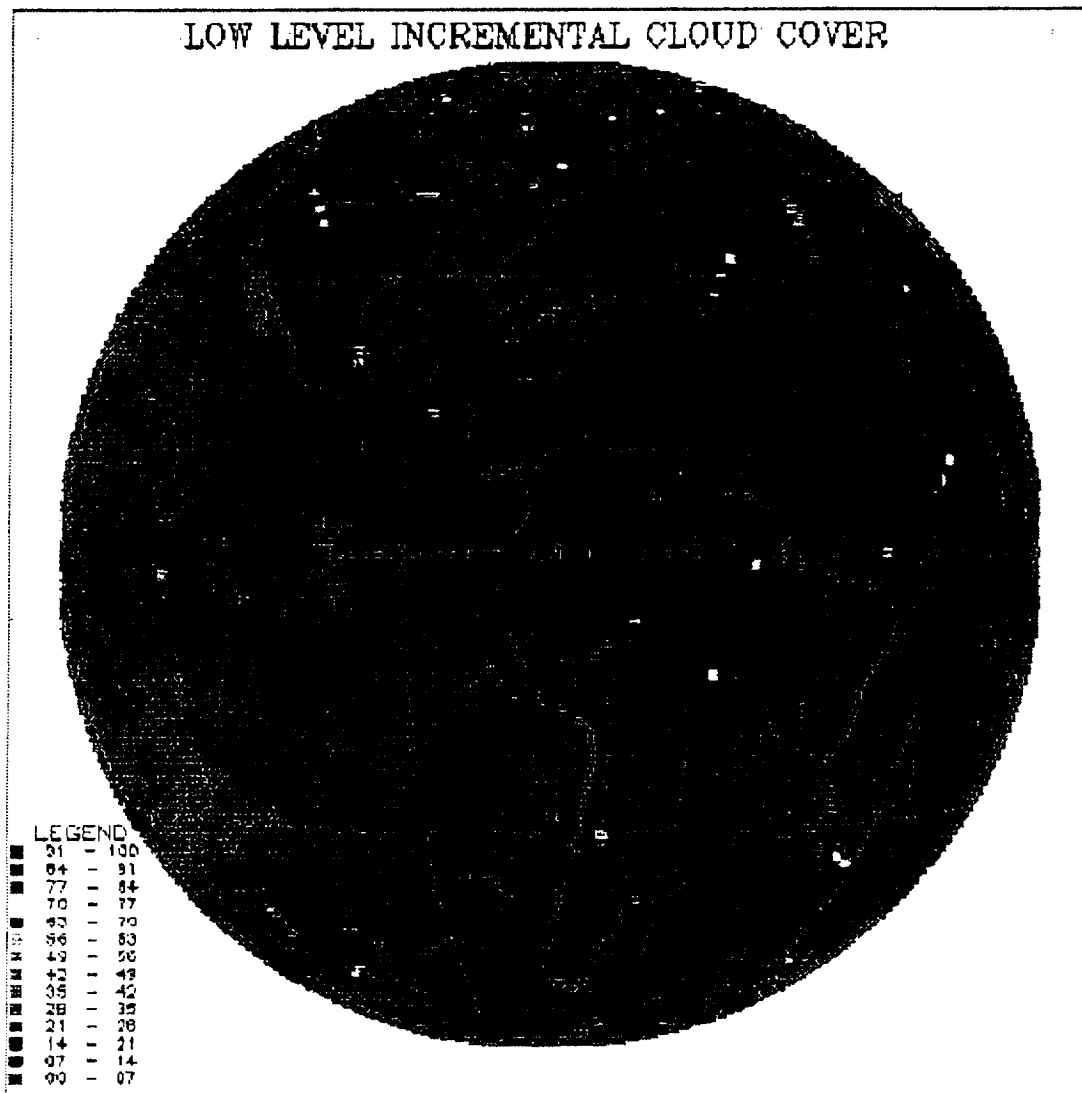


Figure A.31

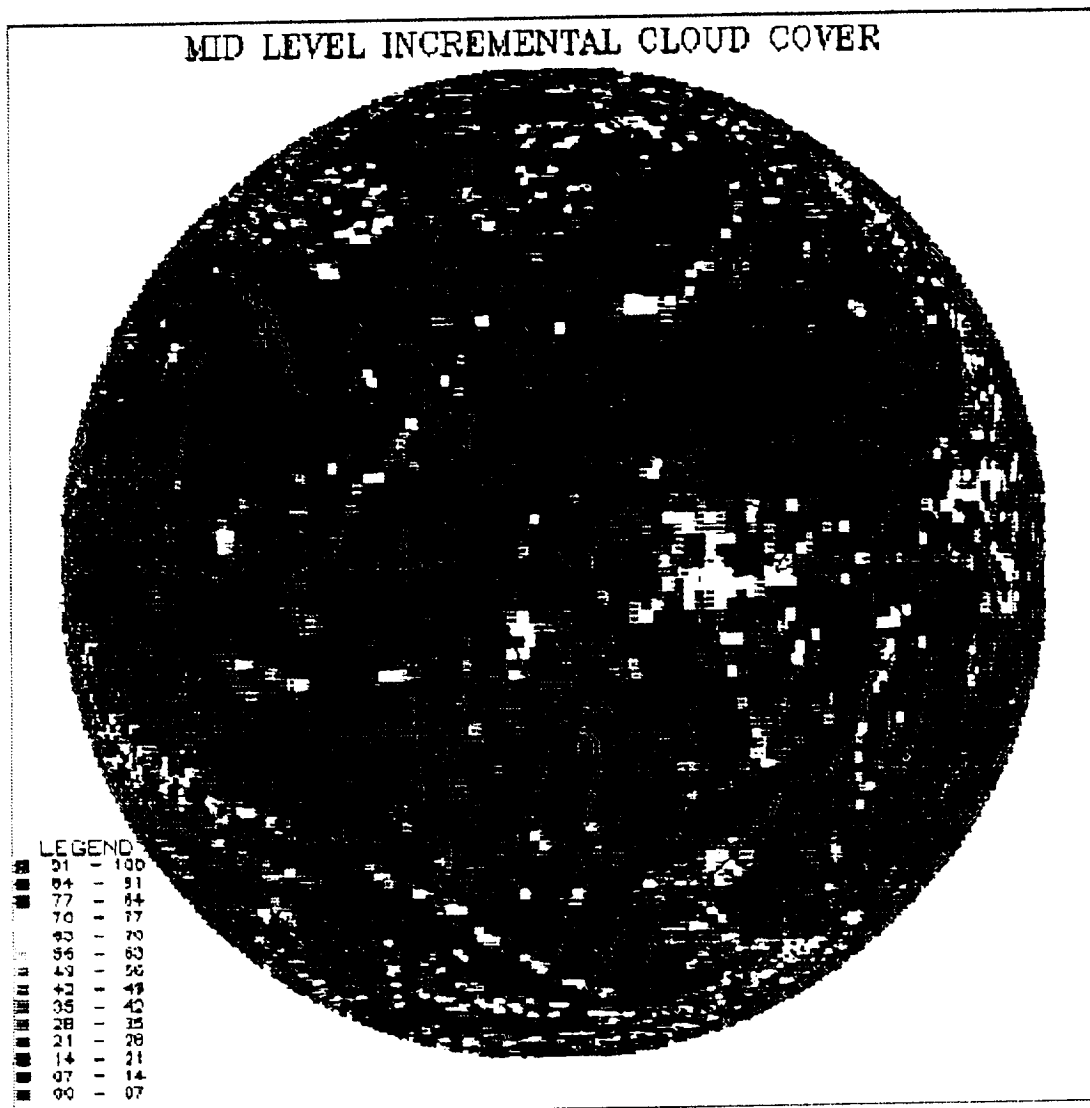


Figure A.32

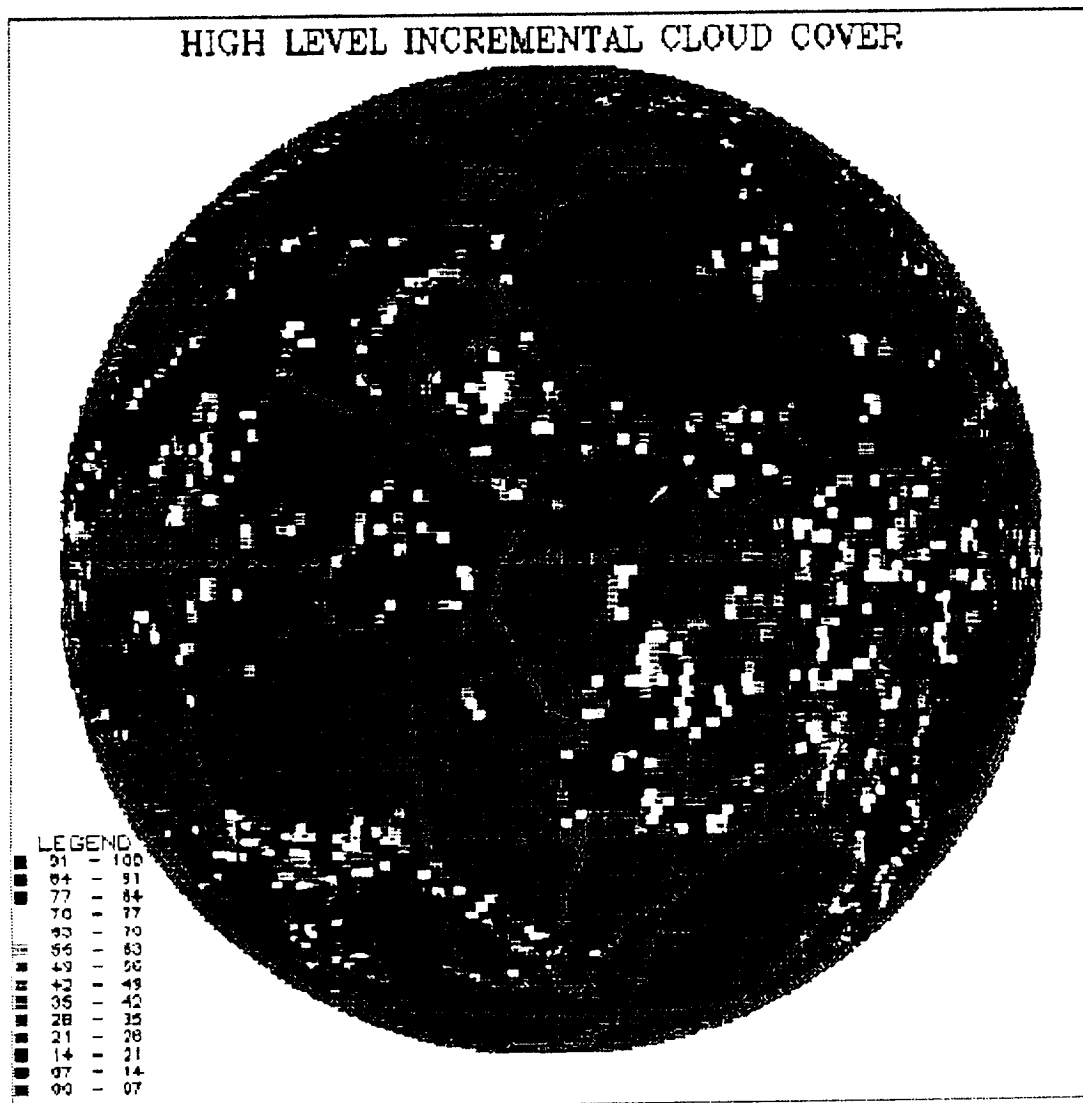


Figure A.33

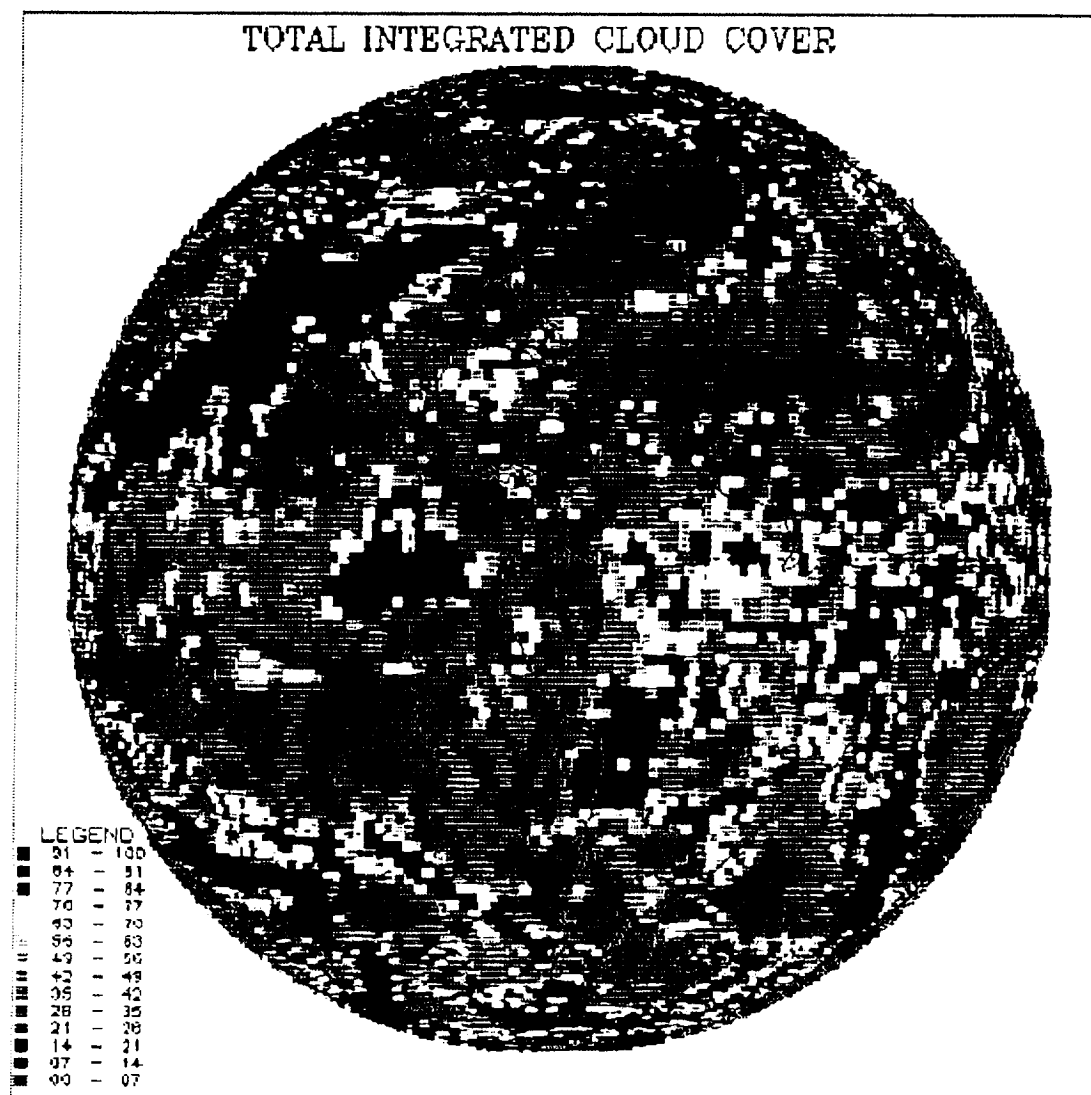


Figure A.34

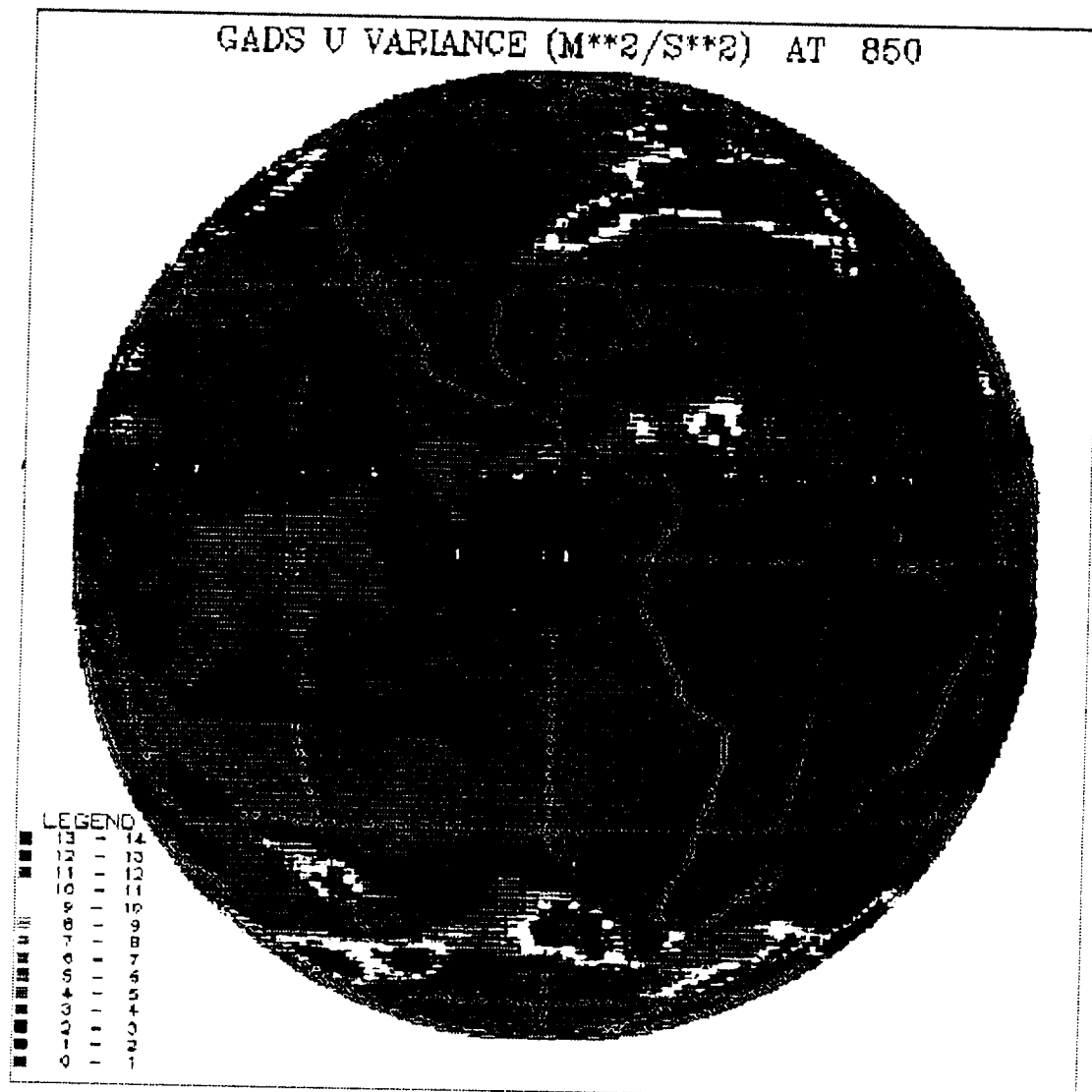


Figure A.35

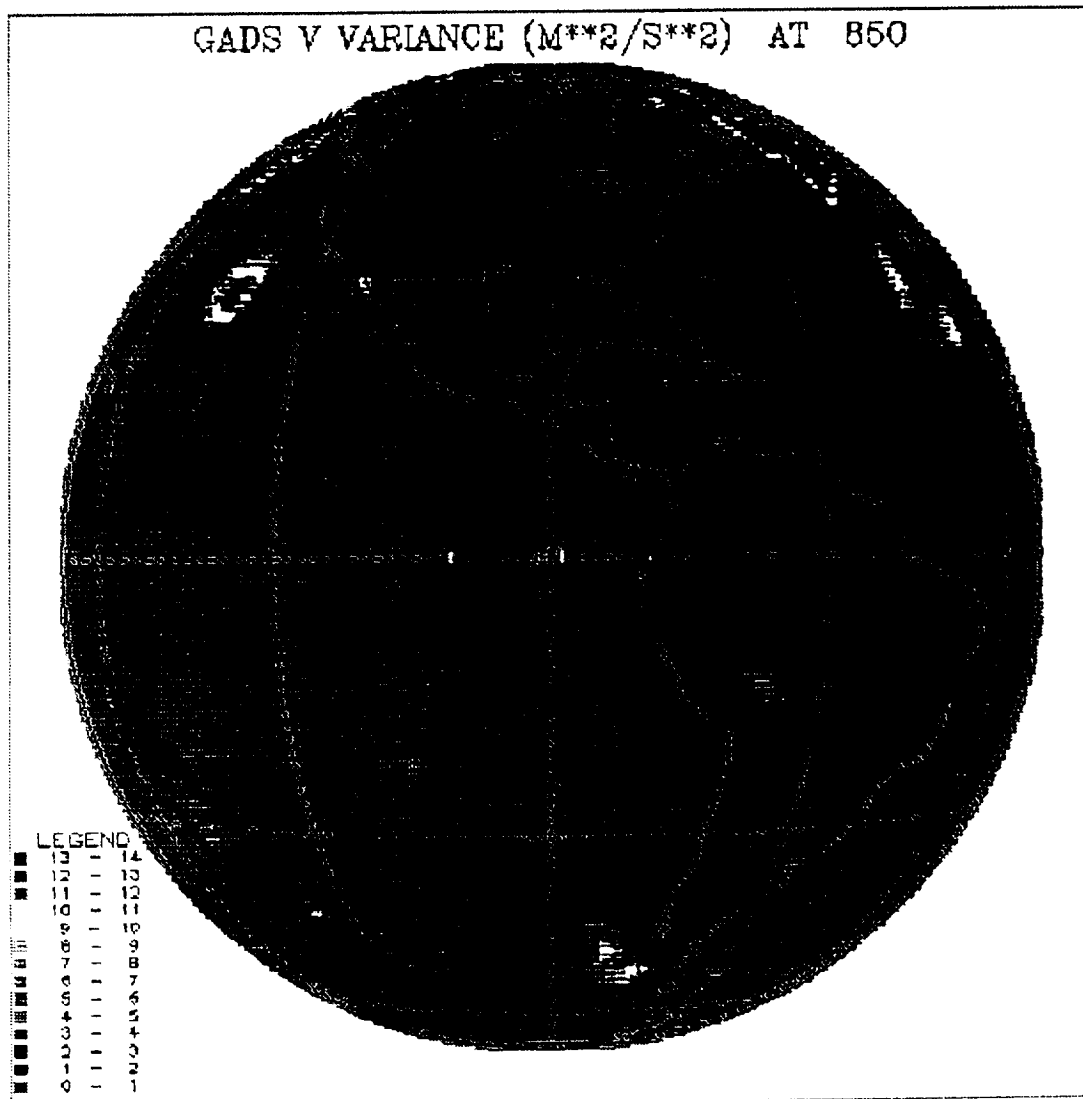


Figure A.36

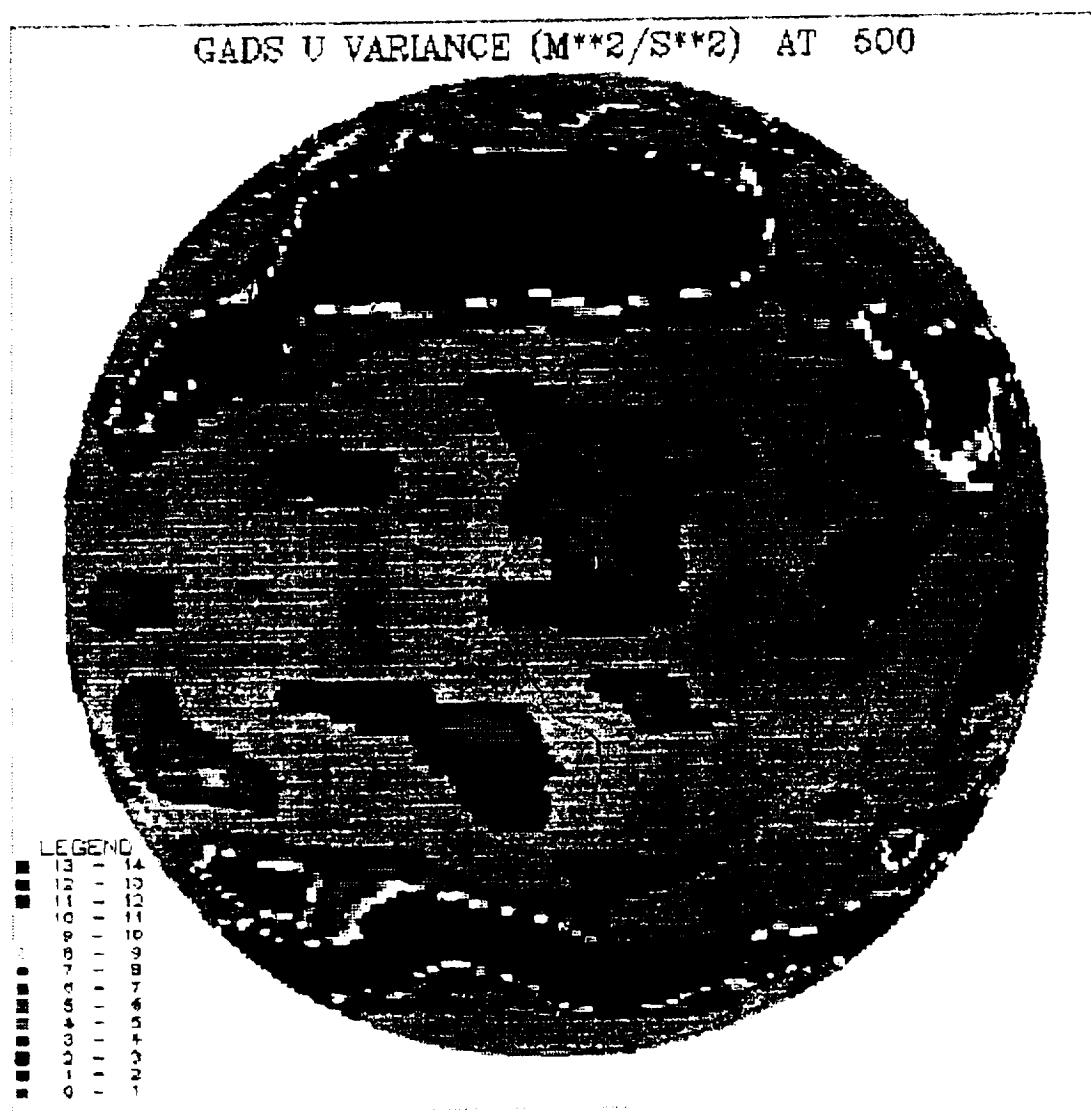


Figure A.37

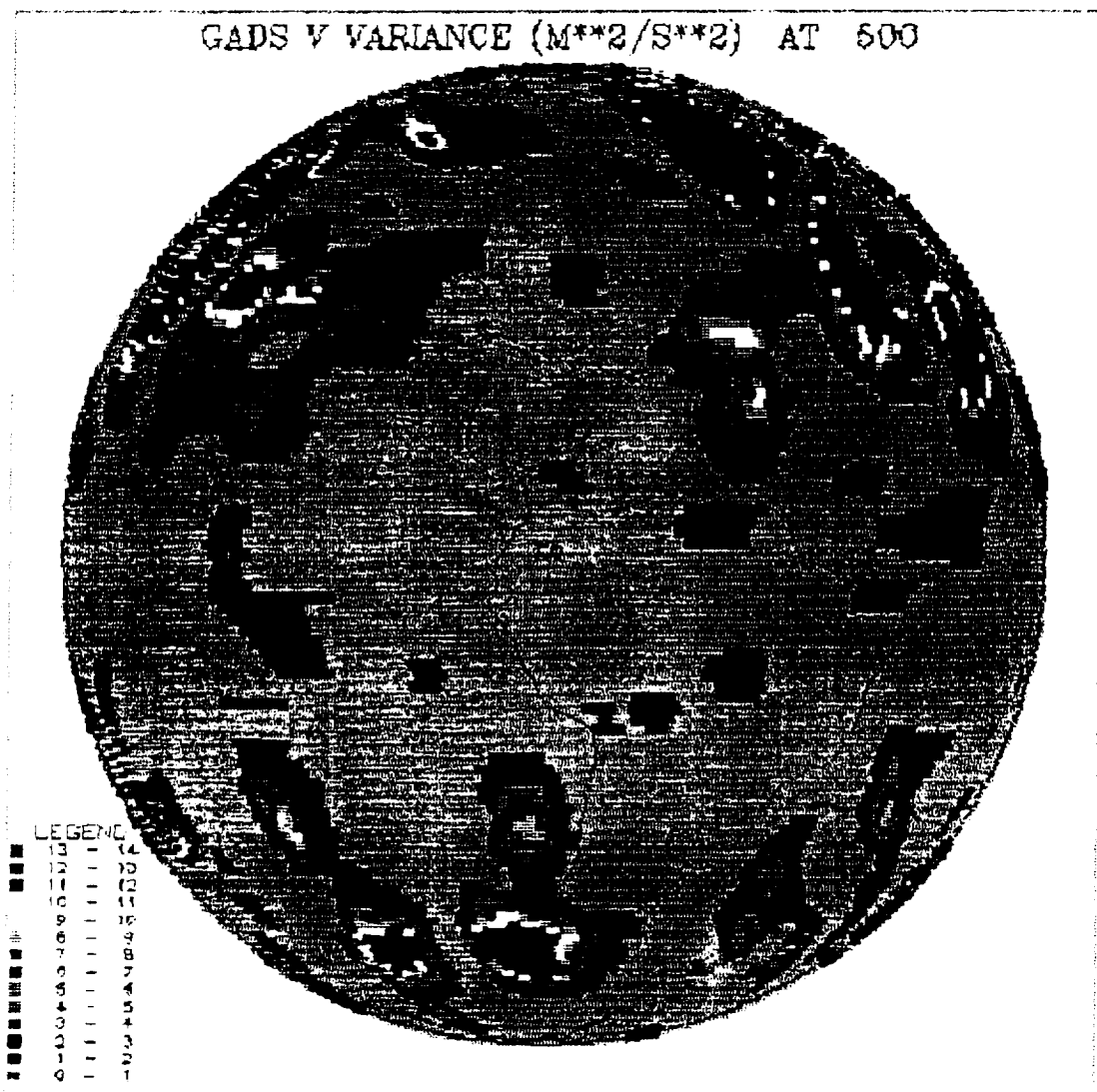


Figure A.38

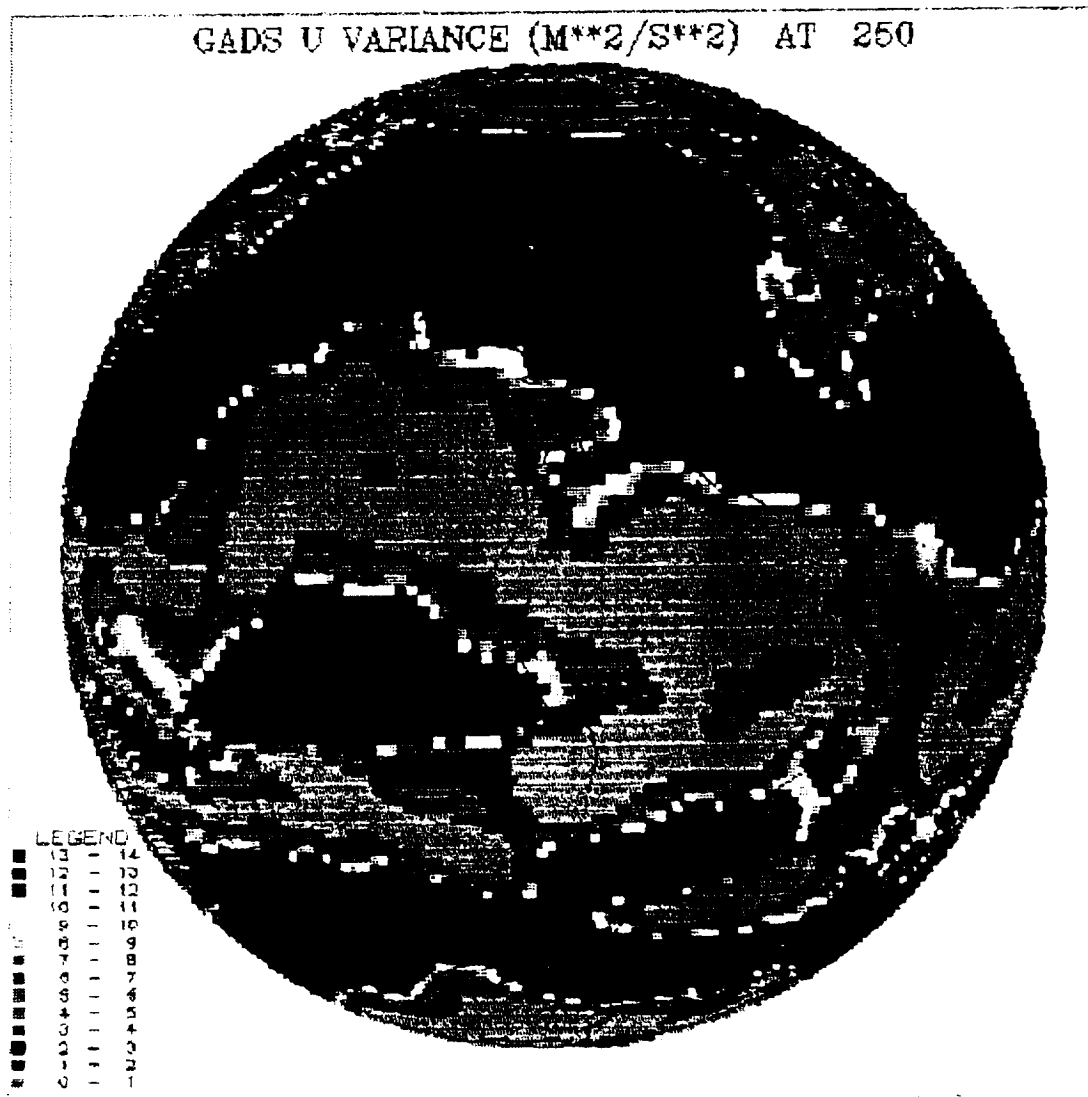


Figure A.39

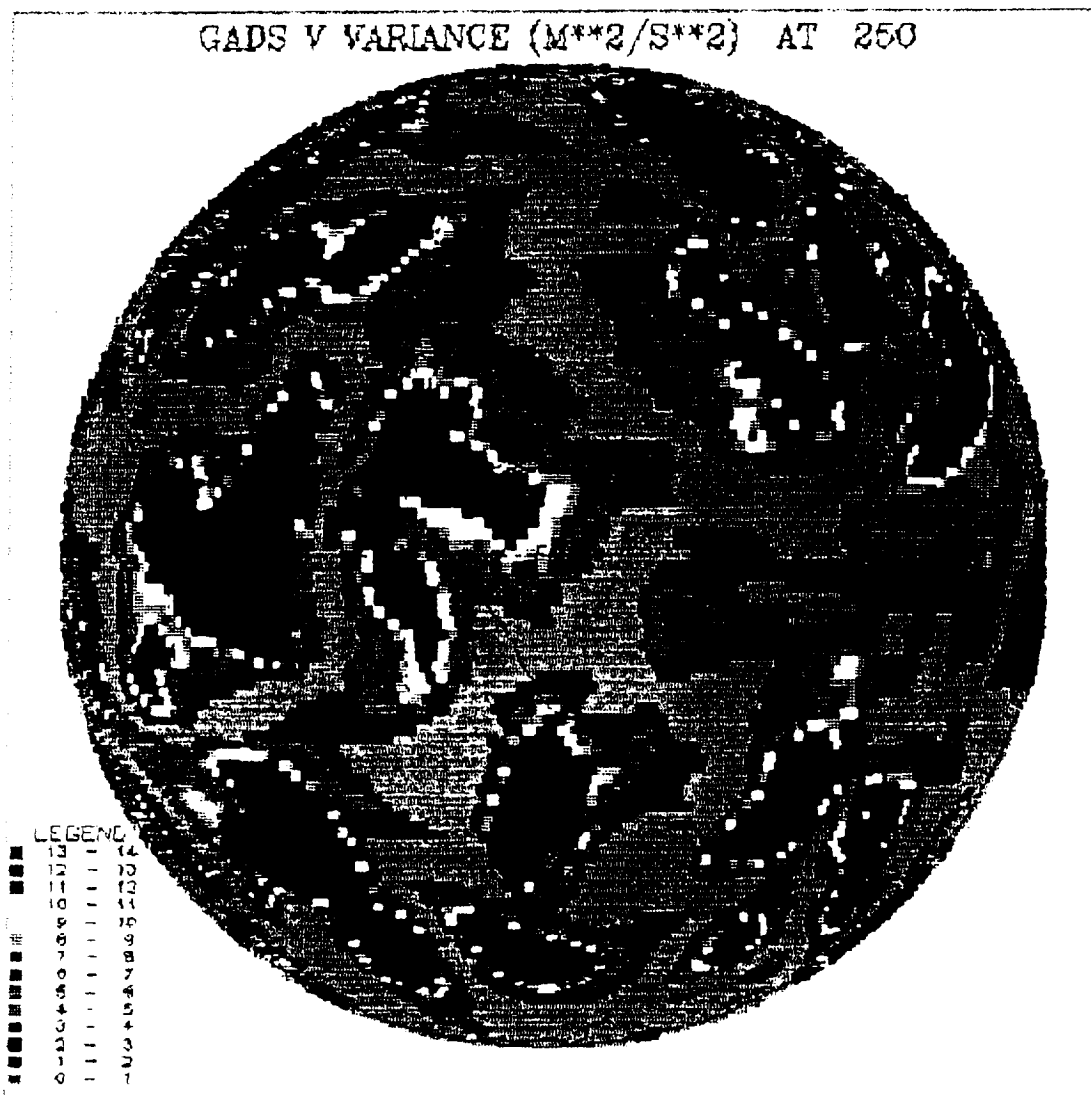


Figure A.40

LSM CONSENSUS CURVES

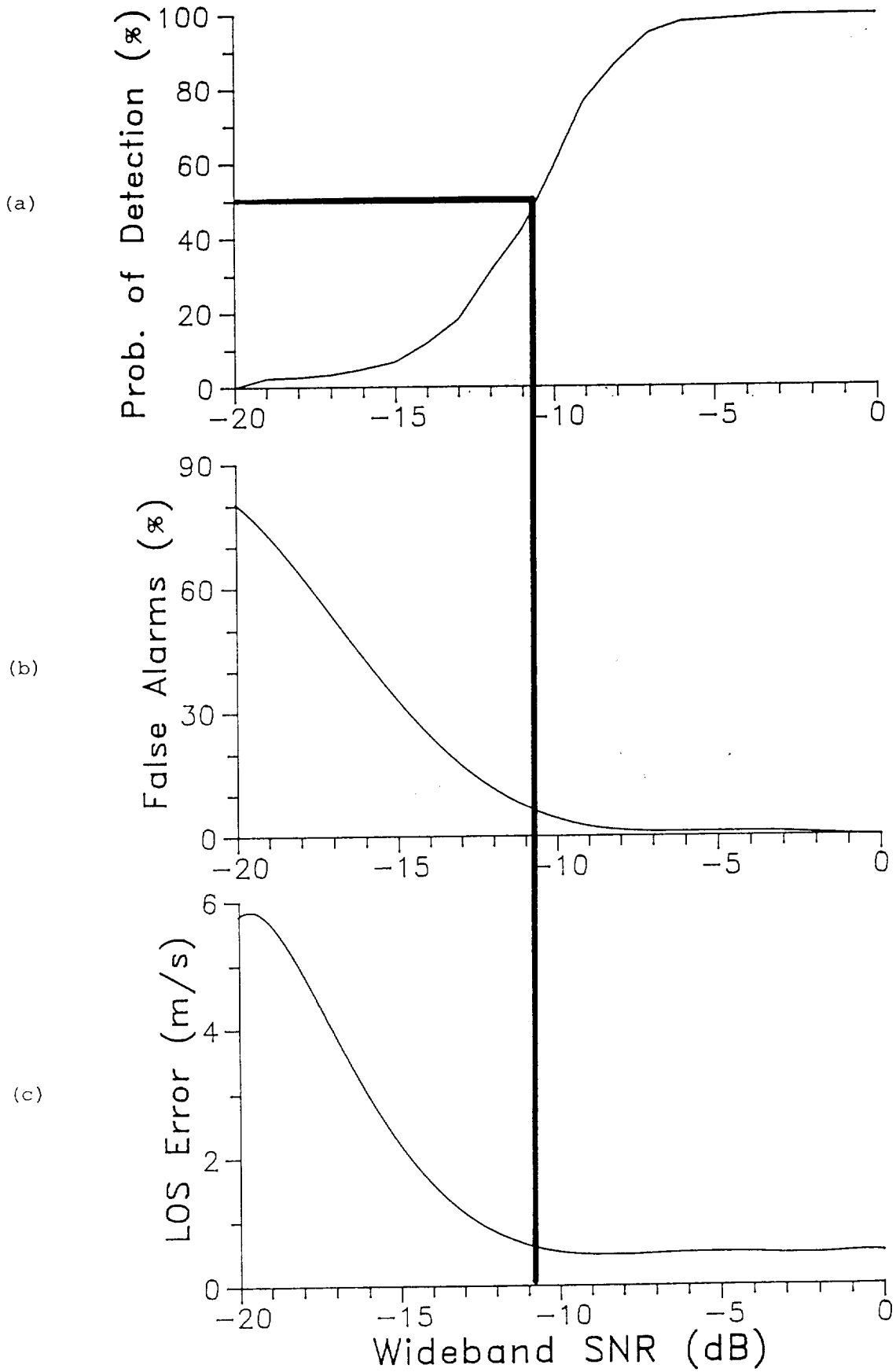


Figure A.41

LAWS PERFORMANCE PLOTS

COLOR OPTION

- ☒ Color
- ☐ Black and White

NUMBER OF LEVELS

- ☒ 14 LEVELS
- ☐ 6 LEVELS

LATITUDE BANDS

- ☒ GLOBAL
- ☐ 90 to 80 N
- ☐ 80 to 70 N
- ☐ 70 to 60 N
- ☐ 60 to 50 N
- ☐ 50 to 40 N (N.H.)
- ☐ 40 to 30 N
- ☐ 30 to 20 N
- ☐ 20 to 10 N
- ☐ 10 to 0 N (EQUATOR)
- ☐ 0 to -10 S
- ☐ -10 to -20 S
- ☐ -20 to -30 S
- ☐ -30 to -40 S
- ☐ -40 to -50 S (S.H.)
- ☐ -50 to -60 S
- ☐ -60 to -70 S
- ☐ -70 to -80 S
- ☐ -80 to -90 S

SELECT INPUT FILE

LDS

UV global

UV actual

EXIT

PRINTER OPTIONS

- ☐ PHASER II
- ☐ OKIDATA 320

Figure A.42

APPENDIX B

1992 OBSERVING SYSTEM SIMULATION EXPERIMENTS

Under contract, SWA was tasked to conduct global OSSEs in co-operative efforts with GSFC and FSU to address orbit/design/configuration issues to assess the science related impacts of various shot management, signal processing and velocity computation algorithms. Five days of LAWS simulations were conducted using the following system configurations

20 joule/1.50 m/4.6 Hz system in a 525 km sunsynchronous orbit,
5 joule/0.75 m/4.6 Hz system in a 525 km sunsynchronous orbit,
0.1 joule/0.50 m/4.6 Hz system in a 200 km sunsynchronous orbit.

The simulated LAWS line-of-sight winds and horizontal wind components were delivered to NASA/GSFC (Atlas) and FSU (Krishnamurti) for assimilation.

One day global LAWS line-of-sight performance charts are shown in Figs. B.1-B.9 for the 20 J, 5 J and the 0.1 J laser system configurations for Nature Run days 16, 19 and 20 January, 1979. The charts give the percentage of time the lidar system can make useful measurements in terms of sufficient backscatter from aerosols, clouds and cirrus clouds. The charts also show the percentage of no returns due to clouds. All three system configurations indicate about 45-60% return from aerosols in the boundary layer. In the troposphere, where aerosols are represented as a background minimum, the 20 J system has 20% returns and the 5 J has less than 2%. The 0.1 J had no returns from aerosols. All three systems showed 0-10% returns from clouds.

One day of global LAWS U, V component (fixed area - 125 km X 125 km) performance charts are shown in Figs. B.10-B.20 for the 20 J, 5 J and the 0.1 J laser system configurations for Nature Run days 16, 19 and 20 January, 1979. The charts give the percentage of time that a lidar system can make good horizontal wind estimates for 5 categories ranging from 1 m/s accuracy to 5 m/s accuracy. Also shown is the percentage of time the system had an insufficient number of shots in the grid area to make a wind estimate. Figures B.10-B.12 give the LAWS performance as a function of the global grids that LAWS made an estimate in, whereas Figs. B.13-B.20 base the LAWS' performance upon the total number of global grids.

Figures B.10-B.12 demonstrate that all three systems can make good boundary layer wind estimates 15 to 20% of the time within 1 m/s accuracy and 30 to 50% of the time within 5 m/s accuracy. In the troposphere, the 20 J system's performance gives good wind estimates 15-25% of the time for 5 m/s or less. On the other hand, the 5 J and the 0.1 J performance is less than

10%. Figures B.13-B.20 illustrate the same relationship between the laser systems, but also considers the total area of the globe in the performance. The graphs show that LAWS could not make a wind estimate in 18% of the global grid areas due to lack of coverage.

In addition, we ran a LAWS simulation for a 0.2 joule/0.60 m/10 Hz system in a 300 km sunsynchronous orbit with a power conservation shot management algorithm (see Section 4.0, Appendix A). The power conservation shot management algorithm only takes lidar shots where groupings of orthogonal shots exist as shown in Fig. B.21. The line-of-sight and horizontal wind products were delivered to Atlas (NASA/GSFC) and to Krishnamurti (FSU) for assimilation.

Global LAWS line-of-sight performance charts for days 1 through 5 are shown in Figs. B.22-B.26. The charts give the percentage time the lidar system can make useful measurements in terms of sufficient backscatter from aerosols, clouds and cirrus clouds. The charts also show the percentage of no returns due to clouds.

Global LAWS U, V component (fixed area - 125 km X 125 km) performance charts for days 1 through 5 are shown in Figs. B.27-B.31. The charts give the percentage time that a lidar system can make good horizontal wind estimates for 5 categories ranging from 1 m/s accuracy to 5 m/s accuracy. Also shown is the percentage of time the system has an insufficient number of shots in the grid area to make a wind estimate. The coverage for the power conservation mode at a 300 km orbit is very small, but the quality of the wind products is extremely high. Figure B.32 shows the global coverage in 24 hours for the 0.2 J configuration.

An upgrade in the LAWS Simulation Model (LSM) - Global Version to include surface level LAWS winds added the option for a line-of-sight (LOS) performance profile with six atmospheric layers: surface, 1000 mb, low clouds, mid clouds, high clouds, and cloud free upper atmosphere. Figure B.33 shows the LOS observations for the 20 J LAWS configuration, where LAWS measurements due to high, middle and low clouds are seen 35%, 20% and 23% of the time, respectively. Conversations with M.J. Post and R. Menzies indicate enhanced backscatter levels due to volcanic eruptions. To bracket expected 20 J LAWS performance, we ran the LSM with aerosol backscatter increased by an order of magnitude higher than the background mode. Figure B.34 shows a potential increase in aerosol LOS winds by 70%, 40% and 50% in the cloud free upper atmosphere, high cloud layer and the mid cloud layer, respectively. Little or no impact is seen in the planetary boundary layer (PBL).

FIGURE CAPTIONS

- Figure B.1: Day 1 global LAWS line-of-sight performance chart for a 20 j lidar system with a 1.5 M diameter telescope. The diagram's statistics are based upon a 1-day LAWS simulation for a 525 km orbit. The chart shows the percentage of time the lidar system can make useful measurements in terms of sufficient backscatter from aerosols, clouds and cirrus clouds throughout the vertical. The chart also shows the percentage of no returns due to clouds.
- Figure B.2: As for Fig. B.1 but for a 5 j lidar system with a 0.75 M diameter telescope.
- Figure B.3: As for Fig. B.1 but for a 0.1 j lidar system with a .5 M diameter telescope based upon a 200 km orbit.
- Figure B.4: As for Fig. B.1 but for Day 4.
- Figure B.5: As for Fig. B.2 but for Day 4.
- Figure B.6: As for Fig. B.3 but for Day 4.
- Figure B.7: As for Fig. B.1 but for Day 5.
- Figure B.8: As for Fig. B.2 but for Day 4.
- Figure B.9: As for Fig. B.3 but for Day 5.
- Figure B.10: Day 1 global LAWS U, V component (fixed area - 125 km x 125 km) performance chart for a 20 j lidar system with a 1.5 M diameter telescope. The diagram's statistics are based upon a 1-day LAWS simulation for a 525 km orbit. The chart gives the percentage of time that the lidar system can make good horizontal wind estimates for five accuracy categories ranging from 1 m/s to 5 m/s and the percentage of insufficient number of shots to make a wind estimate. The performance chart is based upon grid areas that LAWS made a measurement in.
- Figure B.11: As for Fig. B.10 but for a 0.1 j lidar system with a .5 M diameter telescope for a 200 km orbit.
- Figure B.12: As for Fig. B.10 but for a 5 j lidar system with a .75 M diameter telescope.

- Figure B.13: As for Fig. B.10 but based upon the global grid areas.
- Figure B.14: As for Fig. B.10 but for Day 4 based upon the global grid areas.
- Figure B.15: As for Fig. B.10 but for Day 5 based upon the global grid areas.
- Figure B.16: Day 1 global LAWS U, V component (fixed area - 125 km x 125 km) performance chart for a 5 j lidar system with a .75 M diameter telescope. The diagram's statistics are based upon a 1-day LAWS simulation for a 525 km orbit. The chart gives the percentage of time that the lidar system can make good horizontal wind estimates for five accuracy categories ranging from 1 m/s to 5 m/s and the percentage of insufficient number of shots to make a wind estimate. The performance chart is based upon the global grid areas.
- Figure B.17: As for Fig. B.15 but for Day 5.
- Figure B.18: As for Fig. B.15 but for a 5 j lidar system with a .75 M diameter telescope for Day 5.
- Figure B.19: As for Fig. B.15 but for a 0.1 j lidar system with a .5 M diameter telescope based upon a 200 km orbit for Day 4.
- Figure B.20: As for Fig. B.15 but for a 0.1 j lidar system with a .5 M diameter telescope based upon a 200 km orbit for Day 5.
- Figure B.21: Space-based Doppler lidar shot pattern using the power conservation shot management algorithm. The orbit was 300 km for a 100 Hz PRF.
- Figure B.22: Day 1 global LAWS line-of-sight performance chart for a 0.2 j lidar system with a 0.6 M diameter telescope. The diagram's statistics are based upon a 1-day LAWS simulation for a 300 km orbit. The charts show the percentage of time the lidar system can make useful measurements in terms of sufficient backscatter from aerosols, clouds and cirrus clouds throughout the vertical. The chart also shows the percentage of no returns due to clouds.
- Figure B.23: As for Fig. B.22 but for Day 2.

- Figure B.24: As for Fig. B.22 but for Day 3.
- Figure B.25: As for Fig. B.22 but for Day 4.
- Figure B.26: As for Fig. B.22 but for Day 5.
- Figure B.27: As for Fig. B.22 but for Day 1 global LAWS U, V component (fixed area - 125 km x 125 km) for global grid areas.
- Figure B.28: As for Fig. B.27 but for Day 2.
- Figure B.29: As for Fig. B.27 but for Day 3.
- Figure B.30: As for Fig. B.27 but for Day 4.
- Figure B.31: As for Fig. B.27 but for Day 5.
- Figure B.32: Global coverage plot for the 0.2 j, 0.6 m system at a 300 km orbit.
- Figure B.33: Global LAWS line-of-sight performance chart for a 20 j lidar system with a 1.5 M diameter telescope. The diagram's statistics are based upon a 1-day LAWS simulation for a 525 km orbit. The chart shows the percentage of time the lida system can make useful measurements in terms of sufficient backscatter from aerosols, clouds and cirrus clouds for 6 atmospheric layers: surface, 1000 mb, low clouds, mid clouds, high clouds and cloud free upper atmosphere. The chart also shows the percentage of cloud obscuration.
- Figure B.34: As for Fig. B.33 with an enhanced aerosol backscatter.

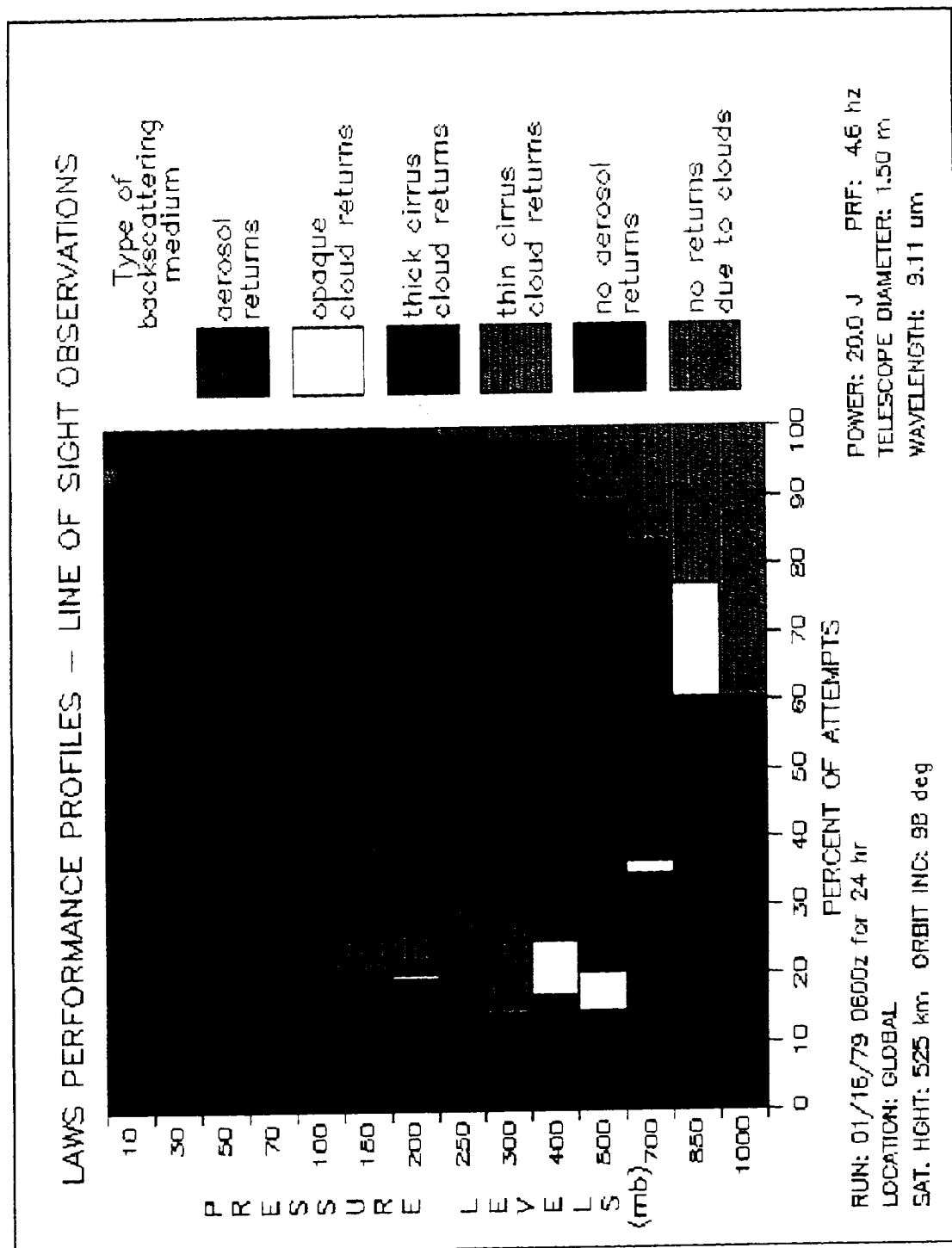


Figure B.1

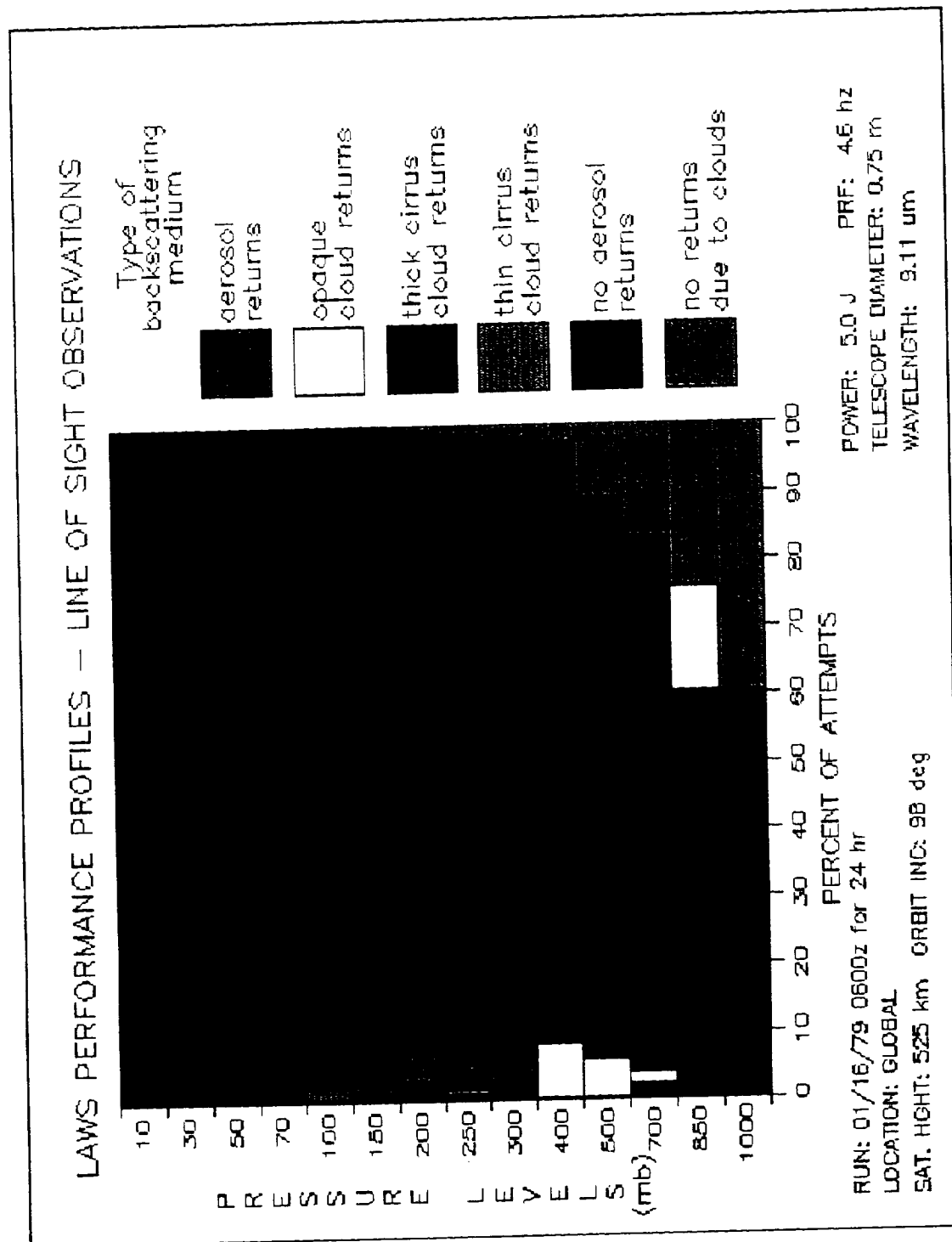


Figure B.2

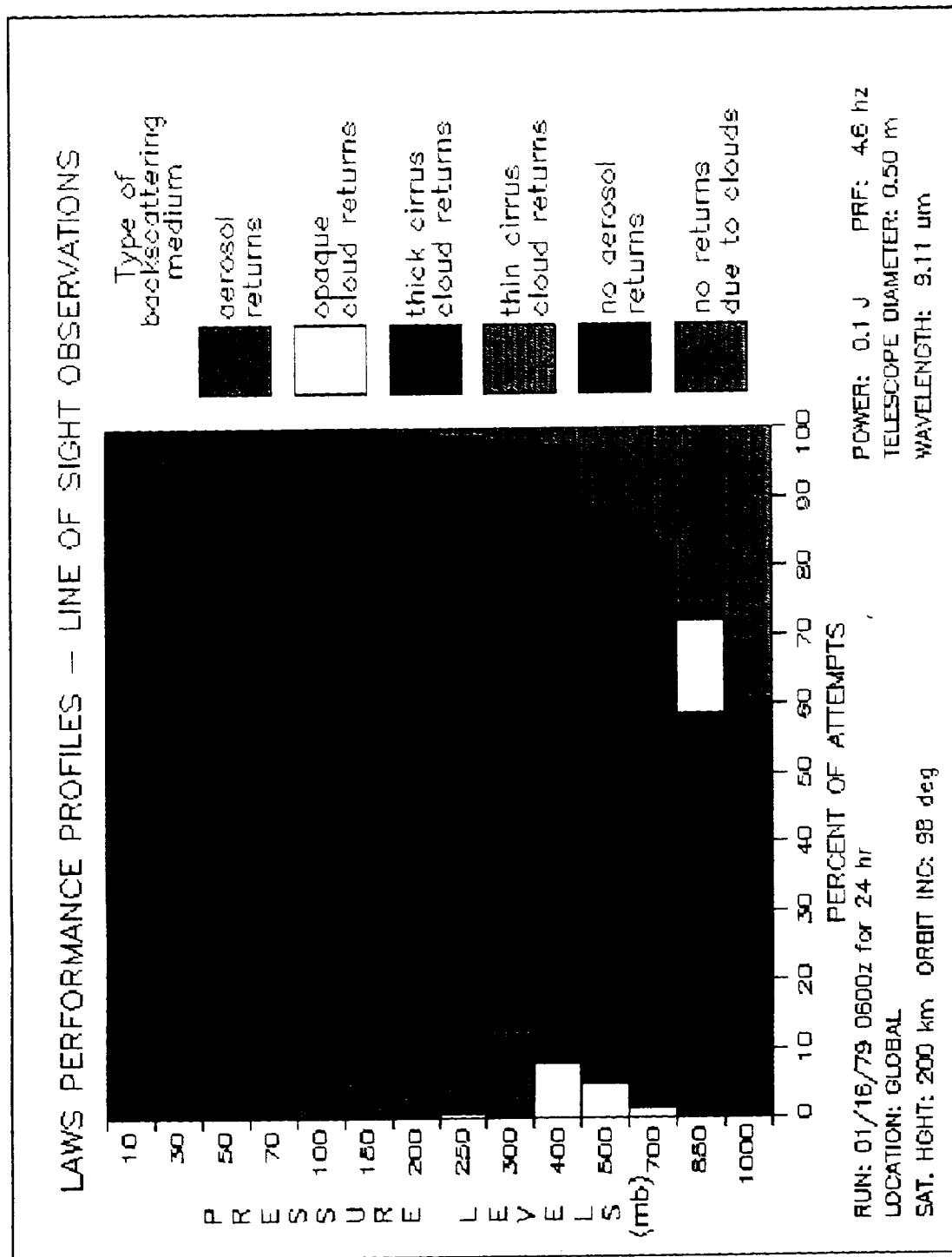


Figure B.3

LAWS PERFORMANCE PROFILES - LINE OF SIGHT OBSERVATIONS

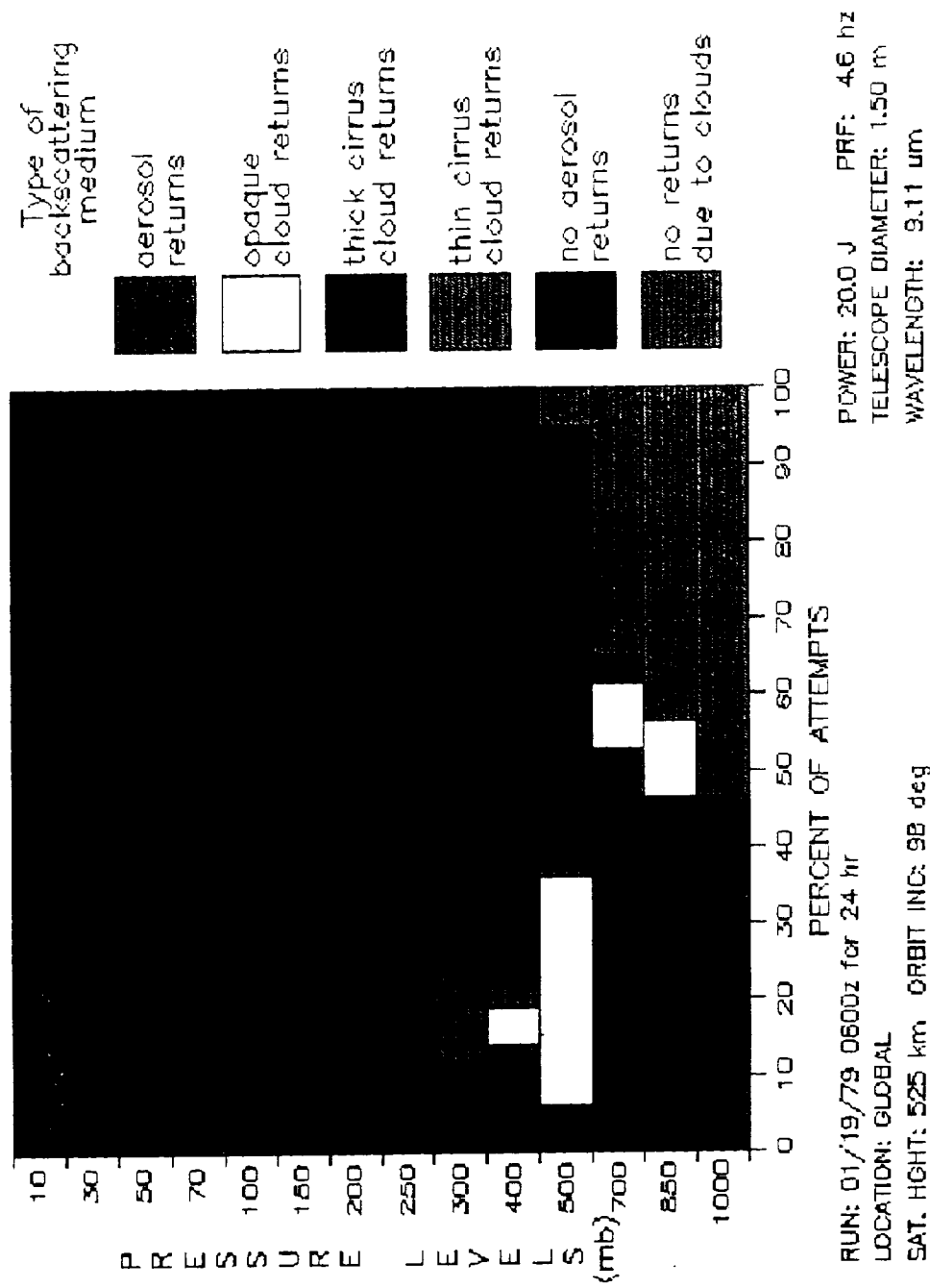


Figure B.4

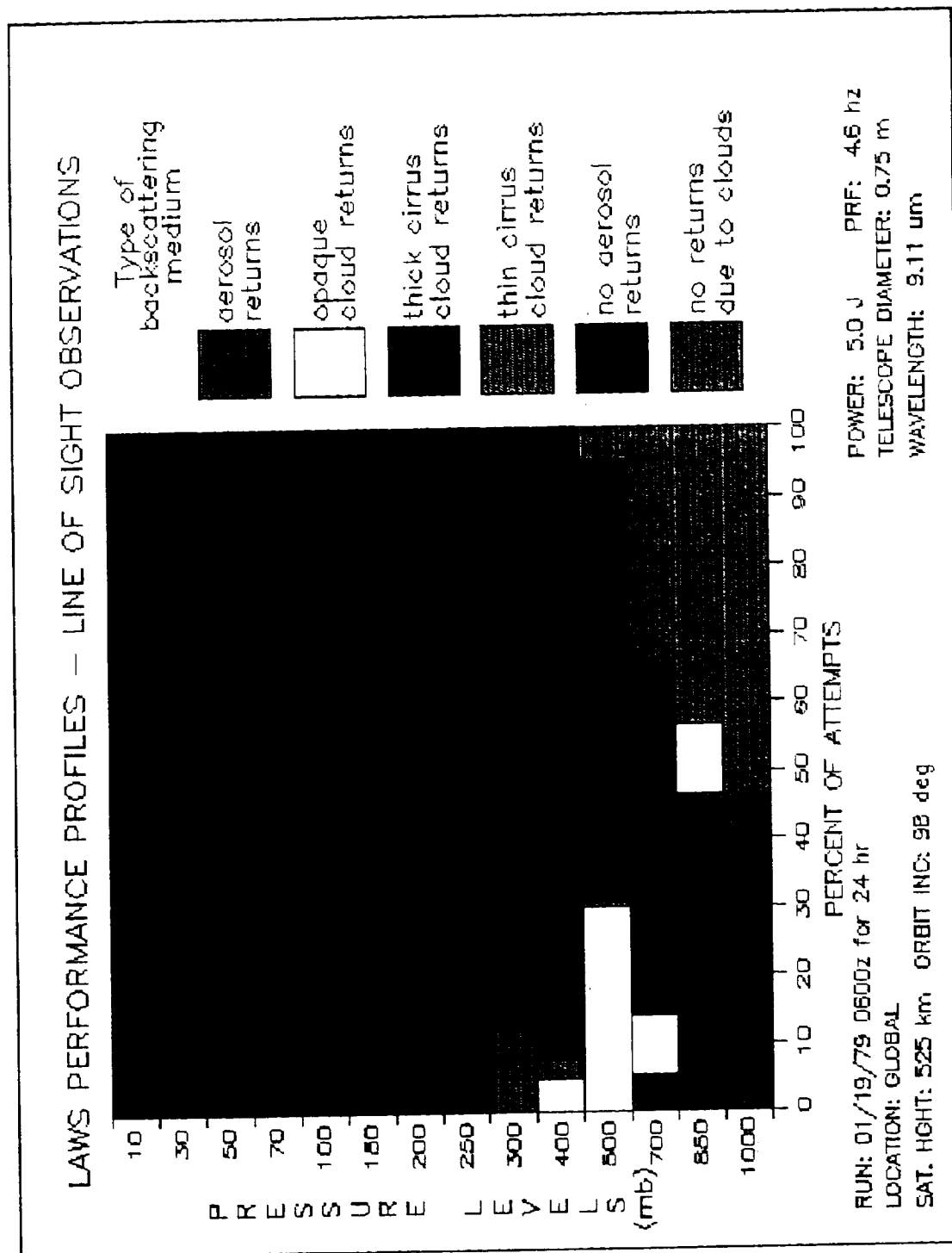


Figure B.5

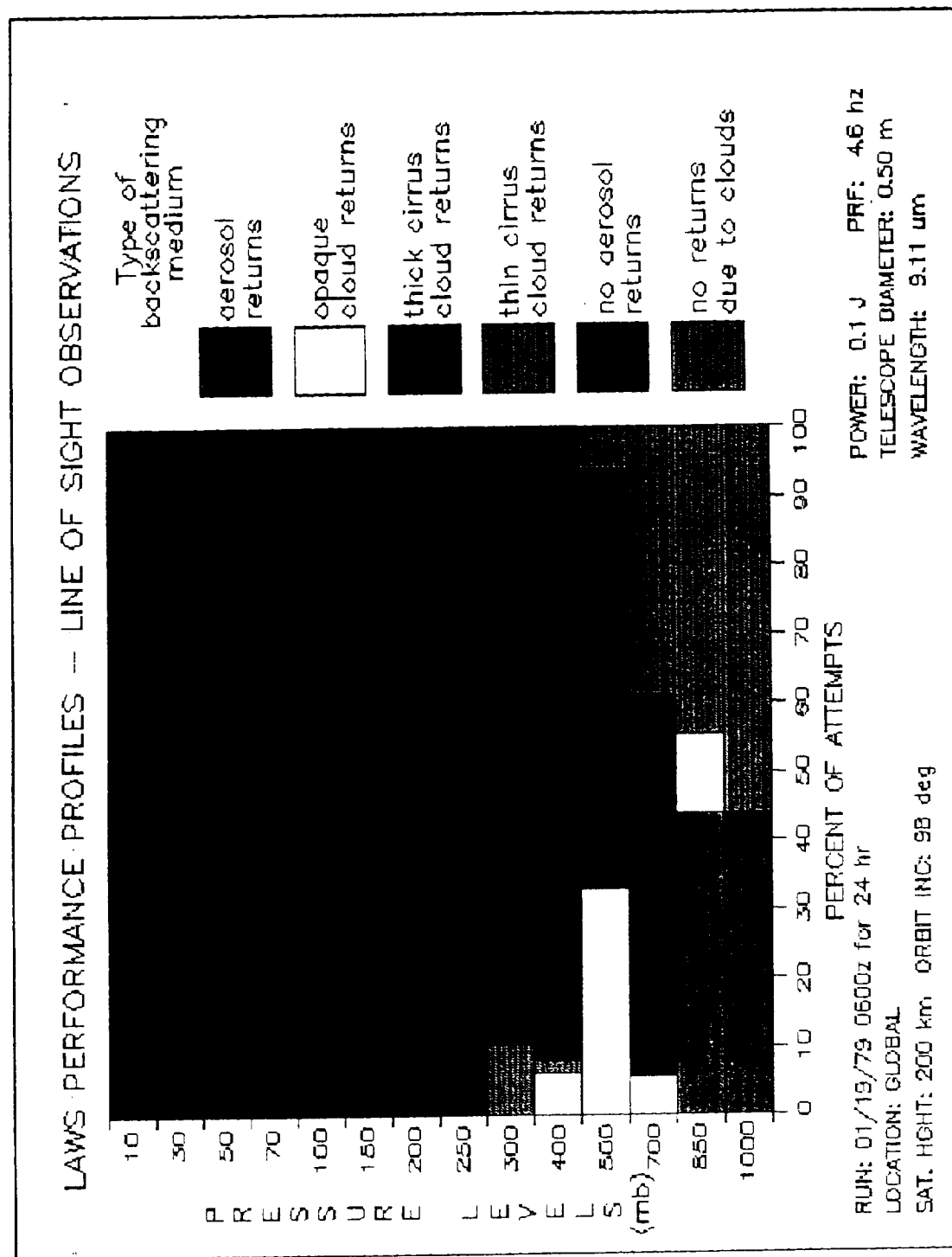


Figure B.6

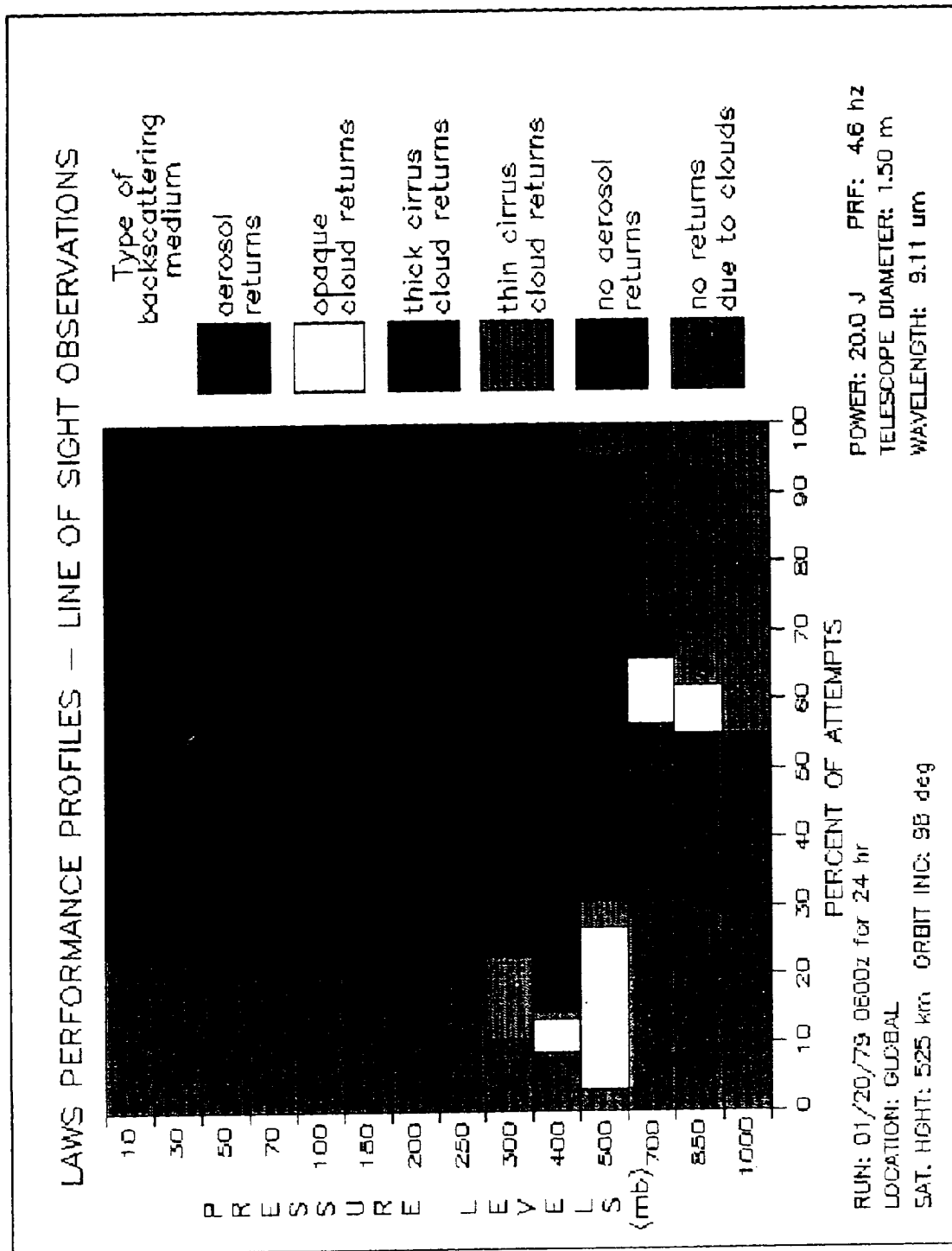


Figure B.7

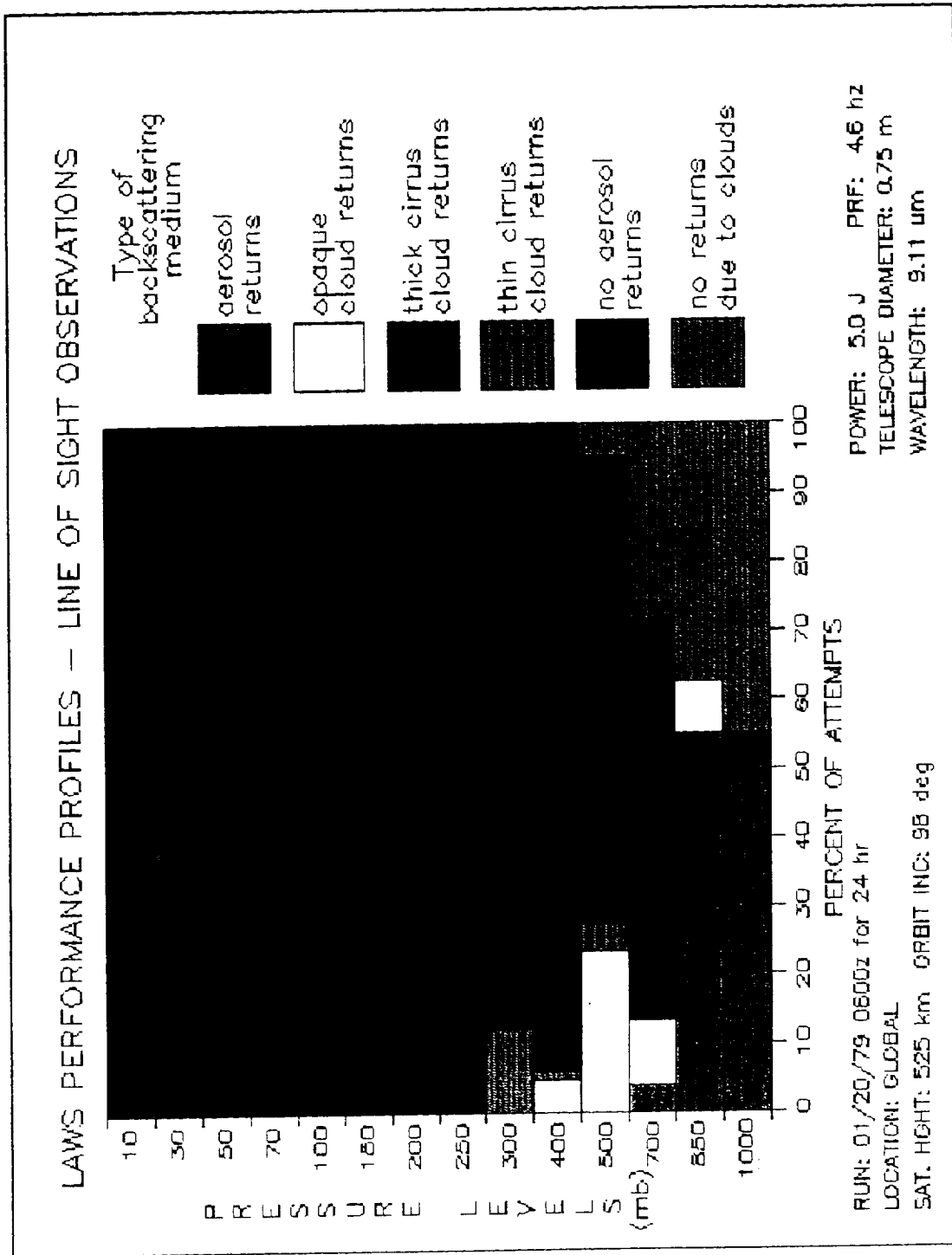


Figure B.8

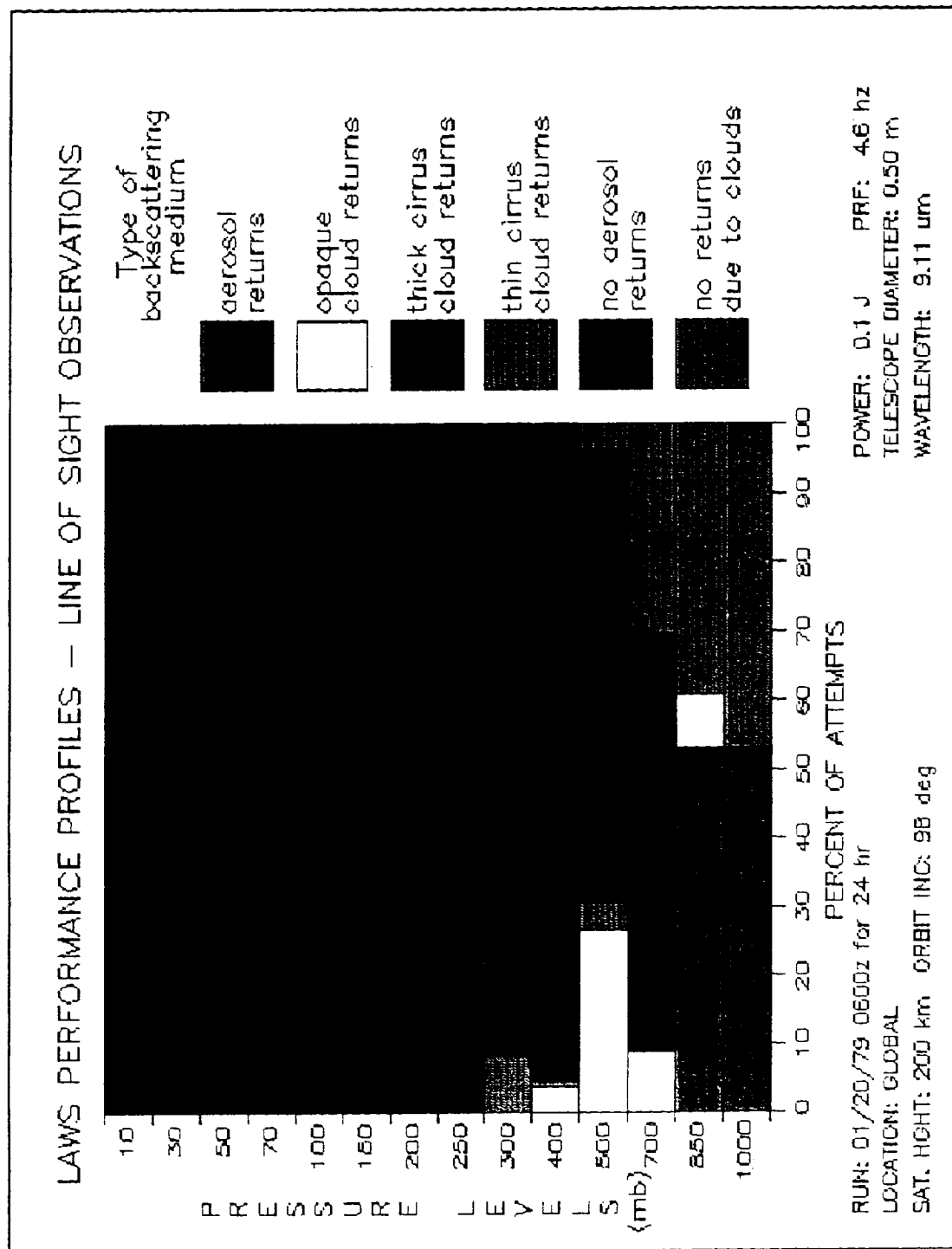
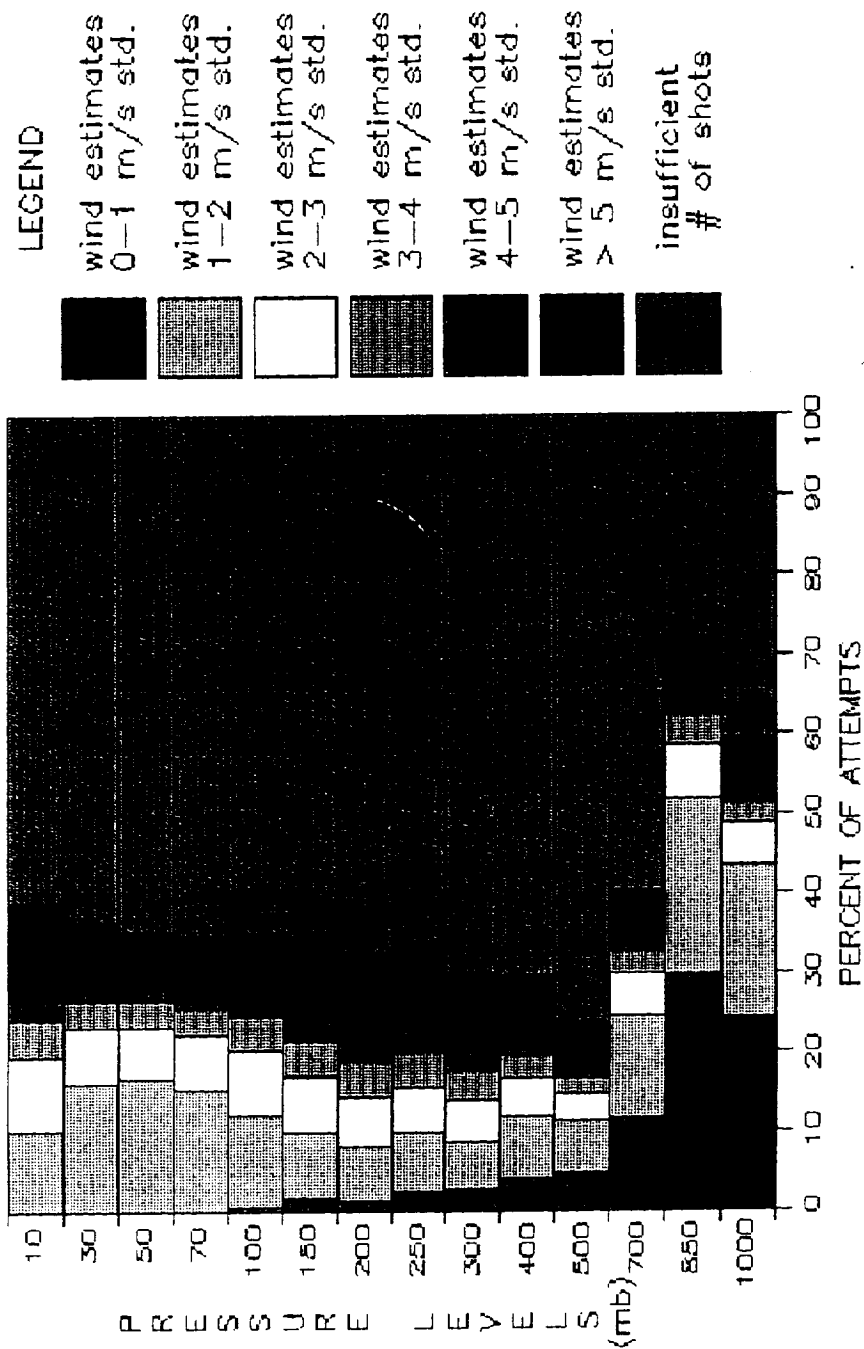


Figure B.9

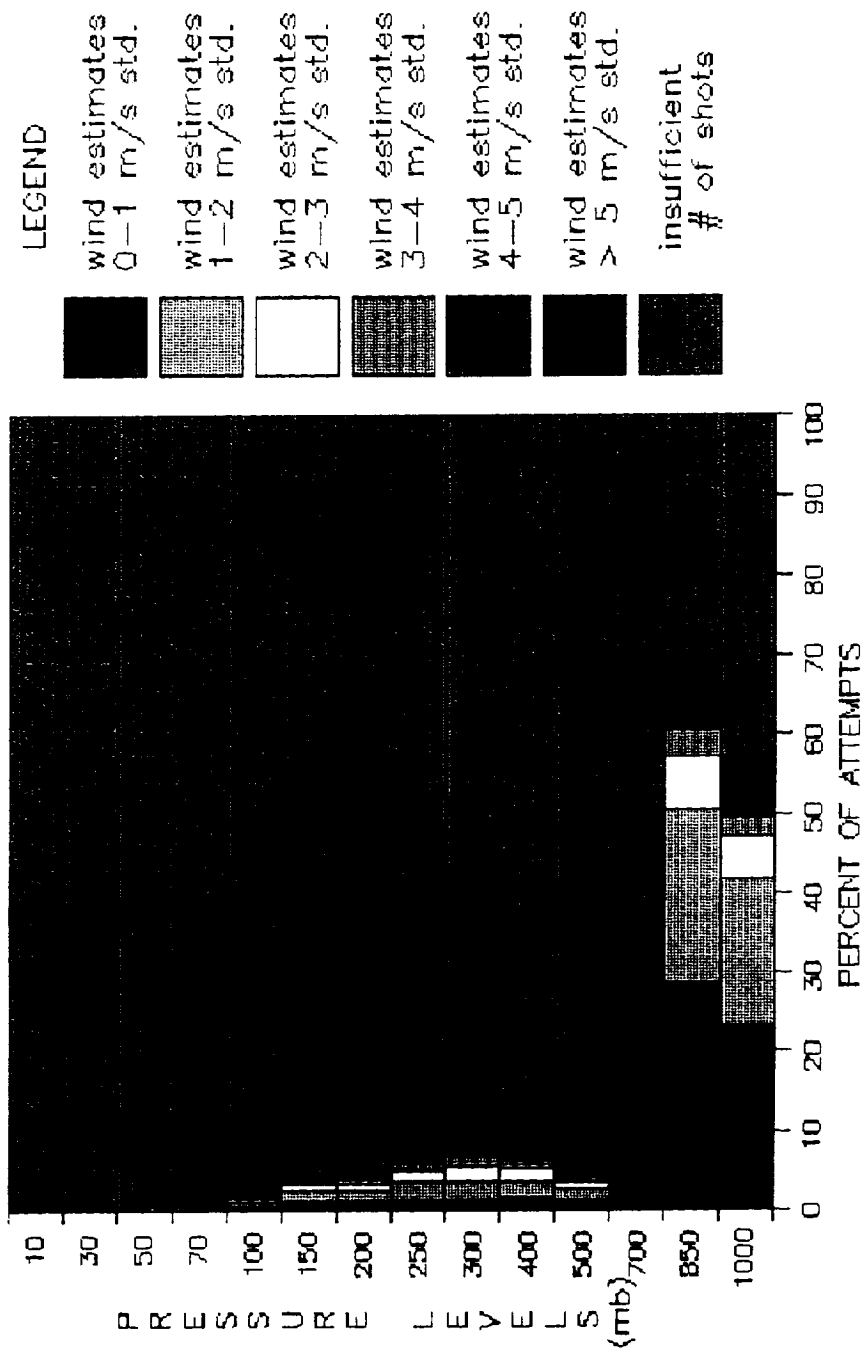
LAWS PERFORMANCE PROFILES - U, V COMPONENT, FIXED AREA



RUN: 01/16/79 0600z for 24 hr
 LOCATION: GLOBAL
 SAT. HGT: 525 km ORBIT INC: 98 deg
 POWER: 20.0 J PRF: 46 hz
 TELESCOPE DIAMETER: 1.50 m
 WAVELENGTH: 9.11 um

Figure B.10

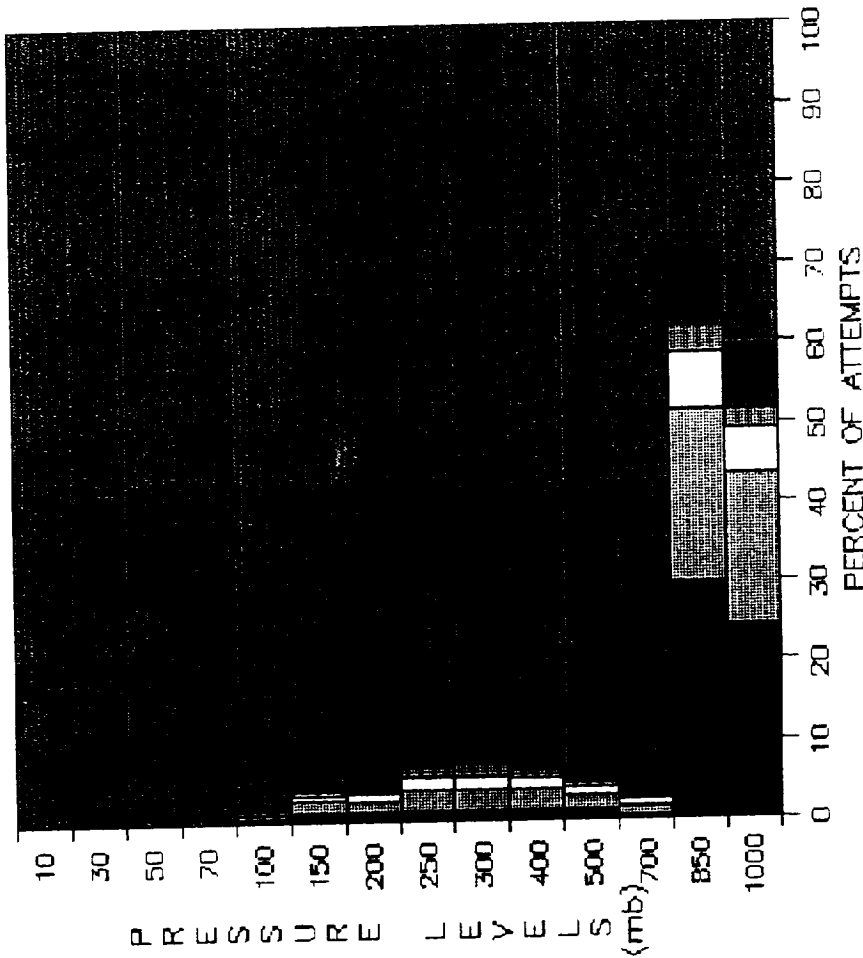
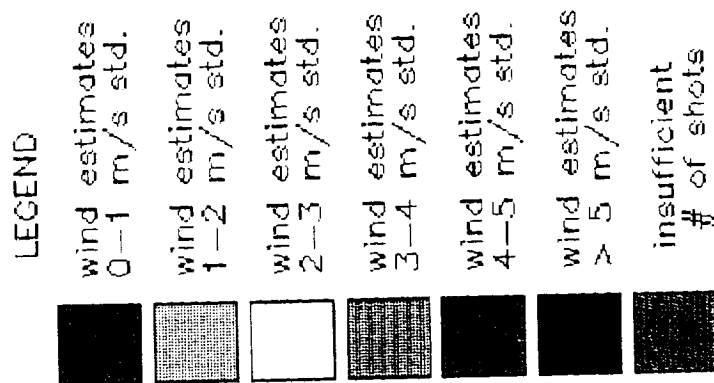
LAWS PERFORMANCE PROFILES - U, V COMPONENT, FIXED AREA



RUN: 01/16/79 0600z for 24 hr
 LOCATION: GLOBAL
 SAT. HGT: 200 km ORBIT INC: 98 deg
 POWER: 0.1 J PRF: 46 hz
 TELESCOPE DIAMETER: 0.50 m
 WAVELENGTH: 9.11 um

Figure B.11

LAWS PERFORMANCE PROFILES -- "U, V COMPONENT, FIXED AREA"

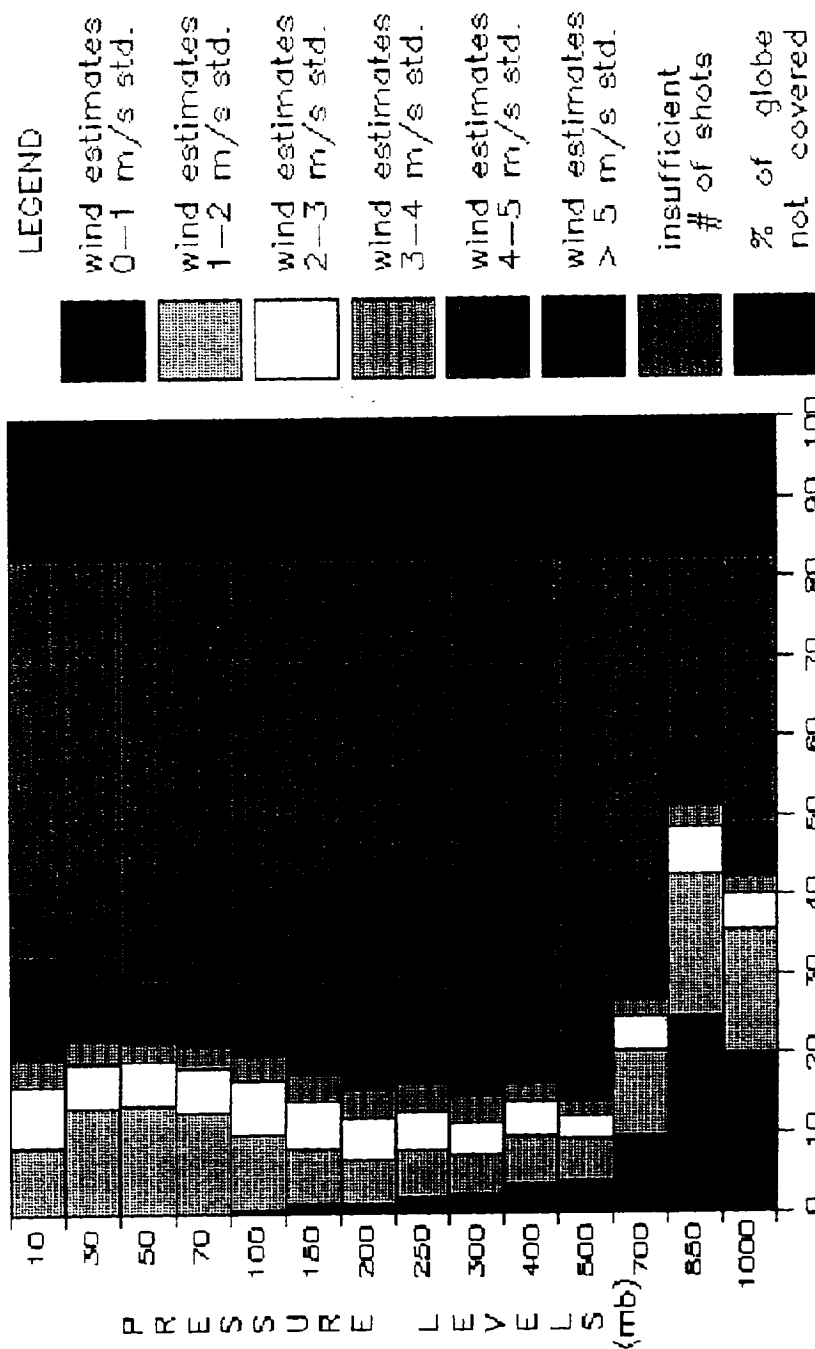


POWER: 5.0 J PRF: 46 hz
TELESCOPE DIAMETER: 0.75 m
WAVELENGTH: 9.11 um

RUN: 01/16/79 0600z for 24 hr
LOCATION: GLOBEAL
SAT. HIGHT: 525 km ORBIT INC: 98 deg

Figure B.12

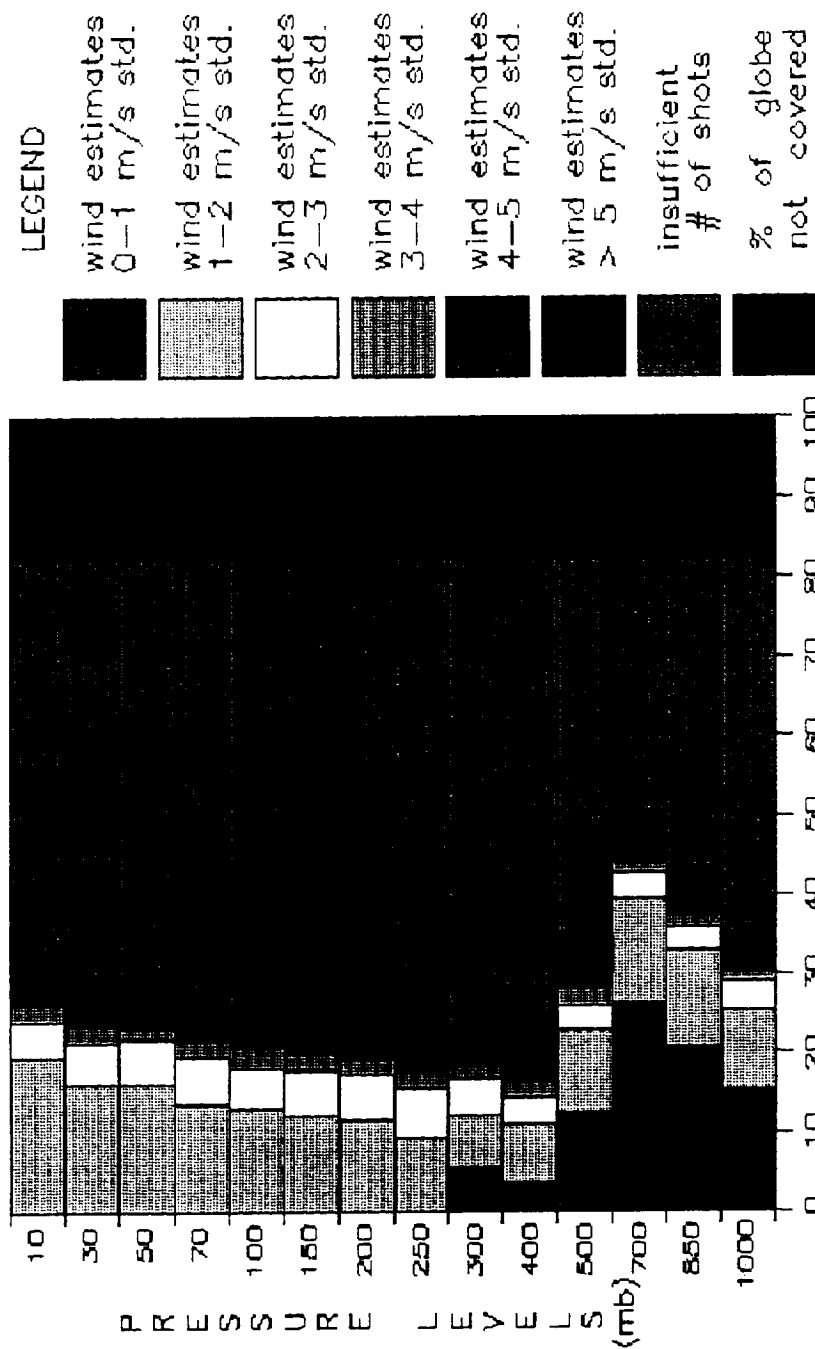
LAWS PERFORMANCE PROFILES — U, V COMPONENT, FIXED AREA



RUN: 01/16/79 0600z for 24 hr
 LOCATION: GLOBAL
 SAT. HGT: 525 km ORBIT INC: 98 deg
 POWER: 20.0 J PRF: 46 hz
 TELESCOPE DIAMETER: 1.50 m
 WAVELENGTH: 9.11 um

Figure B.13

LAWS PERFORMANCE PROFILES - U, V COMPONENT, FIXED AREA



RUN: 01/19/79 0600z for 24 hr
 LOCATION: GLOBAL
 SAT. HIGHT: 525 km ORBIT INC: 98 deg
 POWER: 200 J PRF: 4.6 hz
 TELESCOPE DIAMETER: 1.50 m
 WAVELENGTH: 9.11 um

Figure B.14

LAWS PERFORMANCE PROFILES - U, V COMPONENT, FIXED AREA

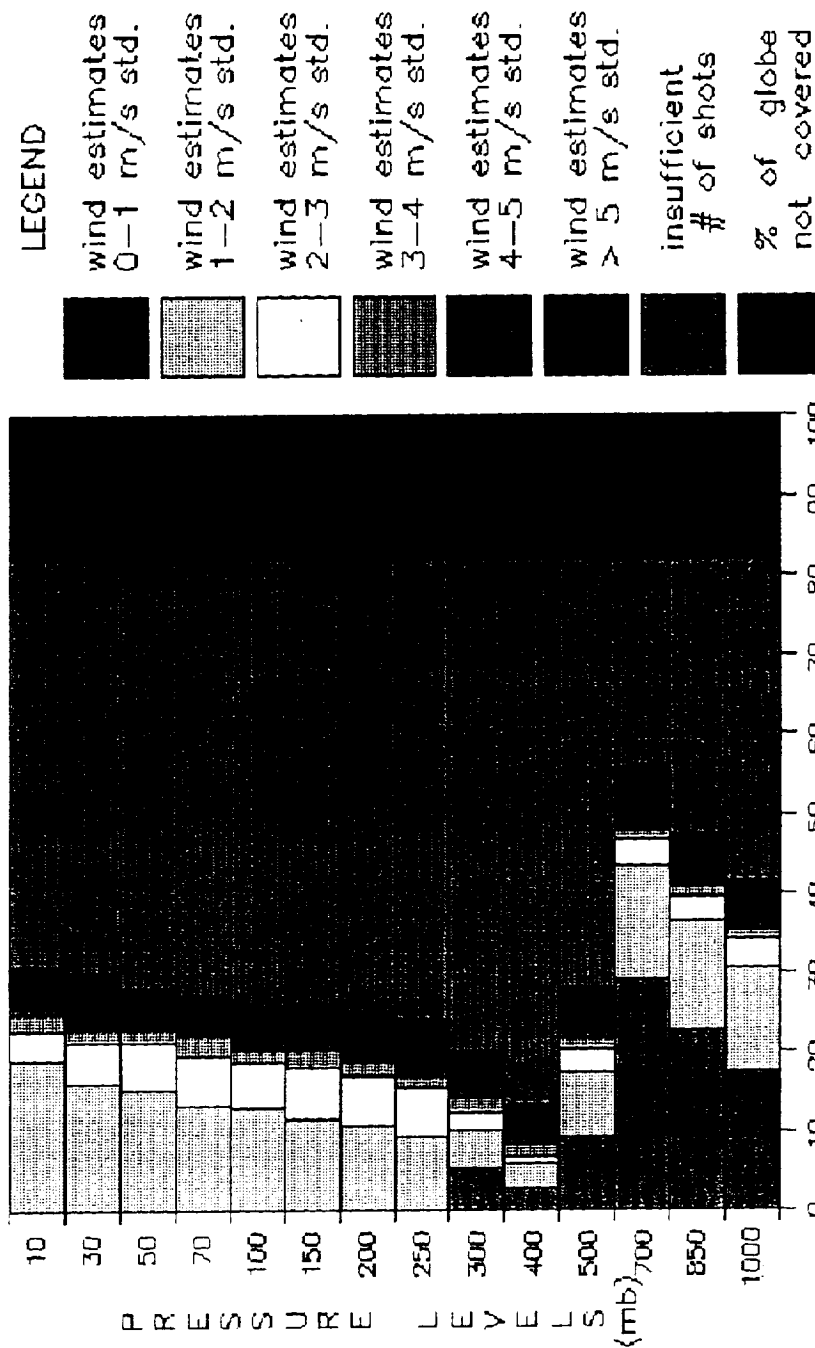
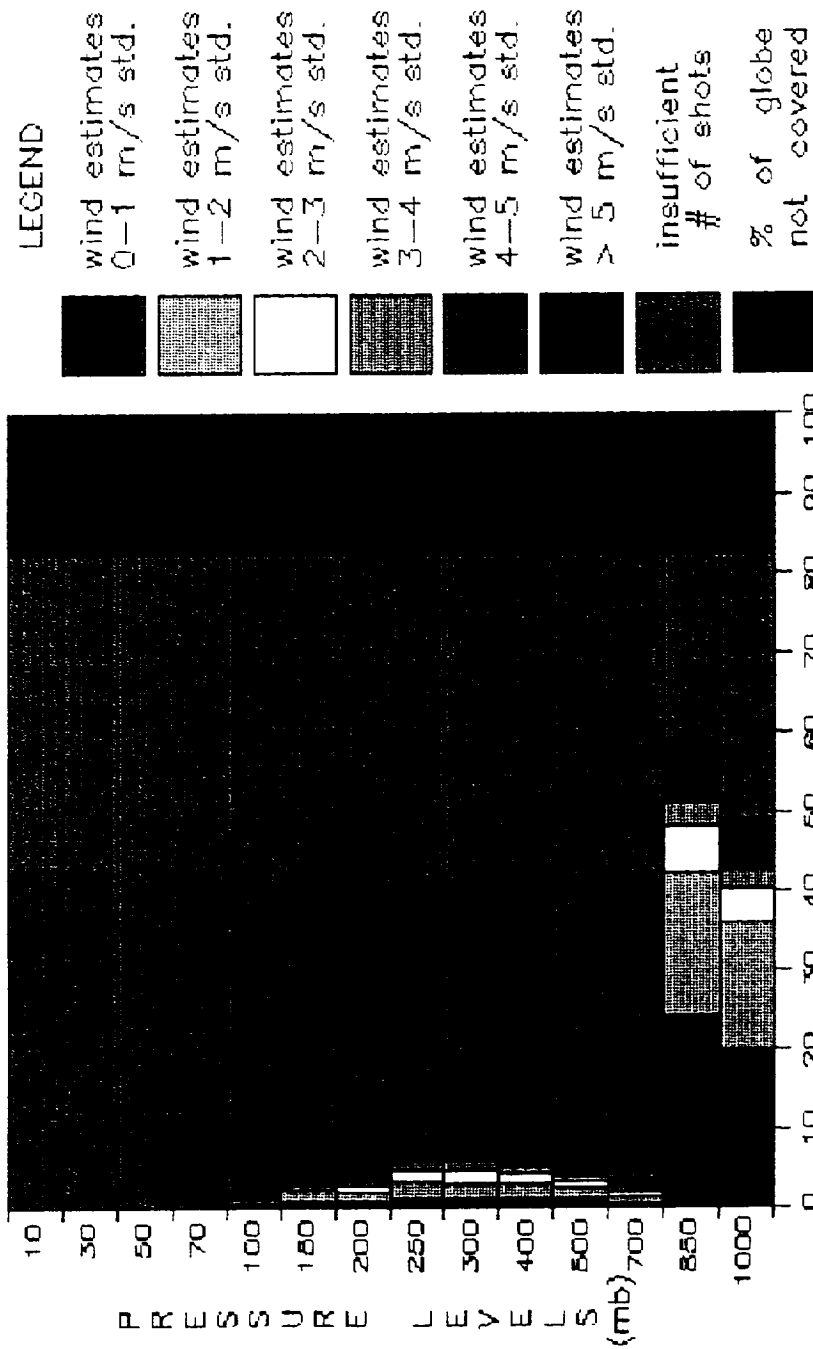


Figure B.15

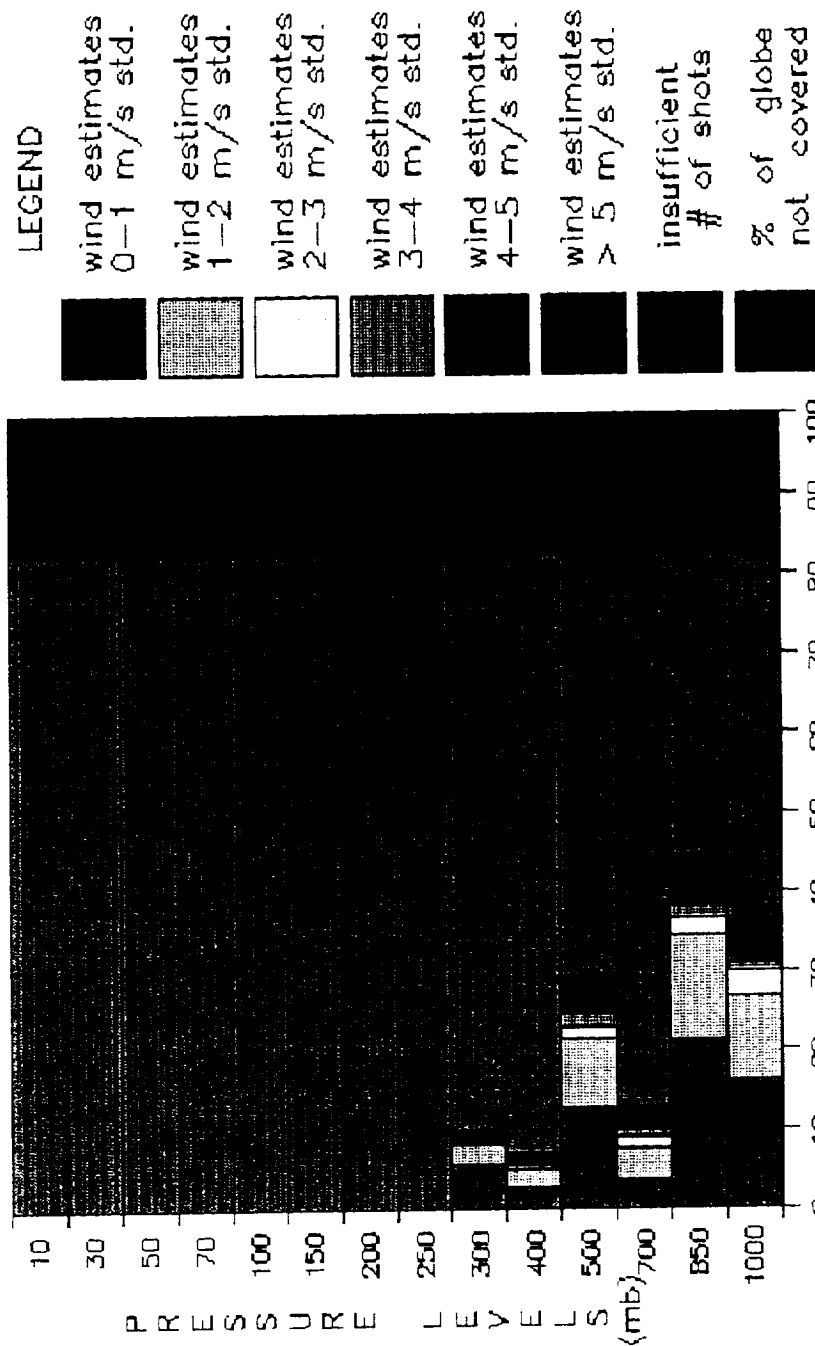
LAWS PERFORMANCE PROFILES - U, V COMPONENT, FIXED AREA



RUN: 01/16/79 0600z for 24 hr
 LOCATION: GLOBAL
 SAT. HGT: 525 km ORBIT INC: 98 deg
 POWER: 5.0 J PRF: 46 hz
 TELESCOPE DIAMETER: 0.75 m
 WAVELENGTH: 9.11 um

Figure B.16

LAWS PERFORMANCE PROFILES - U, V COMPONENT, FIXED AREA



RUN: 01/19/79 0600z for 24 hr
 LOCATION: GLOBAL
 SAT. HGT: 525 km ORBIT INC: 98 deg

POWER: 5.0 J PRF: 4.6 hz
 TELESCOPE DIAMETER: 0.75 m
 WAVELENGTH: 9.11 um

Figure B.17

LAWS PERFORMANCE PROFILES — U, V COMPONENT, FIXED AREA

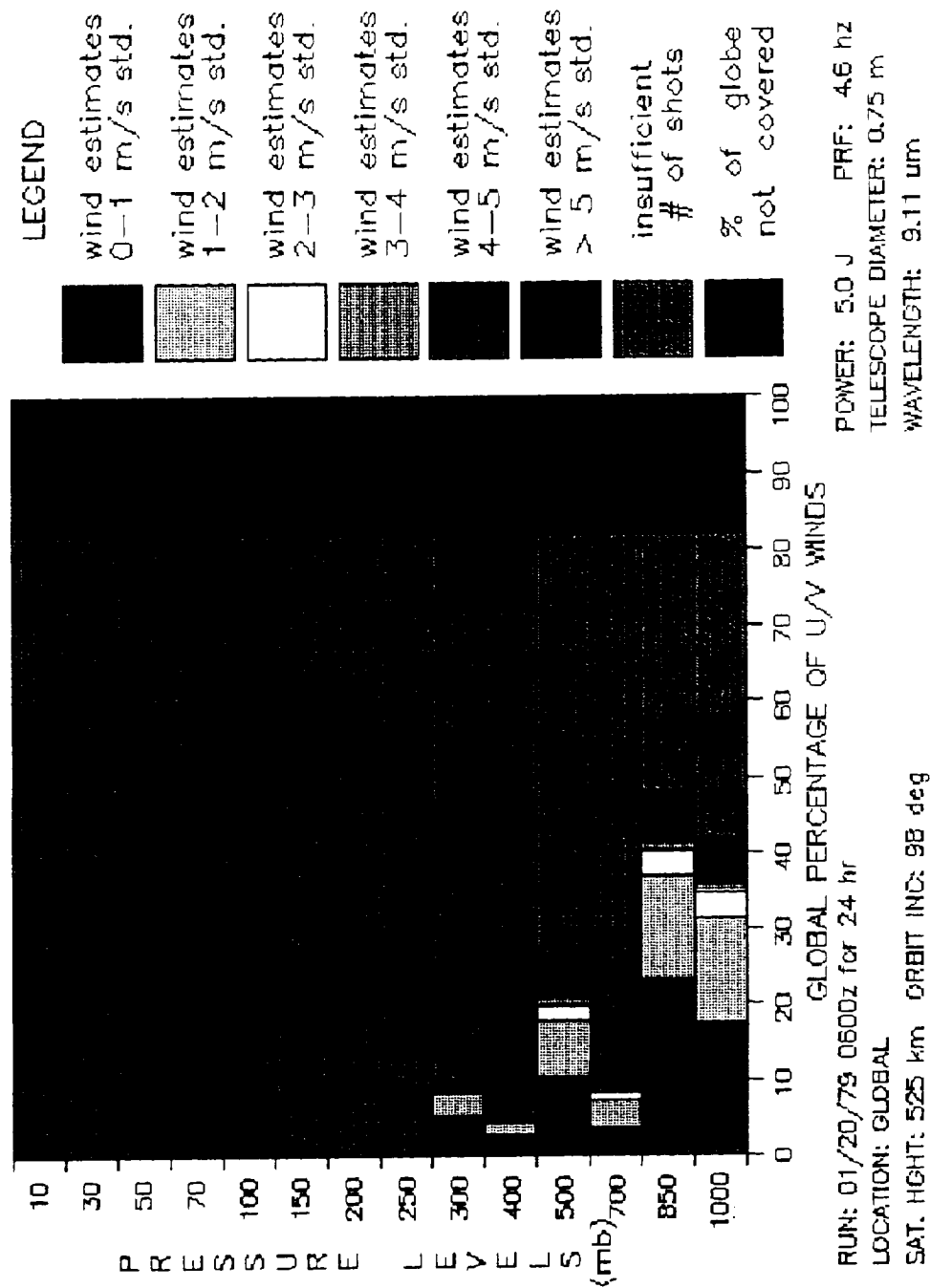


Figure B.18

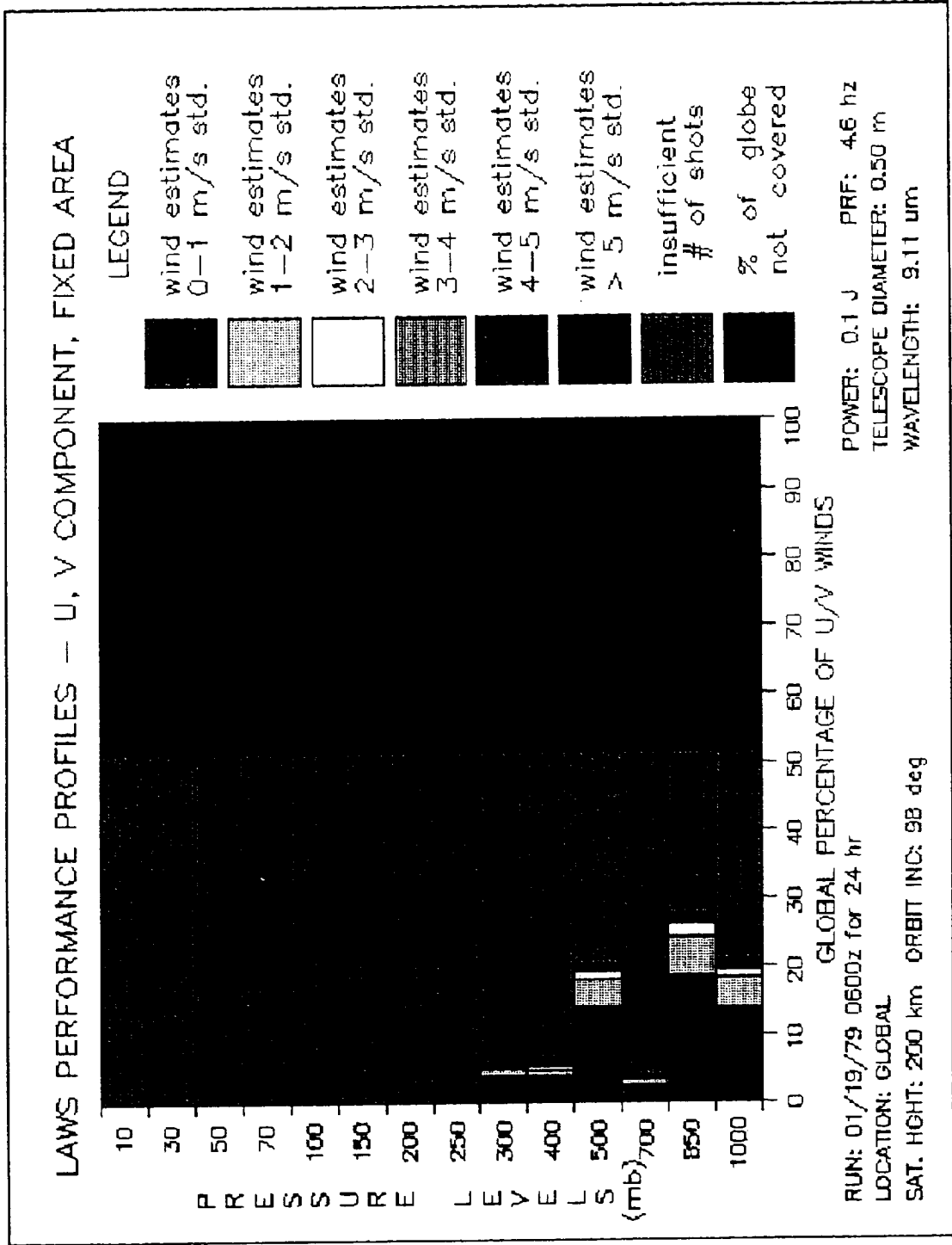


Figure B.19

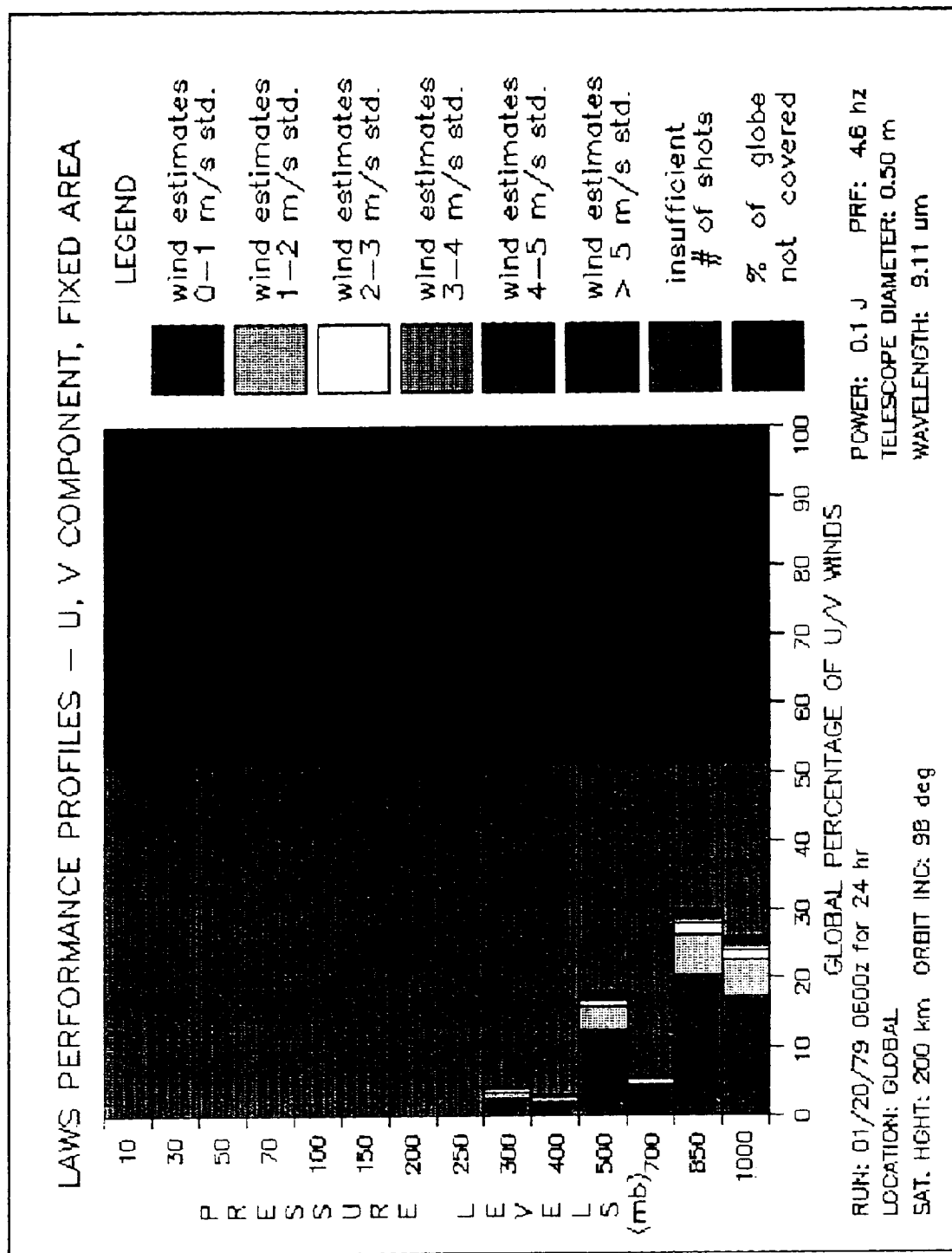


Figure B.20

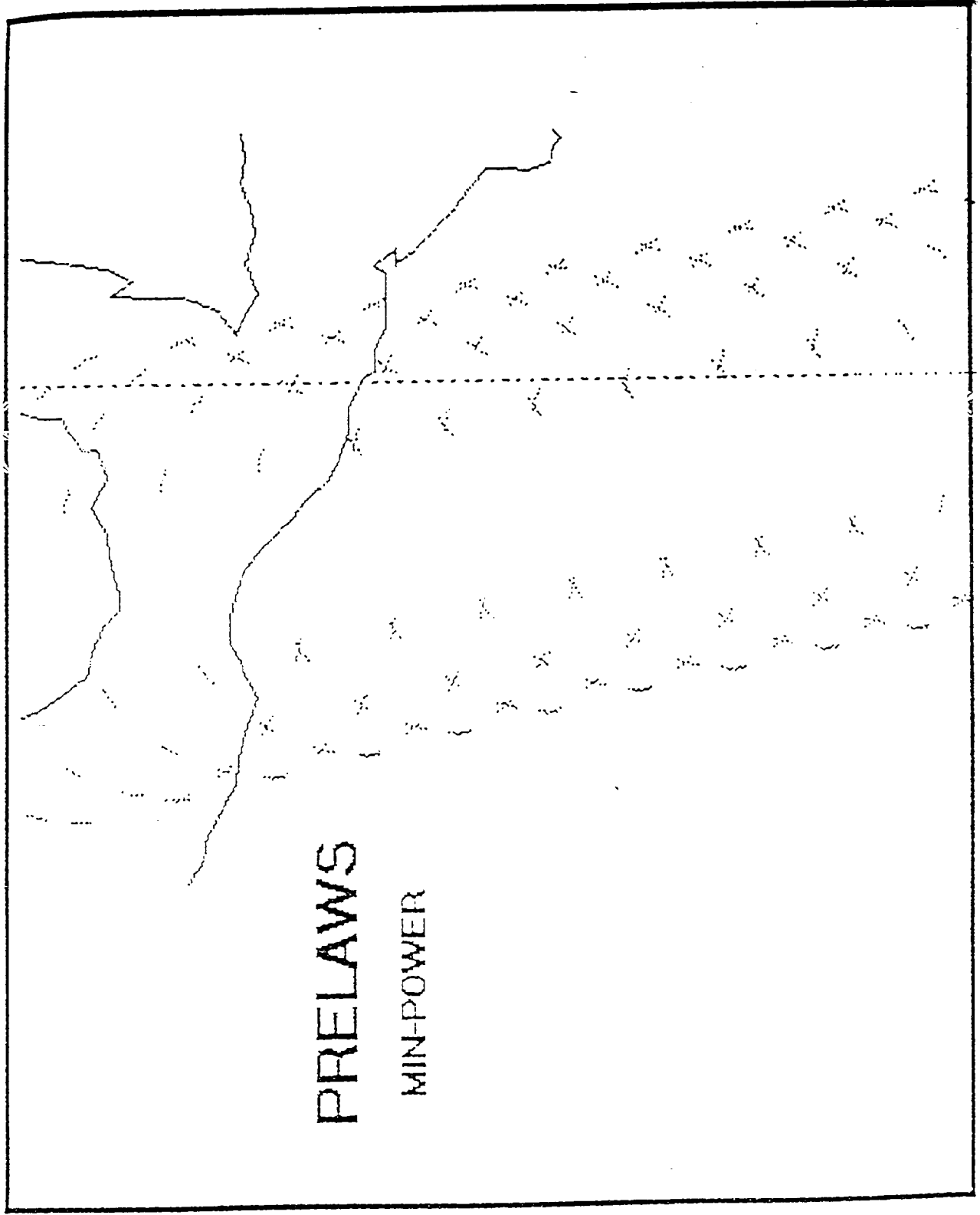


Figure B.21

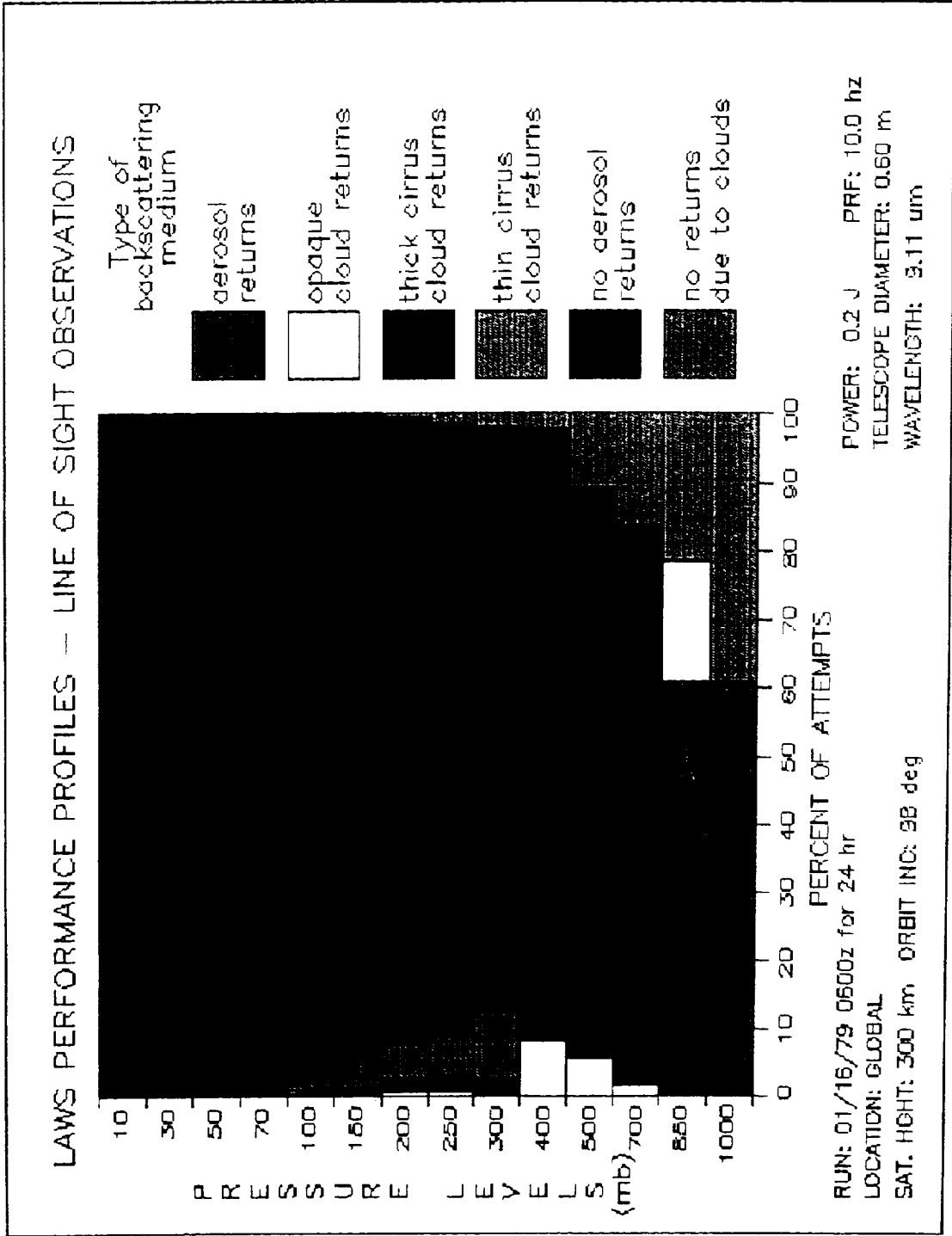


Figure B.22

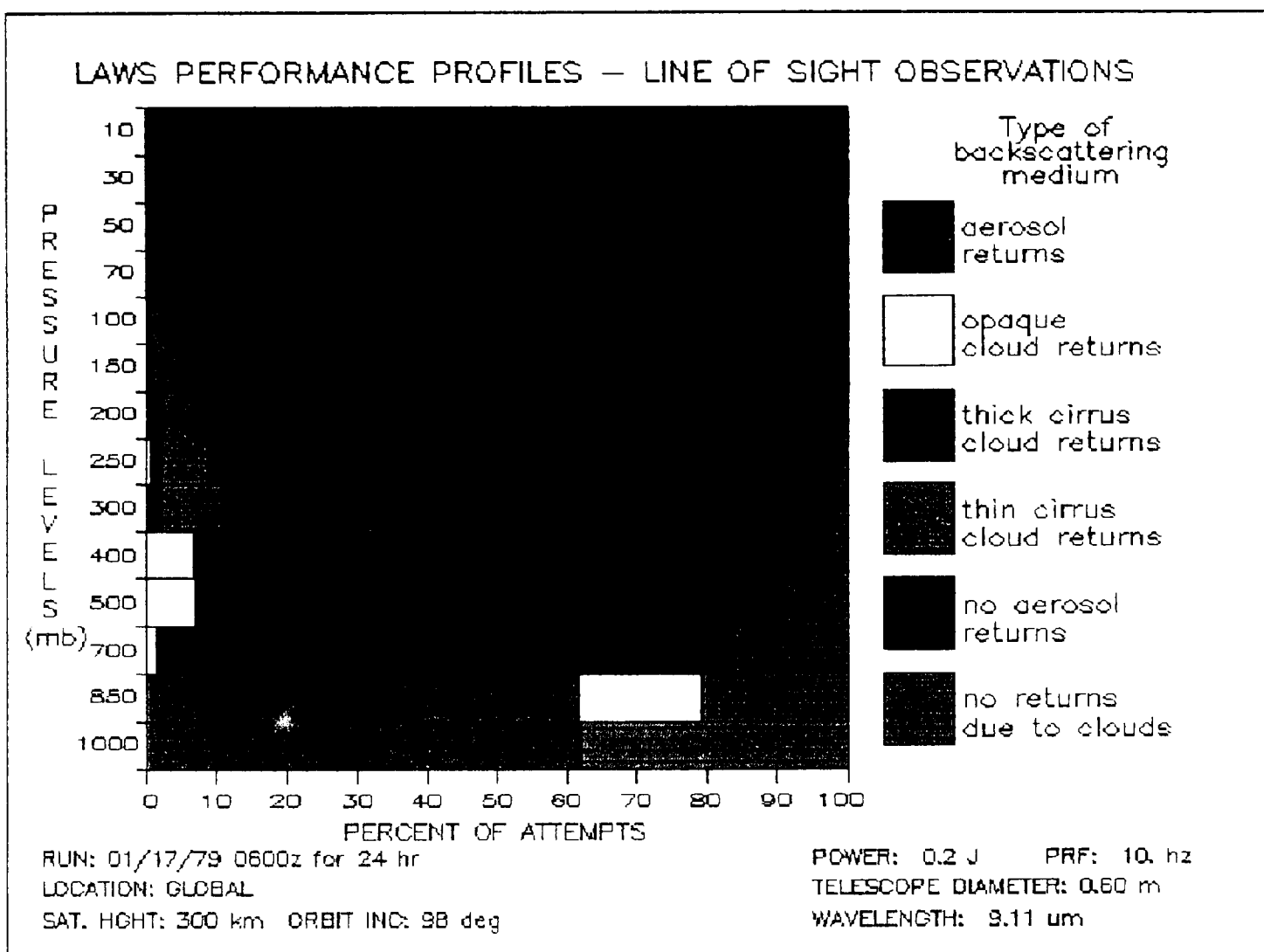


Figure B.23

Figure B.24

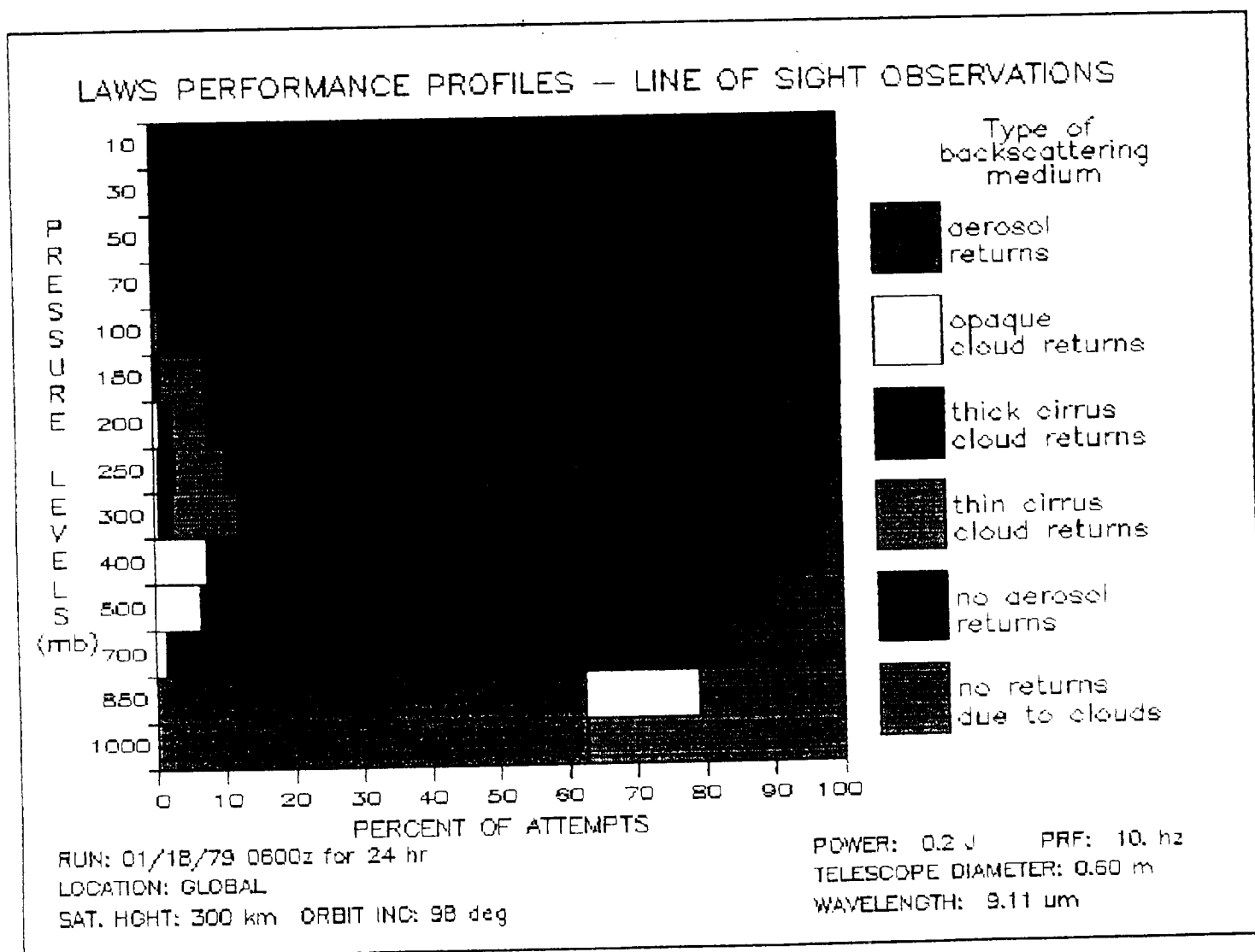


Figure B.25

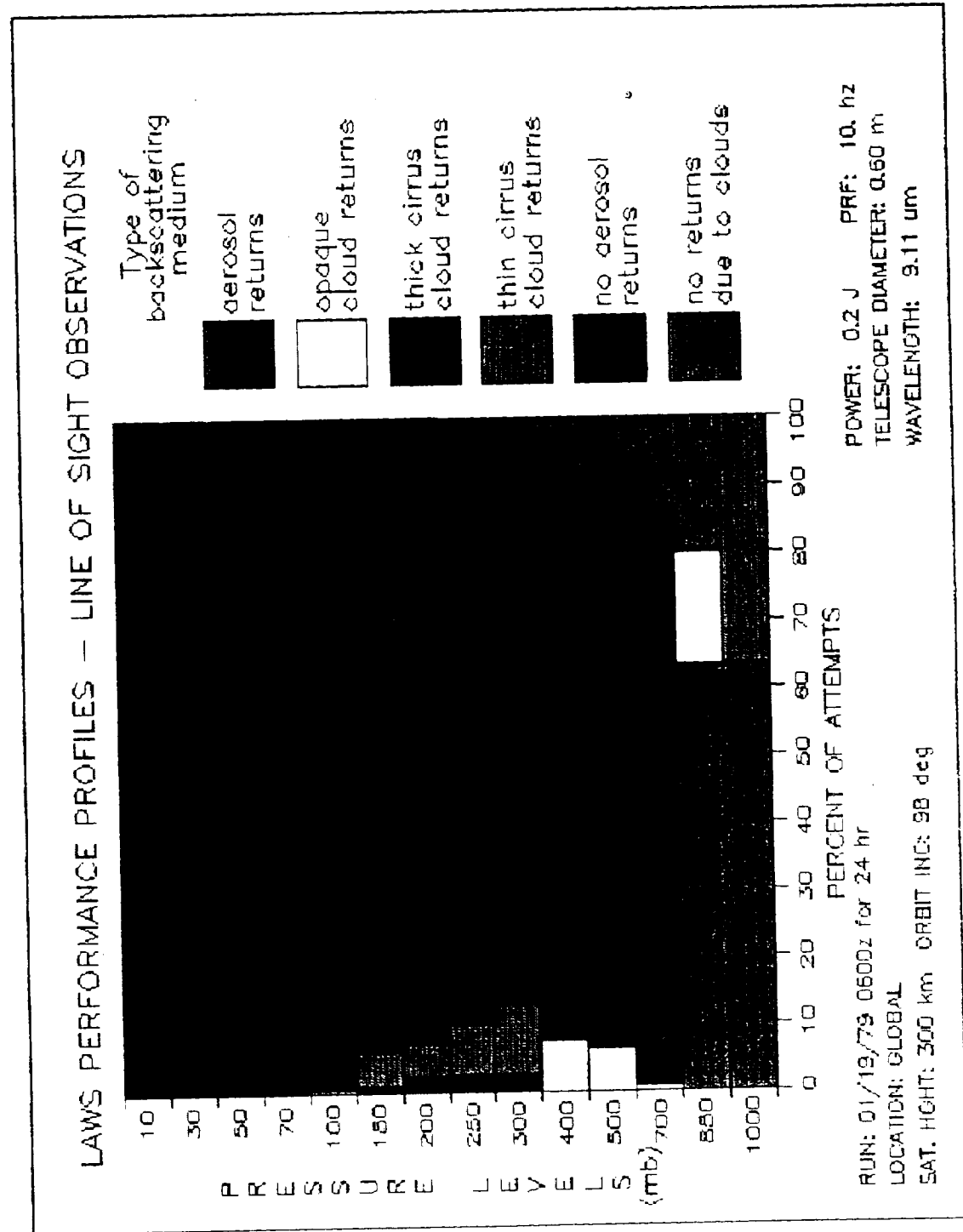
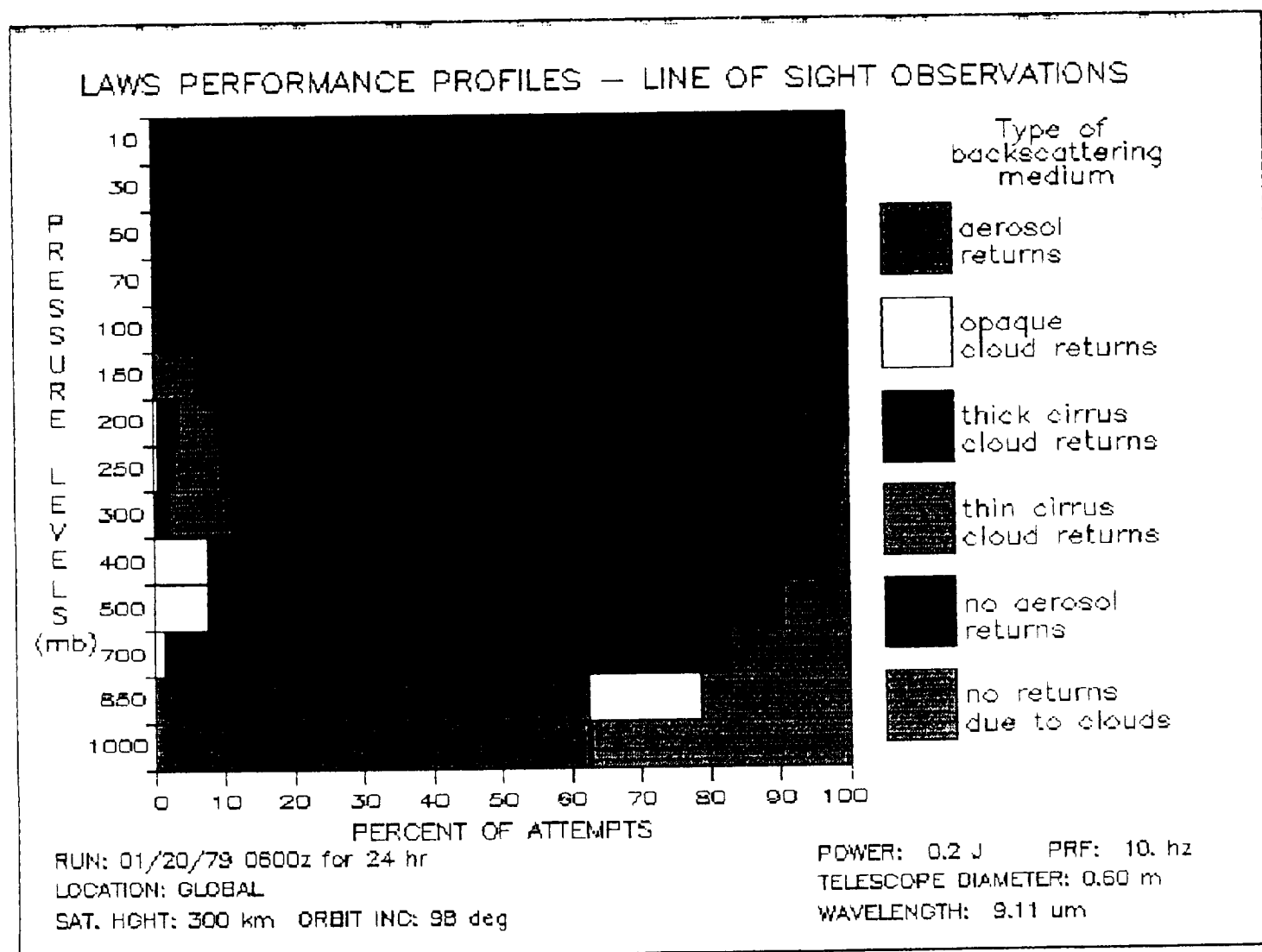


Figure B.26



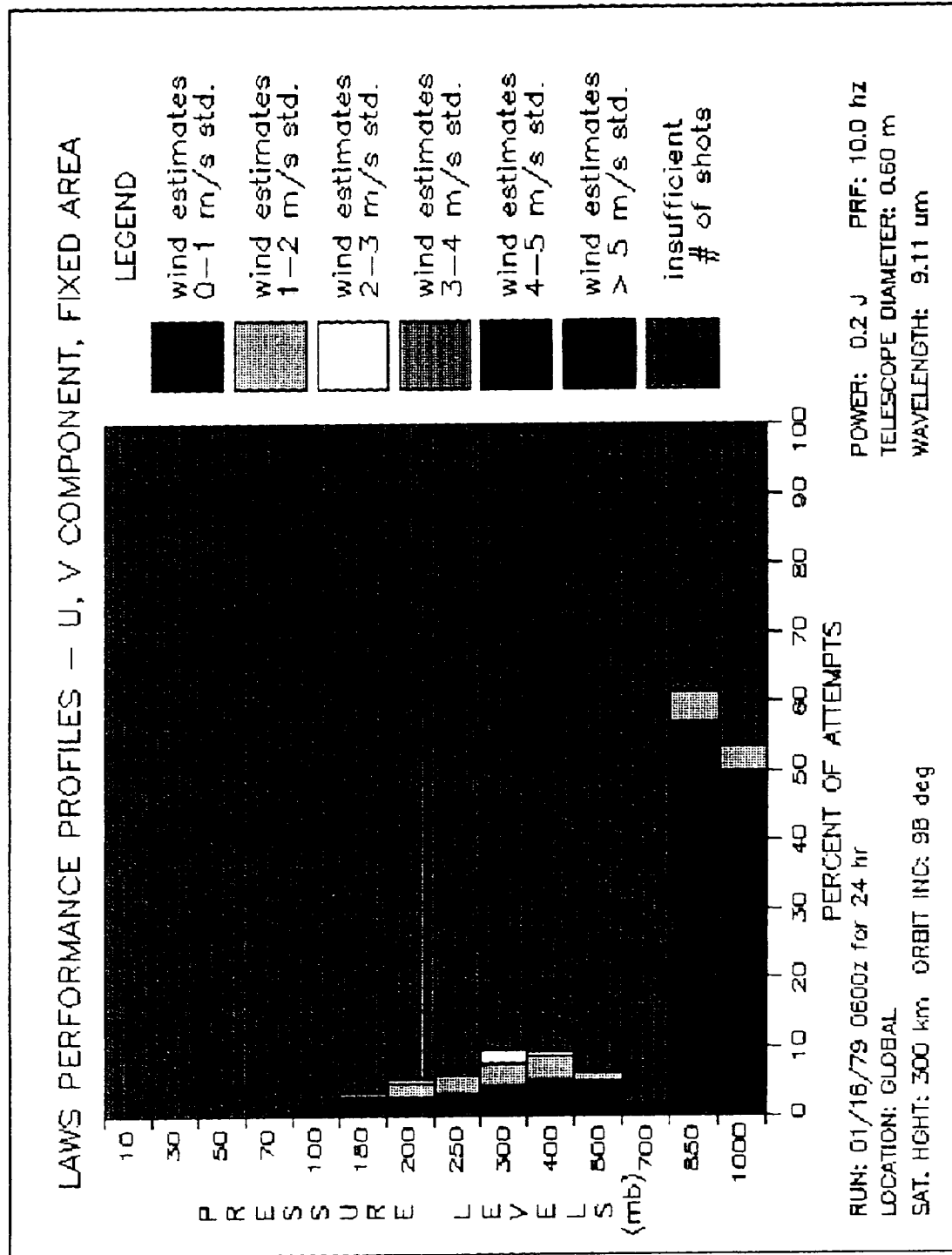
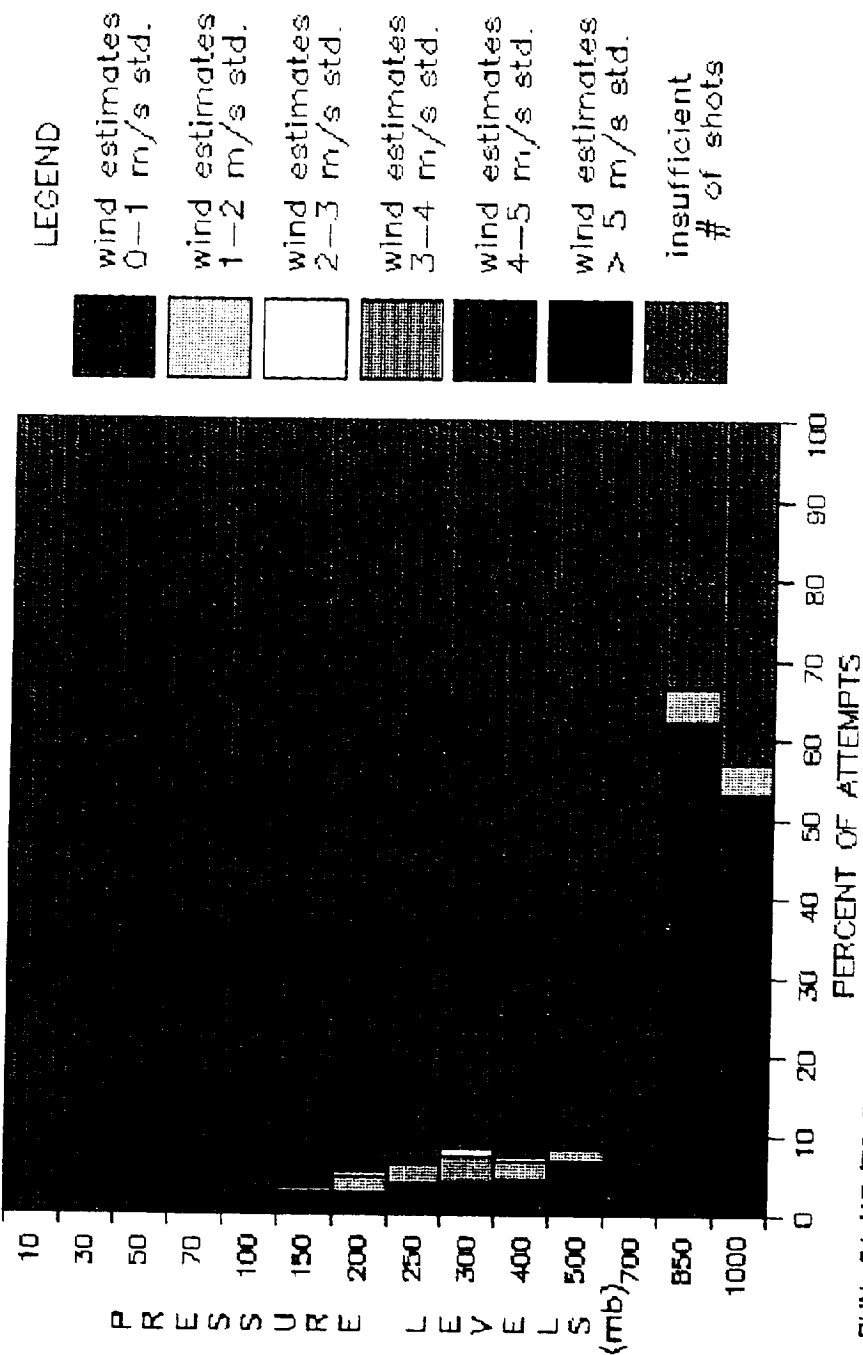


Figure B.27

LAWS PERFORMANCE PROFILES - U, V COMPONENT, FIXED AREA



POWER: 0.2 J PRF: 10. hz
TELESCOPE DIAMETER: 0.60 m
WAVELENGTH: 9.11 um

RUN: 01/17/79 0600z for 24 hr
LOCATION: GLOBAL
SAT. HGT: 300 km ORBIT INC: 98 deg

Figure B.28

LAWS PERFORMANCE PROFILES - U, V COMPONENT, FIXED AREA

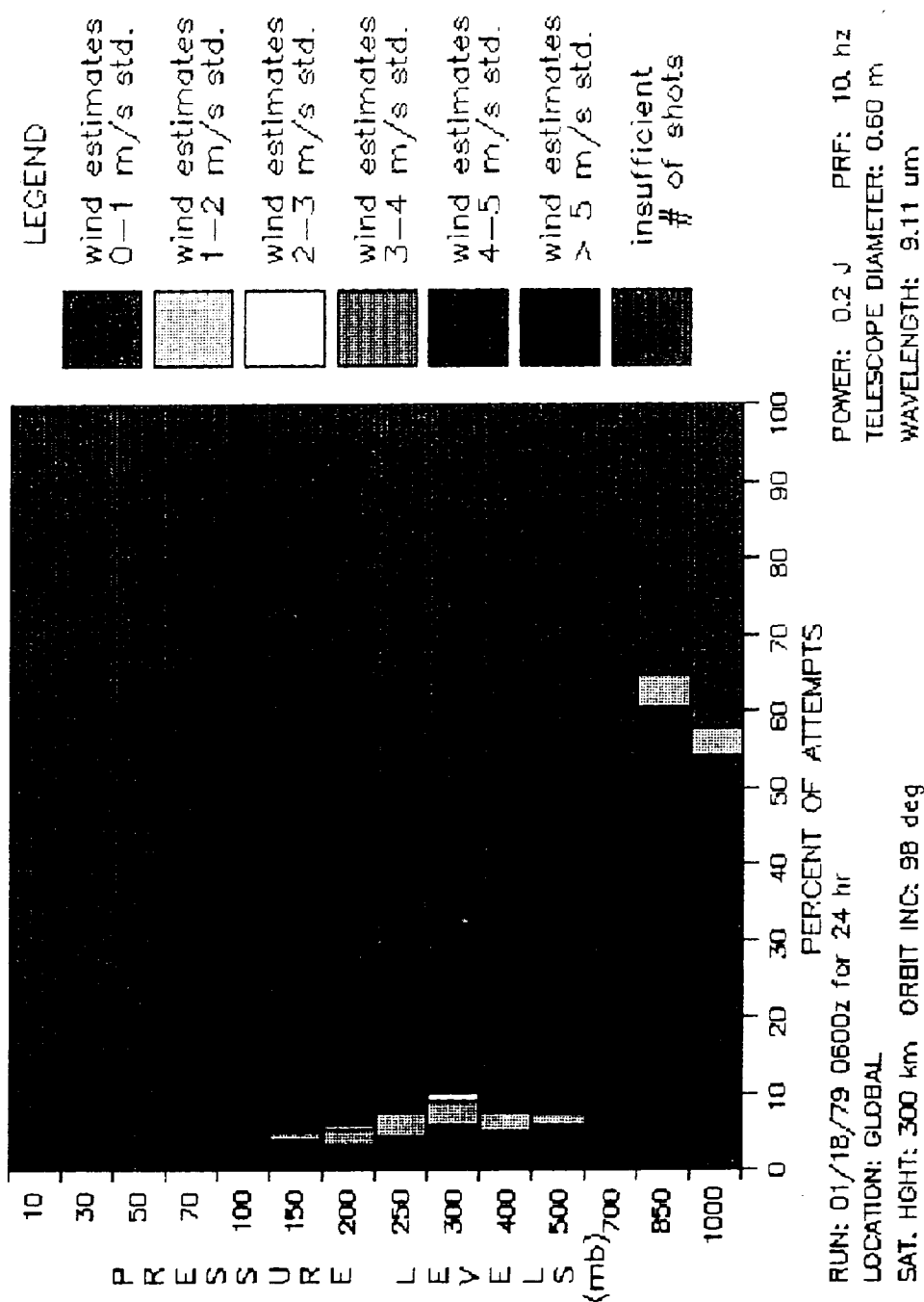
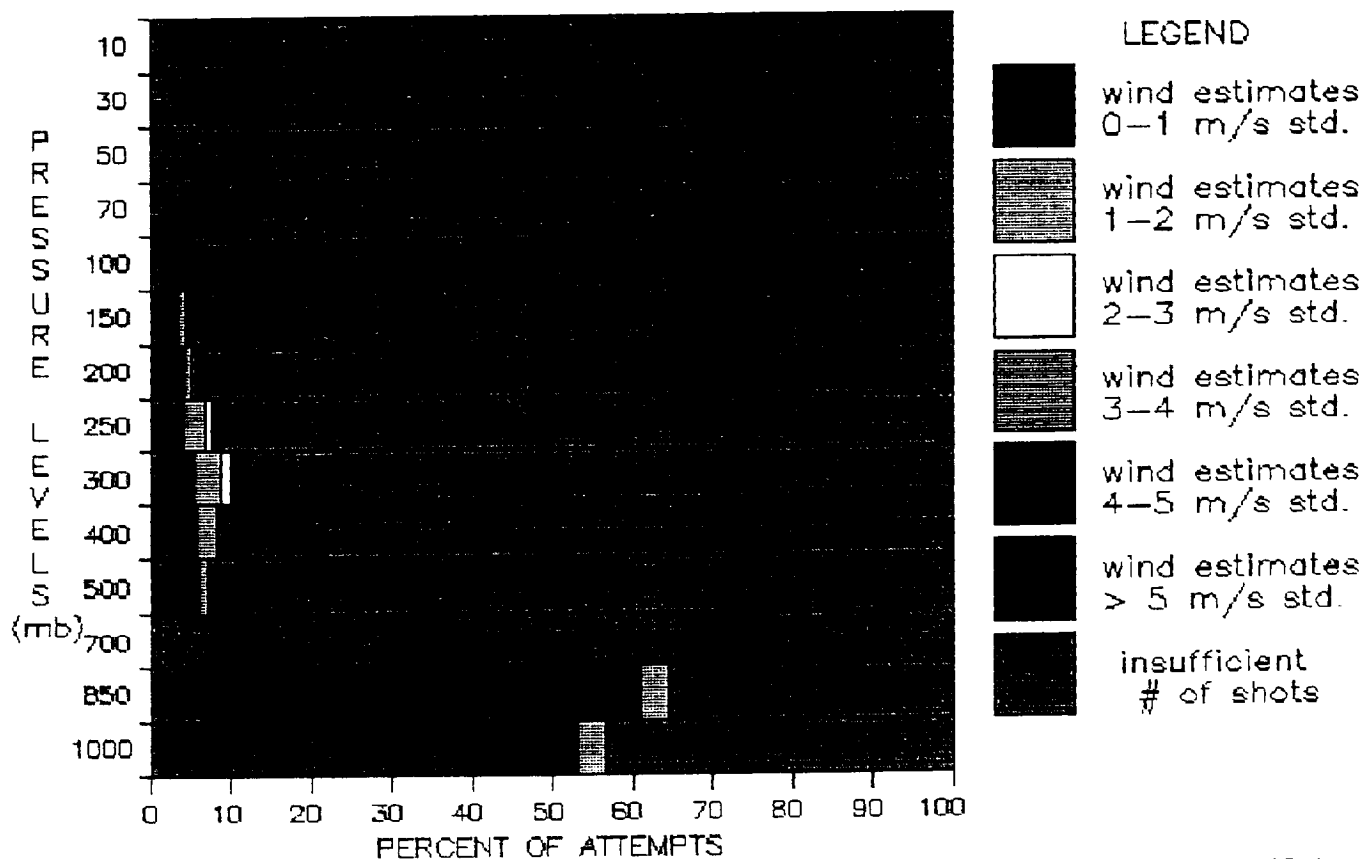


Figure B.29

LAWS PERFORMANCE PROFILES - U, V COMPONENT, FIXED AREA

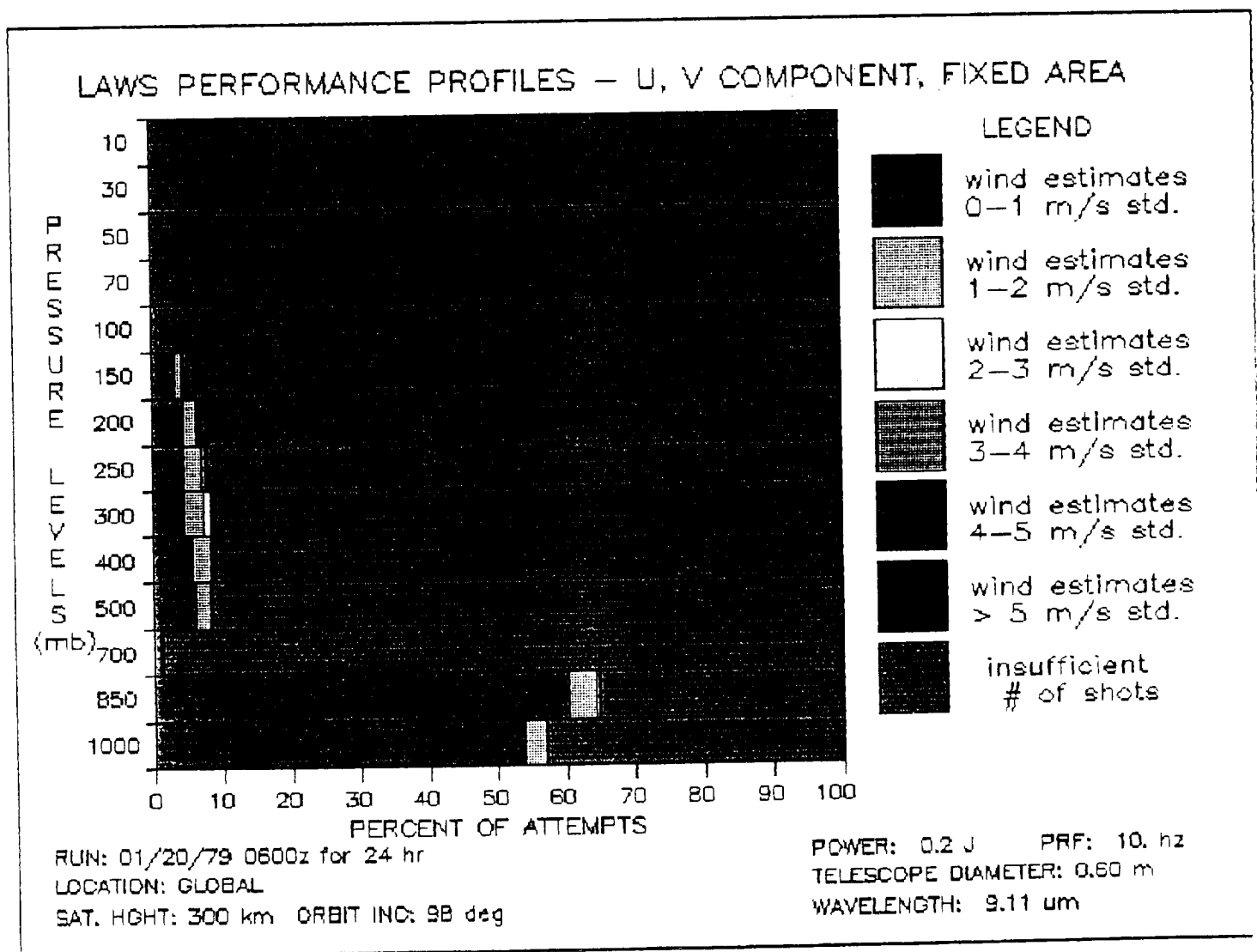


RUN: 01/19/79 0600z for 24 hr
 LOCATION: GLOBAL
 SAT. HIGHT: 300 km ORBIT INC: 98 deg

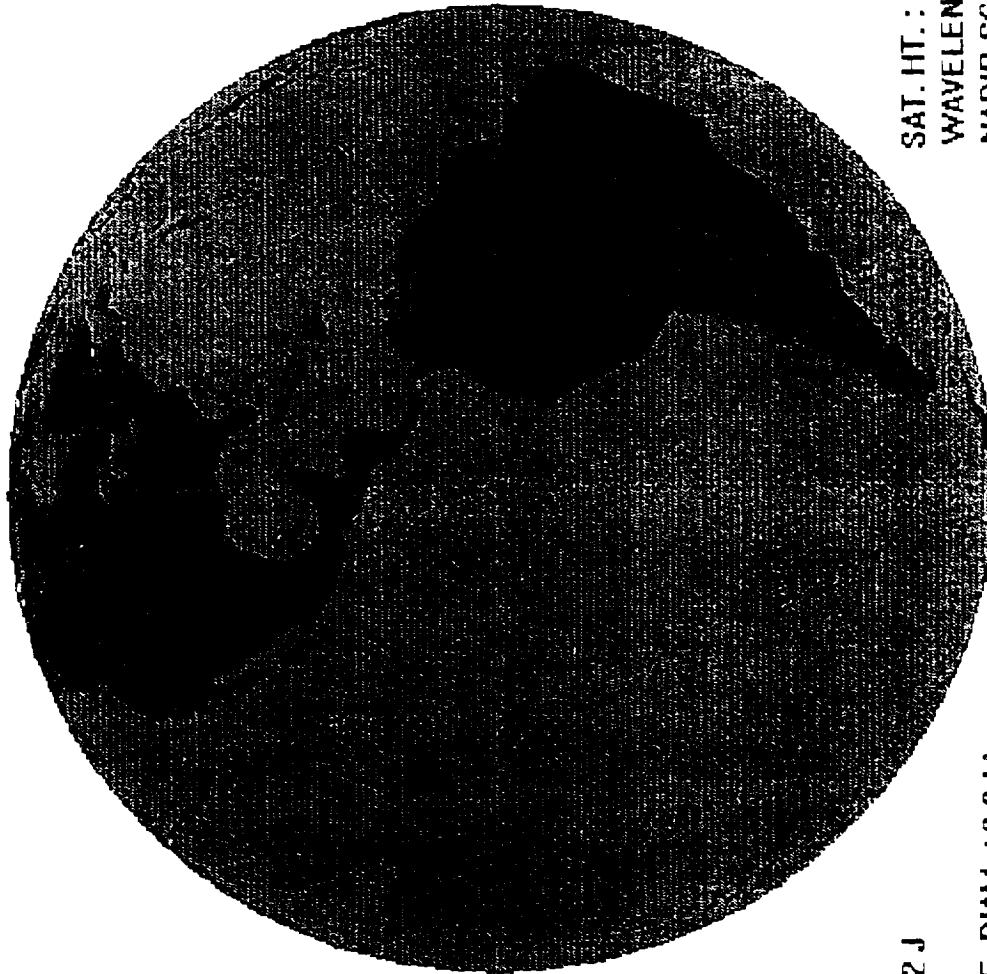
POWER: 0.2 J PRF: 10. hz
 TELESCOPE DIAMETER: 0.60 m
 WAVELENGTH: 9.11 um

Figure B.30

Figure B.31



LAWS SIMULATED HORIZONTAL WINDS AT 1000 MB



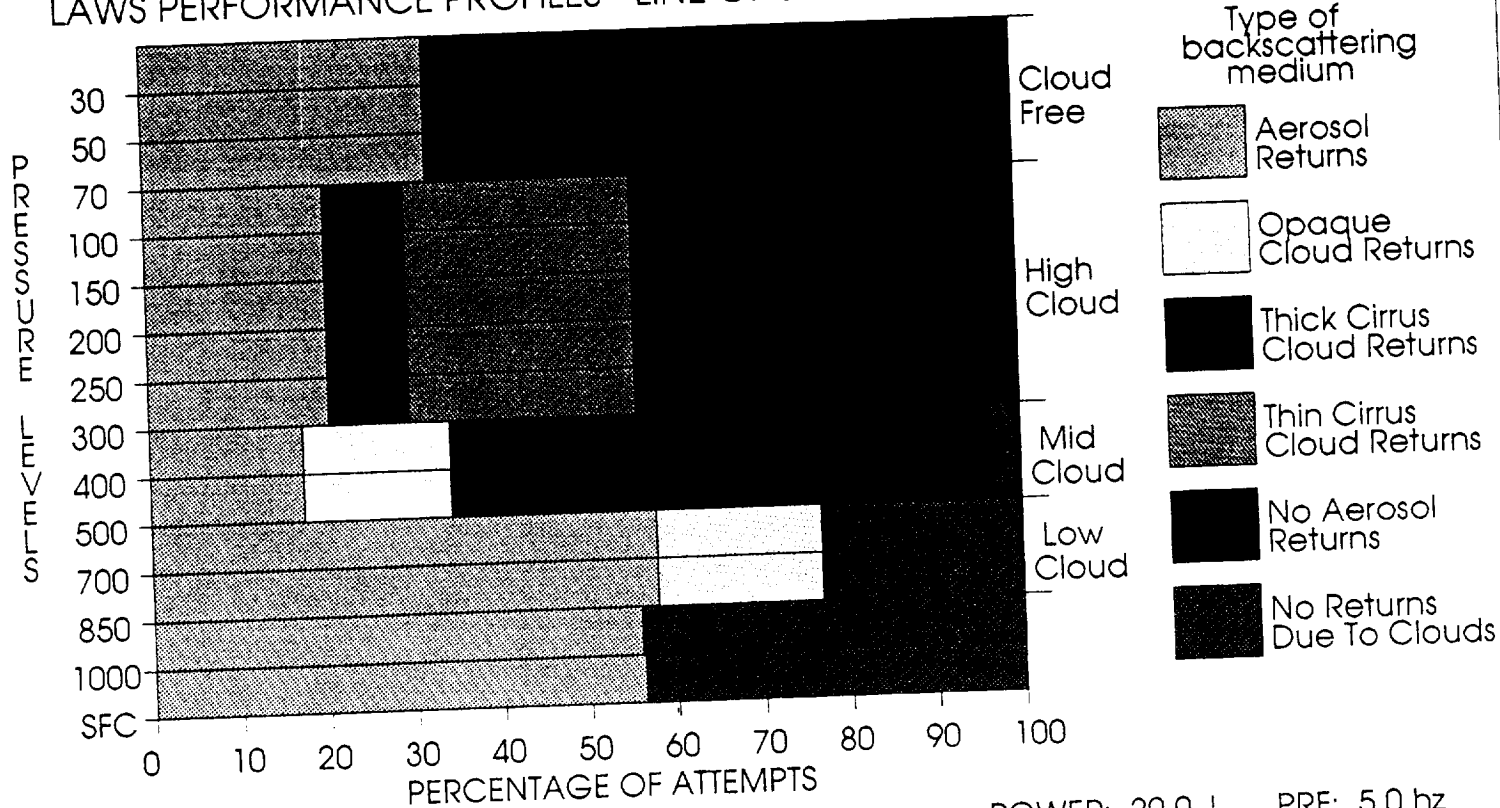
POWER: 0.2 J
PRF: 10 HZ
TELESCOPE DIAM.: 0.6 M

SAT. HT.: 300 KM
WAVELENGTH: 9.11 μ m
NADIR SCAN ANGLE: 30

24 HR SIMULATION

Figure B.32

LAWS PERFORMANCE PROFILES - LINE OF SIGHT OBSERVATIONS

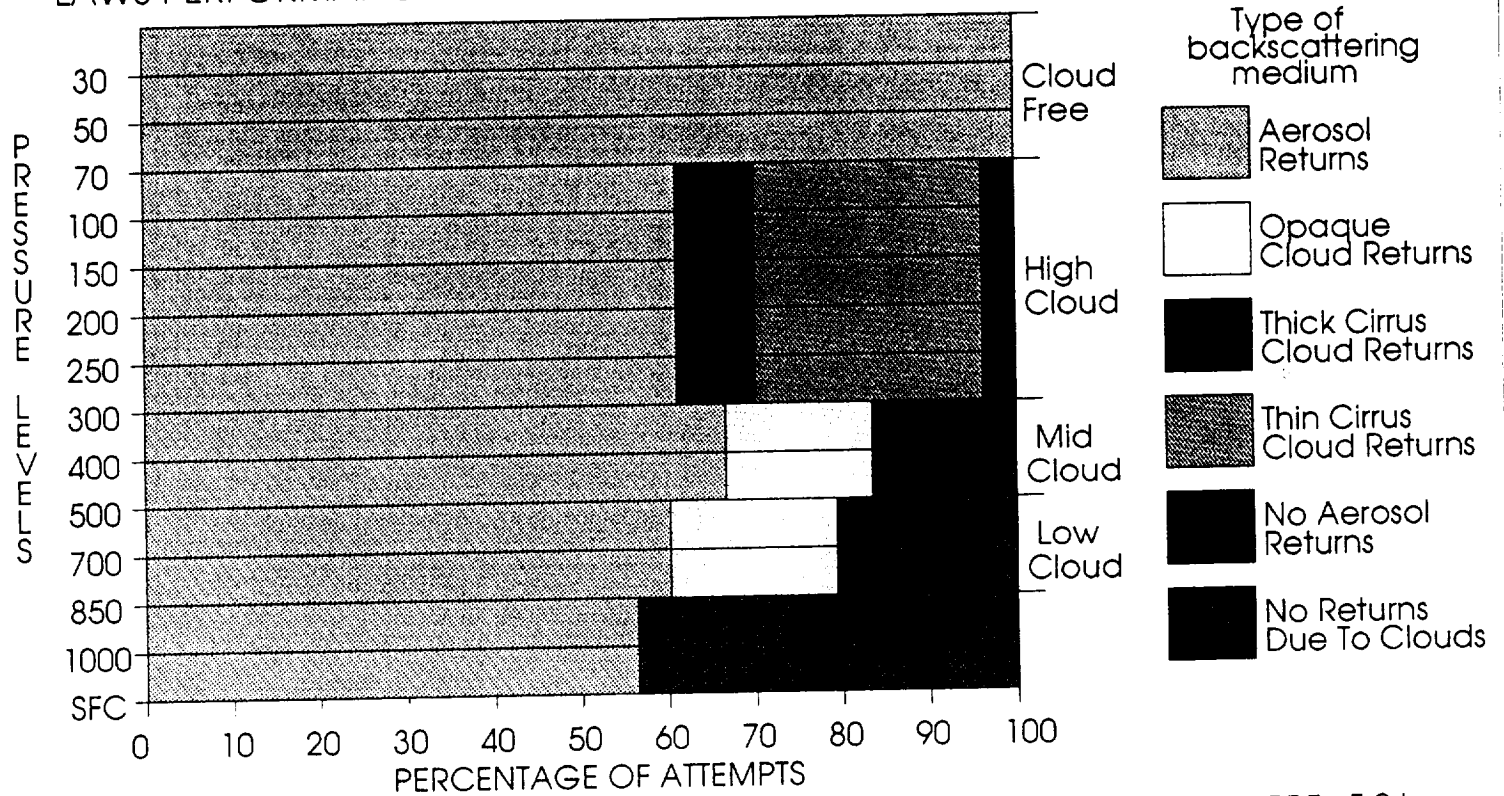


RUN: 01/16/79 0600z for 24 hr
 LOCATION: GLOBAL
 SAT. HGHT: 525 km ORBIT INC: 98 deg

POWER: 20.0 J PRF: 5.0 hz
 TELESCOPE DIAMETER: 1.50 m
 WAVELENGTH: 9.11 um

Figure B.33

LAWS PERFORMANCE PROFILES - LINE OF SIGHT OBSERVATIONS



RUN: 01/16/79 0600z for 24 hr
 LOCATION: GLOBAL
 SAT. HGHT: 525 km ORBIT INC: 98 deg

POWER: 20.0 J PRF: 5.0 hz
 TELESCOPE DIAMETER: 1.50 m
 WAVELENGTH: 9.11 um

Figure B.34

APPENDIX C
1991 OBSERVING SYSTEM SIMULATION EXPERIMENTS

Under contract, SWA was tasked to conduct global OSSEs in co-operative efforts with GSFC and FSU that are critical to the selection of orbit configurations for LAWS. We completed 5-day LAWS simulations with the following system configurations:

Perfect: 20 joule/1.5 m/4.6 Hz system in a 705 km-polar,
Perfect: 20 joule/1.5 m/4.6 Hz system in a 450 km-polar,
Perfect: 20 joule/1.5 m/4.6 Hz system in a 450 km-equatorial,
Perfect: 20 joule/1.5 m/4.6 Hz system in a 525 km-polar,
Perfect: 20 joule/1.5 m/4.6 Hz system in a 575 km-equatorial,
Realistic: 20 joule/1.5 m/4.6 Hz system in a 525 km-polar,
Realistic: 20 joule/1.5 m/4.6 Hz system in a 575 km-equatorial.

The simulated LAWS line-of-sight winds and horizontal wind components were delivered to NASA/GSFC (Atlas) and FSU (Krishnamurti) for assimilation.

Figures C.1-C.4 illustrate 12 hour coverage from the 450 km polar and equatorial perfect LAWS simulations. The perfect LAWS simulations considered cloud effects and terrain as the only mechanism to terminate a lidar shot.

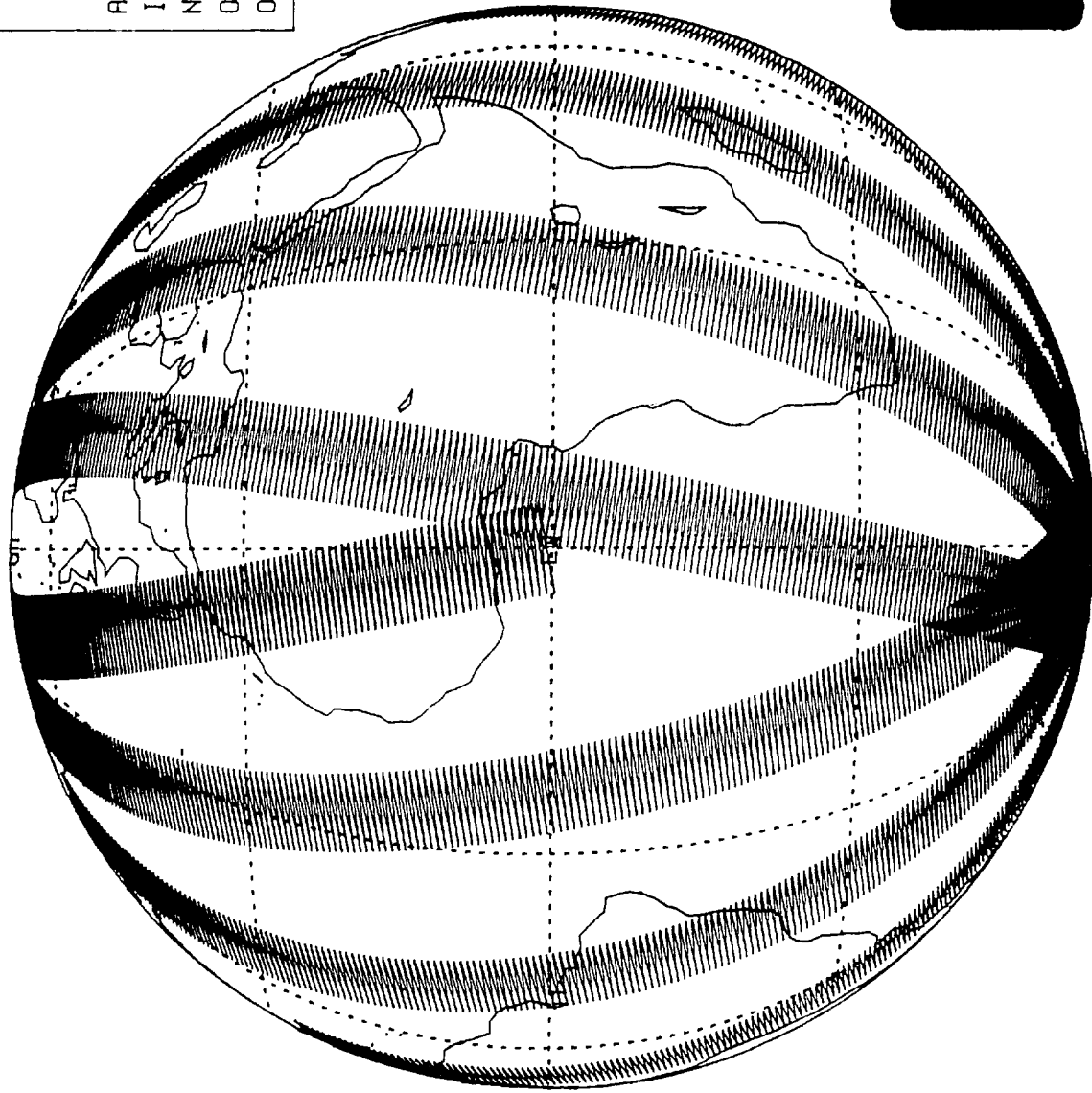
Simulated LAWS winds and associated observational errors were computed for five ECMWF days and two satellite orbits (i.e., 575/55 and 525/98). These LSM runs considered the effects of clouds, cirrus clouds, aerosols, molecular attenuation, terrain, and sampling scale turbulence. Figures C.5-C.8 depict the 500 mb and the 1000 mb level Nature Run input winds for comparison with the LAWS winds shown in Figs. C-9-C.12. Cloud obscurations are noted by circled cross hairs. LAWS winds with observational errors greater than 25 m/s are not plotted.

FIGURE CAPTIONS

- Figure C.1: Equatorial view of a LAWS global 12 hour coverage for a satellite orbit of 450 km and an inclination angle of 98 degrees. The nadir scan angle is 45 degrees.
- Figure C.2: Polar view of a LAWS global 12 hour coverage for a satellite orbit of 450 km and an inclination angle of 98 degrees. The nadir scan angle is 45 degrees.
- Figure C.3: Equatorial view of a LAWS global 12 hour coverage for a satellite orbit of 450 km and an inclination angle of 55 degrees. The nadir scan angle is 45 degrees.
- Figure C.4: Polar view of a LAWS global 12 hour coverage for a satellite orbit of 450 km and an inclination angle of 55 degrees. The nadir scan angle is 45 degrees.
- Figure C.5: ECMWF Nature Run winds (0000z) over the United States at 1000 mb. Cloud obscurations are noted by circled cross hairs. LAWS winds with observational errors greater than 25 m/s are not plotted. The satellite orbit was at 525 km and 98 degree inclination.
- Figure C.6: ECMWF Nature Run winds (0600z) winds over the United States at 1000 mb. Comparison of ECMWF winds over the United States, for the 500 mb level, to "realistic" simulated LAWS winds. Cloud obscurations are noted by circled cross hairs. LAWS winds with observational errors greater than 25 m/s are not plotted. The satellite orbit was at 575 km and 55 degree inclination.
- Figure C.7: ECMWF Nature Run winds (0000z) winds over the United States at 500 mb. Cloud obscurations are noted by circled cross hairs. LAWS winds with observational errors greater than 25 m/s are not plotted. The satellite orbit was at 525 km and 98 degree inclination.
- Figure C.8: ECMWF Nature Run winds (0600z) winds over the United States at 500 mb. Comparison of ECMWF winds over the United States, for the 500 mb level, to "realistic" simulated LAWS winds. Cloud obscurations are noted by circled cross hairs. LAWS winds with observational errors greater than 25 m/s are not plotted. The satellite orbit was at 575 km and 55 degree inclination.

- Figure C.9: Simulated (realistic) LAWS winds over the United States at 1000 mb. Cloud obscurations are noted by circled cross hairs. LAWS winds with observational errors greater than 25 m/s are not plotted. The satellite orbit was at 525 km and 98 degree inclination.
- Figure C.10: Simulated (realistic) LAWS winds over the United States at 1000 mb. Comparison of ECMWF winds over the United States, for the 500 mb level, to "realistic" simulated LAWS winds. Cloud obscurations are noted by circled cross hairs. LAWS winds with observational errors greater than 25 m/s are not plotted. The satellite orbit was at 575 km and 55 degree inclination.
- Figure C.11: Simulated (realistic) LAWS winds over the United States at 500 mb. Cloud obscurations are noted by circled cross hairs. LAWS winds with observational errors greater than 25 m/s are not plotted. The satellite orbit was at 525 km and 98 degree inclination.
- Figure C.12: Simulated (realistic) LAWS winds over the United States at 500 mb. Comparison of ECMWF winds over the United States, for the 500 mb level, to "realistic" simulated LAWS winds. Cloud obscurations are noted by circled cross hairs. LAWS winds with observational errors greater than 25 m/s are not plotted. The satellite orbit was at 575 km and 55 degree inclination.

LAWS 12 HOUR COVERAGE



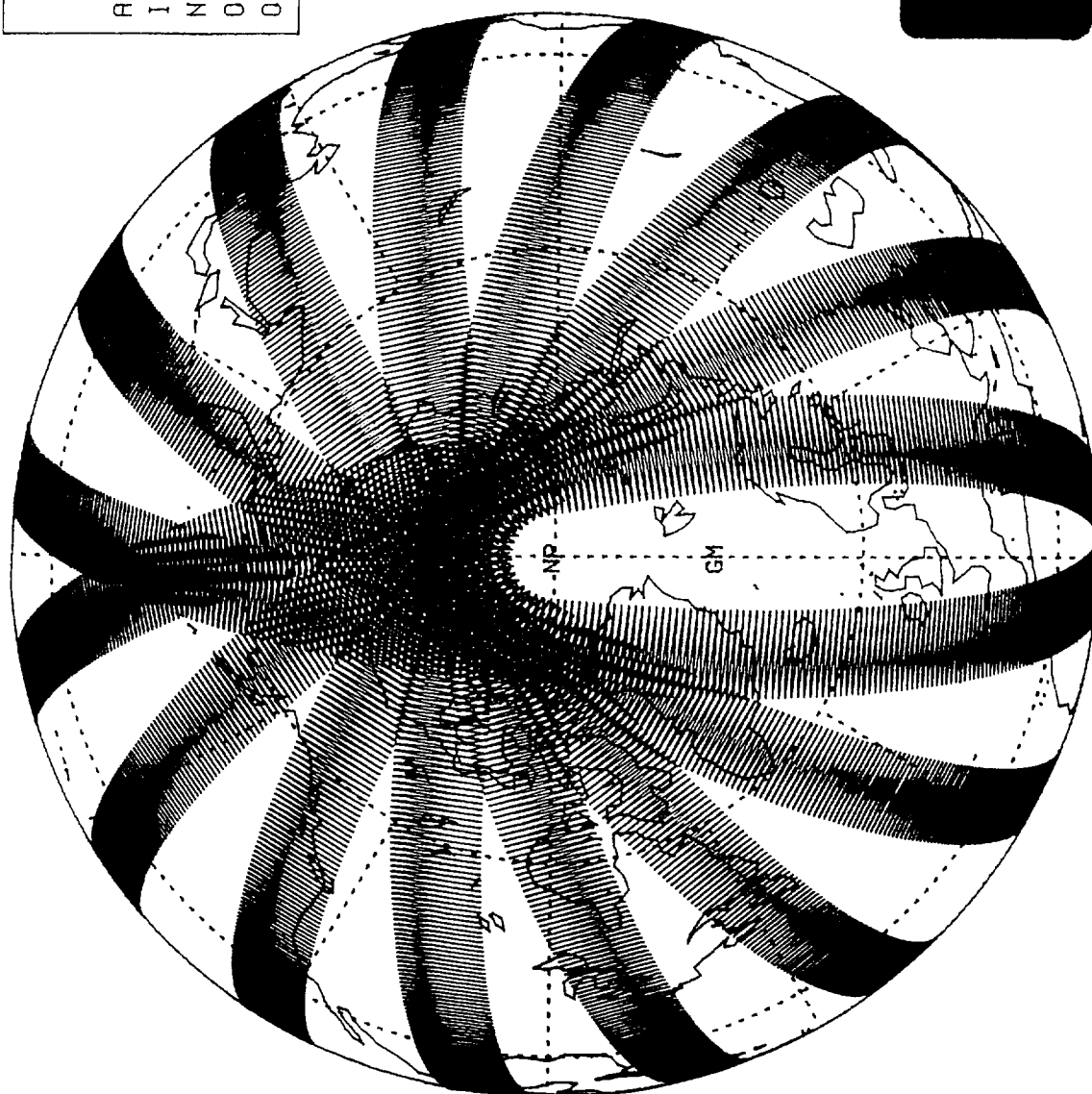
LEGEND

ALTITUDE	450 KM
INCLINATION	98 DEG
NADIR ANGLE	45 DEG
ORBIT VEL.	7.65 KM/S
ORBIT PERIOD	93 MIN



Figure C.1

LAWS 12 HOUR COVERAGE



LEGEND

ALTITUDE	450 KM
INCLINATION	98 DEG
NADIR ANGLE	45 DEG
ORBIT VEL.	7.65 KM/S
ORBIT PERIOD	93 MIN



Figure C.2

LAWS 12 HOUR COVERAGE

LEGEND	
ALTITUDE	450 KM
INCLINATION	55 DEG
NADIR ANGLE	45 DEG
ORBIT VEL.	7.65 KM/S
ORBIT PERIOD	93 MIN

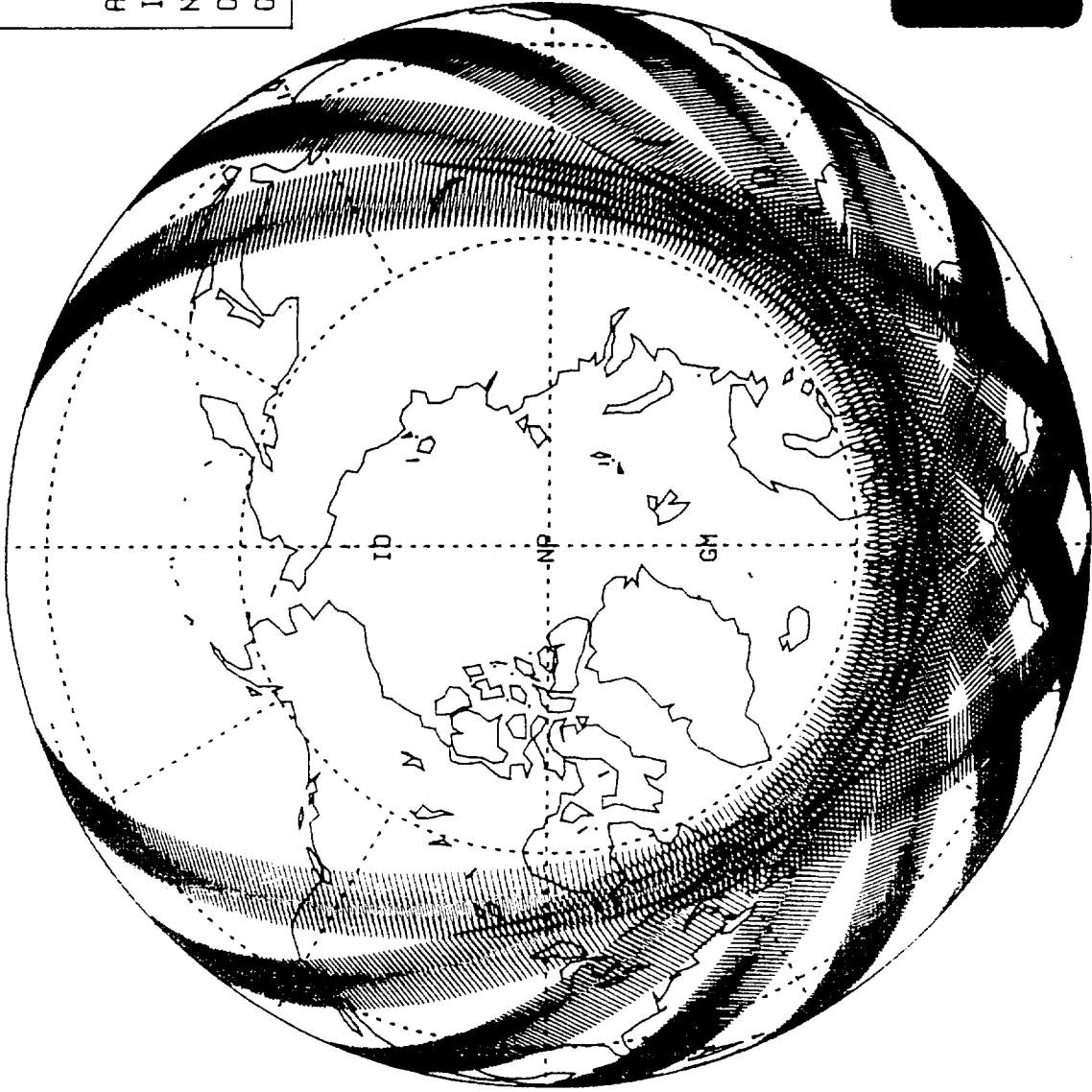


Figure C.3

LAWS 12 HOUR COVERAGE

<u>LEGEND</u>	
ALTITUDE	450 KM
INCLINATION	55 DEG
NADIR ANGLE	45 DEG
ORBIT VEL.	7.65 KM/S
ORBIT PERIOD	93 MIN

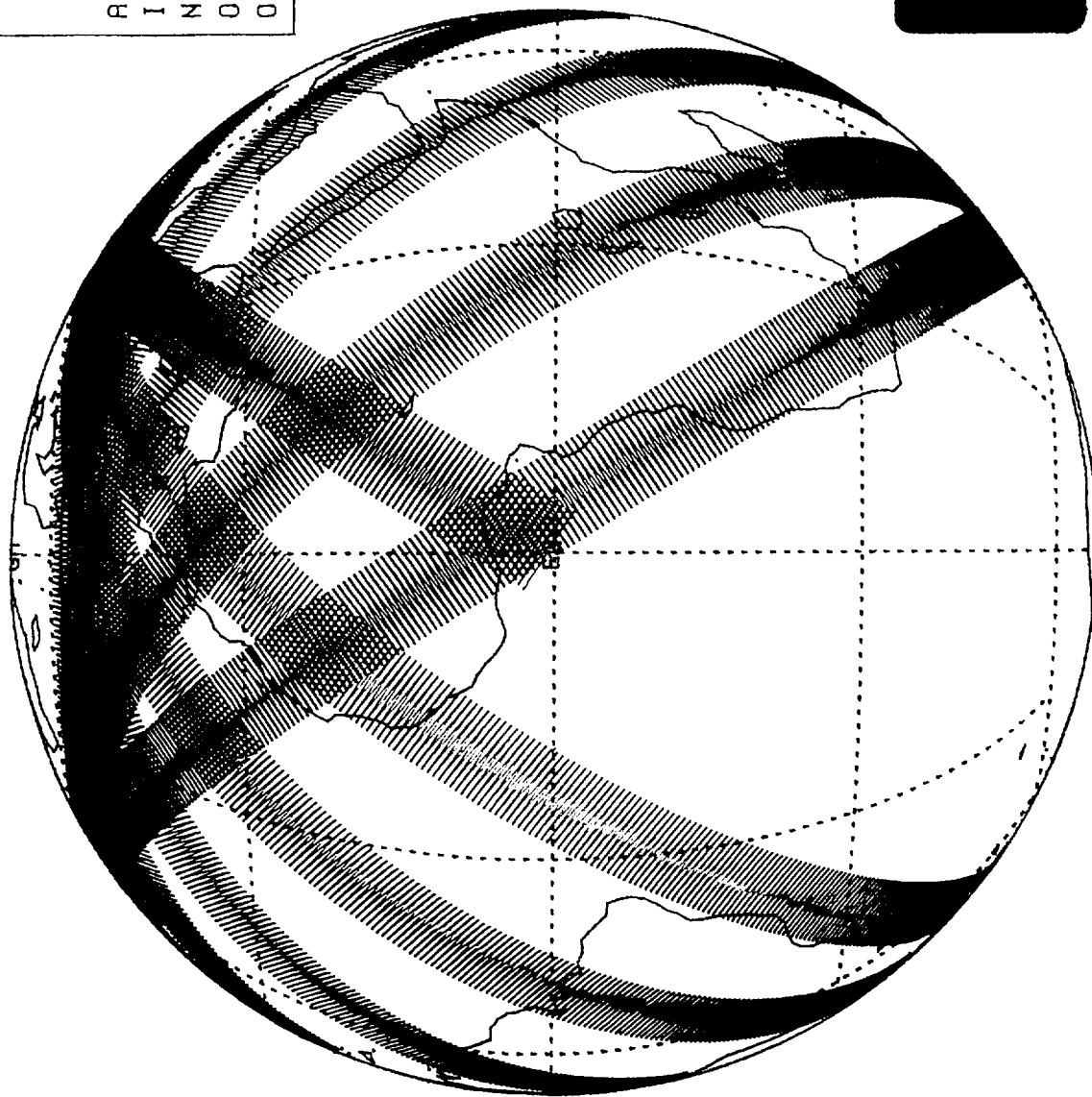
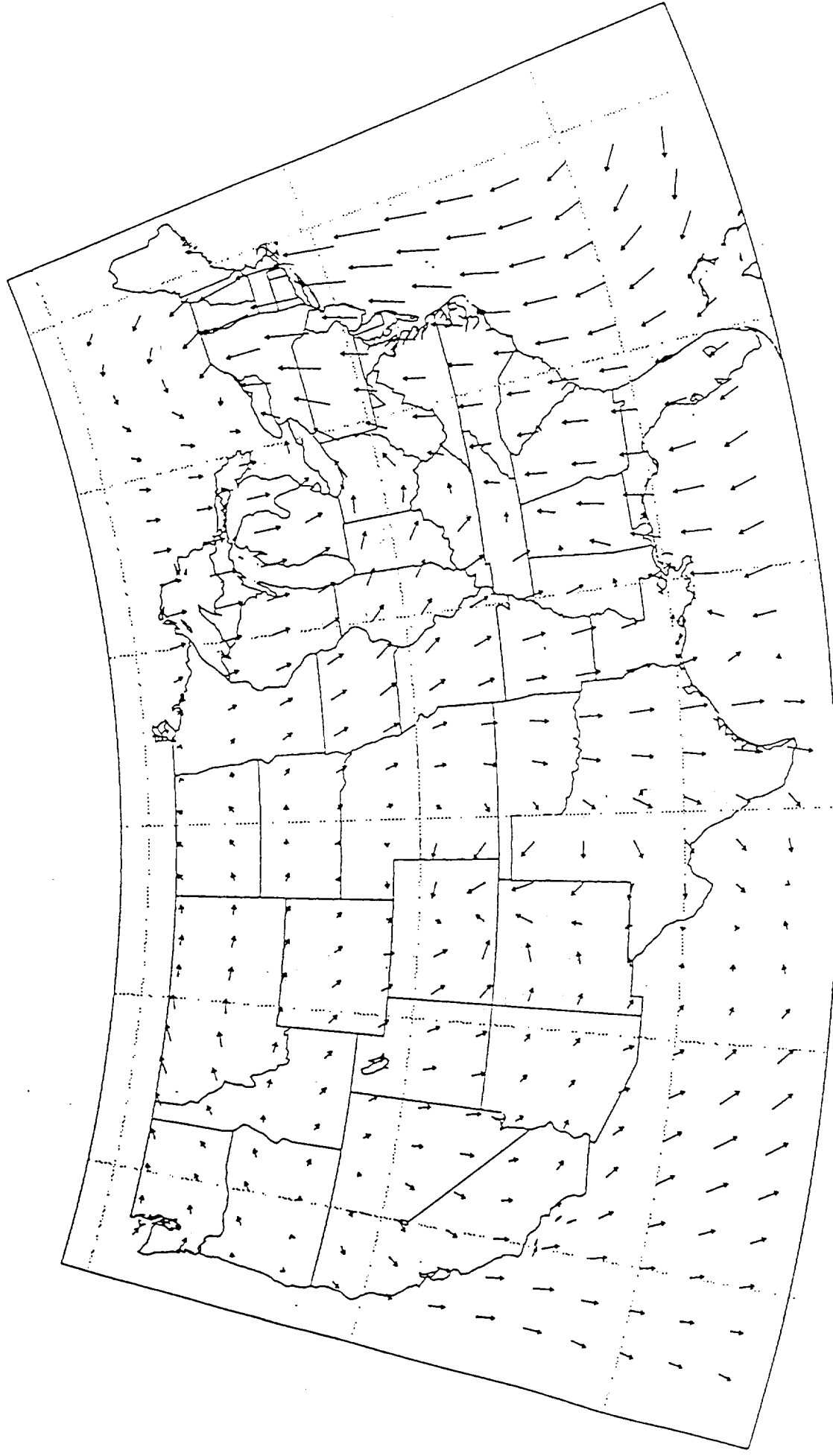


Figure C.4

—



ECMWF Horizontal Winds Over The United States



(surface) 10 Nov 1979 06:00

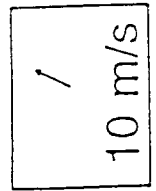


Figure C.6

ECMWF Horizontal Winds Over The United States

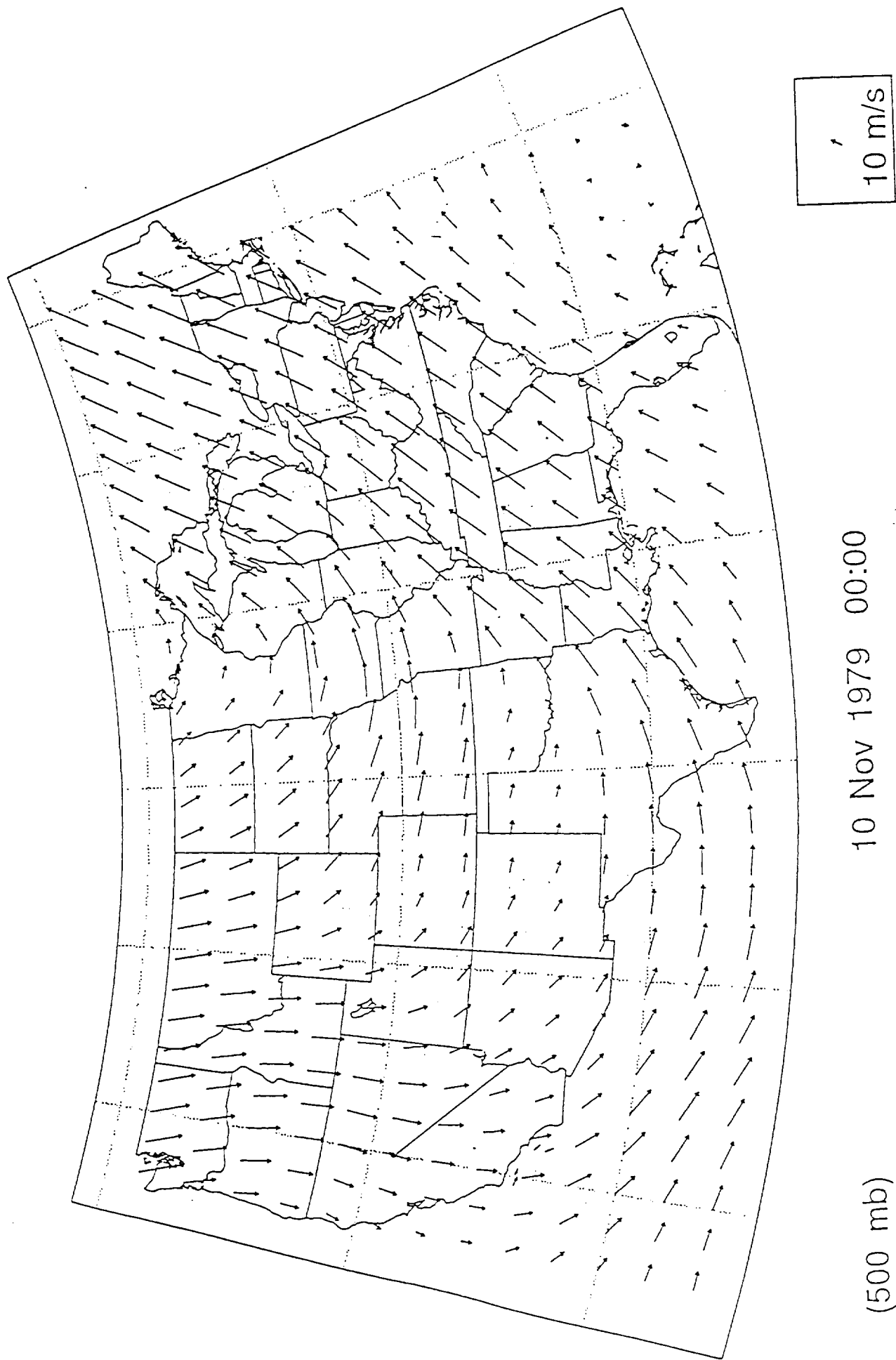


Figure C.7

ECMWF Horizontal Winds Over The United States

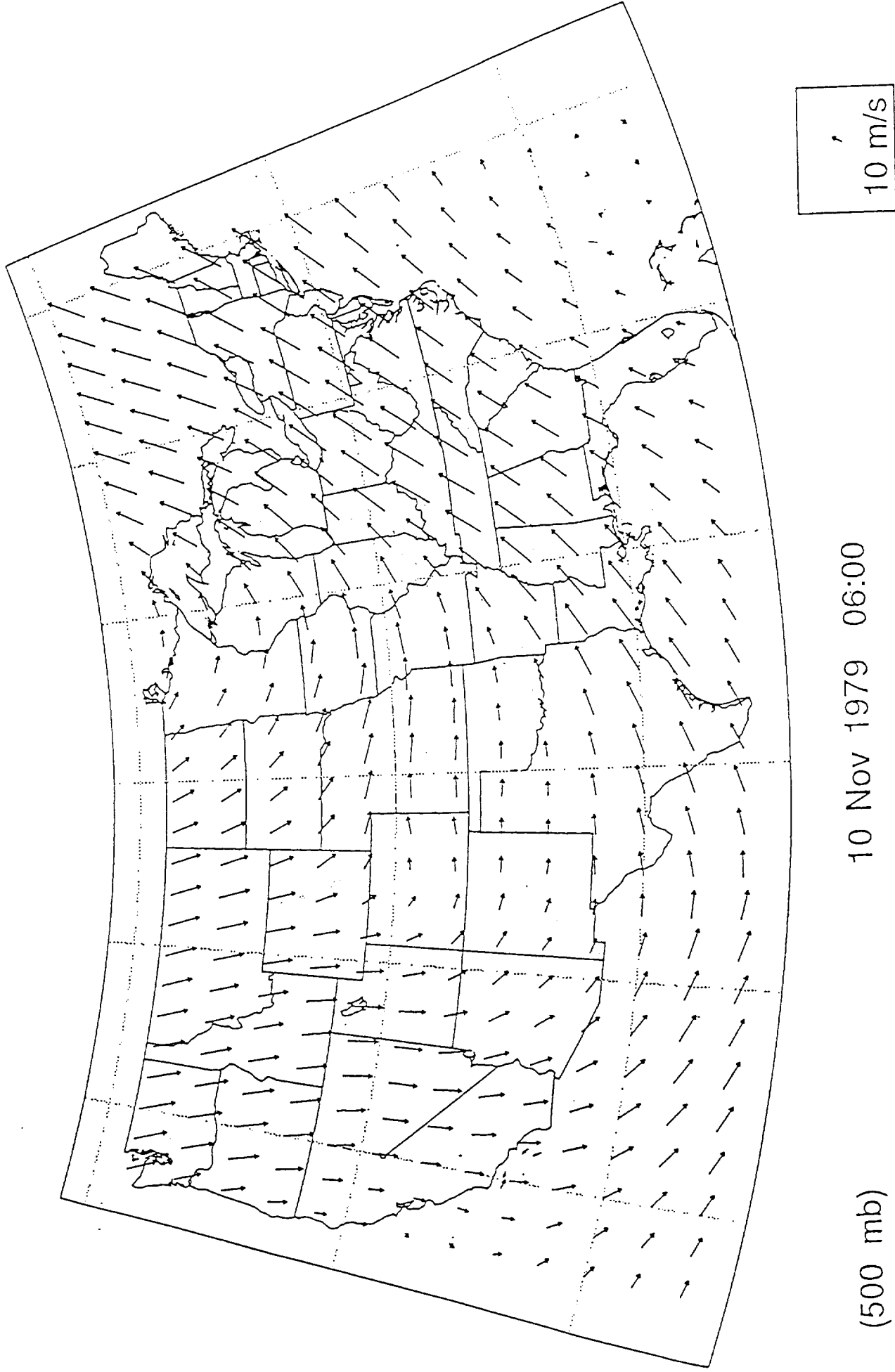


Figure C.8

LAWS WINDS OVER THE UNITED STATES

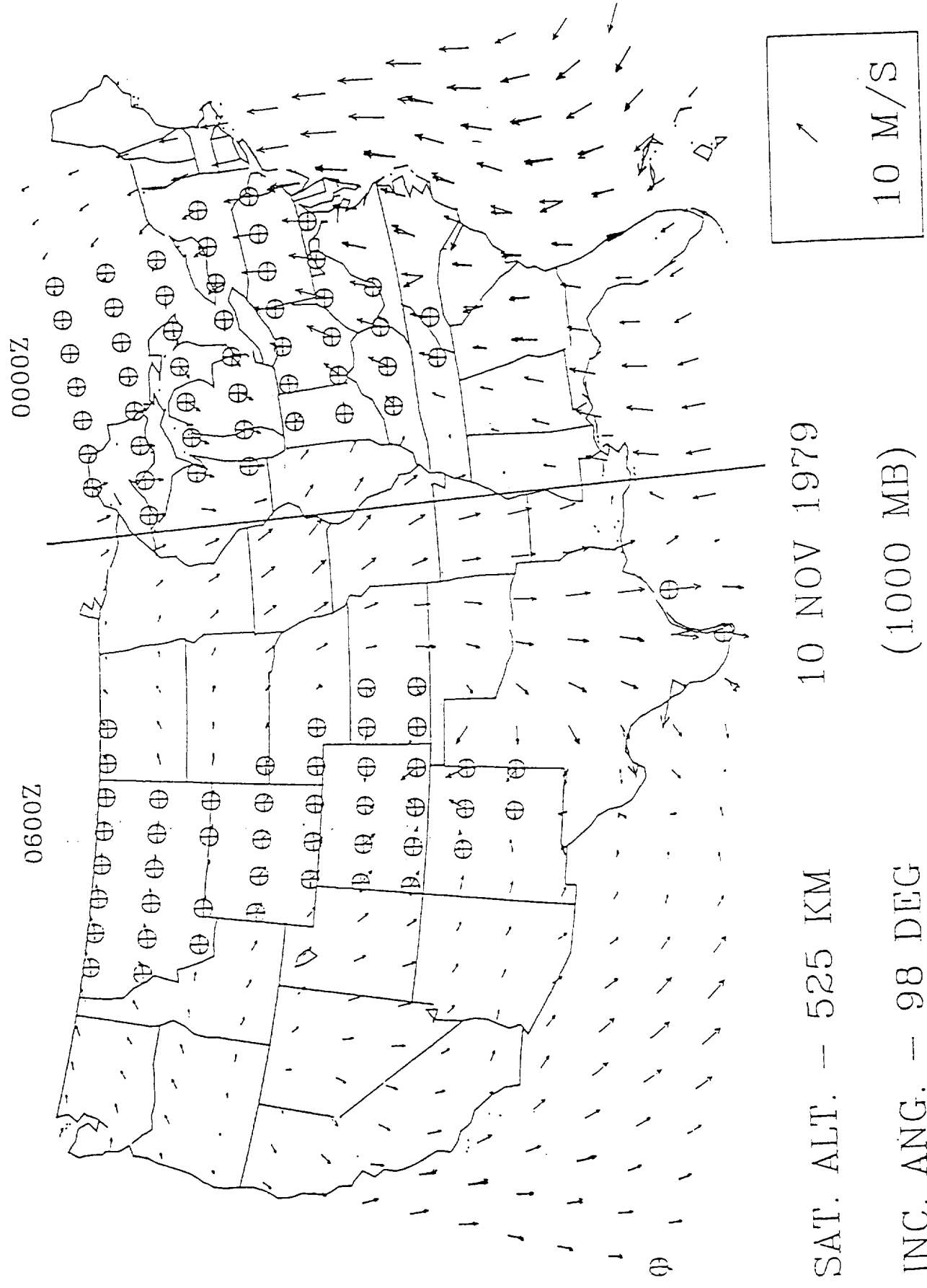


Figure C.9

LAWS WINDS OVER THE UNITED STATES

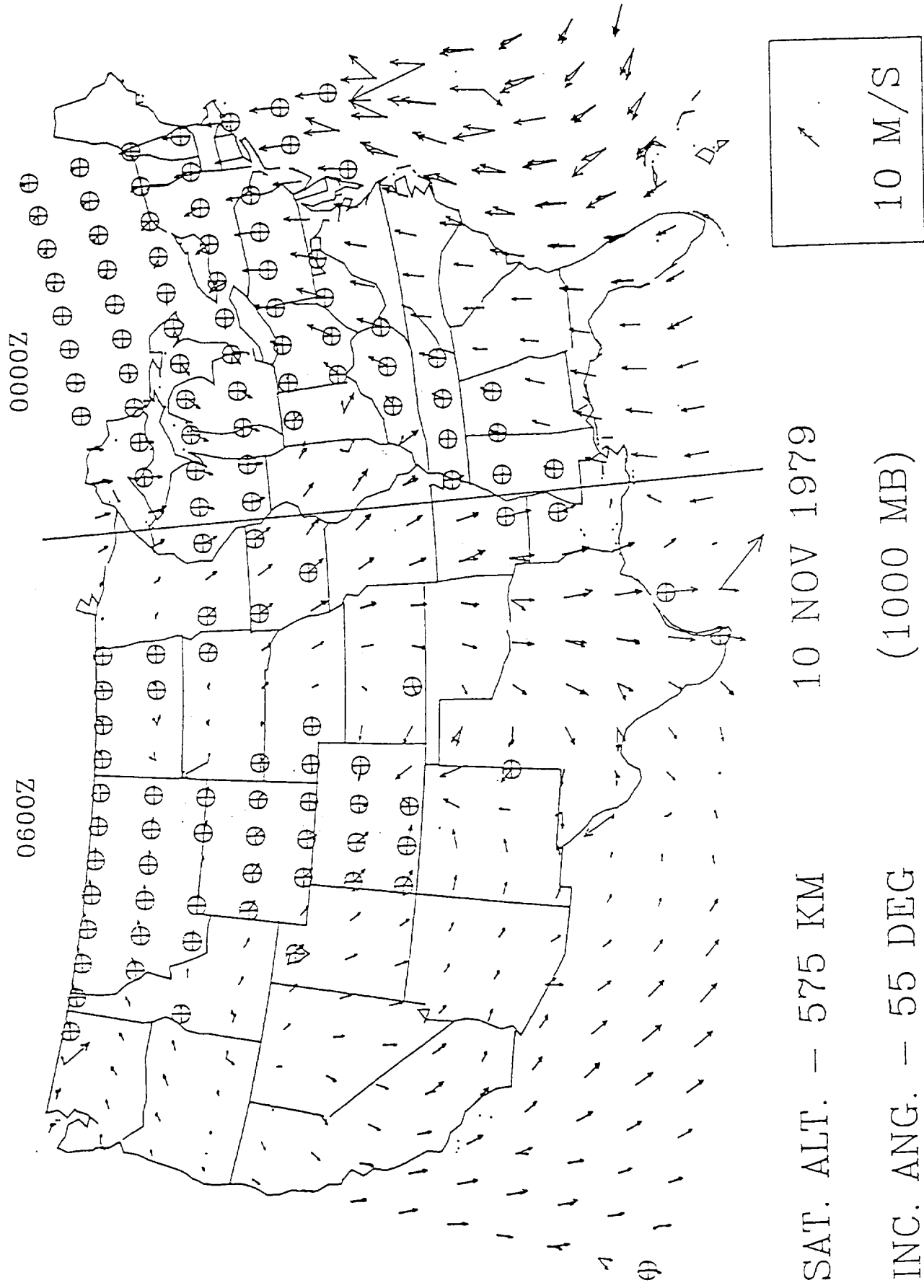
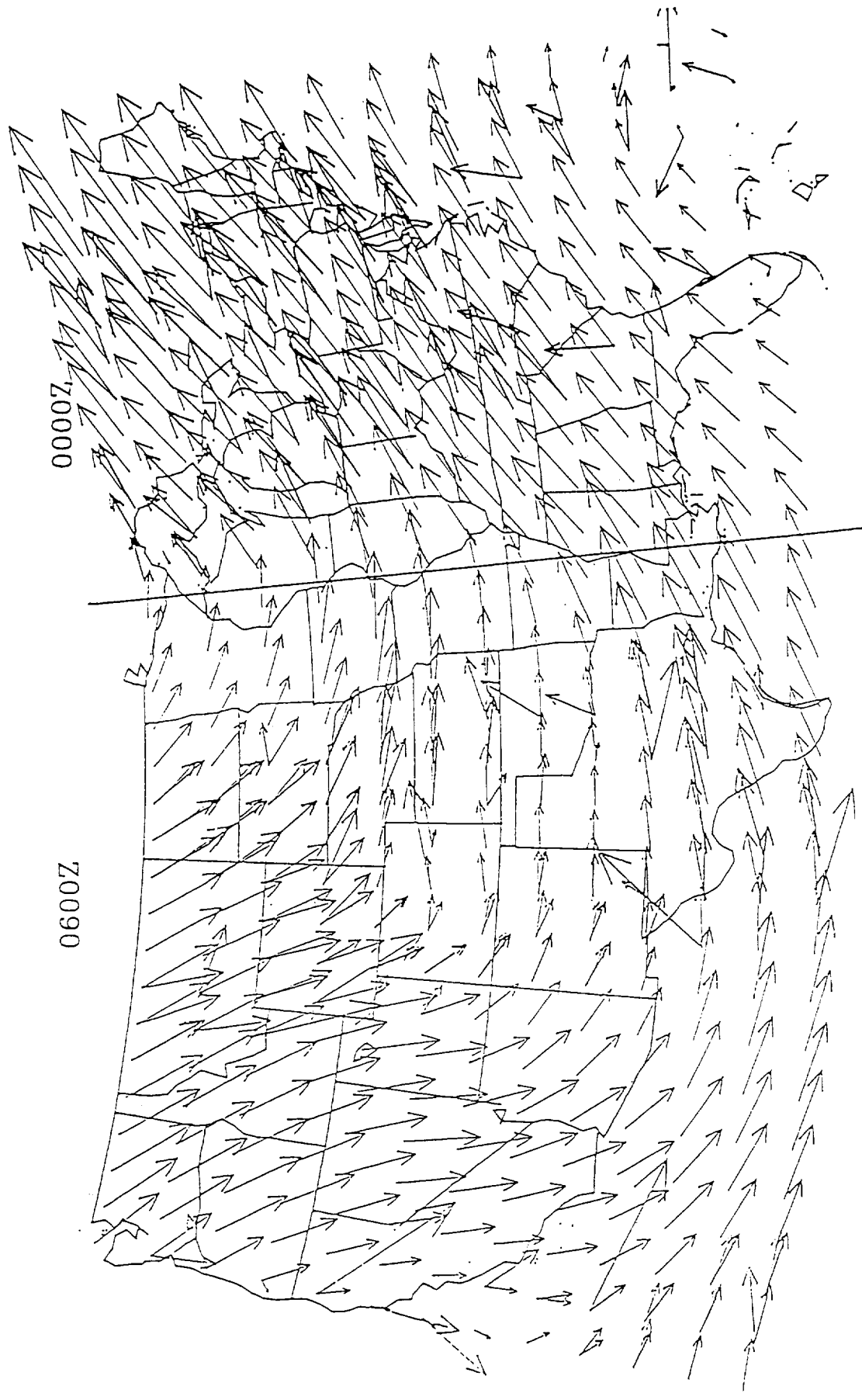


Figure C.10

LAW'S WINDS OVER THE UNITED STATES



10 M/S

10 NOV 1979

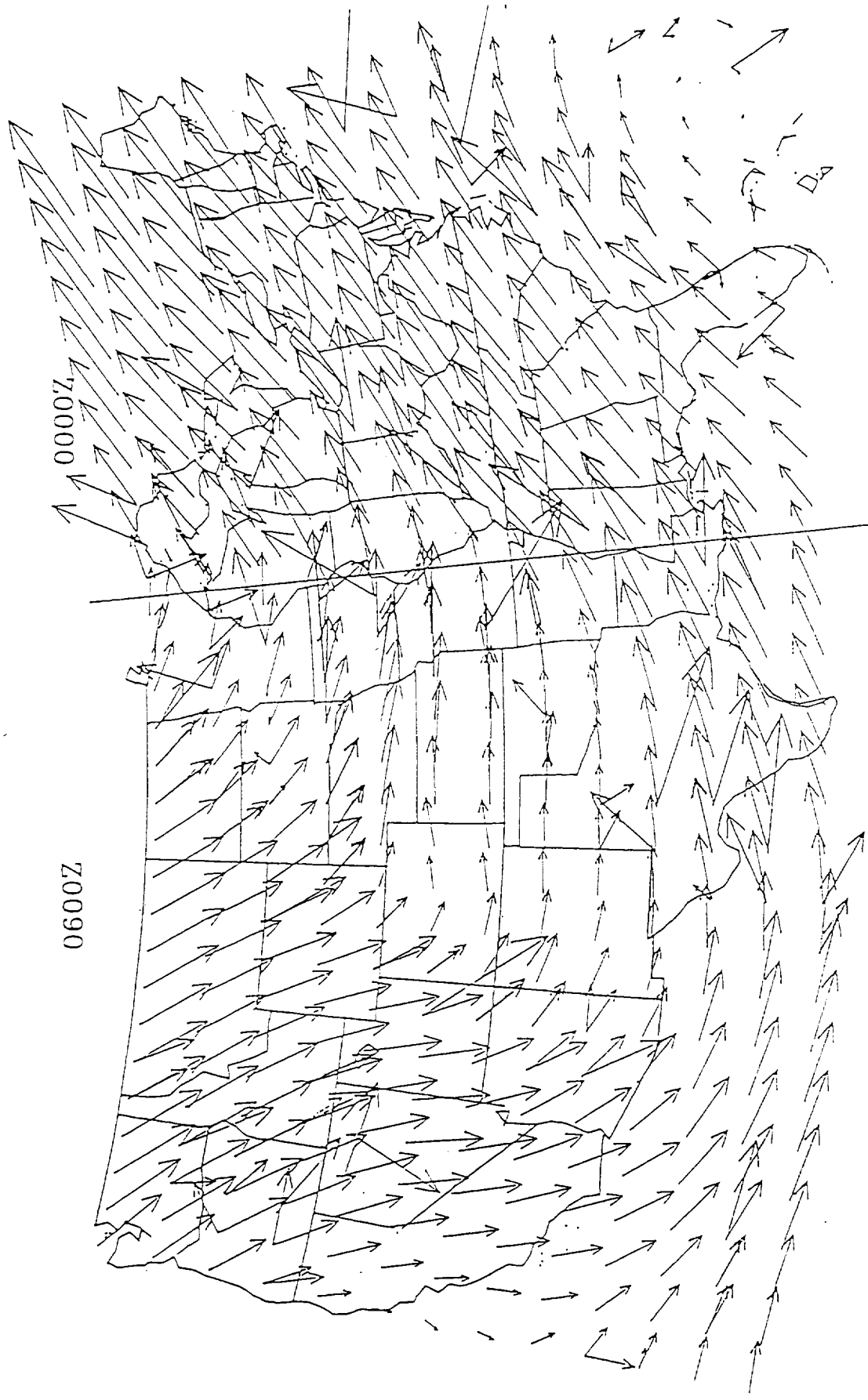
SAT. ALT. - 525 KM

(500 MB)

INC. ANG. - 98 DEG

Figure C.11

LAWS WINDS OVER THE UNITED STATES



SAT. ALT. - 575 KM 10 NOV 1979

INC. ANG. - 55 DEG (500 MB)

Figure C.12

APPENDIX D GROUND-BASED DOPPLER LIDAR STUDIES

1.0 Signal Processing Tools and Data Display Models

Validation of the LMSg model has been a priority under the current contract. While GLOBE has improved the basis for modeled backscatter, the ground-based Doppler lidar at MSFC has provided some checks on assumed atmospheric variability parameterization and signal processing performance.

Many of the expectations for the performance of a space-based Doppler lidar are based upon the experienced gained from ground-based (and to a lesser extent airborne) systems. In particular, the LAWS concepts are derived from programs at NOAA and NASA - programs that have ground-based systems with pulse rates of 30-100 Hz and signal processing based upon the pulse-pair algorithm involving 3-50 shots per estimate. A space-based system will probably operate at < 20 Hz and each shot will be processed separately. SWA's experiments, therefore, have required that the single shot In-phase and Quadrature time series be recorded for post processing. Since the data volumes involved with single shot recording are much greater than the MSFC data system can handle, only 2 shots per record were recorded.

SWA has developed and refined a series of computer tools that are designed to process and analyze NASA/MSFC ground-based Doppler lidar polypulse-pair and single shot data. The models are the Pre-processor models, FFT Model, Sine Fit Model, PPI/UV and Range Display Models, Shot Pairing Model and the SNR/Consensus Model. Figure D.1 is a flow diagram that defines SWA's ground-based processing operations and conventions.

The NASA/MSFC ground-based lidar data pre-processor reads the raw NASA/MSFC data files providing data record counts to reformat the data into either VAD files (MSFC.VAD) for scanning angles or RANGE files (MSFC.RAN) for fixed scan angles. For single shot data, the models correct for the in-phase and quadrature data for offset and gain. For the scanning data sets, the models create line-of-sight wind velocity files (MSFC.PPI) for the PPI/UV Display Model and velocity/azimuth/signal (MSFC.VAS) files for the sine fit model.

After the polypulse-pair and single shot data sets are reformatted, the in-phase and quadrature single shot data is run through a FFT model to produce line-of-sight wind (LOS) velocities. Throughout this effort, we have evaluated several FFT models (MathLIB, MathCAD, numerical recipes, etc.) for Doppler lidar data processing. It became evident that a FORTRAN source code FFT model not only provides more flexibility (such as applying unity amplitude windowing) over a commercial off the shelf product, but is also faster. One VADS' worth of lidar

processing is approximately 7136 FFTs and takes 20 minutes on a 486 PC.

In an attempt to establish "ground truth" winds using poly-pulse data and in order to compute U/V horizontal wind components for the PPI/UV displays, SWA developed two sine wave fitting models that work with incomplete and extremely noisy data sets. The first model is a Fortran coded "brute force" model that tries to best fit the data by varying amplitude, phase and vertical offset for many combinations. Data filtering based on signal strength is used to remove wild data points. This model goes through many iterations to arrive at a best fit and is computationally expensive. Also, the sine fits have to be visually examined to evaluate the quality of the fits and to assess whether the applied filter was too weak or too strong. The second model was developed in Visual Basic and allows the user to quickly move the best sine fit around the data by changing amplitude, phase and offset. These sine fits are saved in MSFC.APO files. Figures D.2 and D.3 are examples of the Visual Basic Sine Fit Model. Figure D.2 shows a fit to unfiltered single shot data at range gate 9. The goodness of fit, 235.9, is not very good. Figure D.3 shows the same data with a signal filter used to remove weak pieces of information. The user was able to hone in the sine fit in seconds and found that the goodness of fit improved to 10.9.

The PPI/UV Display Model uses the MSFC.PPI line-of-sight velocity data file from the pre-processor model to produce a Plan Position Indicator plot (see Section 2.0). The model also uses the APO file from the Sine Fit Model to compute a vertical distribution of horizontal wind components. The RANGE Display Model uses the MSFC.RAN line-of-sight velocity data files from the pre-processor model to produce range verses elapsed time plots (see Section 2.0).

A space-based wind sounder will produce a pattern of shots that will provide generally bi-perspective samples within 100x100 km target areas. The angle between the two perspectives will vary depending upon the location of the target areas relative to the sub-satellite ground track. The wind estimate error will also vary with the geometry of the bi-perspective samples. The Ground-Based Shot Pairing Model processes the Doppler lidar data to yield shot combinations that are similar to those that will be achieved from space. Wind components are calculated for a range of bi-perspective shot pairs, which are compared to the true components "ground truth" derived from the sine fitted poly-pulsed pair VAD (see Section 2.0).

2.0 Ground-Based Studies

During the course of this effort, SWA cooperated with NASA/MSFC ground-based Doppler lidar engineers to produce a

series of lidar experiments to address issues such as system stability, amplitude averages, accuracy versus SNR, winds from cirrus decks, single shot pairing and associated errors. Table D.1 lists the NASA/MSFC data sets produced under this effort.

Table D.1. NASA/MSFC Ground-Based Doppler Lidar Data Sets

DATE	TYPE	AZM	ELV	#FILES	COMMENTS
07/10/92	SSHT	VAD	42	3	PARTLY CLOUDY
07/10/92	SSHT	VAD	74	1	PARTLY CLOUDY
07/10/92	PPP	VAD	42	1	PARTLY CLOUDY
07/10/92	PPP	FIX	3.8	1	MOUNTAIN
07/10/92	PPP	VAD	42	2	PARTLY CLOUDY
07/10/92	PPP	VAD	74	1	PARTLY CLOUDY
07/17/92	SSHT	FIX	3	1	MOUNTAIN
07/17/92	SSHT	FIX	3	2	SINE WAVE
07/17/92	SSHT	VAD	42	3	CLOUDY
07/17/92	SSHT	VAD	70	4	CLOUDY
07/17/92	PPP	FIX	3	1	MOUNTAIN
07/17/92	PPP	VAD	42	2	CLOUDY
07/17/92	PPP	VAD	70	2	CLOUDY
10/19/92	PPP	FIX	3	1	MOUNTAIN
10/19/92	PPP	FIX	90	1	CIRRUS
10/19/92	PPP	RHI	90	5	CIRRUS
02/27/93	SSHT	FIX	3.5	1	MOUNTAIN
02/27/93	SSHT	FIX	4.2	4	TOWER
02/27/93	SSHT	FIX	1	4	BLD 4200, PWR MODS
02/27/93	SSHT	FIX	3.5	1	MOUNTAIN
02/27/93	PPP	FIX	3.5	1	MOUNTAIN
02/27/93	PPP	FIX	4.2	4	TOWER
02/27/93	PPP	FIX	1	4	BLD 4200, PWR MODS
02/27/93	PPP	FIX	1	1	MOUNTAIN
03/01/93	SSHT	FIX	3.5	2	MOUNTAIN

03/01/93	SSHT	FIX	44	5	CLEAR, HIGH CLOUDS
03/01/93	SSHT	VAD	45	1	CLEAR, HIGH CLOUDS
03/01/93	PPP	FIX	3.5	3	MOUNTAIN
03/01/93	PPP	FIX	44	5	CLEAR, HIGH CLOUDS
03/01/93	PPP	VAD	45	1	CLEAR, HIGH CLOUDS
05/26/93	SSHT	FIX	4	1	MOUNTAIN
05/26/93	SSHT	FIX	1.8	1	BLG 4200
05/26/93	SSHT	FIX	1.8	2	NOISE
05/26/93	PPP	FIX	4	1	MOUNTAIN
05/26/93	PPP	FIX	1.8	1	BLG 4200
05/26/93	PPP	FIX	1.8	2	NOISE
05/27/93	SSHT	FIX	4	1	MOUNTAIN
05/27/93	SSHT	VAD	45	4	BKN CLOUDS, PWR MOD
05/27/93	PPP	FIX	4	1	MOUNTAIN
05/27/93	PPP	VAD	45	1	BKN CLOUDS, PWR MOD
05/28/93	SSHT	FIX	3.3	1	MOUNTAIN
05/28/93	SSHT	FIX	90	3	SUNNY, HIGH CLOUDS
05/28/93	PPP	FIX	3.3	1	MOUNTAIN
05/28/93	PPP	FIX	90	1	SUNNY, HIGH CLOUDS
06/03/93	SSHT	FIX	3.8	1	MOUNTAIN
06/03/93	SSHT	FIX	45	1	IN WIND DIRECTION
06/03/93	SSHT	FIX	45	1	IN CROSS WIND
06/03/93	PPP	FIX	3.8	1	MOUNTAIN
06/03/93	PPP	VAD	45	1	
06/03/93	PPP	FIX	45	1	IN WIND DIRECTION
06/03/93	PPP	FIX	45	1	IN CROSS WIND
07/07/93	SSHT	FIX	STEP	3	SUNNY
07/07/93	PPP	FIX	STEP	3	SUNNY

2.1 Frequency Stability

We examined three poly-pulse processed data sets to evaluate the frequency stability of the NASA/MSFC Doppler lidar wind returns from several stationary targets such as a mountain,

building 4200 and a tower. Figure D.4 shows range versus time LOS wind velocity plots for returns off the building (~2.5 km). Figure D.5 shows the line-of-sight velocity, at range gate 8, as a function of time for returns off the same building. The LOS velocities varied with a σ of $\sim .05 \text{ m s}^{-1}$.

2.2 SNR Studies

Ground-based Doppler lidar system data was collected, processed and analyzed in an attempt to determine a critical signal-to-noise ratio (SNR) value below which it is unlikely to obtain reasonable single shot measurements (Dieudonné, 1992, Appendix G). The proposed, theoretical value for such an SNR is somewhat unclear due to the relative nature of the classification of "good" estimates. However, for narrow band signals the general postulate is that an SNR of 0 dB is the point below which "good" estimates are unobtainable. Additionally, there is a theoretical notion that 5 dB is the point after which there is a consistent breakdown in measurement capabilities.

In processing the single shot data, VADS were used to identify a sequence of range gates where only noise existed. Figure D.6 shows the shot-by-shot average amplitudes of the signals in range gates 17 through 27. The average noise threshold is around 5.25 in arbitrary units. Figure D.7 is a velocity azimuth display (VAD) of the single shot data filtered along each shot by the average noise found in range gates 17-27. Using a VAD sine fitting model, vertical soundings were computed.

Single shot wind velocity estimates were analyzed per range gate for all azimuth angles. In this particular scenario, gates 8 through 15 were observed to have well defined, coherent single shot returns. Thus, a least squares sine fit routine was applied to the poly-pulse pair data in each of these eight gates, and the resulting sine fit was used as the representation for true wind velocity in each gate. In this way, the difference between each single shot wind estimate in gates 8 through 15 and the corresponding poly-pulse pair sine fit was calculated in order to analyze the accuracy of single shot estimates. The SNR value corresponding to all single shot estimates was also determined. From this information, the standard deviation of single shot estimates from poly-pulse pair "truth" was obtained for a range of SNR_N values. Figure D.8 shows the percentage of total single shot wind velocity estimates per SNR_N value which were less than the threshold values of 5 m/s, 4 m/s, 3 m/s, 2 m/s and 1 m/s. The trend in Fig. D.8 was as expected, i.e., better estimates were obtained at higher SNR_N . Additionally, Fig. D.8 shows that to obtain accurate single shot estimates to within 1 m/s 50% of the time an SNR_N value of about 2.5 dB is necessary. Likewise, to obtain accurate estimates to within 5 m/s 50% of the time an SNR_N value of approximately -2 dB is needed. This verified generally held expectations that an SNR (narrow band) of about 0

dB is the limit in obtaining "good" single shot estimates about 50% of the time. Finally, Fig. D.8 verifies another "rule of thumb" that confidence in single shot wind velocity estimates rapidly decreases for SNR_N values below 5 dB.

2.3 Cirrus Studies

We processed single shot and poly-pulse scanning data for July 10, 1992, 1623Z, which had a high thin cirrus cloud present. Each data set was noise filtered and least squares fit to a sine wave to establish "ground truth" winds. Figures D.9 and D.10 give examples of the sine fits, using the FORTRAN sine fitting model, for a series of range gates going from a strong SNR region to a weak SNR region for both unfiltered and filtered data. At range gate 5, the signal-to-noise (SNR) was very low. At range gates 6-15 there were strong signals to make LOS estimates. However, at range gate 16, the single shot data showed loss of signal where the poly-pulse data (50 shot averages) was able to make a LOS measurement. Only noise was found from range gates 17-29. The cirrus cloud provided signal at range gates 30-32 as seen in Fig. D.11 and D.12.

We selected the MSFC cirrus cloud data sets from July 17, 1992, 1623Z, to look at a time series of four sequential VADS, shown in Figs. D.13-D.16. The lidar wind information from the cirrus clouds appears to be very variable. A longer time series of lidar data is needed to examine this closer.

On May 28, 1993, the MSFC lidar was held in a fixed scan with an elevation angle at near zenith. At around 10 km, a thin cirrus deck was reported. Figures D.17-D.24 depict the poly-pulse lidar wind velocities and amplitudes for 400 seconds. As seen in Figs. D.23 and D.24, the cirrus return ends at around 370 seconds. Figure D.25 shows a time series at range gate 36 (cirrus deck) for the amplitude and wind velocity.

On October 19, 1992, the lidar was pointing straight up in a non-scanning mode at a thin cirrus deck. Figure D.26 is a range versus time wind velocity plot showing the cirrus deck at around the 41st range gate. Figure D.27 shows the vertical wind speeds as a function of range gate around the cirrus layer. For comparison, Fig. D.28 shows the vertical wind speeds for the mid-troposphere (strong SNR to weak SNR). The variance found in the mid-troposphere was approximately half that found in the cirrus layer.

2.4 Shot Pairing

As stated in Section 1.0 above, a space-based wind sounder will produce a pattern of shots that will provide bi-perspective samples within 100x100 km target areas. The ground-based data from July 10, 1992, 1623Z, was processed to yield shot

combinations that are similar to those that will be achieved from space. Wind components were calculated for a range of bi-perspective shot pairs and compared to the true components derived from the sine fitted poly-pulse pair VAD. Figures D.29 and D.30 illustrate the distribution of errors for the U, V and total speed errors for unfiltered range gates 8-14 (high SNR) and for filtered range gates 30-31 (cirrus deck).

On May 27, 1993, the MSFC lidar ran a time series of scans (10 VADS) with an elevation angle of 45 degrees. Figure D.31 is a PPI diagram for the first VAD of poly-pulse data. We processed all ten VADS through the SWA ground-based Doppler lidar data processor. Each data set was noise filtered and least squares fit to a sine wave (see Section 1.0). Wind components were calculated for a range of bi-perspective shot pairs and compared to the true components derived from the sine fitted poly-pulsed pair VAD (see Section 1.0). Figures D.32-D.37 illustrate the distribution of errors for the U, V and total speed errors for unfiltered range gates 10-15 (high SNR).

2.5 Consensus Studies

Of primary interest to the measurement of winds from space is the development of optimal signal processing algorithms. The Cramer-Rao lower bound is considered to be the ultimate target for algorithm performance. At this time, we expect to have an algorithm that is within 5-8 dB of that bound (Fig. D.38 from John Anderson, University of Wisconsin). As part of our ground-based lidar research, we began assessing several processing algorithms. Since a consensus approach has been adopted for simulation studies, the ground-based data were processed to evaluate that technique.

The consensus algorithm is modeled after similar processing schemes used with radar data. Basically, the lidar time series along a single line-of-sight is subdivided into range gates (approximately the same duration as the lidar pulse) that represents independent samples of the atmosphere within a specified layer. In the 9 km case, the layer is 1 km thick and there are ~ 4-5 independent range gates. When three or more of the five LOS velocity estimates agree within 2 m s^{-1} , a consensus is declared and the average LOS component is used in subsequent calculations of the horizontal wind components. Since the noisy bandwidth of the signal processing is $\pm 25 \text{ m s}^{-1}$, there is always a possibility that consensus may be achieved randomly - such consensus are referred to as false alarms.

The claim by the signal processing community is that the consensus algorithm should perform similar to the Capon estimates noted in Fig. D.38.

On May 27, 1993, the MSFC lidar ran a time series of scans (10 vads) with an elevation angle of 45 degrees. In Section 2.2 above, we provide a discussion on how we processed the ten VADS of poly-pulsed data through the SWA ground-based Doppler lidar data processor to produce wind components and errors that are calculated for a range of bi-perspective shot pairs. We also used these data to populate our consensus algorithm to further evaluate the LAWS consensus signal processing technique. Some very preliminary results based upon 3 VADS of 1623 are shown in Fig. D.39. To note is the much sharper fall-off of performance (percentage of estimates that meet consensus) than that expected from the curves in Fig. D.38.

2.6 Backscatter Inhomogeneity Feasibility Studies

On July 7, 1993, the MSFC lidar performed a series of very low angle fixed scans varying from 2.5 degrees to 4 degrees to test if this configuration could be used to examine the backscatter and wind inhomogeneities in the boundary layer. Figures D.40-D.43 show the poly-pulsed wind velocities and amplitudes for elevations 2.5 degrees and 4 degrees, respectively. Strong lidar signals can be seen in the 7 to 10 range gate areas. Figures D.44-D.47 show a time series for both elevation angles at range gate 8 (high SNR) and at the range gate where the signal hits the mountain.

FIGURE CAPTIONS

- Figure D.1: Flow diagram for the SWA ground-based Doppler lidar processing operations.
- Figure D.2: Visual basic sine fit mode display for an unfiltered sine fit to NASA/MSFC ground-based Doppler lidar data.
- Figure D.3: As for Fig. D.2 except for filtered data.
- Figure D.4: NASA/MSFC line-of-sight wind velocities as a function of range and time for a stationary target (building).
- Figure D.5: NASA/MSFC line-of-sight wind velocities as a function of time a range gate 8 for a stationary target (building).
- Figure D.6: Amplitude averages for one VAD of processed NASA/MSFC single shot data in range gates 17 through 27. Each average is considered to be a noise threshold for each lidar shot.
- Figure D.7: A PPI diagram of NASA/MSFC single shot ground-based Doppler lidar data. Line of shot wind velocities and horizontal wind components are shown as a function of height.
- Figure D.8: Accuracy vs. SNR for single shots within one 220 shot VAD. A total of 5060 wind estimates were used to populate a 1 dB resolution SNR histogram. The median SNR was ~ 6-7 dB.
- Figure D.9: Sine fits to unfiltered NASA/MSFC single shot ground-based Doppler lidar data for range gates 12 (strong SNR) to 17 (weak SNR).
- Figure D.10: Sine fits to filtered NASA/MSFC single shot ground-based Doppler lidar data for range gates 12 (strong SNR) to 17 (weak SNR).
- Figure D.11: Display of Doppler lidar data processed with a poly-pulse pair algorithm using 50 sequential shots. Vertical profile is obtained with sine fitting of individual range gates. The lidar was operated at 110 Hz.
- Figure D.12: Display of single shot Doppler lidar data taken at 1.5° azimuthal increments. These were data were taken at the same time as those shown in Fig. D.11.

- Figure D.13: Display of processed NASA/MSFC single shot ground-based Doppler lidar data taken at 1.5° azimuthal increments for July 17, 1992 at 16:24:44. Vertical profile is obtained with sine fitting of individual range gates. The lidar was operated at 110 Hz.
- Figure D.14: As for Fig. D.13 but for 16:26:25.
- Figure D.15: As for Fig. D.13 but for 16:28:06.
- Figure D.16: As for Fig. D.13 but for 16:29:48.
- Figure D.17: Unfiltered poly-pulse ground-based Doppler lidar line-of-sight wind velocities as a function of range and time. Cirrus cloud returns are shown at range gates 33-38. The data was taken at 11:27:44 for 5/28/93 with an elevation angle at near zenith.
- Figure D.18: Unfiltered poly-pulse ground-based Doppler lidar amplitudes as a function of range and time. Cirrus cloud returns are shown at range gates 33-38. The data was taken at 11:27:44 for 5/28/93 with an elevation angle at near zenith.
- Figure D.19: As for Fig. D.17 but for data taken at 11:29:24.
- Figure D.20: As for Fig. D.18 but for data taken at 11:29:24.
- Figure D.21: As for Fig. D.17 but for data taken at 11:31:04.
- Figure D.22: As for Fig. D.18 but for data taken at 11:31:04.
- Figure D.23: As for Fig. D.17 but for data taken at 11:32:44.
- Figure D.24: As for Fig. D.18 but for data taken at 11:32:44.
- Figure D.25: A time series at range gate 36 (cirrus deck) of poly-pulse ground-based Doppler lidar line-of-sight wind velocities and amplitude. The data was taken on 5/28/93 with an elevation angle at near zenith.
- Figure D.26: NASA/MSFC line-of-sight wind velocities as a function of range and time for a cirrus deck at range gate 41.
- Figure D.27: Vertical wind speed as a function of range and SNR near a cirrus deck.
- Figure D.28: As for Fig. D.27 but for the mid-troposphere.

- Figure D.29: Distribution of U, V, and total wind speed errors computed from unfiltered single shot lidar data at strong SNR range gates (8-14).
- Figure D.30: As for Fig. D.29 but for filtered single shot lidar data at a cirrus deck (range gates 30-31).
- Figure D.31: A PPI diagram of poly-pulse ground-based Doppler lidar line-of-sight wind velocities and horizontal wind velocities. The data was taken at 13:45:59 for 5/27/93.
- Figure D.32: Distribution of U, V, and total wind speed errors computed from unfiltered poly-pulse lidar data at range gate 10 (strong SNR). The data was for 13:45:59 on 5/27/93.
- Figure D.33: As for Fig. D.32 for range gate 11 (strong SNR). The data was for 13:45:59 on 5/27/93.
- Figure D.34: As for Fig. D.32 for range gate 12 (strong SNR). The data was for 13:45:59 on 5/27/93.
- Figure D.35: As for Fig. D.32 for range gate 13 (strong SNR). The data was for 13:45:59 on 5/27/93.
- Figure D.36: As for Fig. D.32 for range gate 14 (strong SNR). The data was for 13:45:59 on 5/27/93.
- Figure D.37: As for Fig. D.32 for range gate 15 (strong SNR). The data was for 13:45:59 on 5/27/93.
- Figure D.38: Fraction of wind estimates with errors < 1 m/s as a function of SNR for four signal processing algorithms; Zrinc CR, Capon estimator simulation, pulse pair theory and pulse pair simulation.
- Figure D.39: Fraction of wind estimates with errors < 2 m/s as a function of narrowband SNR based upon 3 VADS of single shot lidar data.
- Figure D.40: Unfiltered poly-pulse ground-based Doppler lidar line-of-sight wind velocities as a function of range and time. The data was taken at 15:16:40 for 7/07/93 with an elevation angle at 2.5 degrees.
- Figure D.41: Unfiltered poly-pulse ground-based Doppler lidar amplitudes as a function of range and time. The data was taken at 15:16:40 for 7/07/93 with an elevation angle at 2.5 degrees.

- Figure D.42: As for Fig. D.40. Data was taken at 15:22:40 for 7/07/93 with an elevation angle at 4.0 degrees.
- Figure D.43: As for Fig. D.41. Data was taken at 15:22:40 for 7/07/93 with an elevation angle at 4.0 degrees.
- Figure D.44: A time series at range gate 8 (strong SNR) of poly-pulse ground-based Doppler lidar line-of-sight wind velocities and amplitude. The data was taken on 7/07/93 with an elevation angle at 2.5 degrees.
- Figure D.45: As for Fig. D.44 but for range gate 10 (mountain return).
- Figure D.46: As for Fig. D.44 but for range gate 8 (strong SNR) with an elevation angle at 4.0 degrees.
- Figure D.47: As for Fig. D.44 but for range gate 10 (mountain return) with an elevation angle at 4.0 degrees.

GROUND-BASED DOPPLAR LIDAR PROCESSING FLOW DIAGRAM

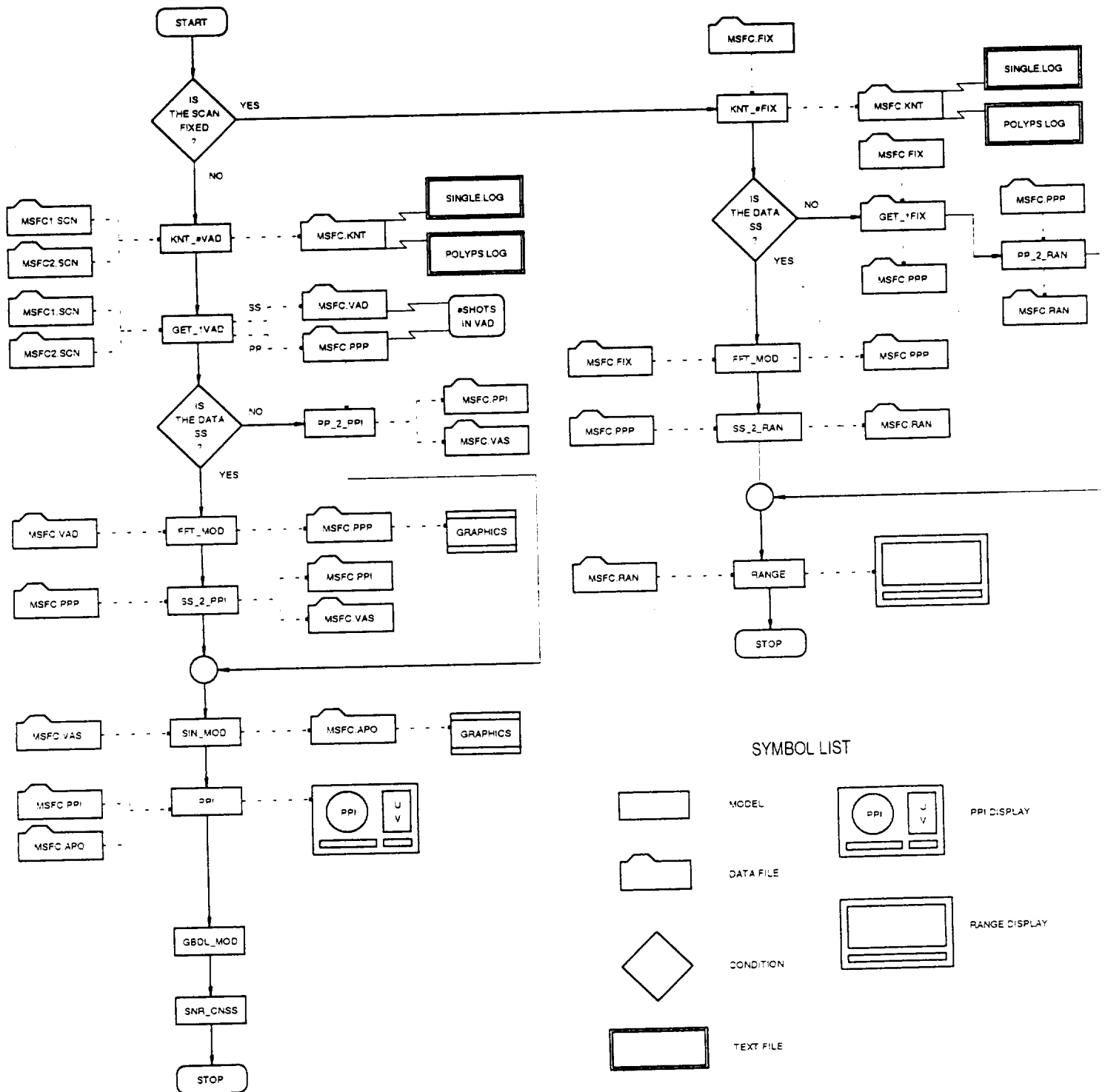


Figure D.1

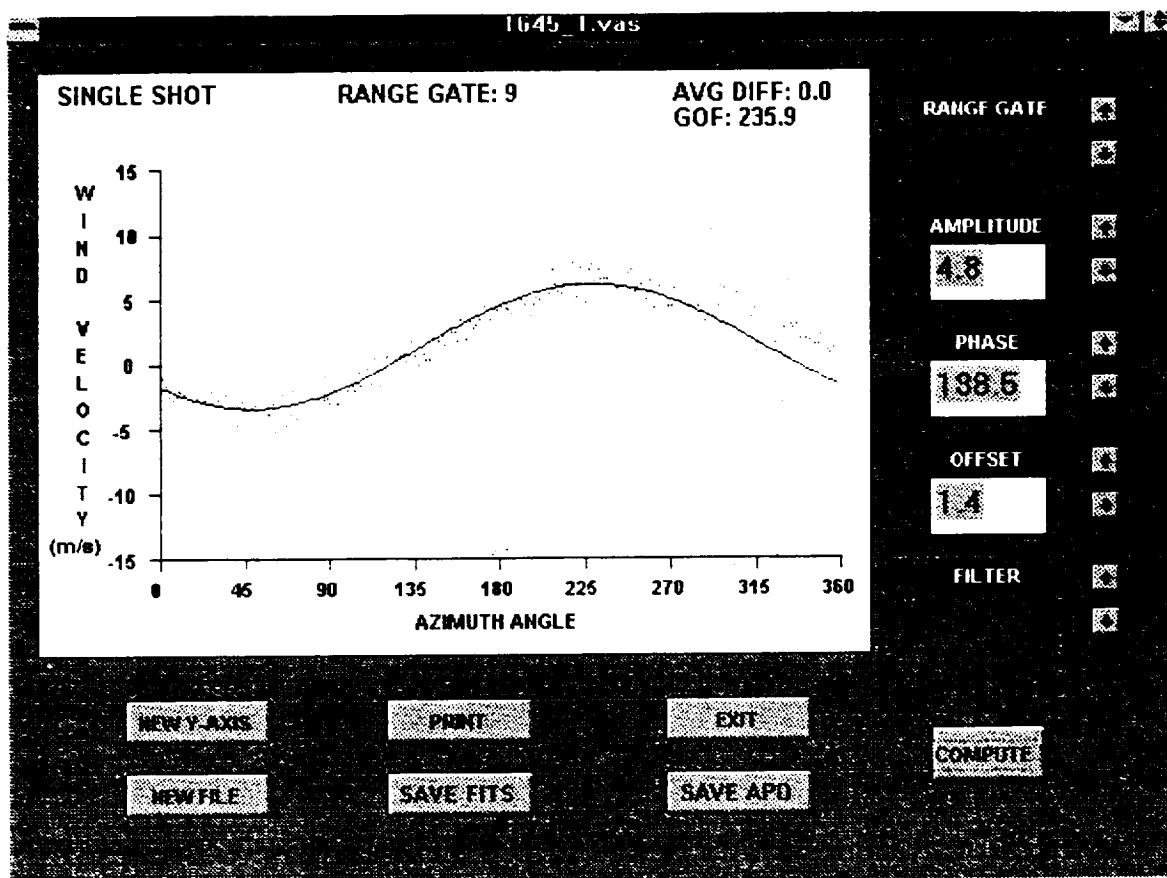


Figure D.2

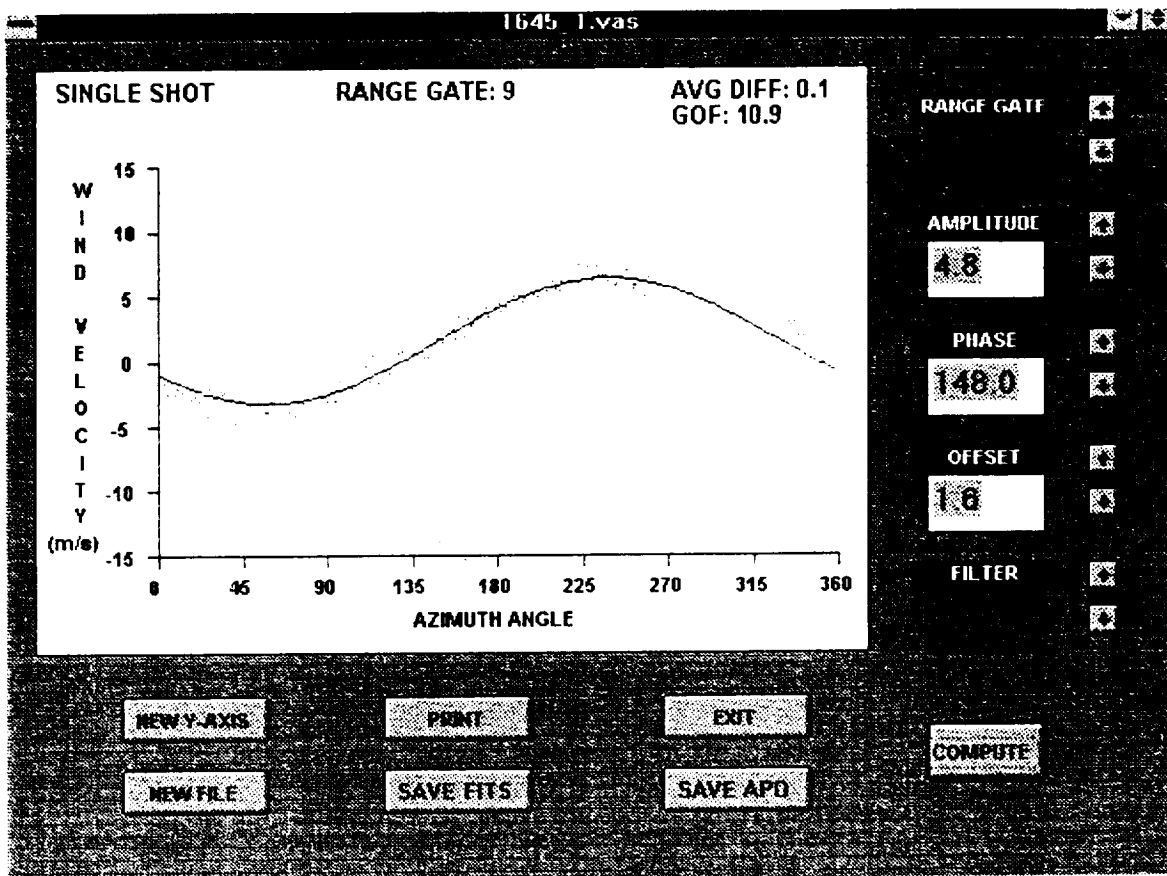


Figure D.3

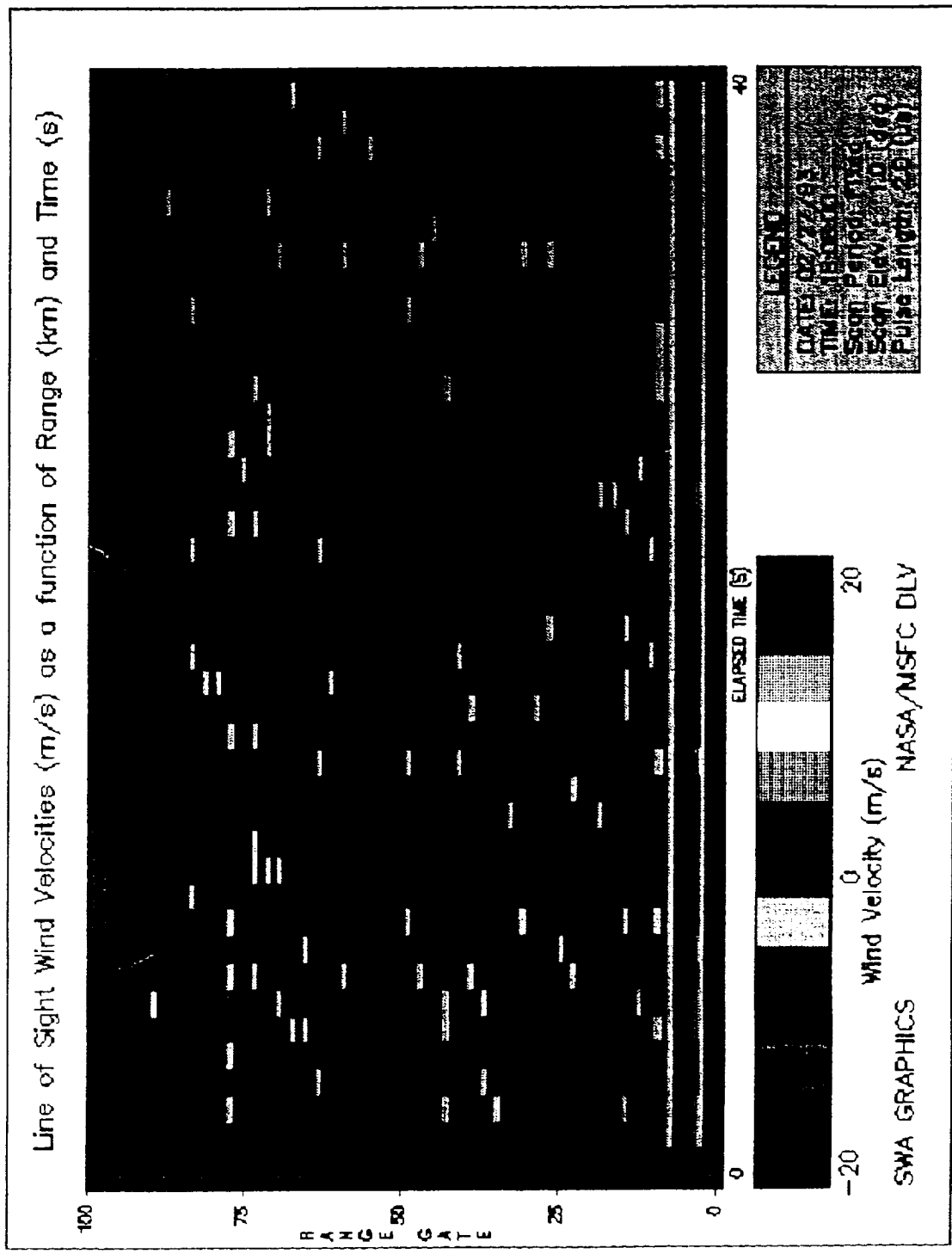


Figure D.4

LINE OF SIGHT VELOCITY FROM A STATIONARY TARGET

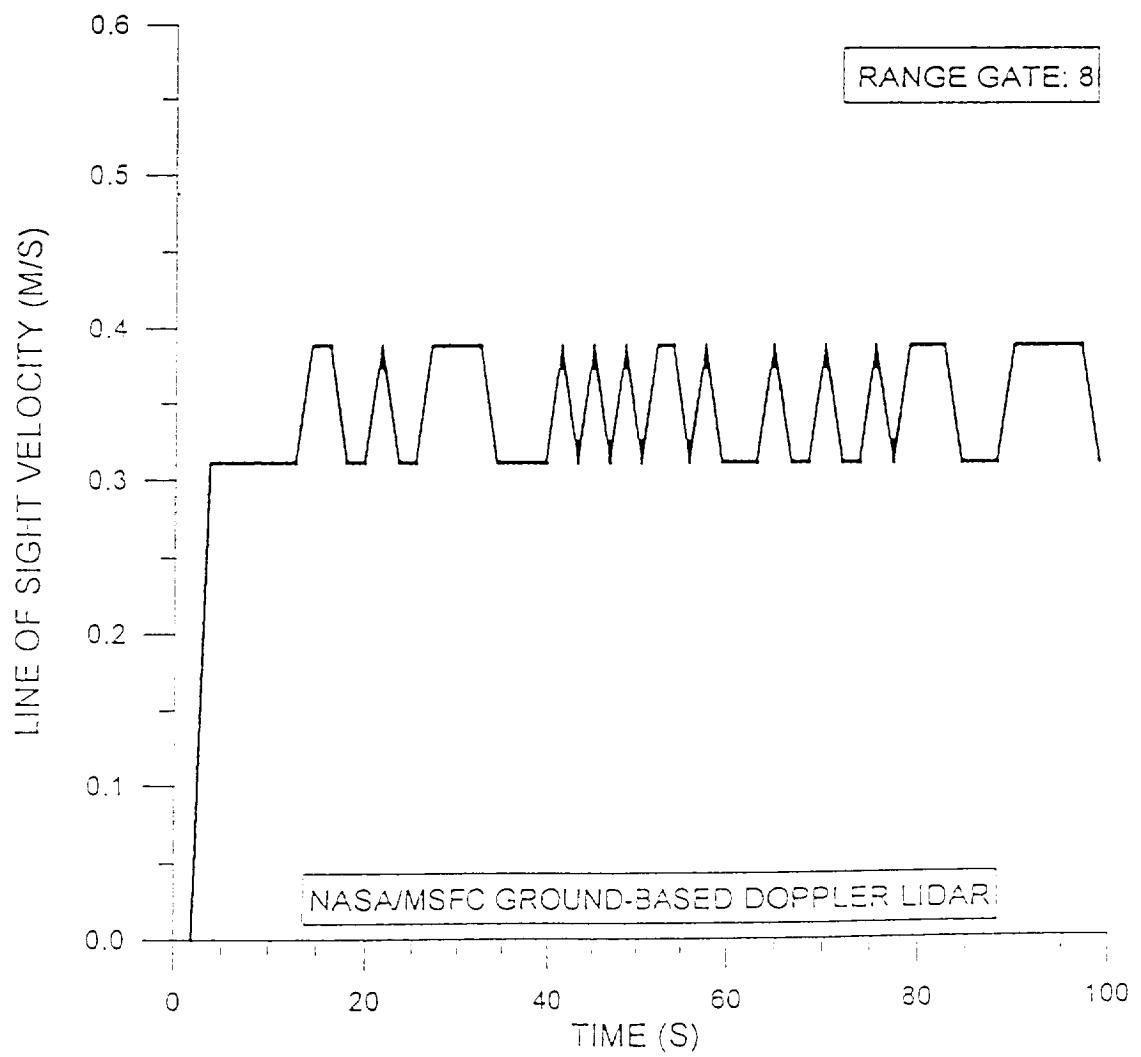


Figure D.5

Average Noise as a Function of Range Gate and Shot Number

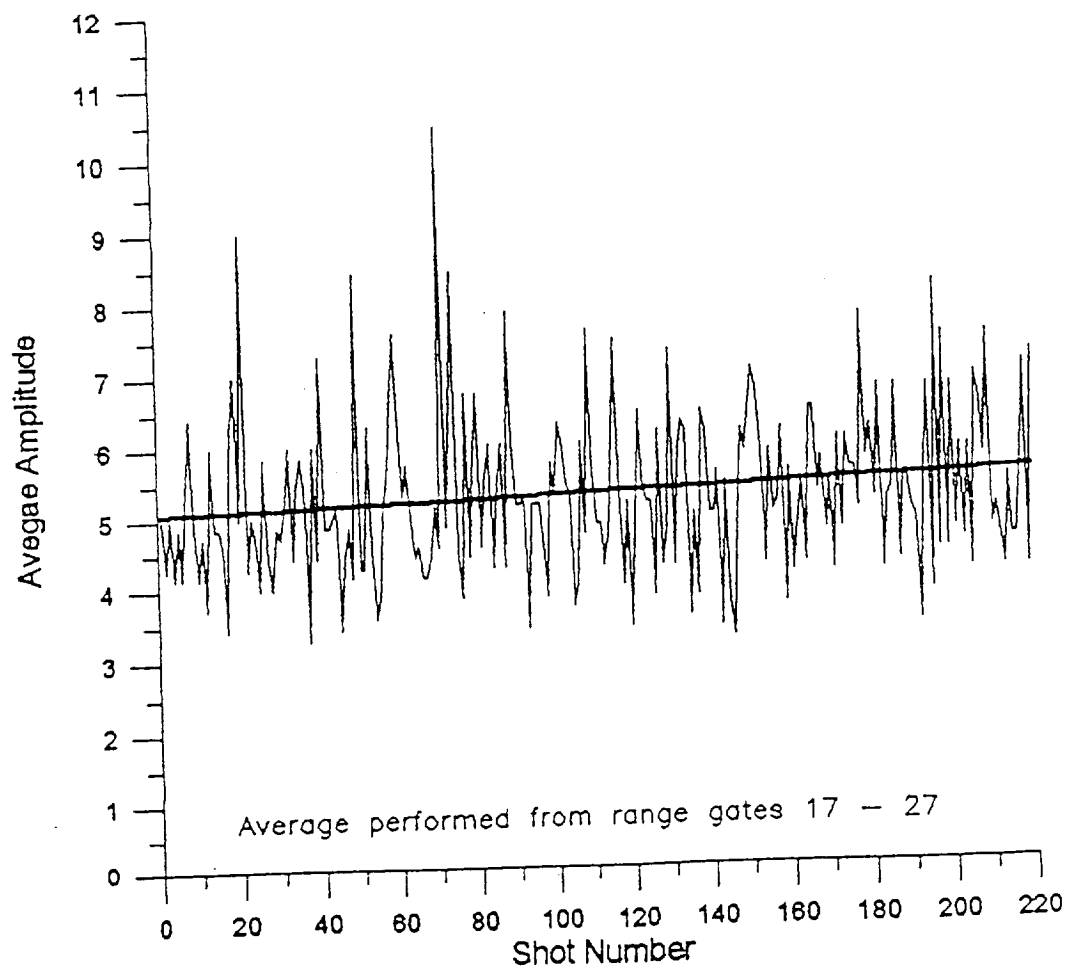
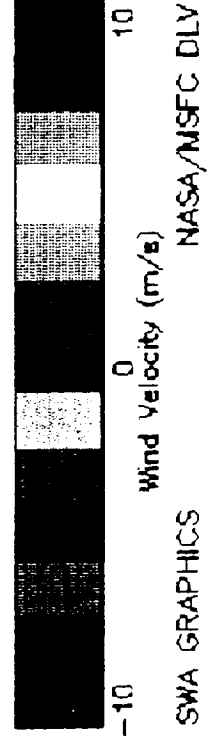
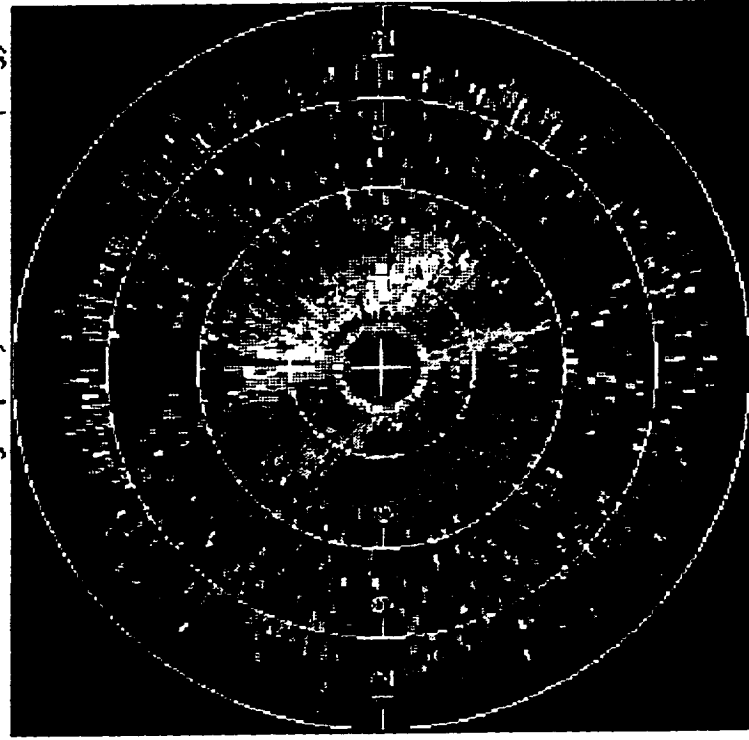


Figure D.6

Line of Sight Wind Velocities (m/s) as a Function of Range (km) and Azimuth (deg)



U and V Lidar Wind Components as a Function of Height (km)

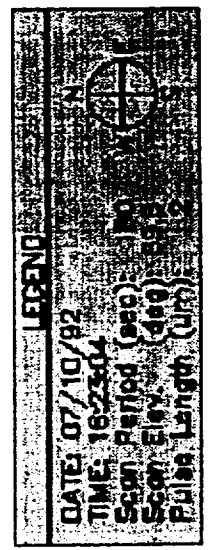
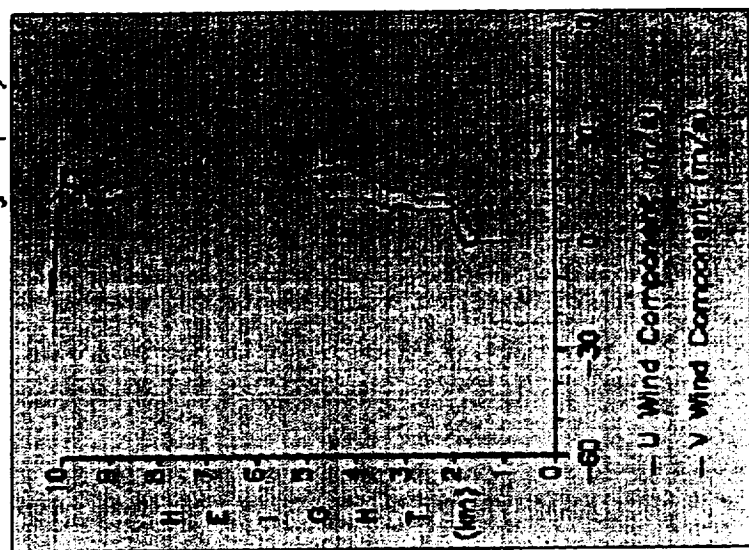


Figure D.7

Accuracy versus SNR

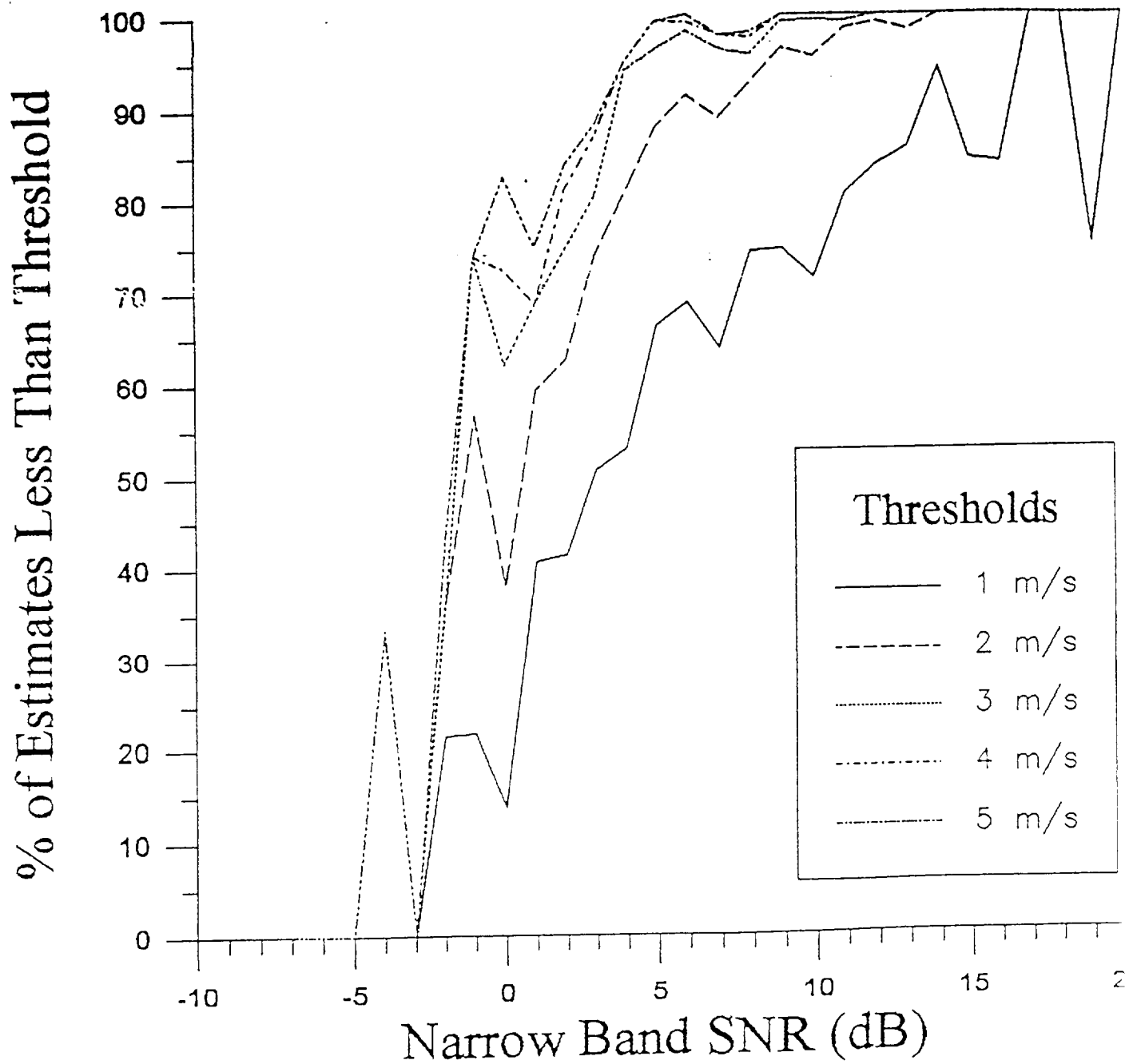


Figure D.8

SINE FIT TO NASA/MSFC GBDL DATA

1623-VAD1

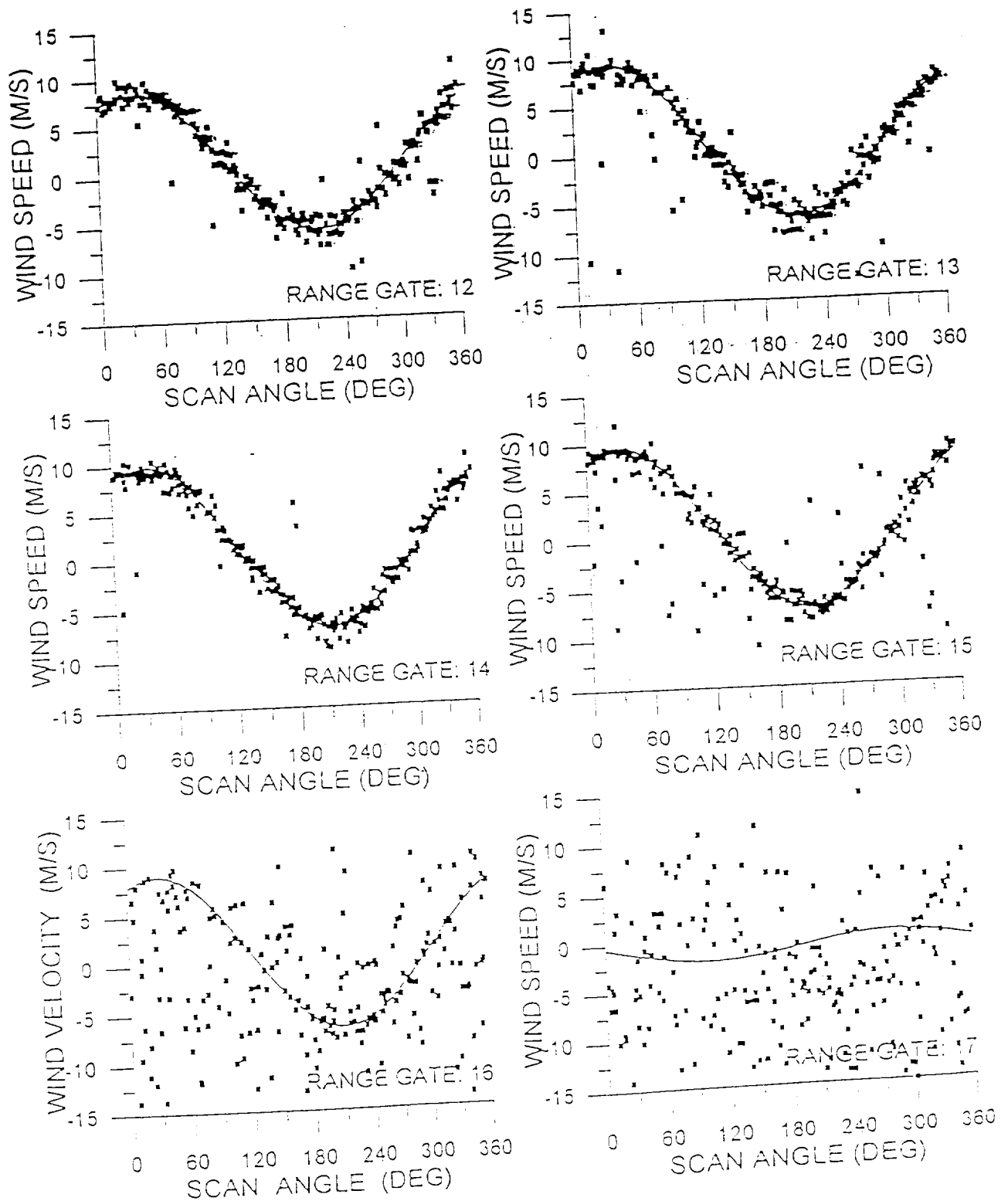


Figure D.9

SINE FIT TO NASA/MSFC GBDL DATA

1623-VAD1

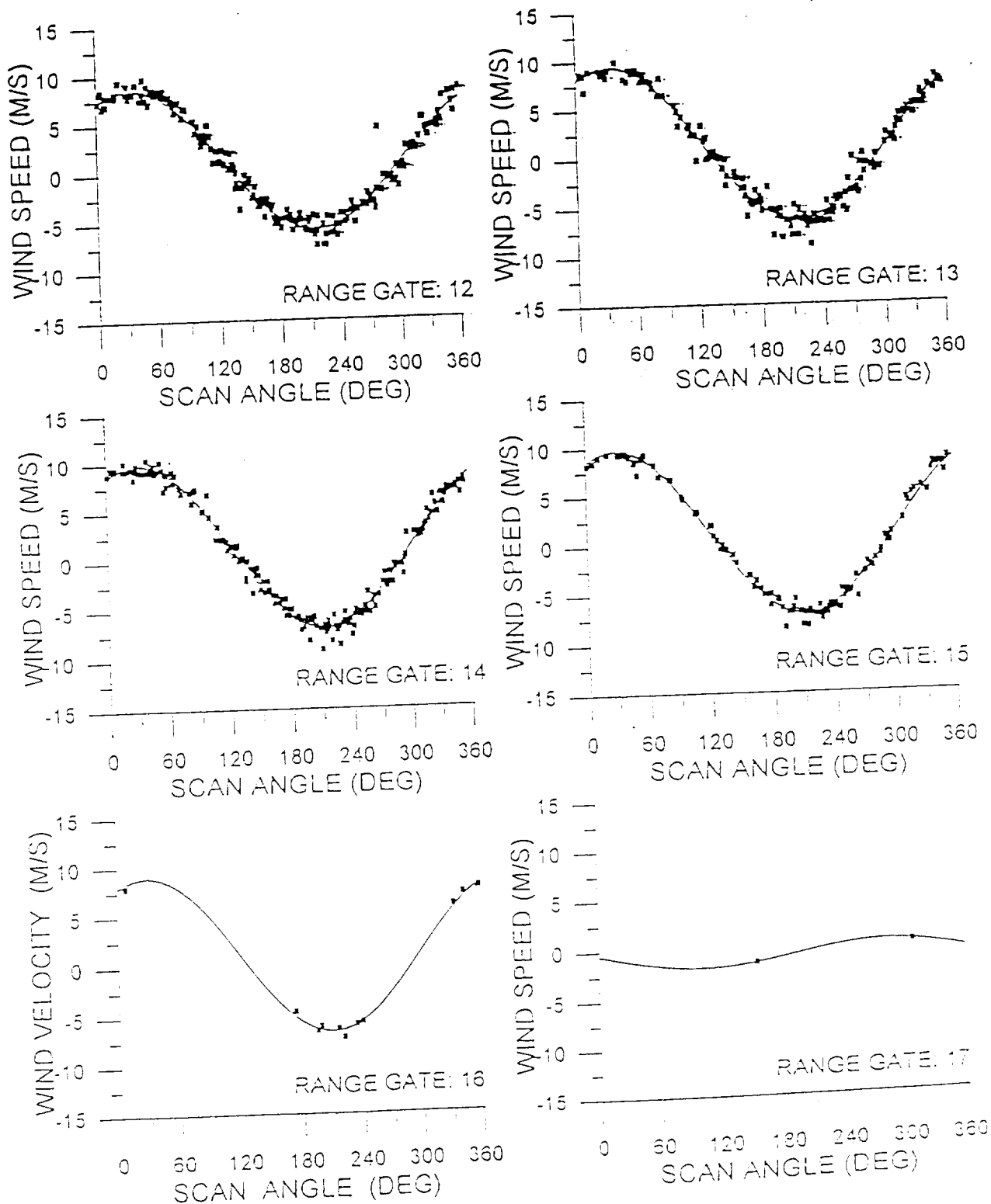
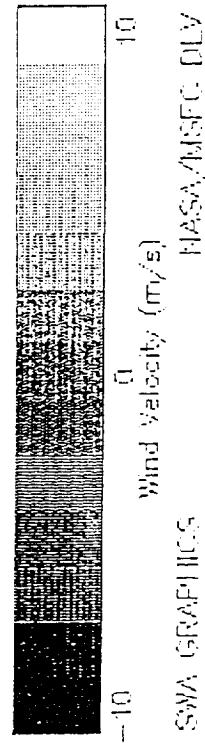
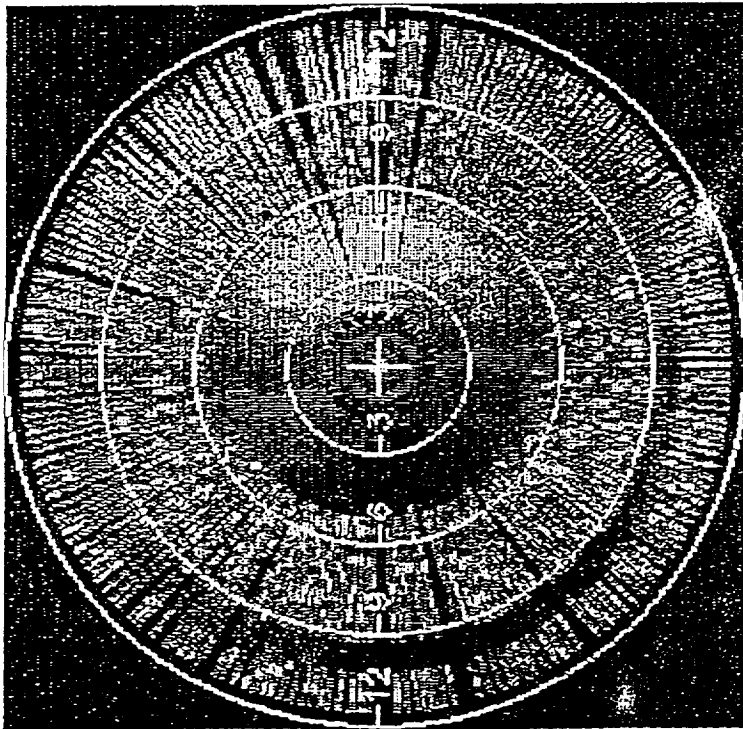


Figure D.10

Line of Sight Wind Velocities (m/s) as a Function of Range (km) and Azimuth (deg)



U and V Lidar Wind Components as a Function of Height (km)

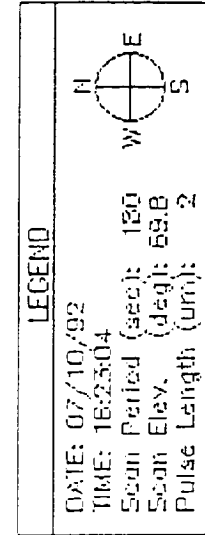
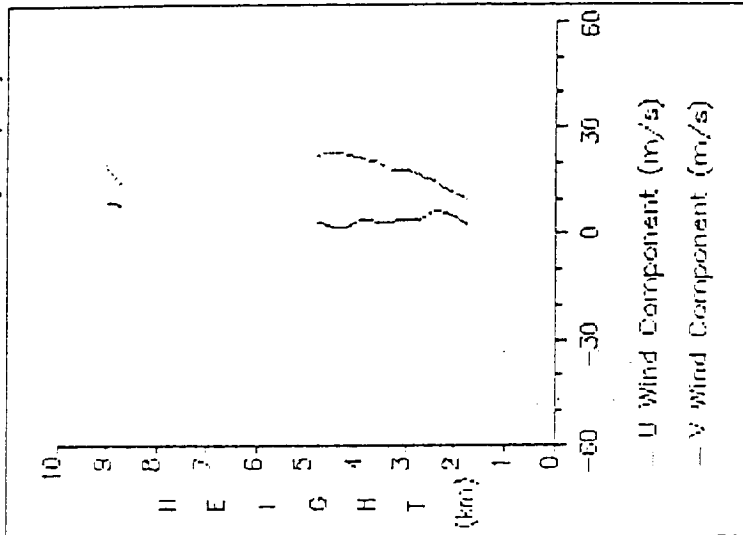


Figure D.11

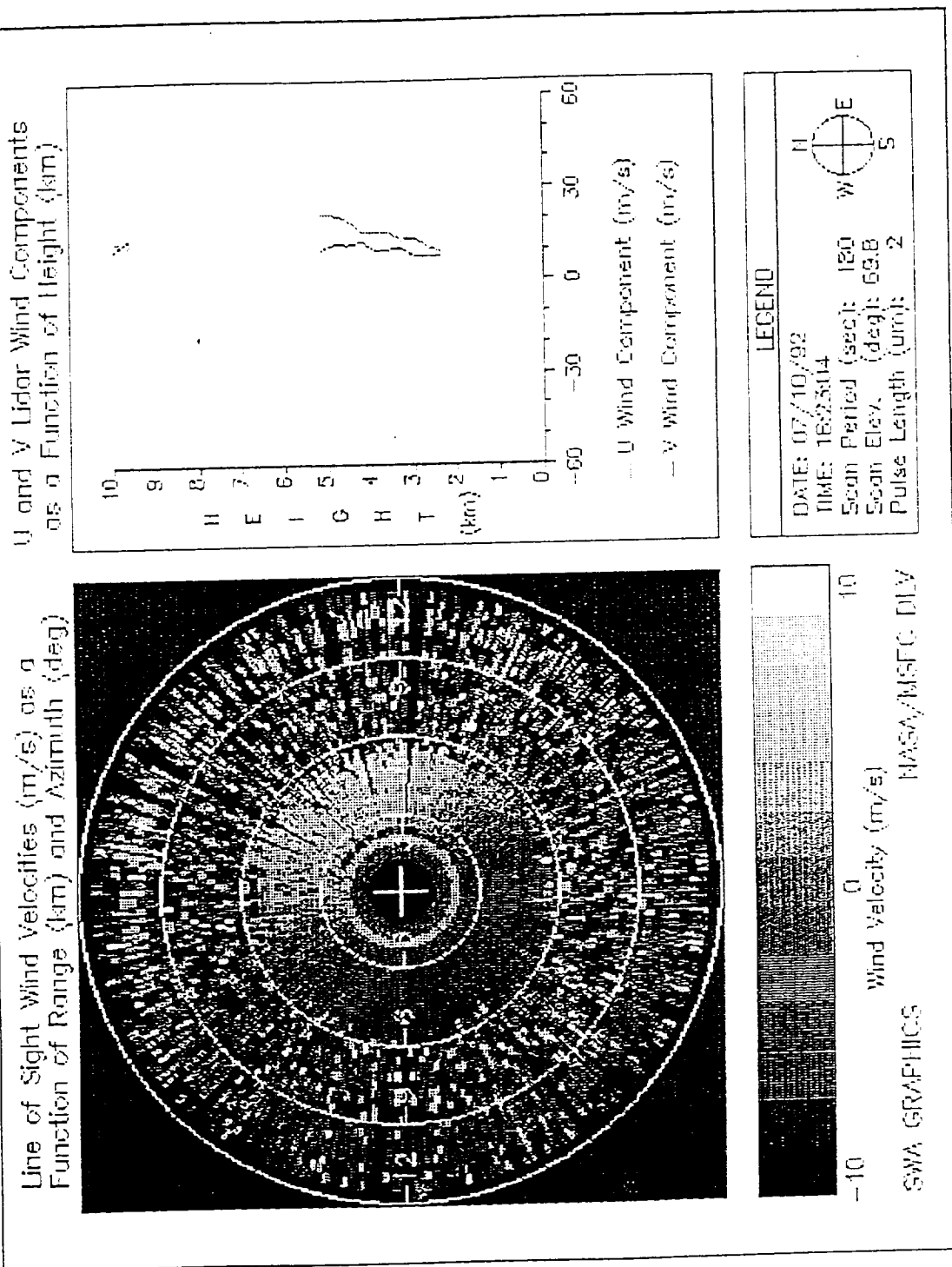


Figure D.12

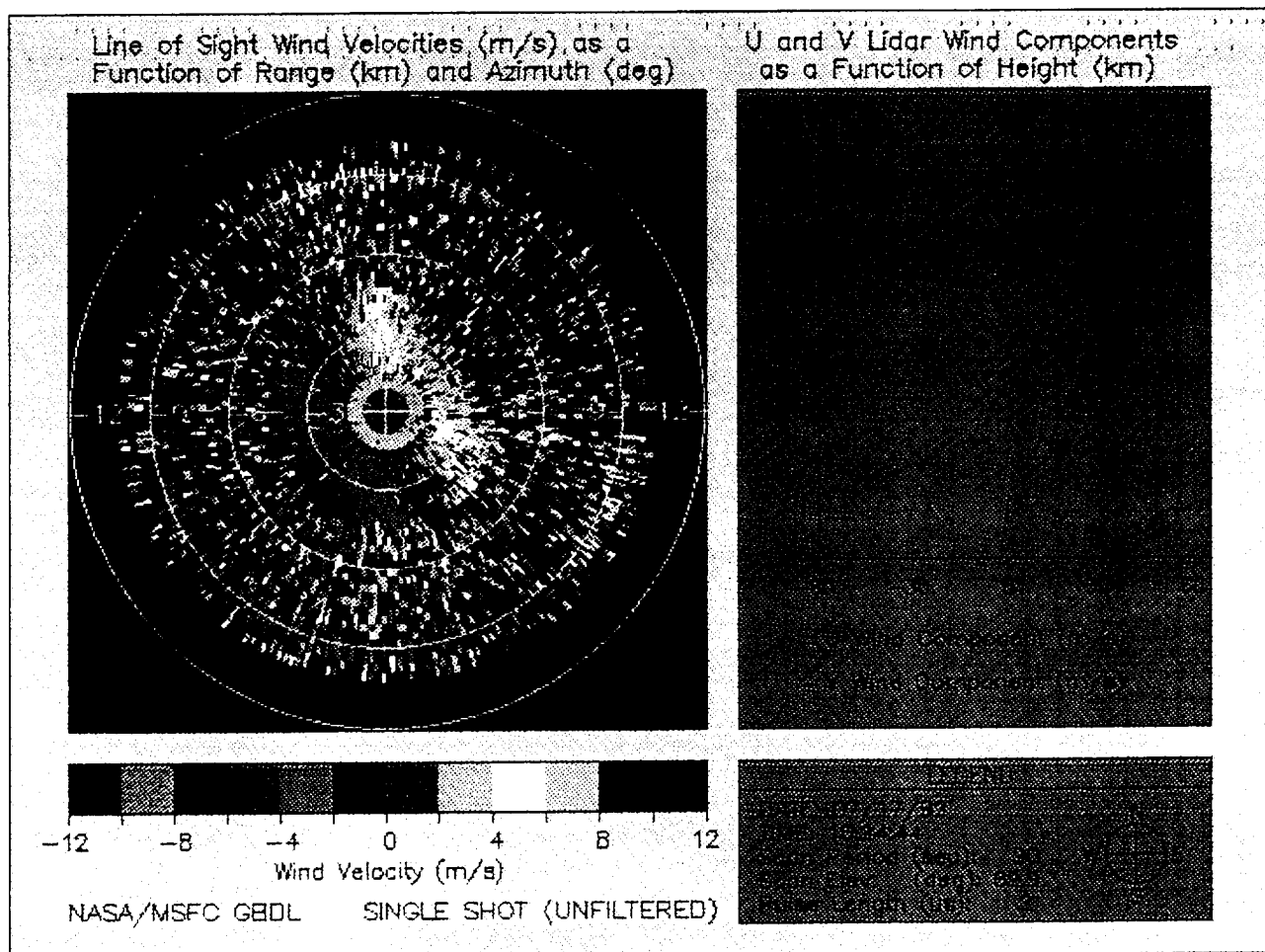


Figure D.13

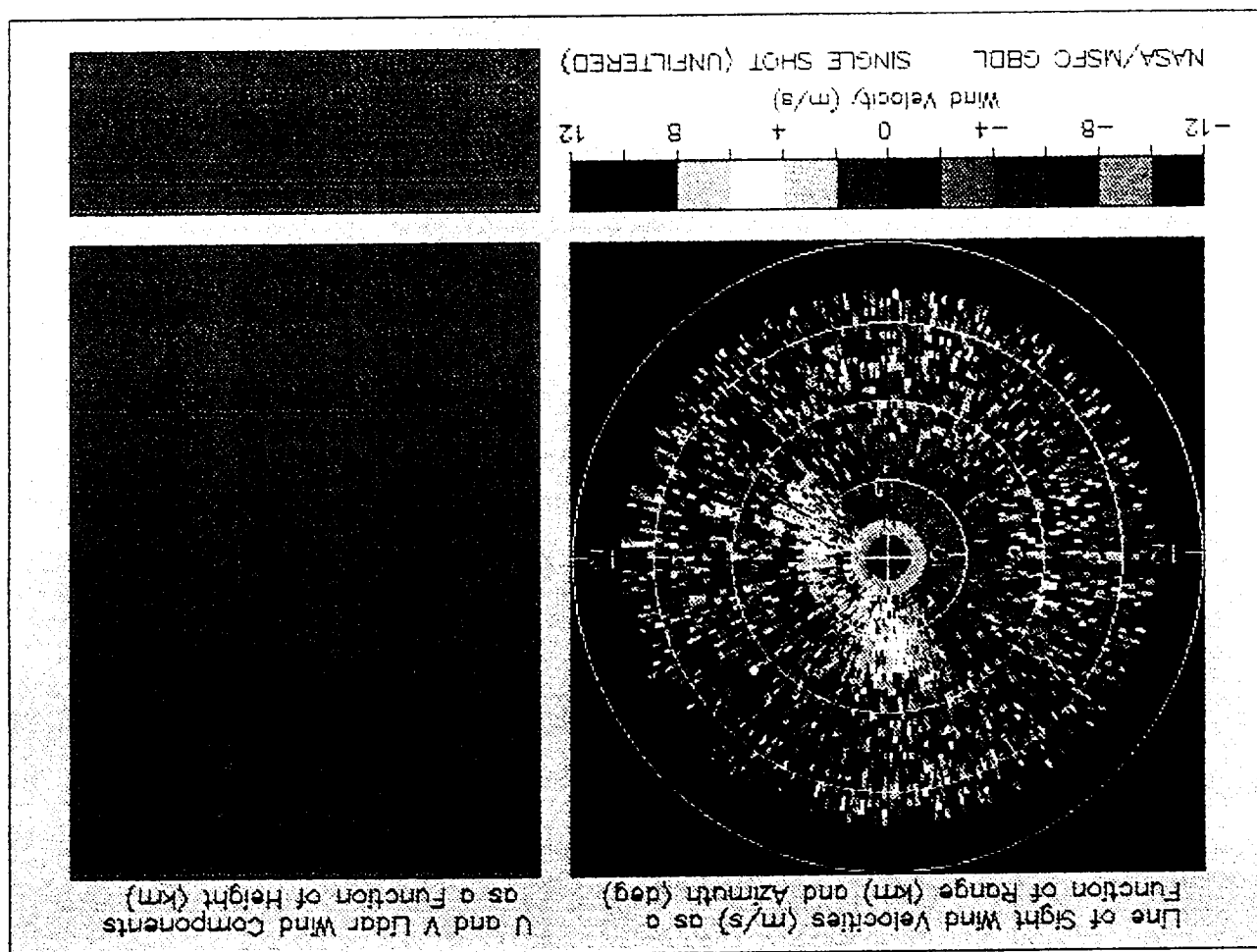


Figure D.14

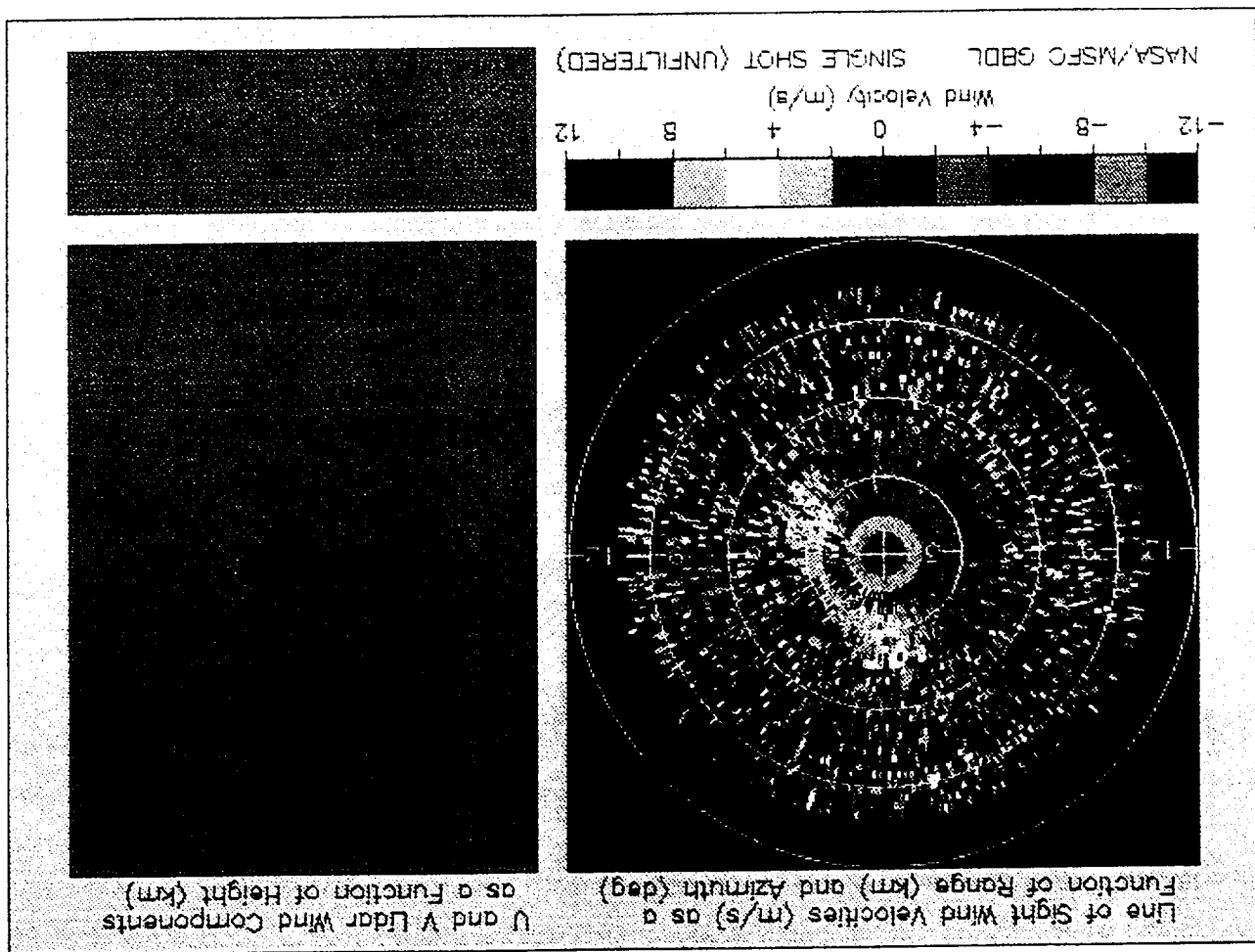


Figure D.15

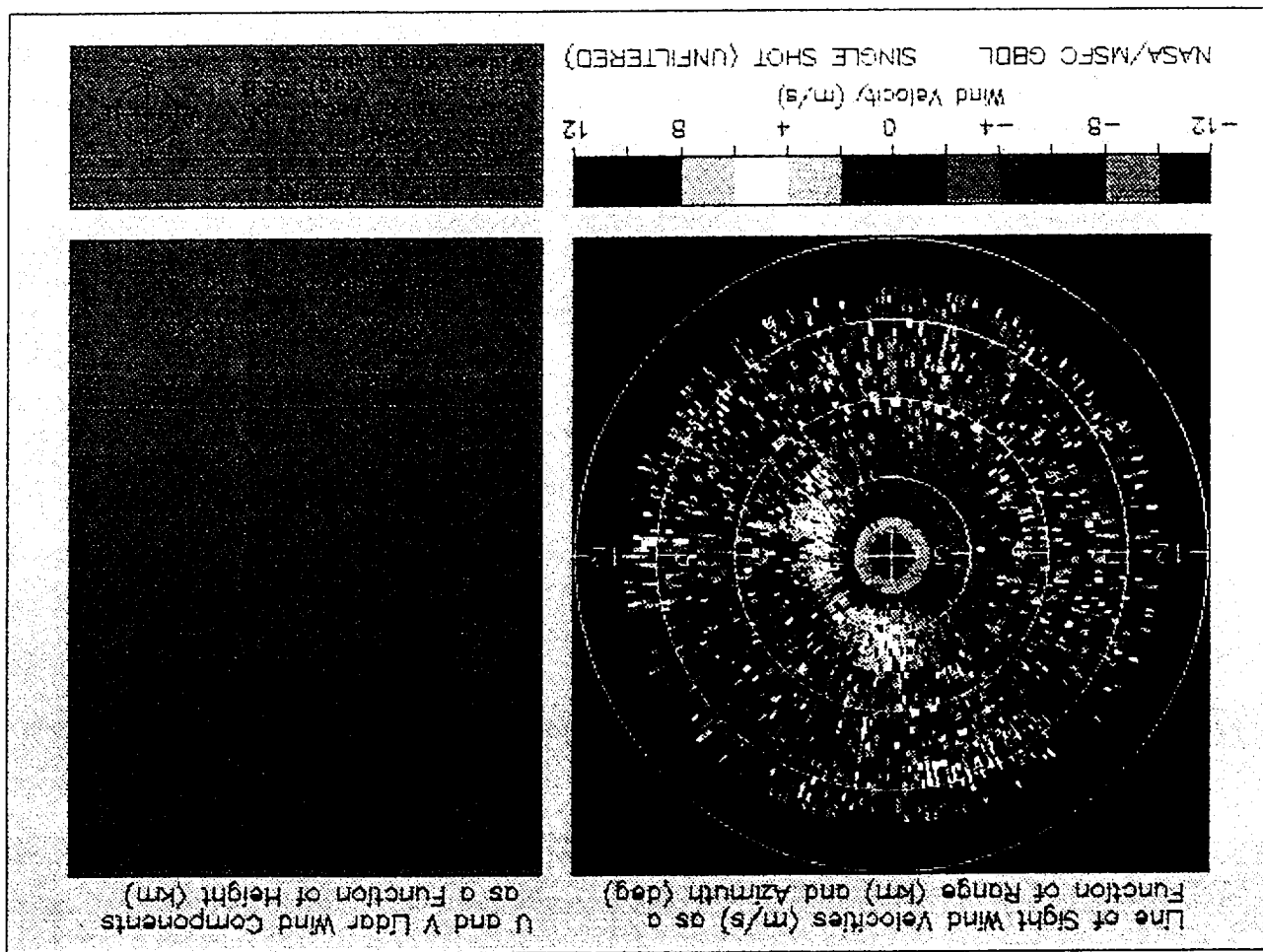


Figure D.16

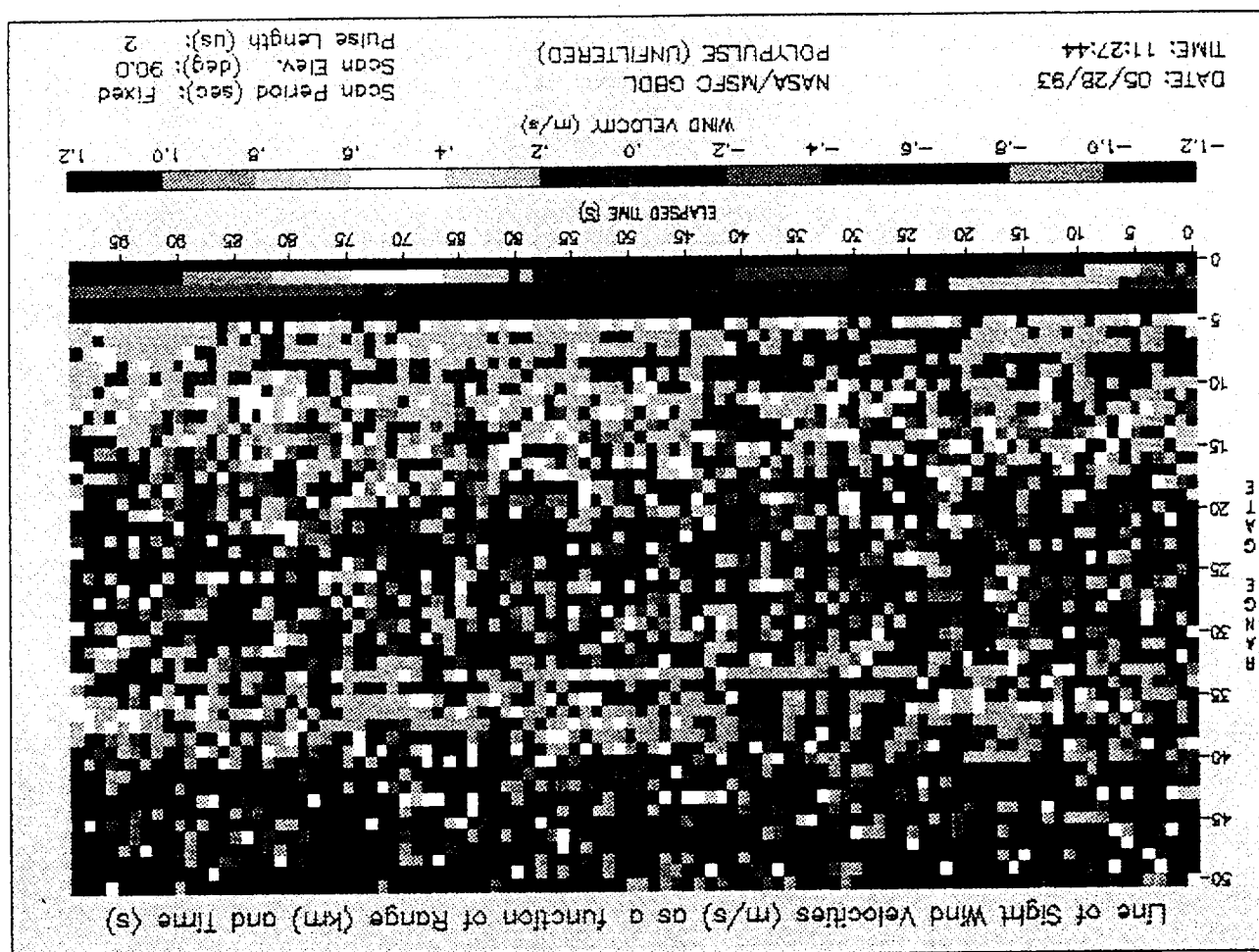


Figure D.17

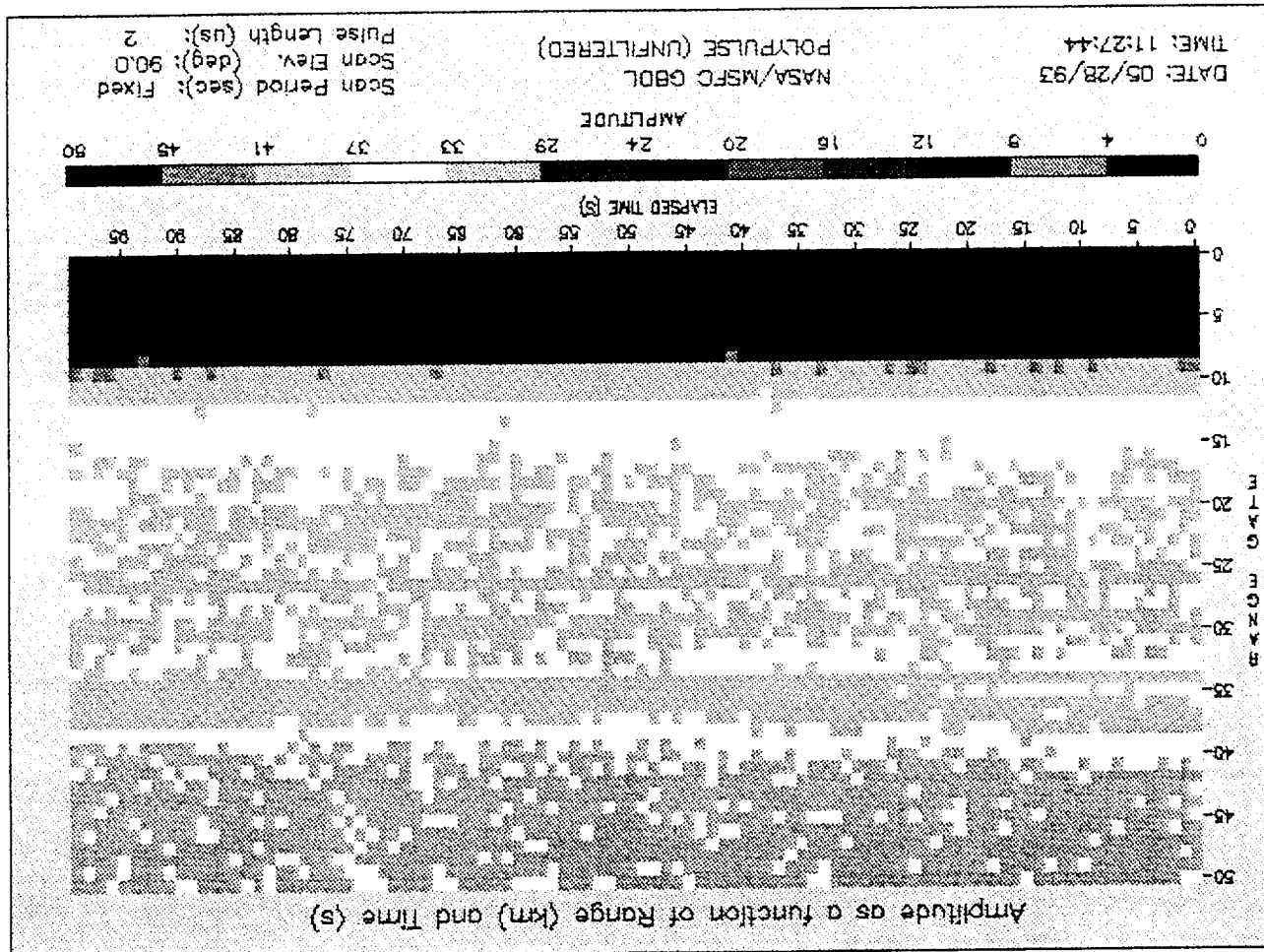


Figure D.18

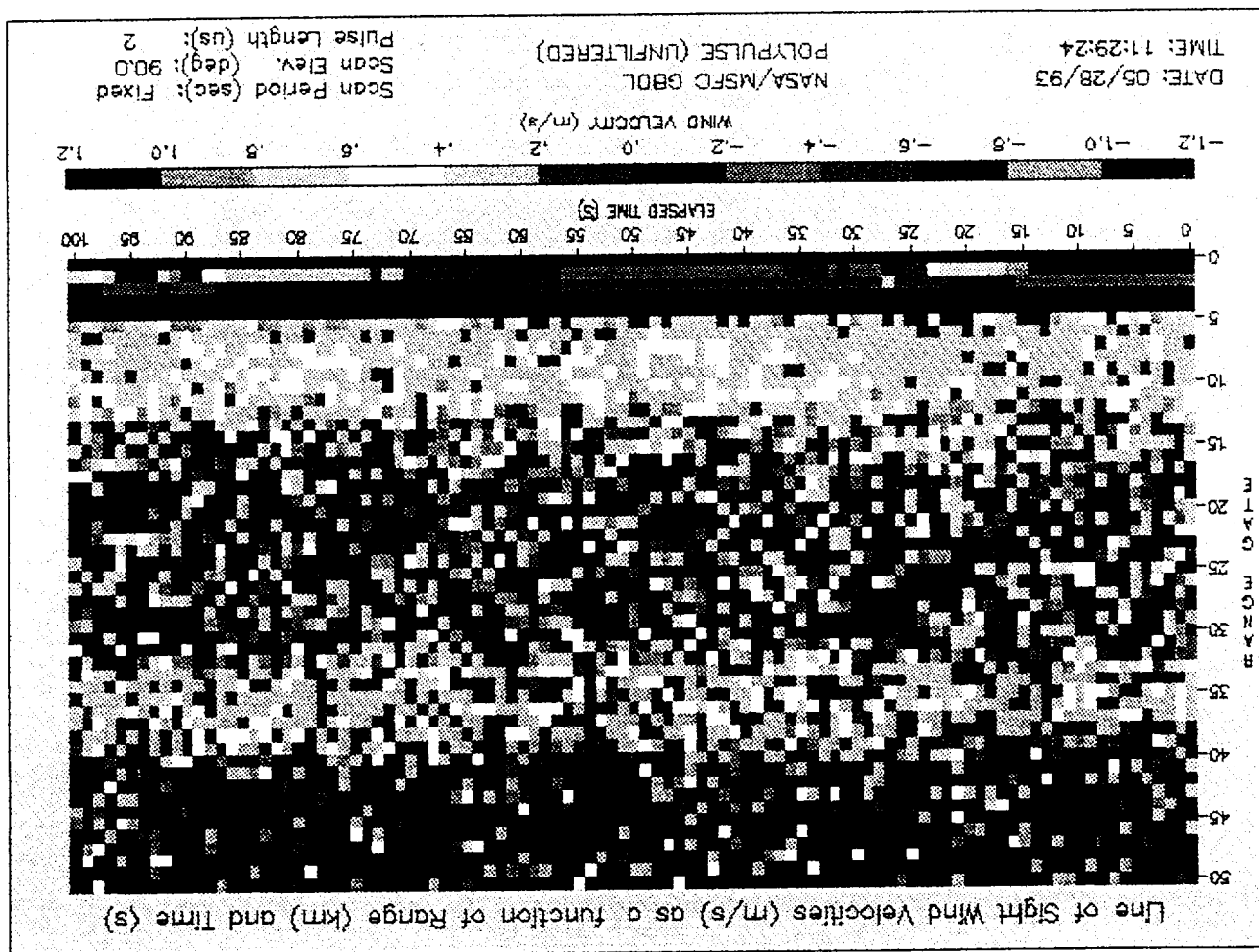


Figure D.19

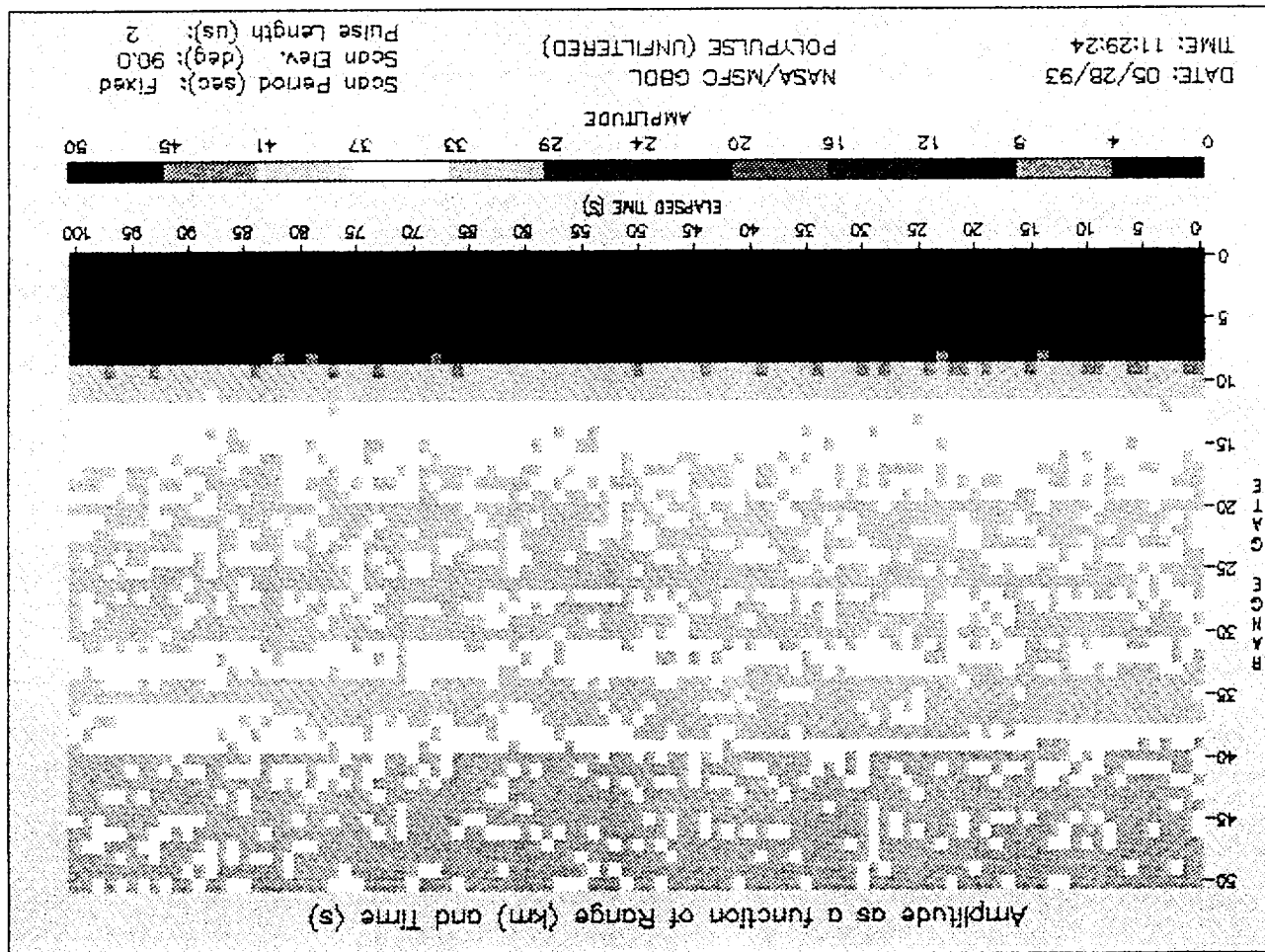


Figure D.20

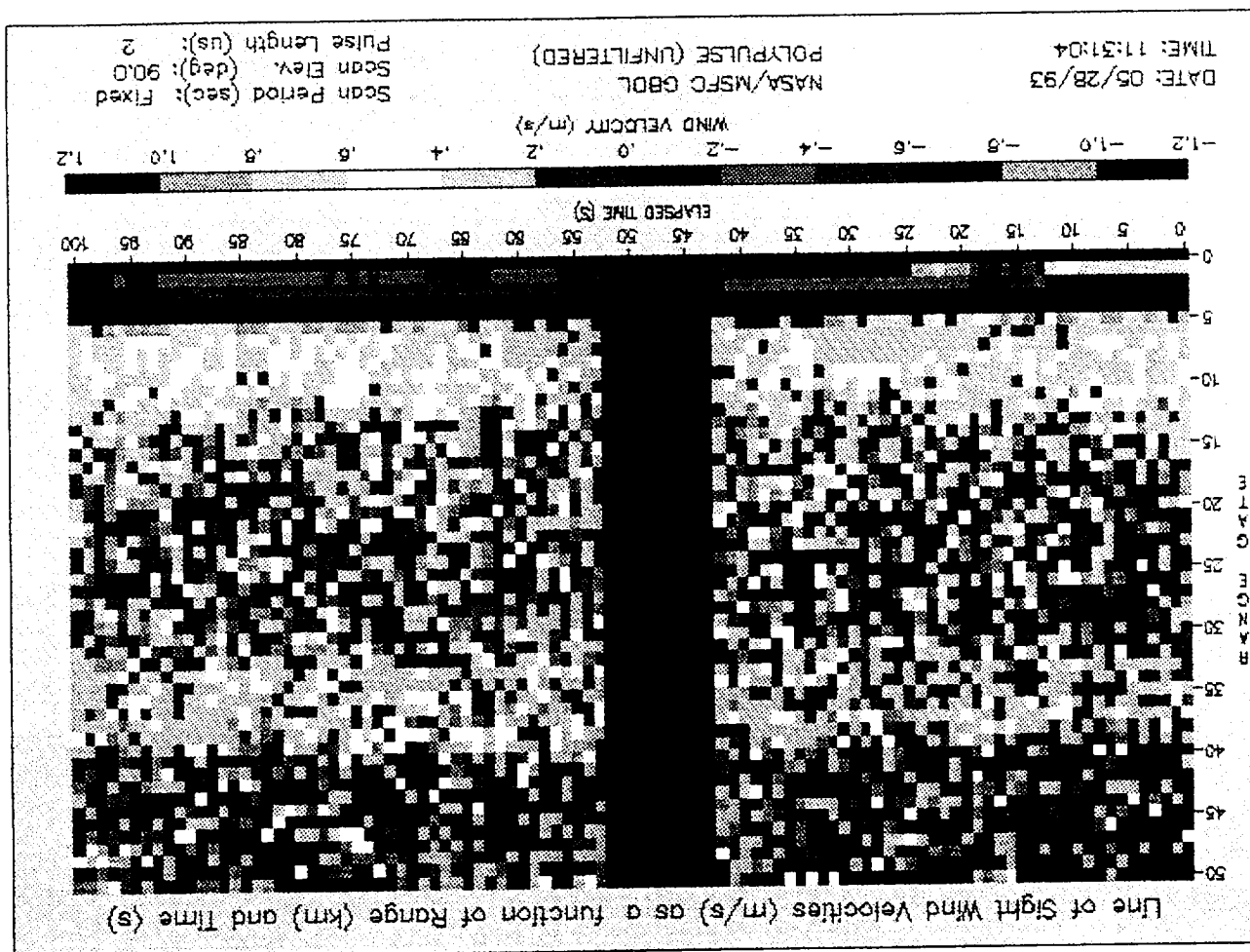


Figure D.21

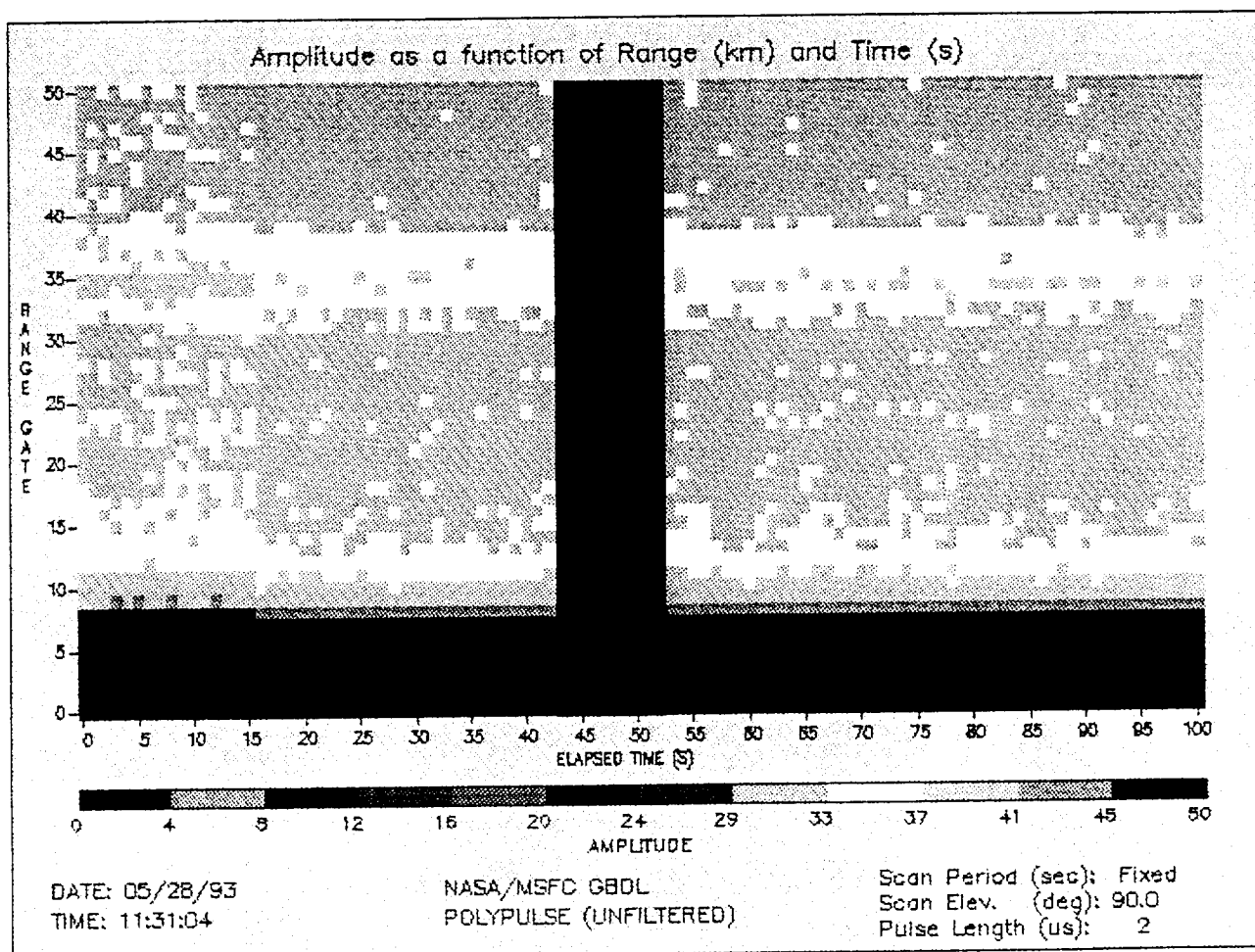


Figure D.22

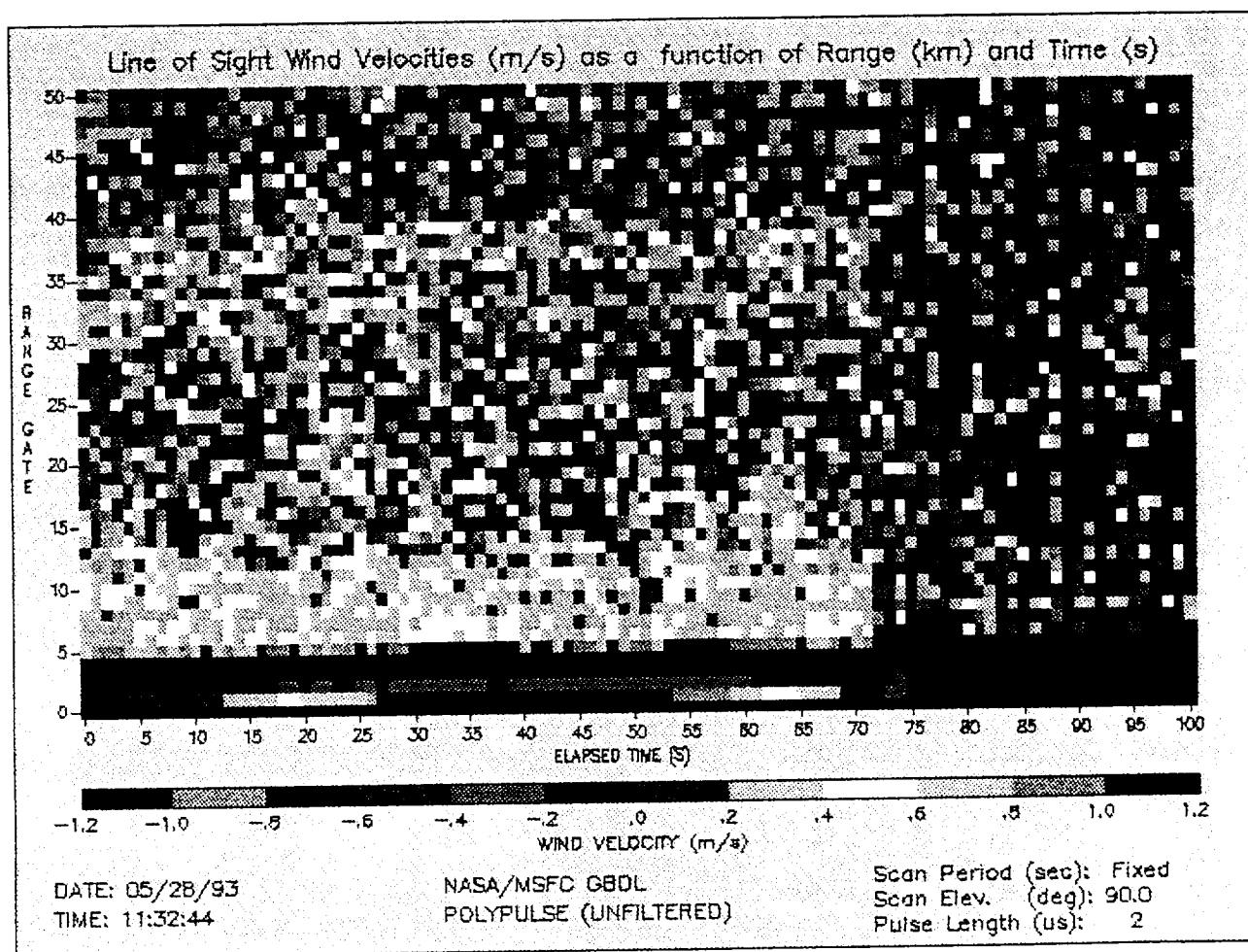


Figure D.23

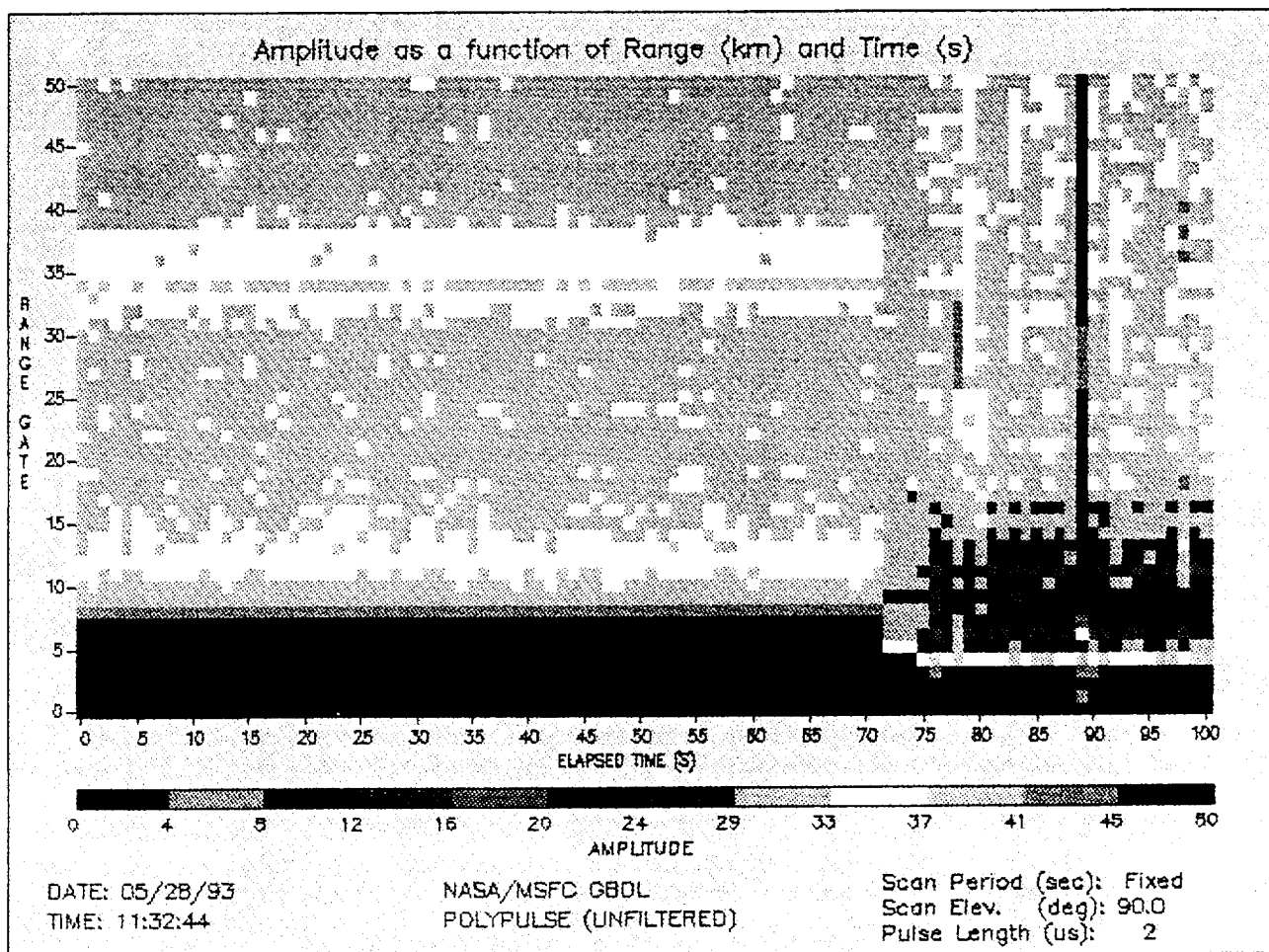


Figure D.24

AMPLITUDE AND LINE OF SIGHT WIND VELOCITY AS A FUNCTION OF TIME (POLYPULSE DATA)

SCAN PERIOD: FIXED
ELEVATION ANG.: 90 DEG

RANGE GATE: 36

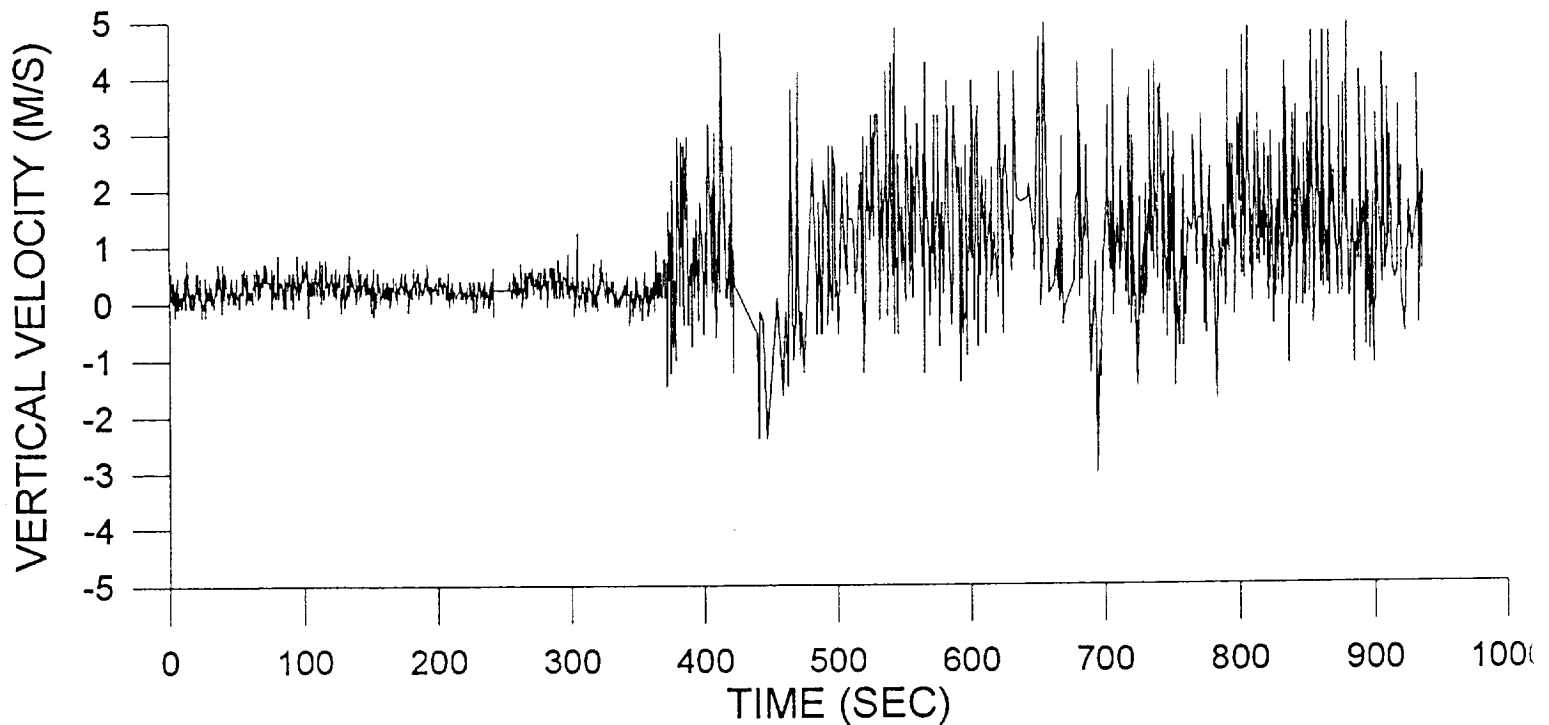
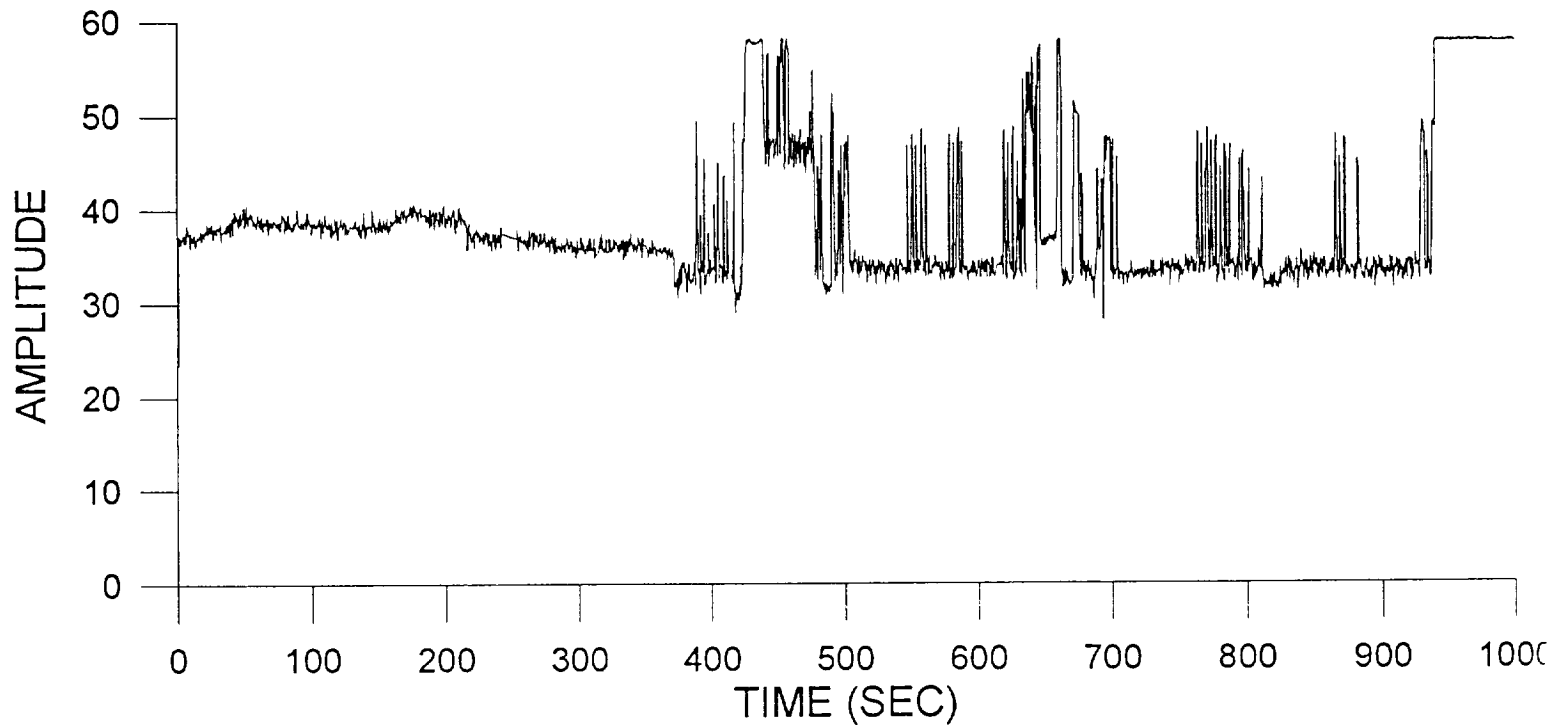


Figure D.25

Line of Sight Wind Velocities (m/s) as a function of Range (km) and Time (s)

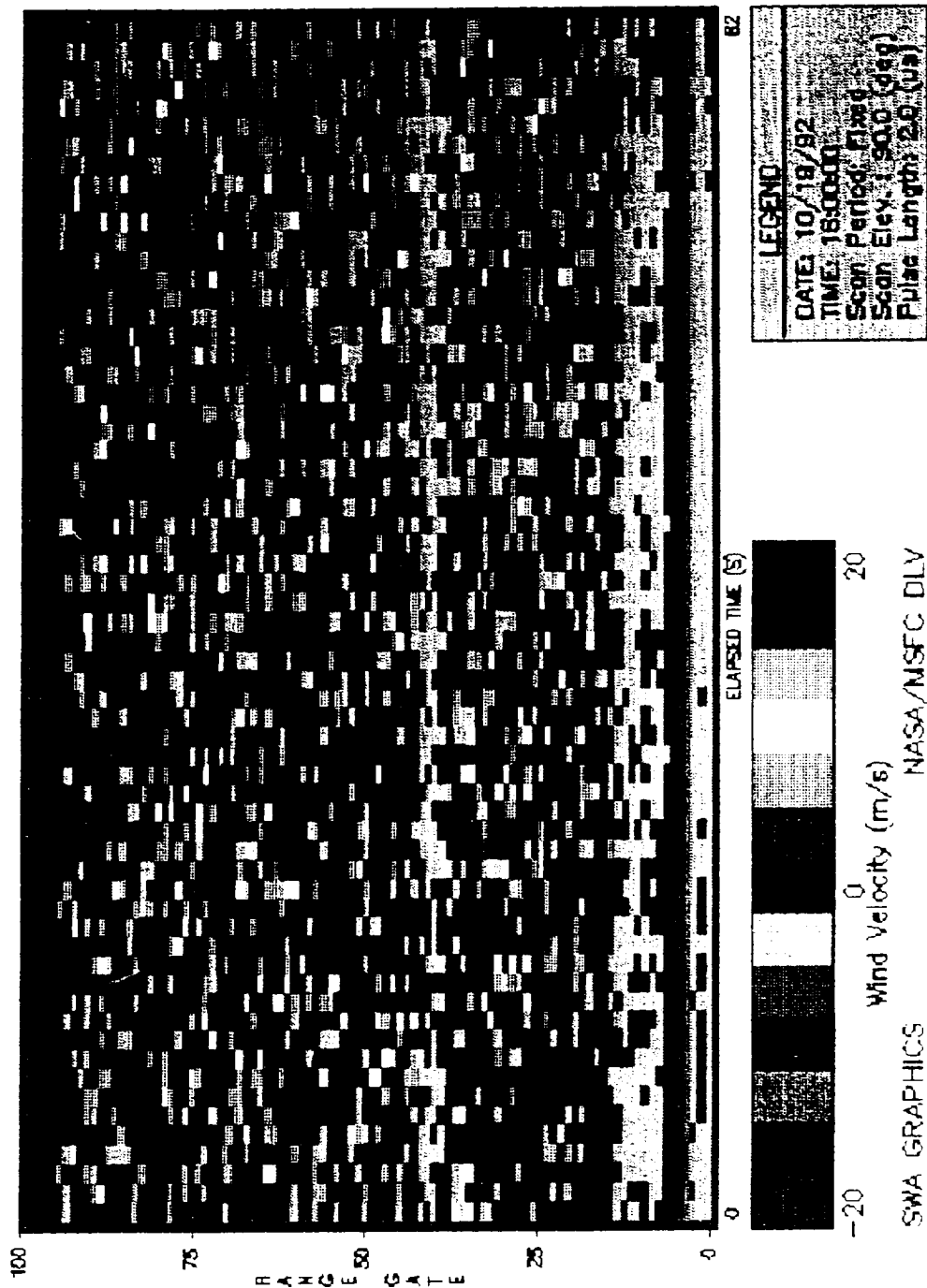


Figure D.26

CIRRUS CLOUD VERTICAL WIND SPEEDS

TIME: 1600 Z

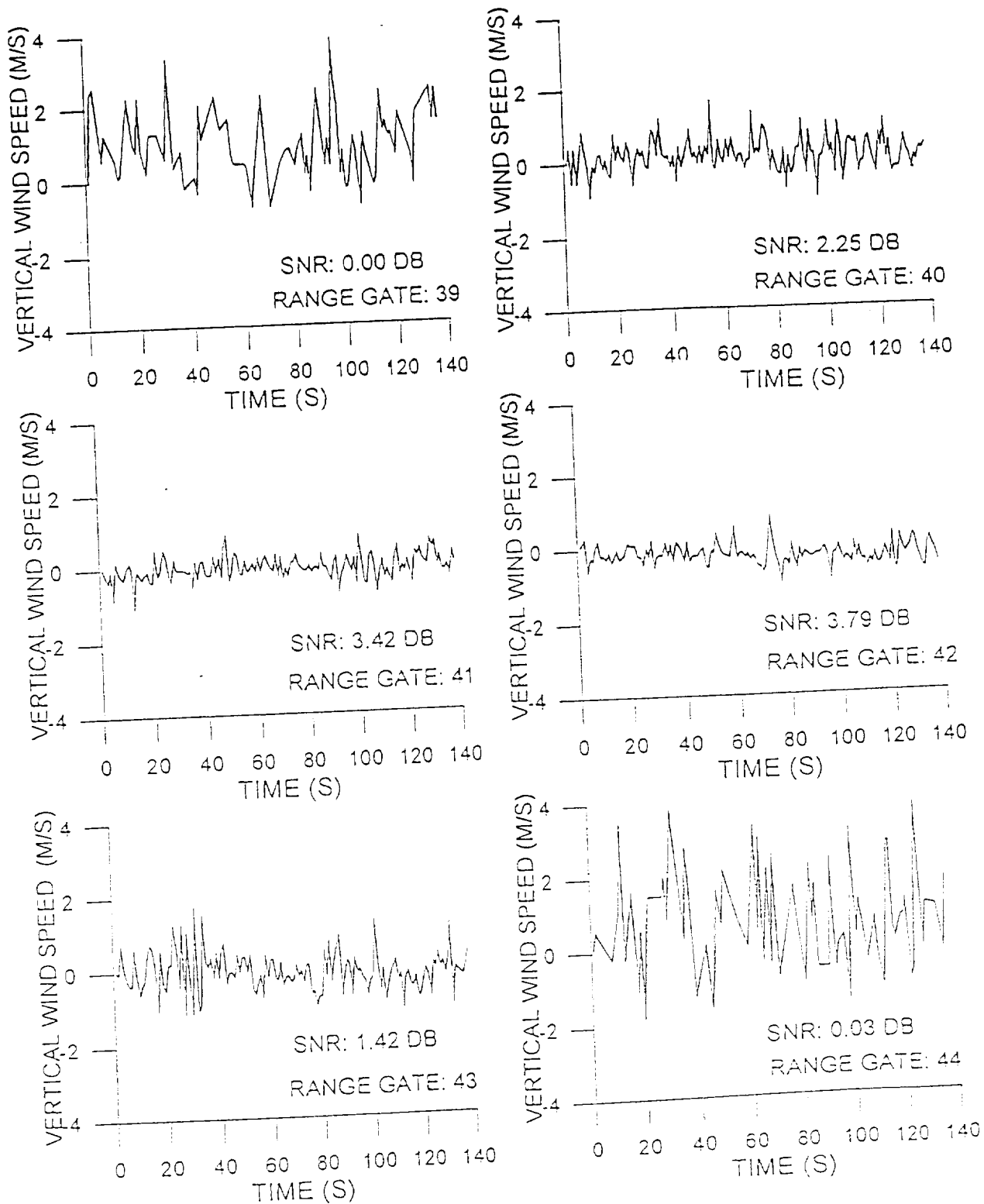


Figure D.27

MID-TROPOSPHERIC VERTICAL WIND SPEED

TIME: 1600 Z

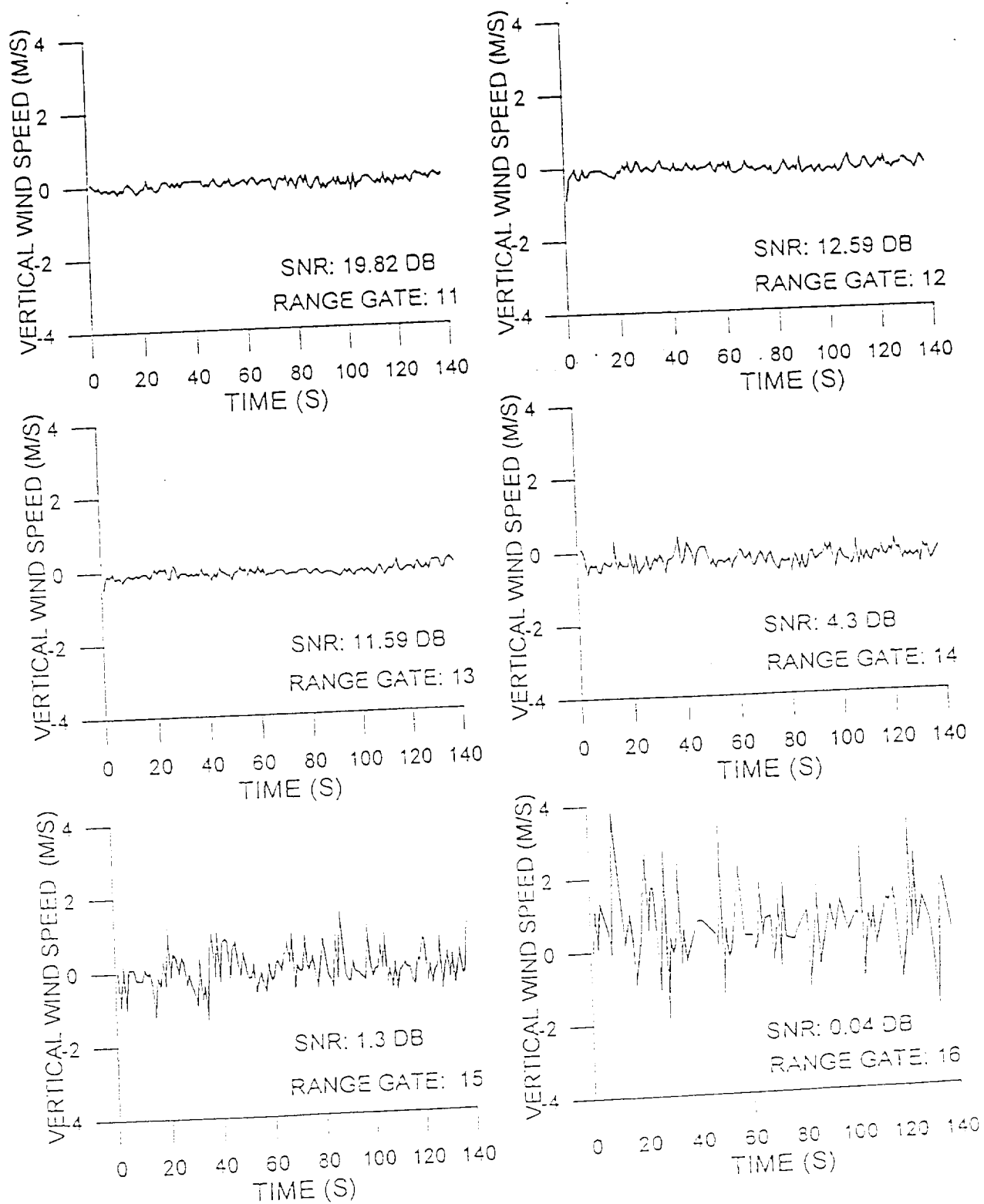


Figure D.28

NASA MSFC GROUND-BASED DOPPLER LIDAR ERRORS RANGE GATES: 8-14

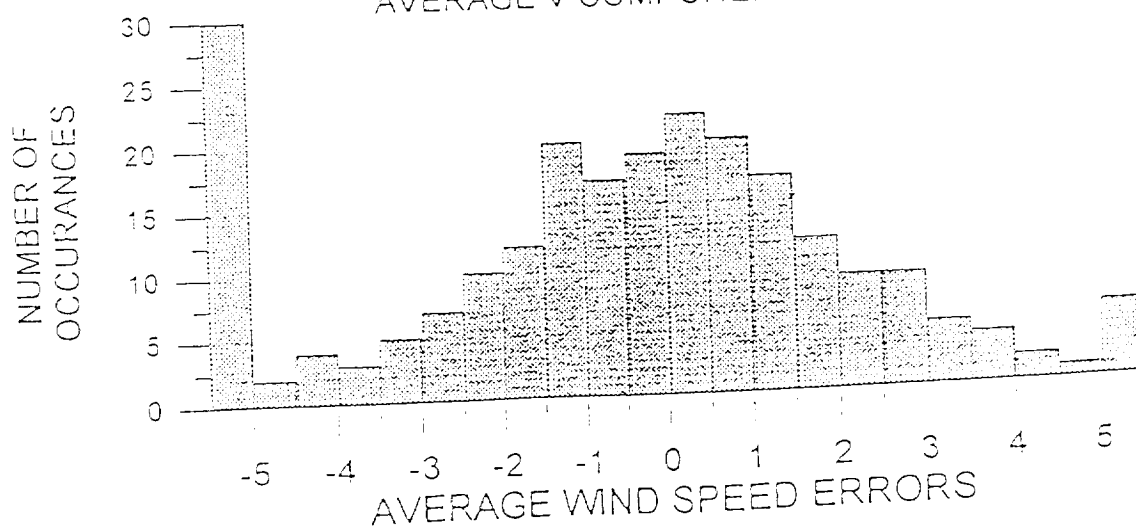
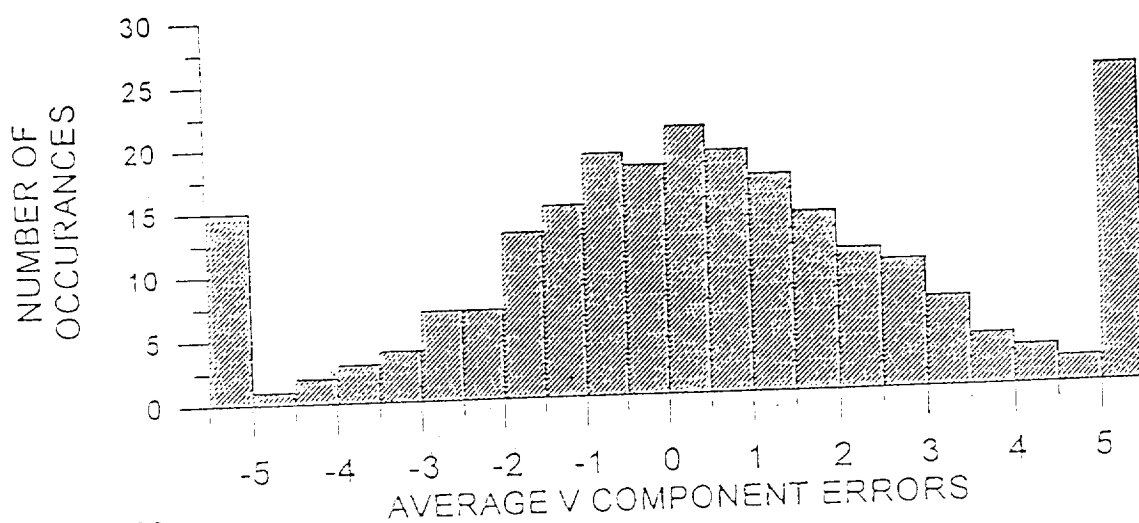
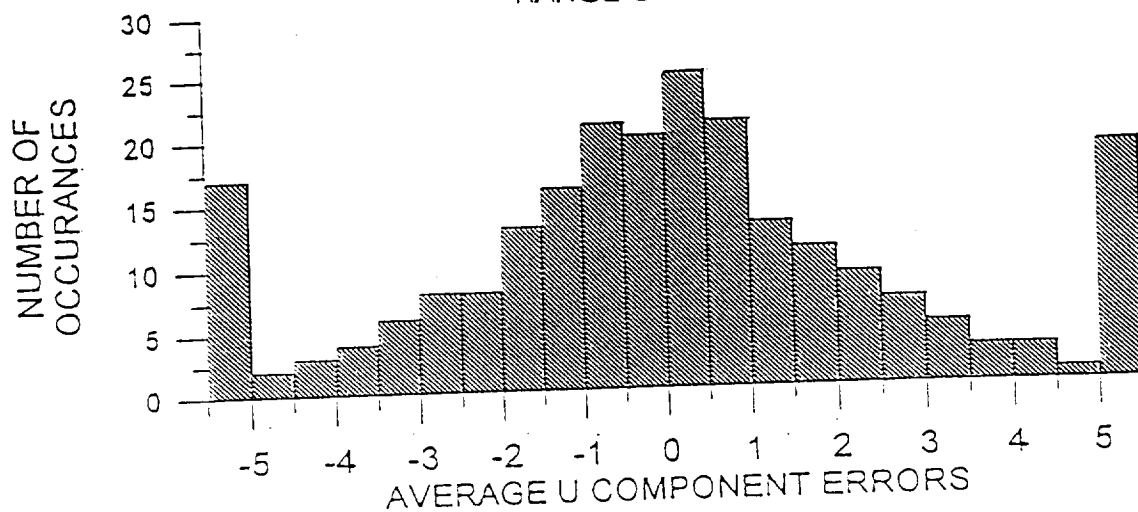


Figure D.29

NASA MSFC GROUND-BASED DOPPLER LIDAR ERRORS RANGE GATES: 30-31 FILTERED

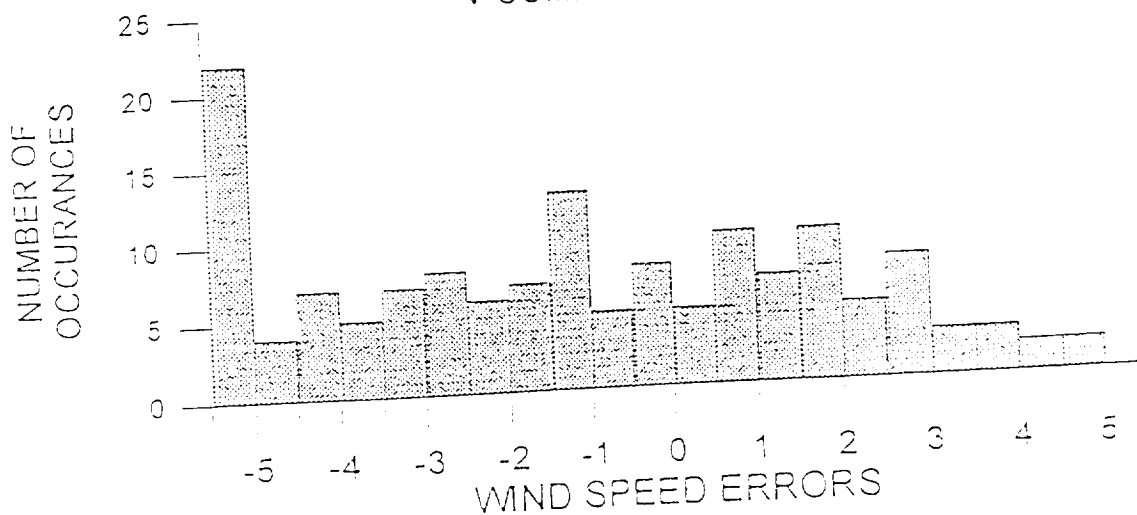
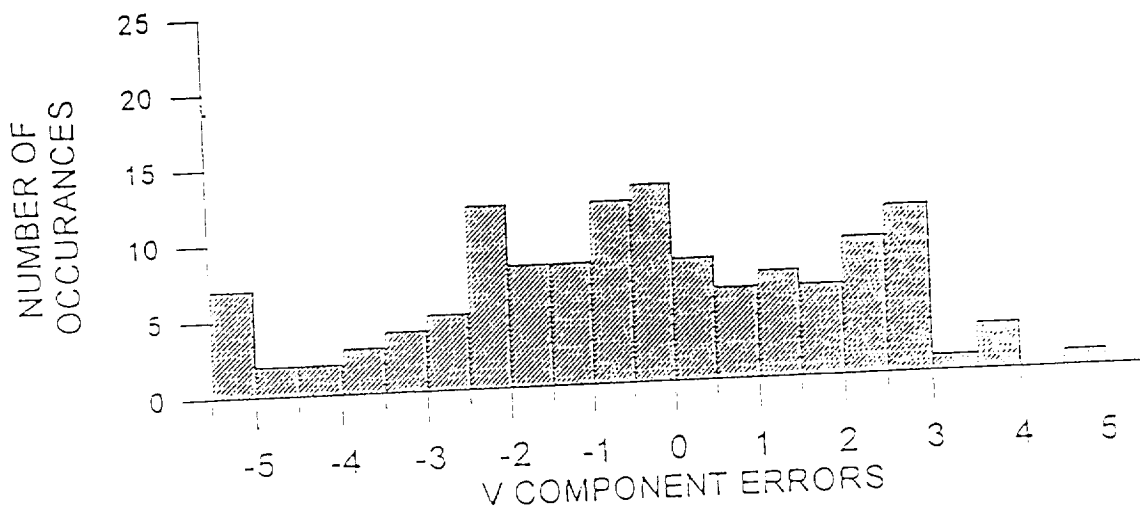
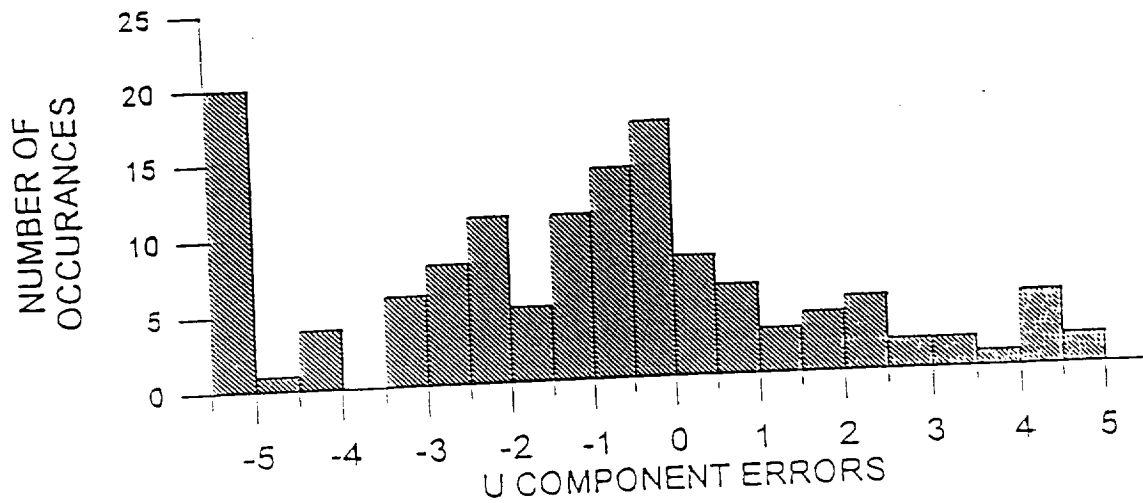


Figure D.30

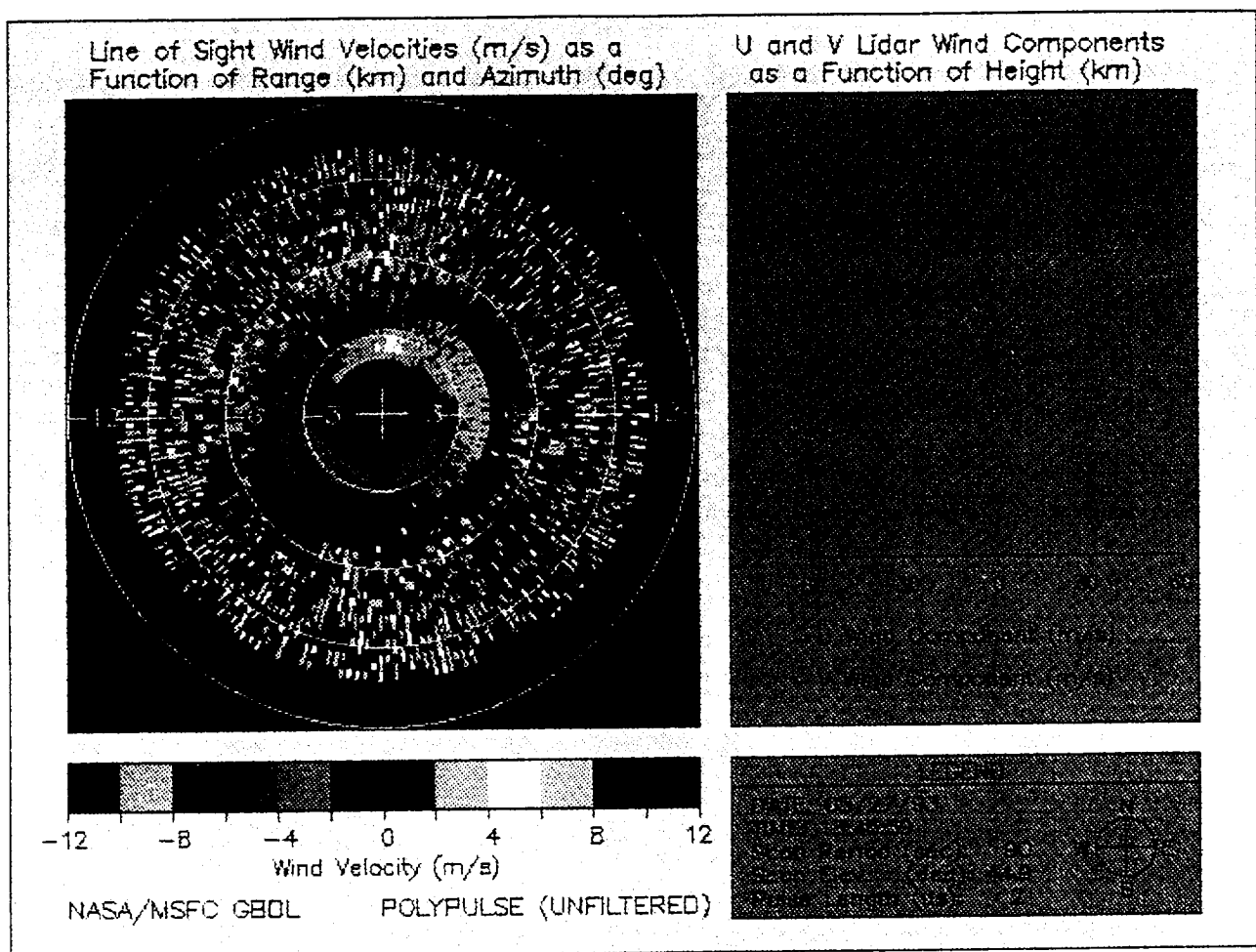
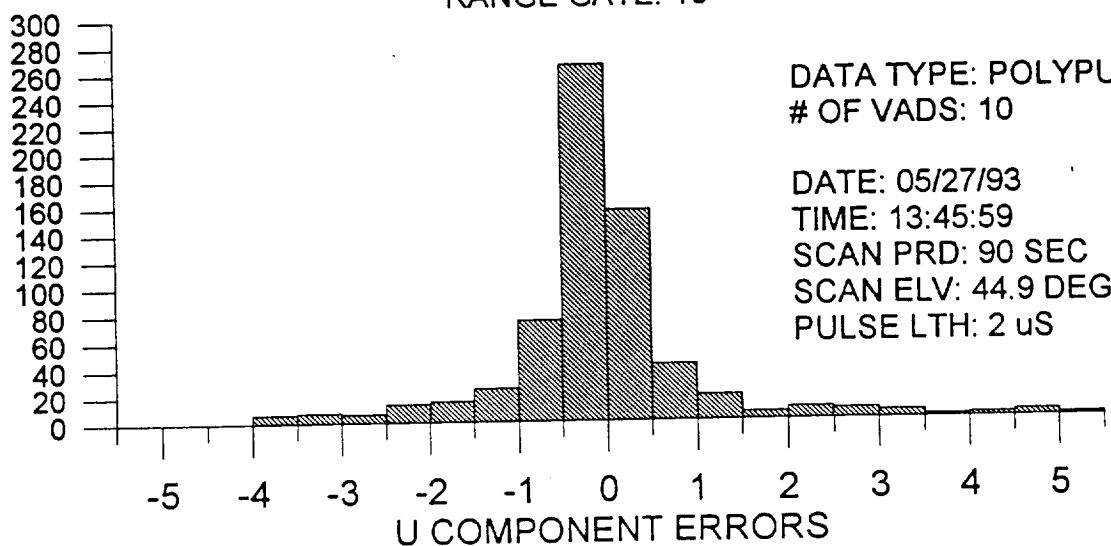


Figure D.31

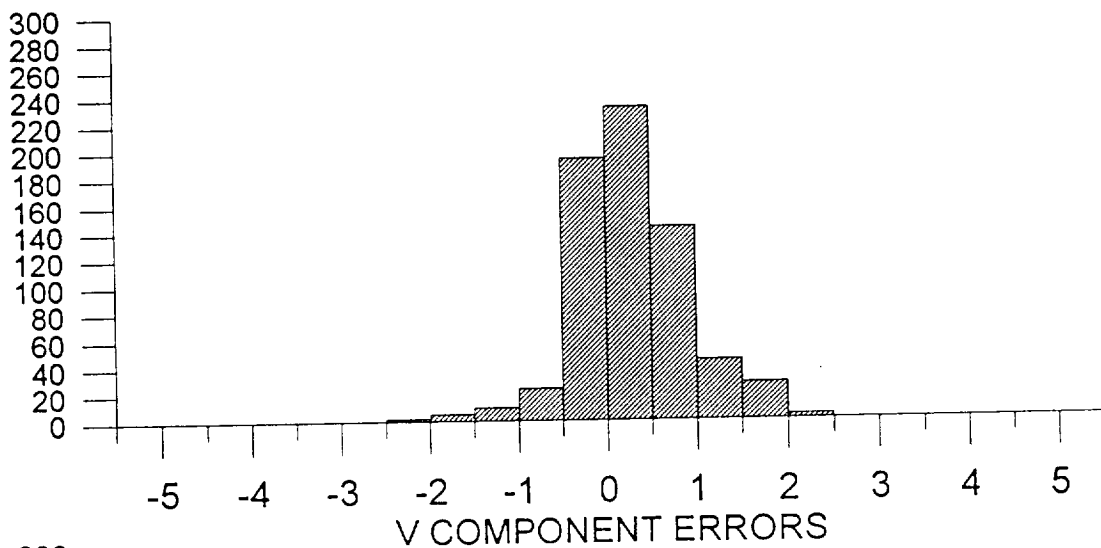
NASA MSFC GROUND-BASED DOPPLER LIDAR ERRORS

RANGE GATE: 10

NUMBER OF OCCURRENCES



NUMBER OF OCCURRENCES



NUMBER OF OCCURRENCES

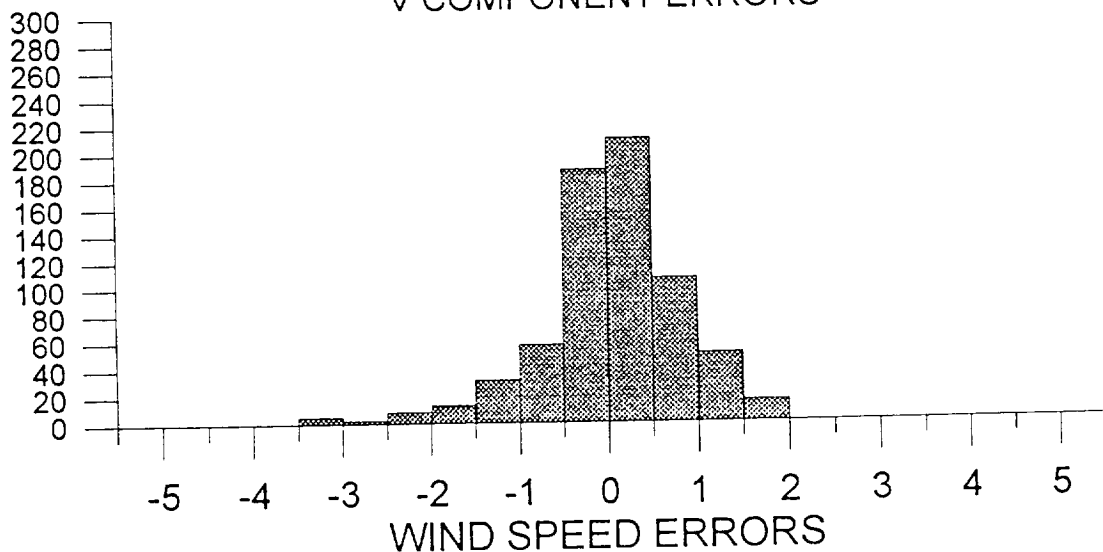
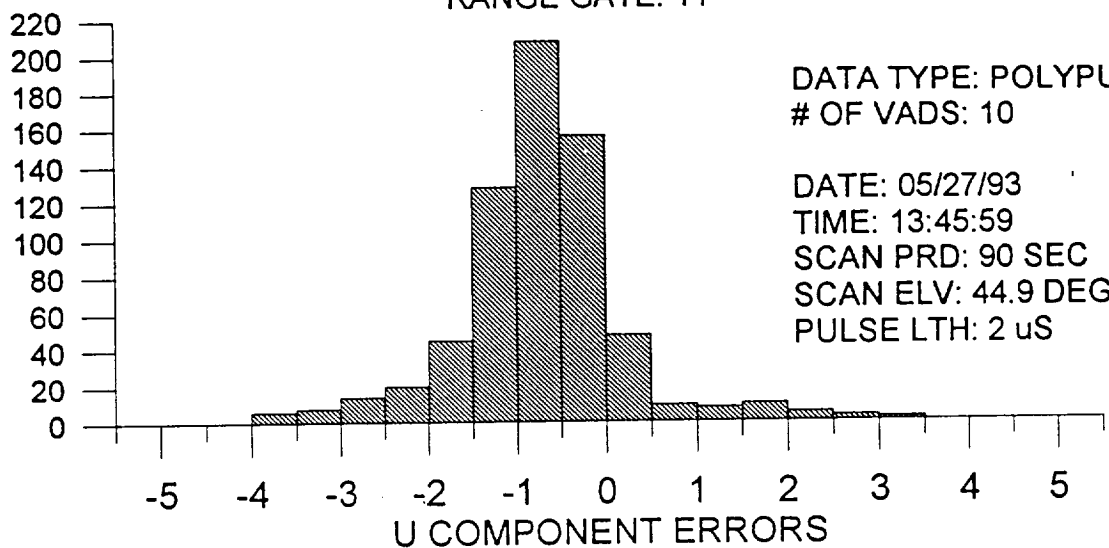


Figure D.32

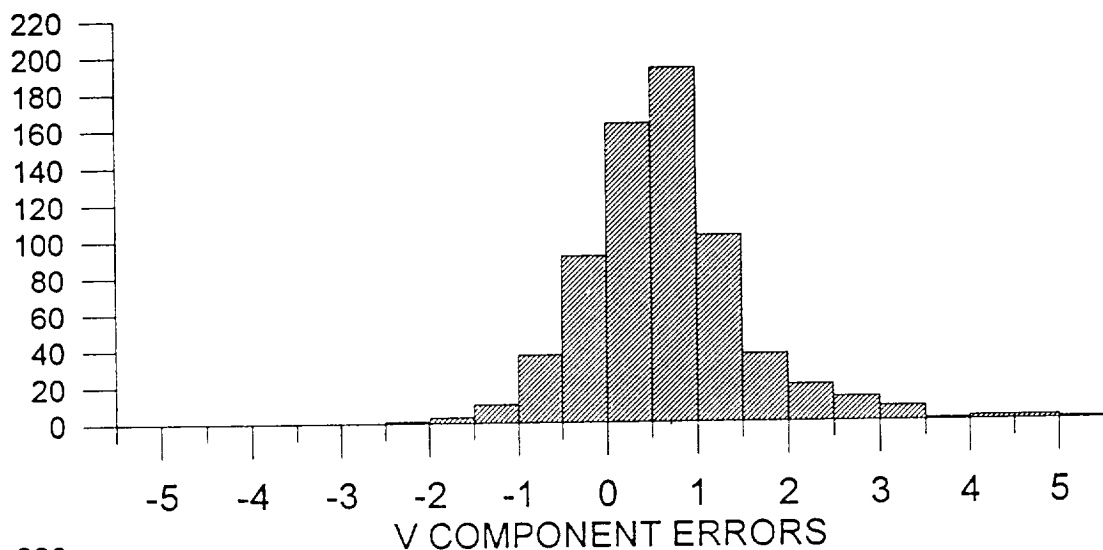
NASA MSFC GROUND-BASED DOPPLER LIDAR ERRORS

RANGE GATE: 11

NUMBER OF OCCURANCES



NUMBER OF OCCURANCES



NUMBER OF OCCURANCES

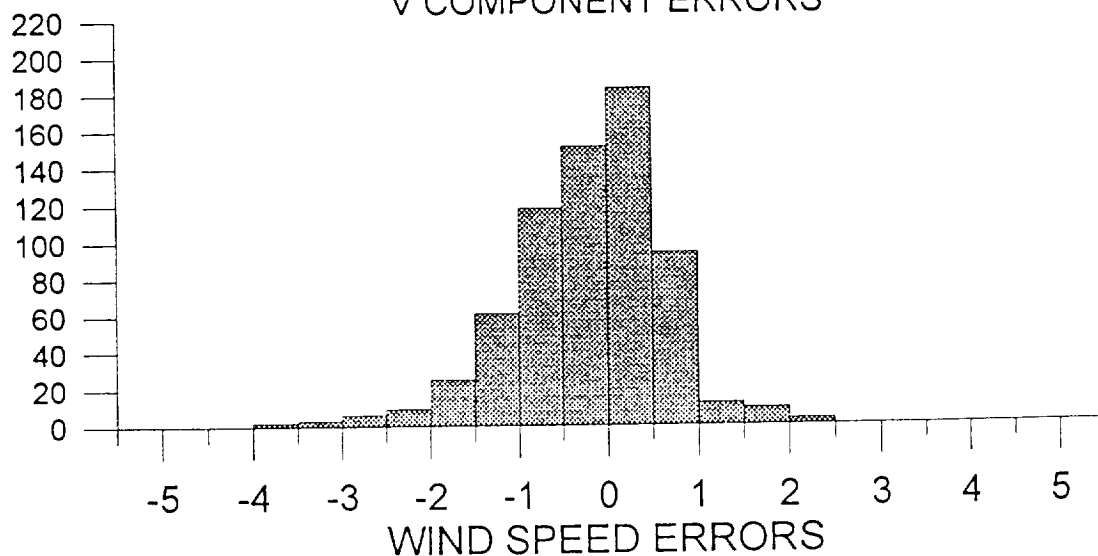


Figure D.33

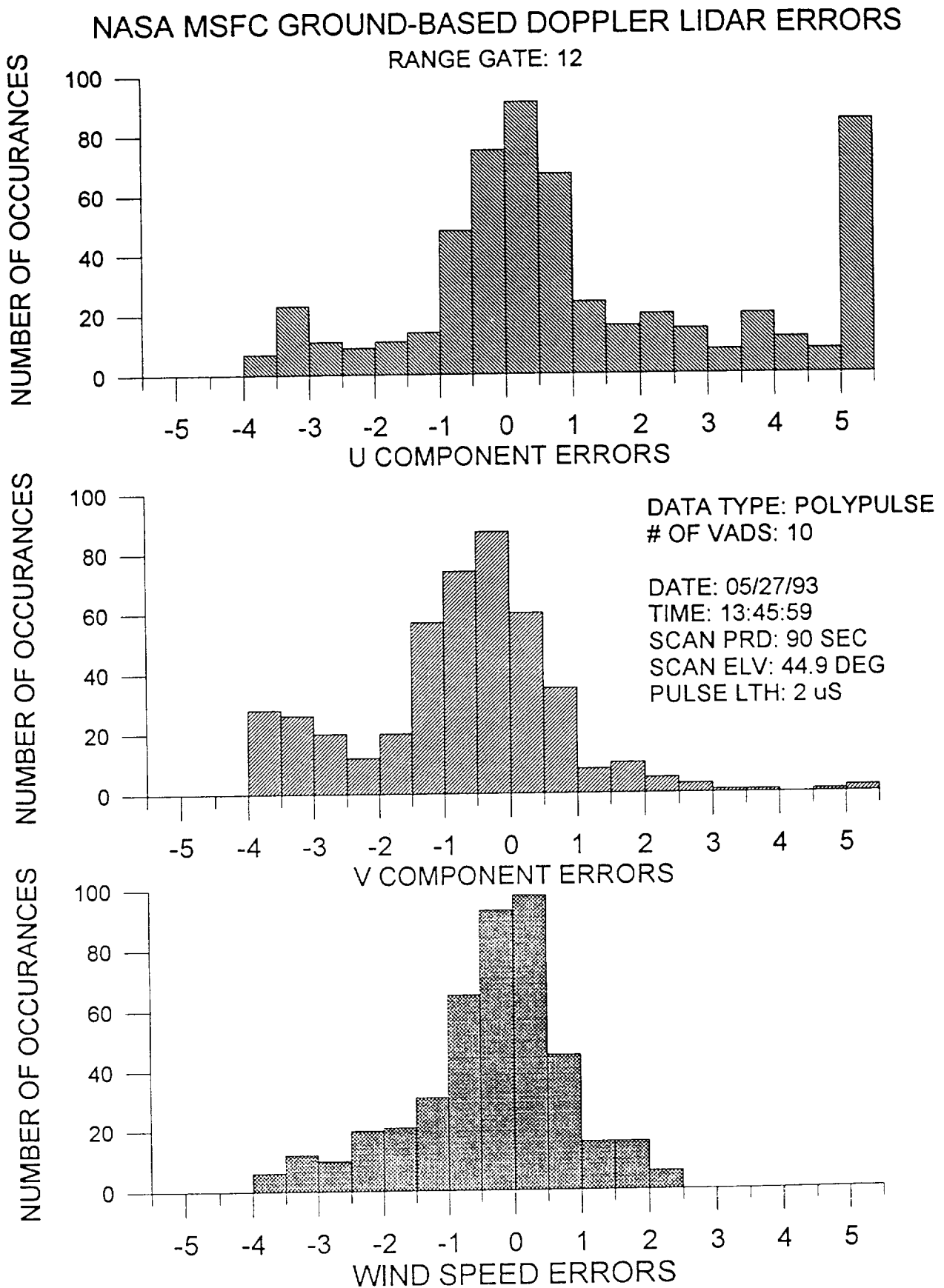


Figure D.34

NASA MSFC GROUND-BASED DOPPLER LIDAR ERRORS RANGE GATE: 13

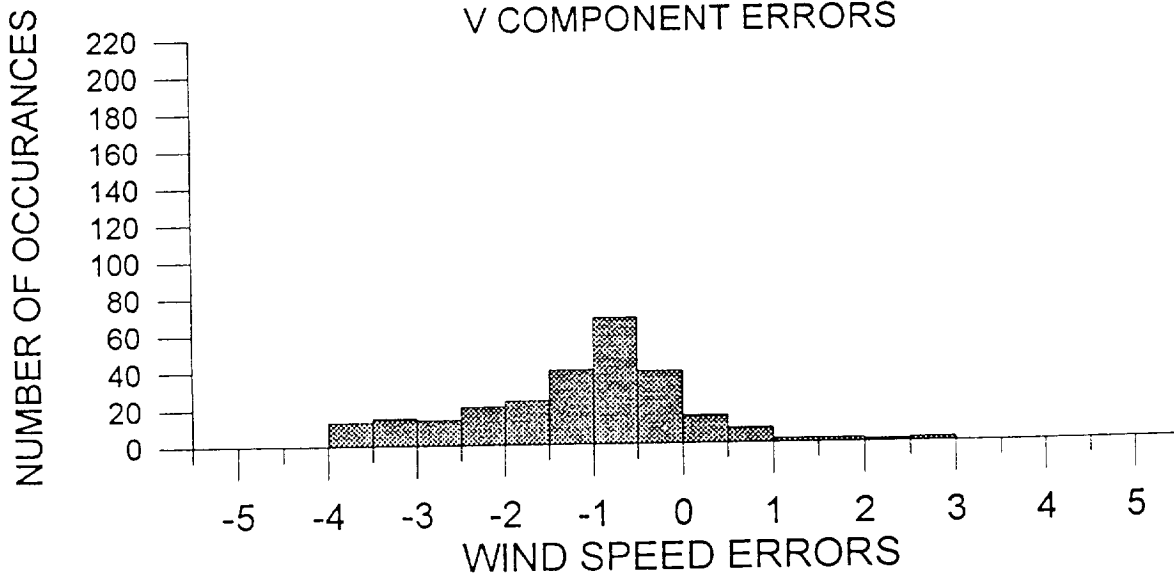
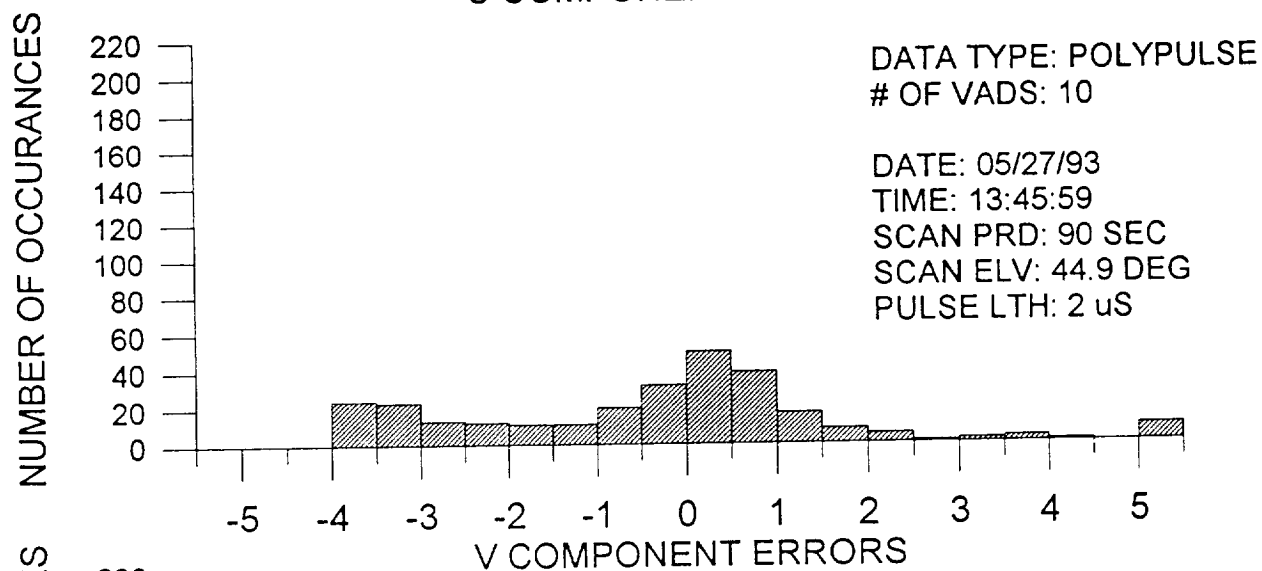
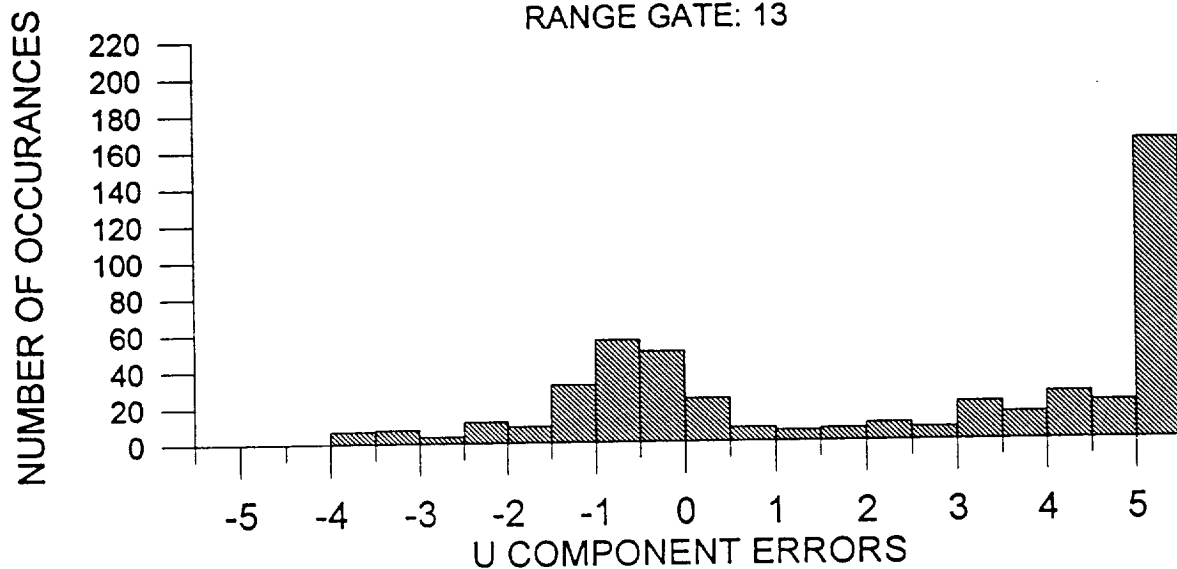


Figure D.35

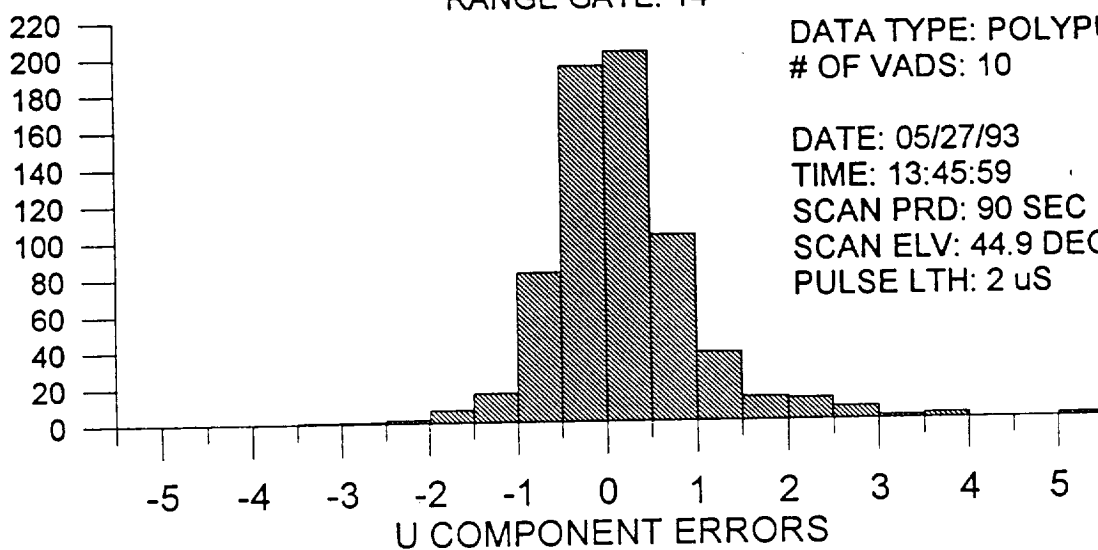
NASA MSFC GROUND-BASED DOPPLER LIDAR ERRORS

RANGE GATE: 14

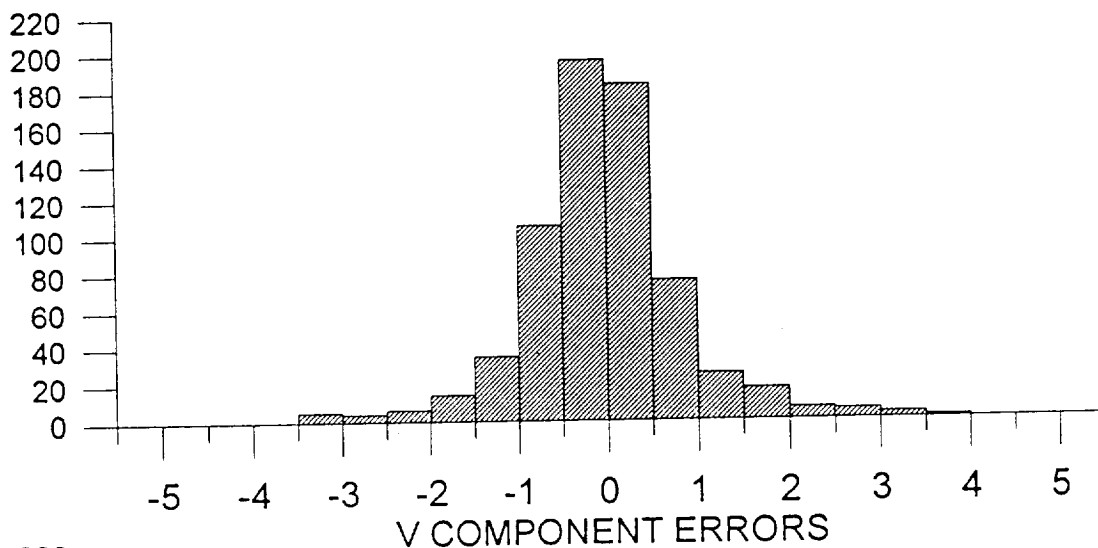
DATA TYPE: POLYPULSE
OF VADS: 10

DATE: 05/27/93
TIME: 13:45:59
SCAN PRD: 90 SEC
SCAN ELV: 44.9 DEG
PULSE LTH: 2 μ S

NUMBER OF OCCURANCES



NUMBER OF OCCURANCES



NUMBER OF OCCURANCES

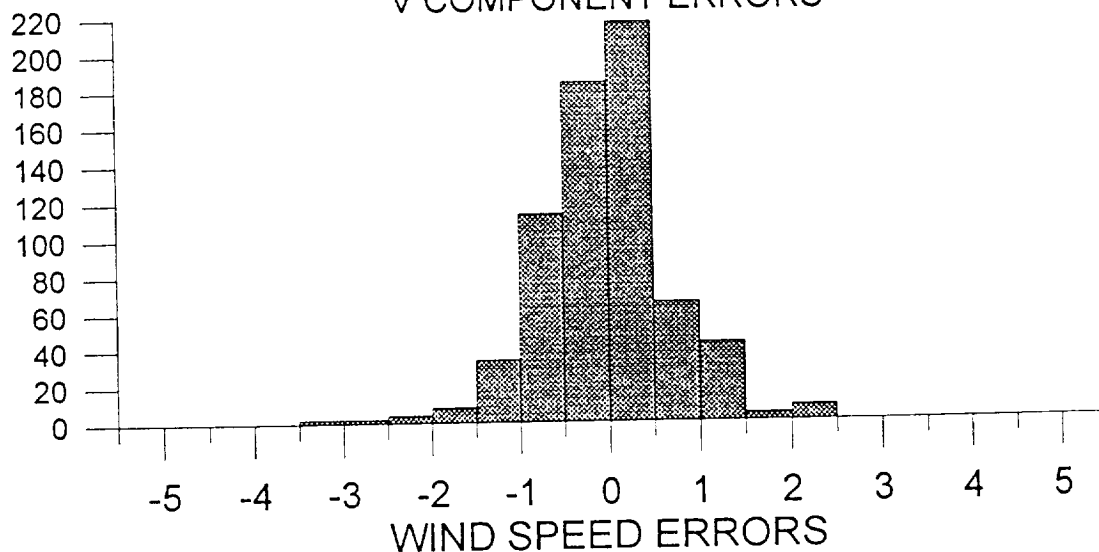


Figure D.36

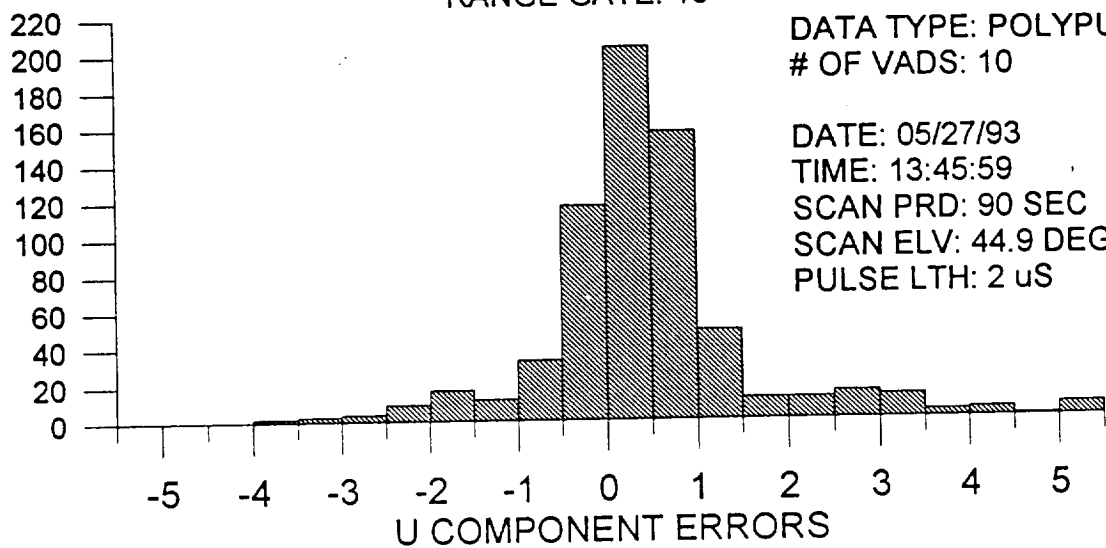
NASA MSFC GROUND-BASED DOPPLER LIDAR ERRORS

RANGE GATE: 15

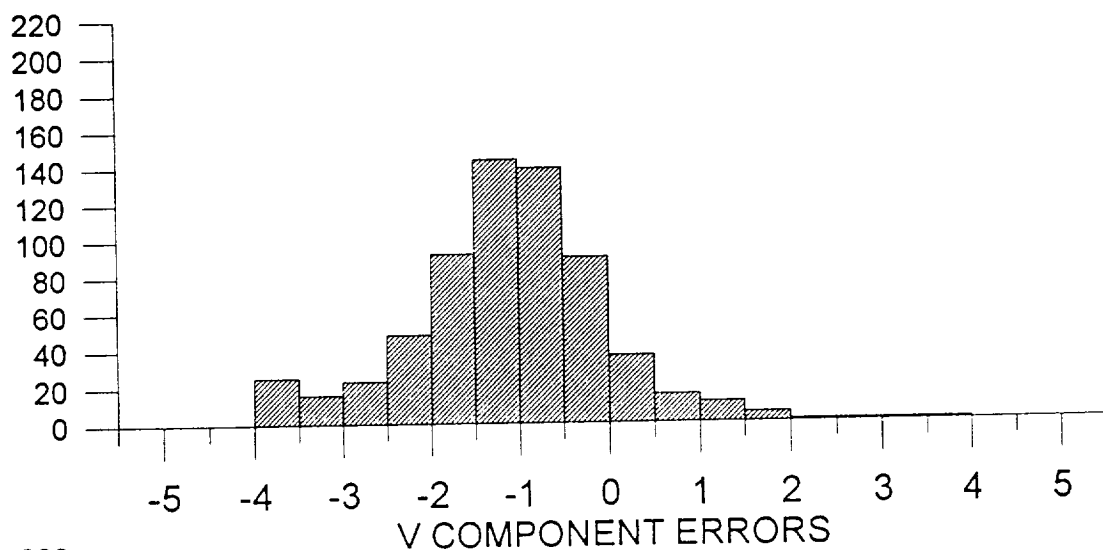
DATA TYPE: POLYPULSE
OF VADS: 10

DATE: 05/27/93
TIME: 13:45:59
SCAN PRD: 90 SEC
SCAN ELV: 44.9 DEG
PULSE LTH: 2 μ S

NUMBER OF OCCURRENCES



NUMBER OF OCCURRENCES



NUMBER OF OCCURRENCES

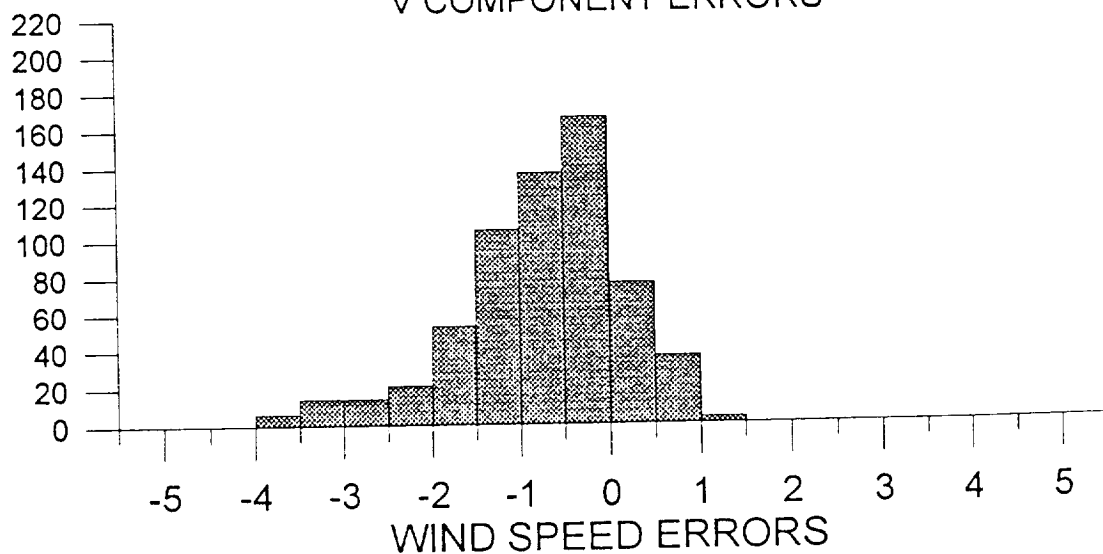


Figure D.37

3.1 μ s Rectangular pulse - No scatterer structure

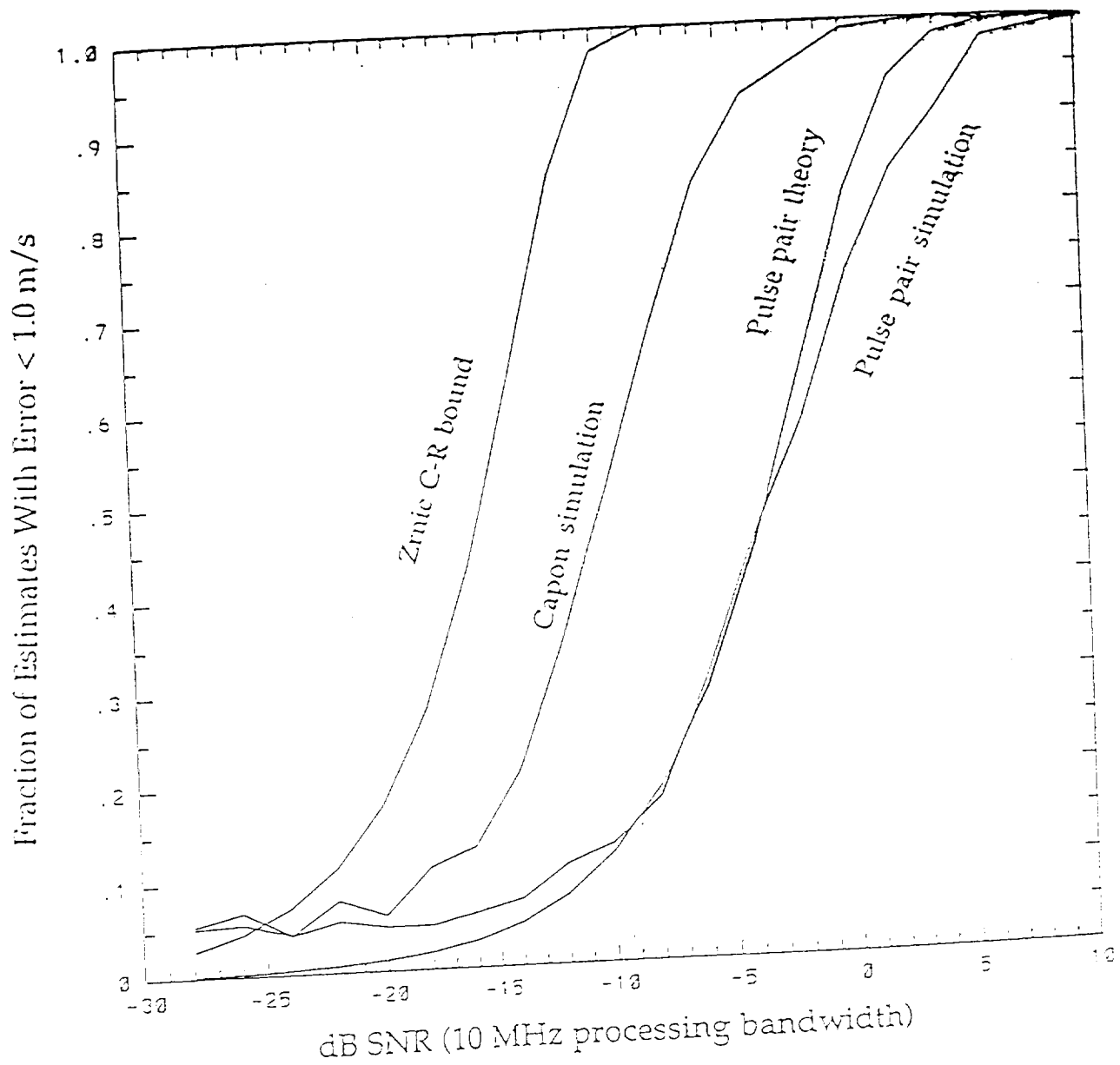


Figure D.38

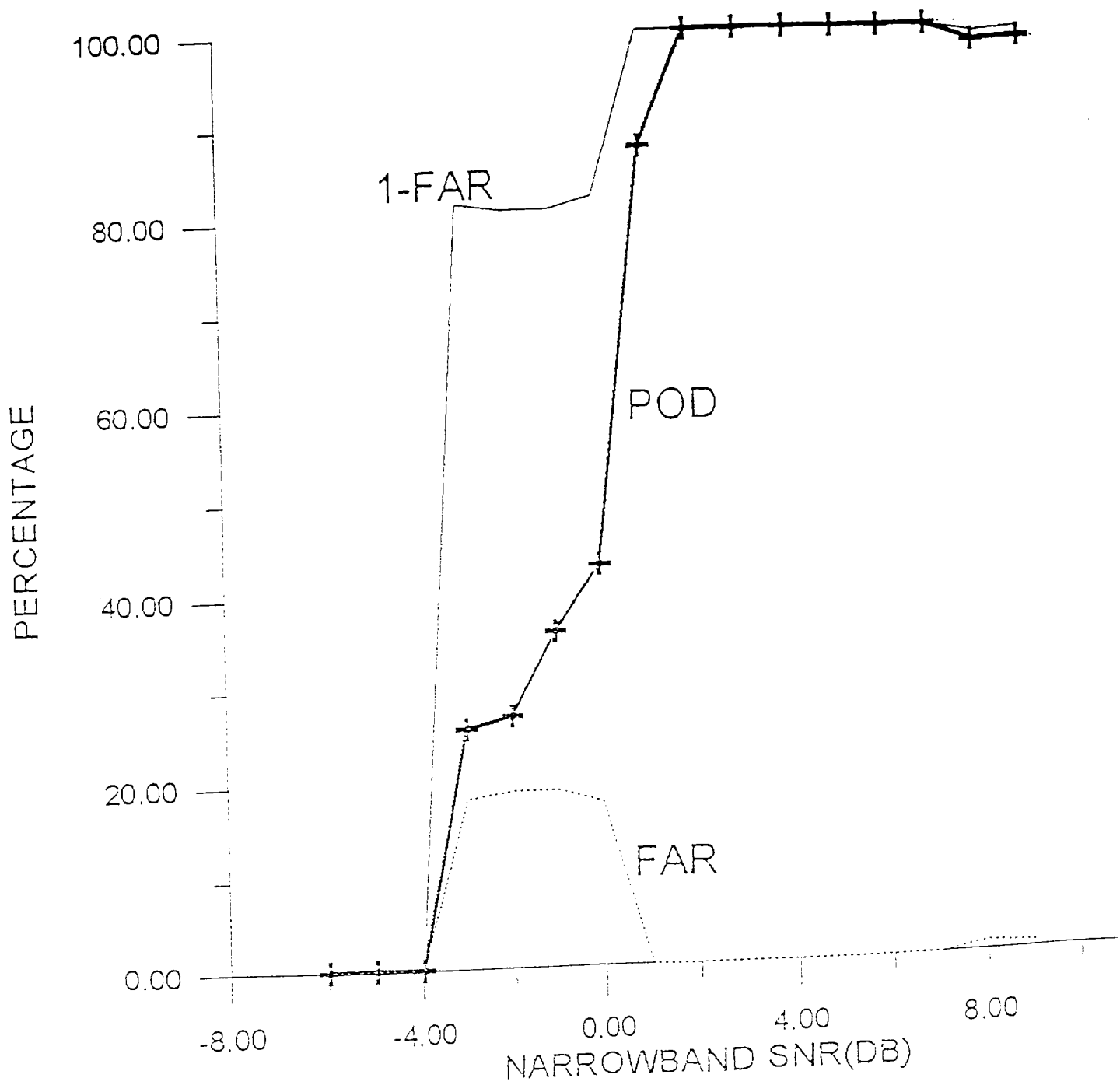


Figure D.39

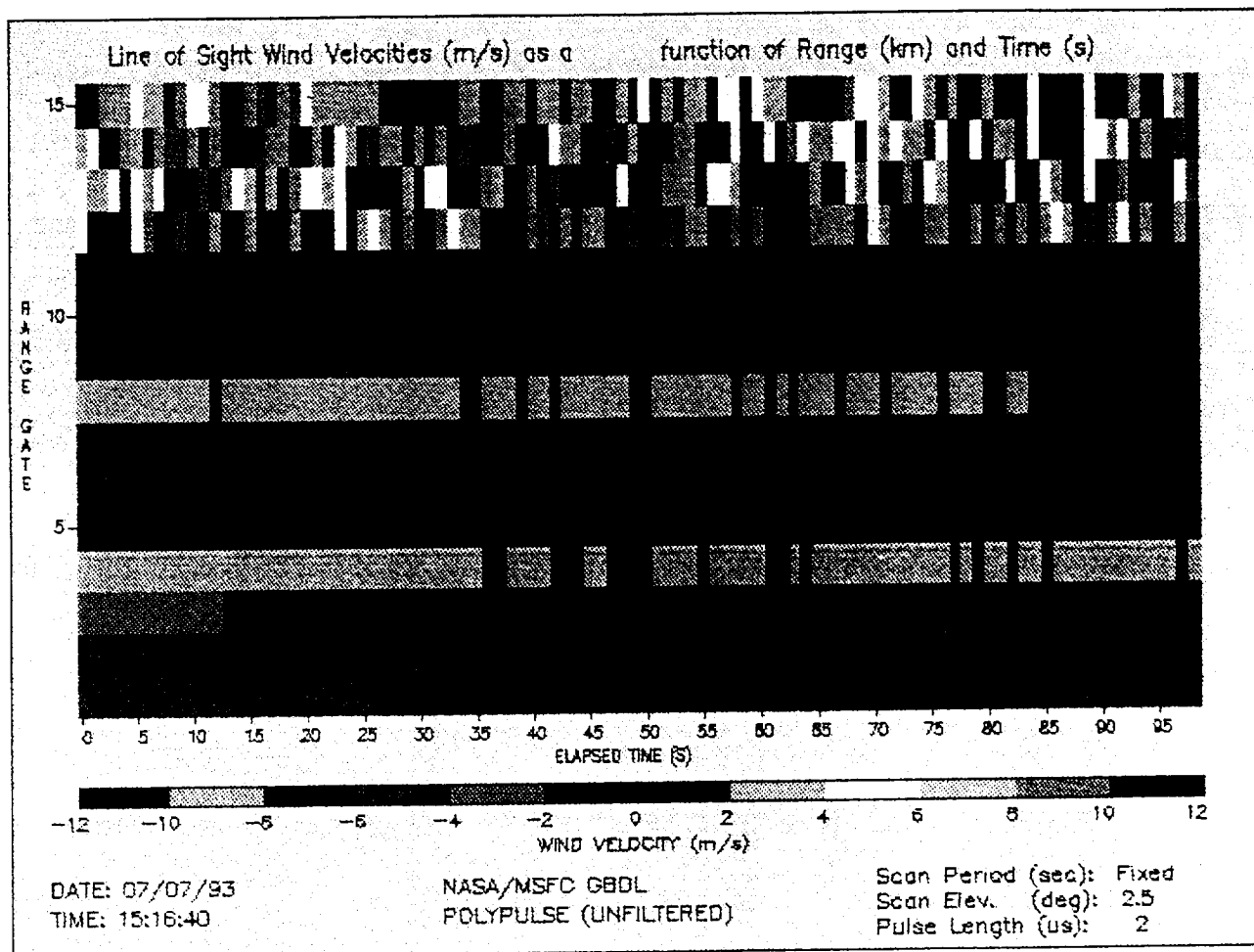


Figure D.40

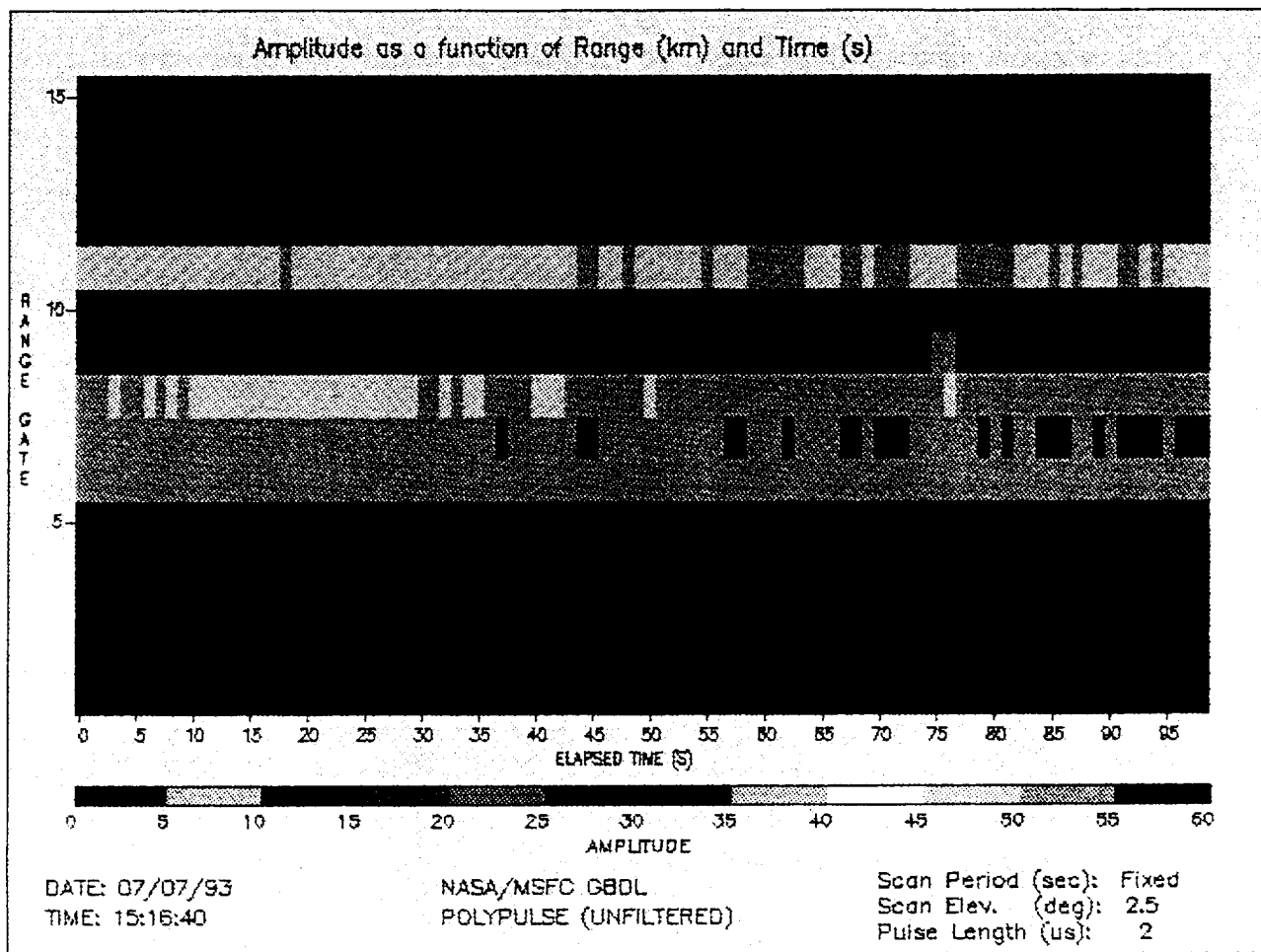


Figure D.41

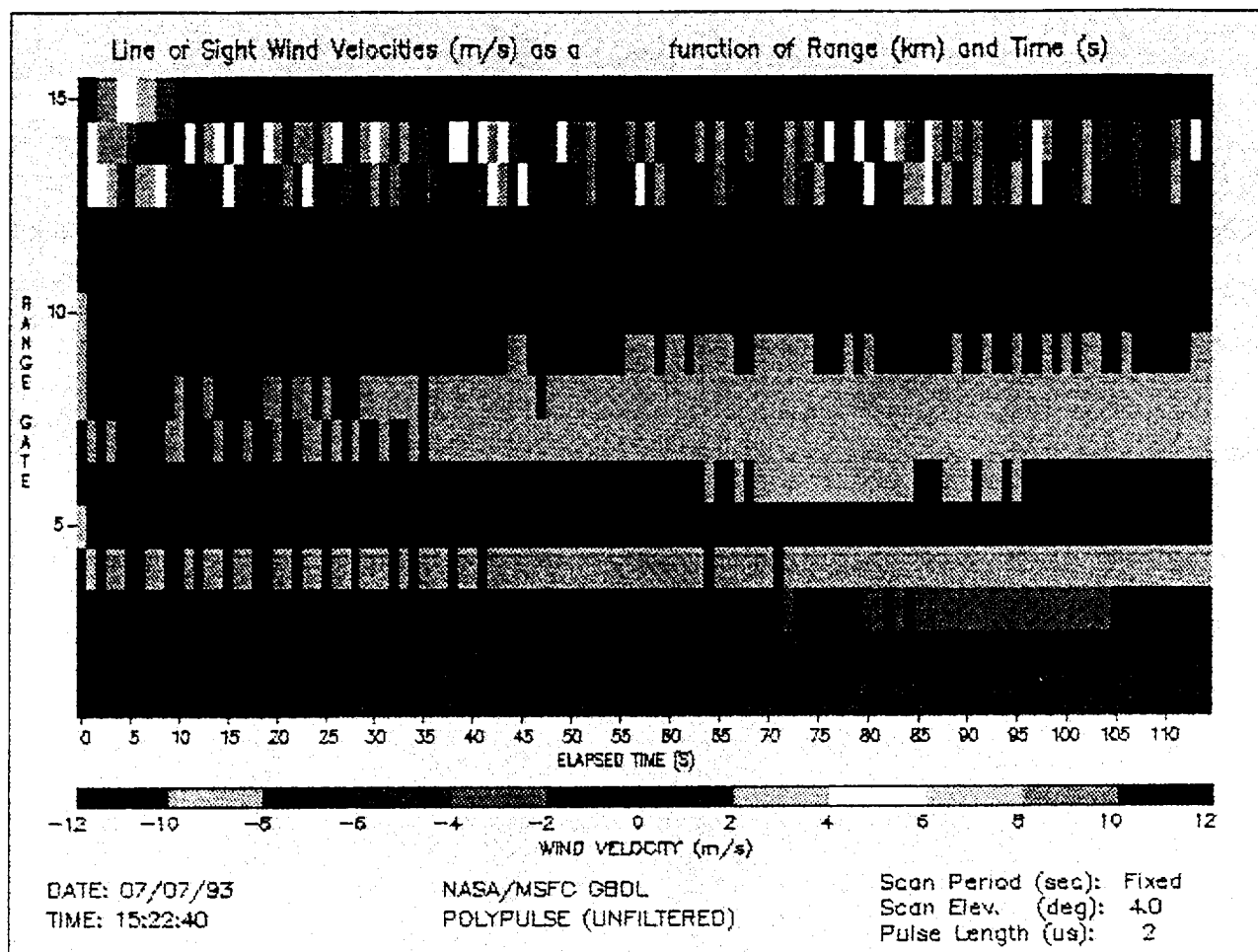


Figure D.42

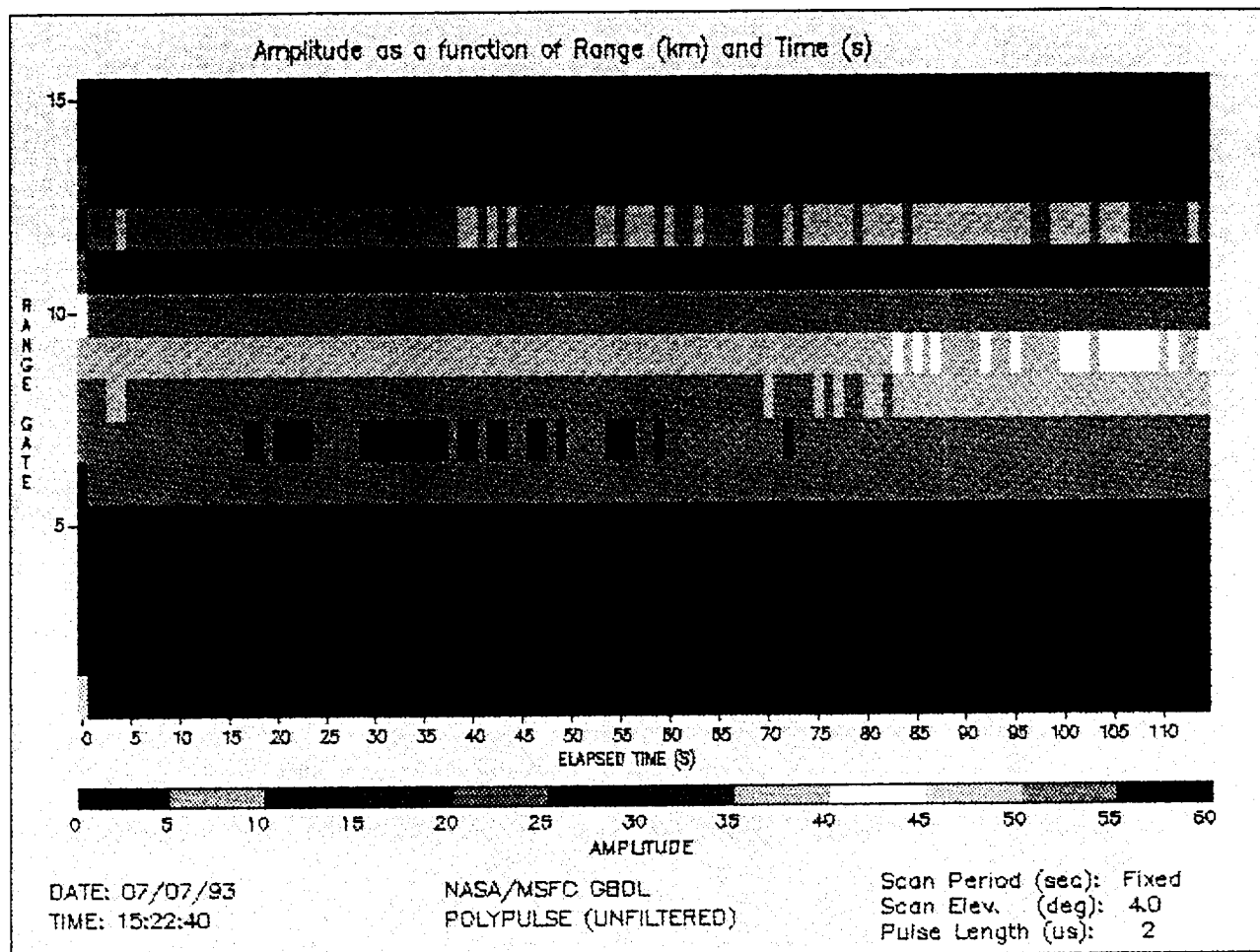


Figure D.43

AMPLITUDE AND LINE OF SIGHT WIND VELOCITY AS A FUNCTION OF TIME (POLYPULSE DATA)

SCAN PERIOD: FIXED
ELEVATION ANG.: 2.5 DEG

RANGE GATE: 8

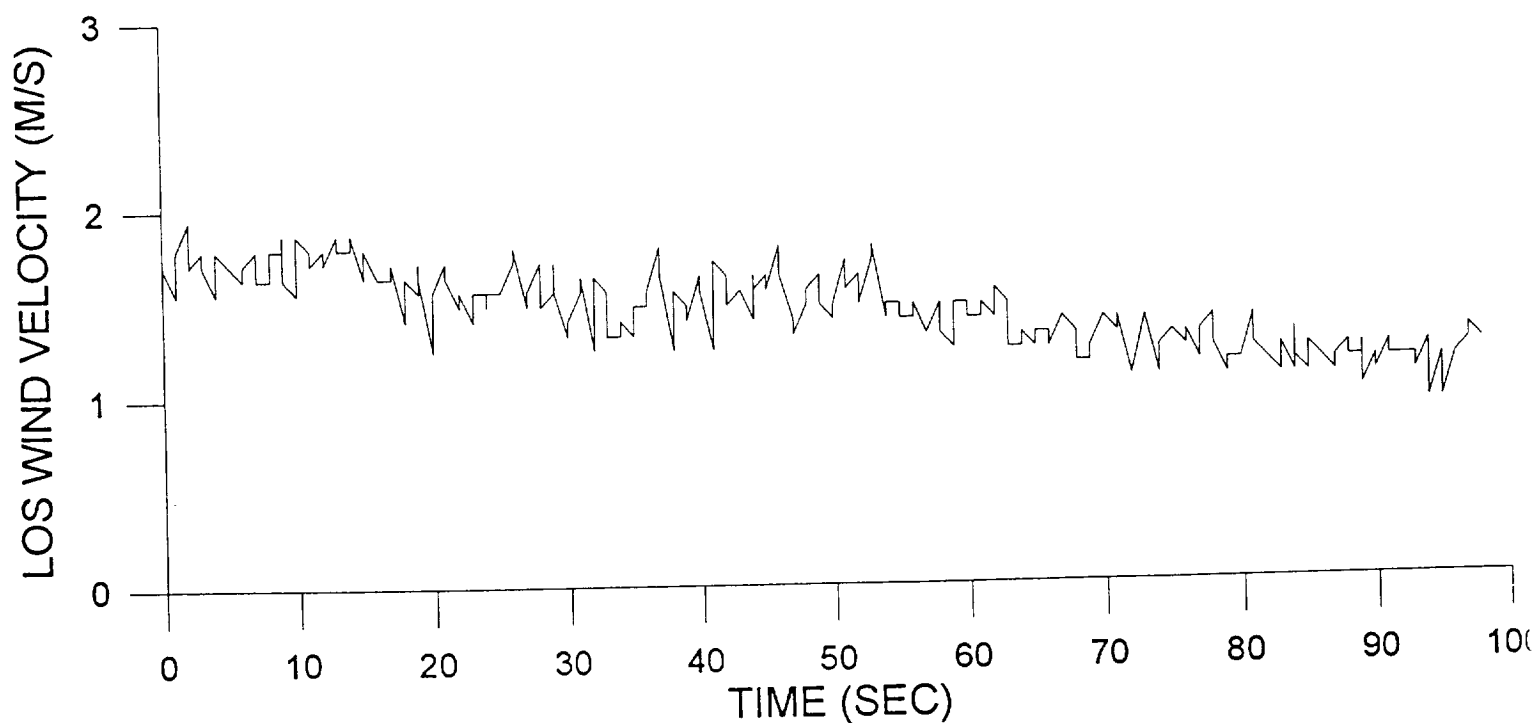
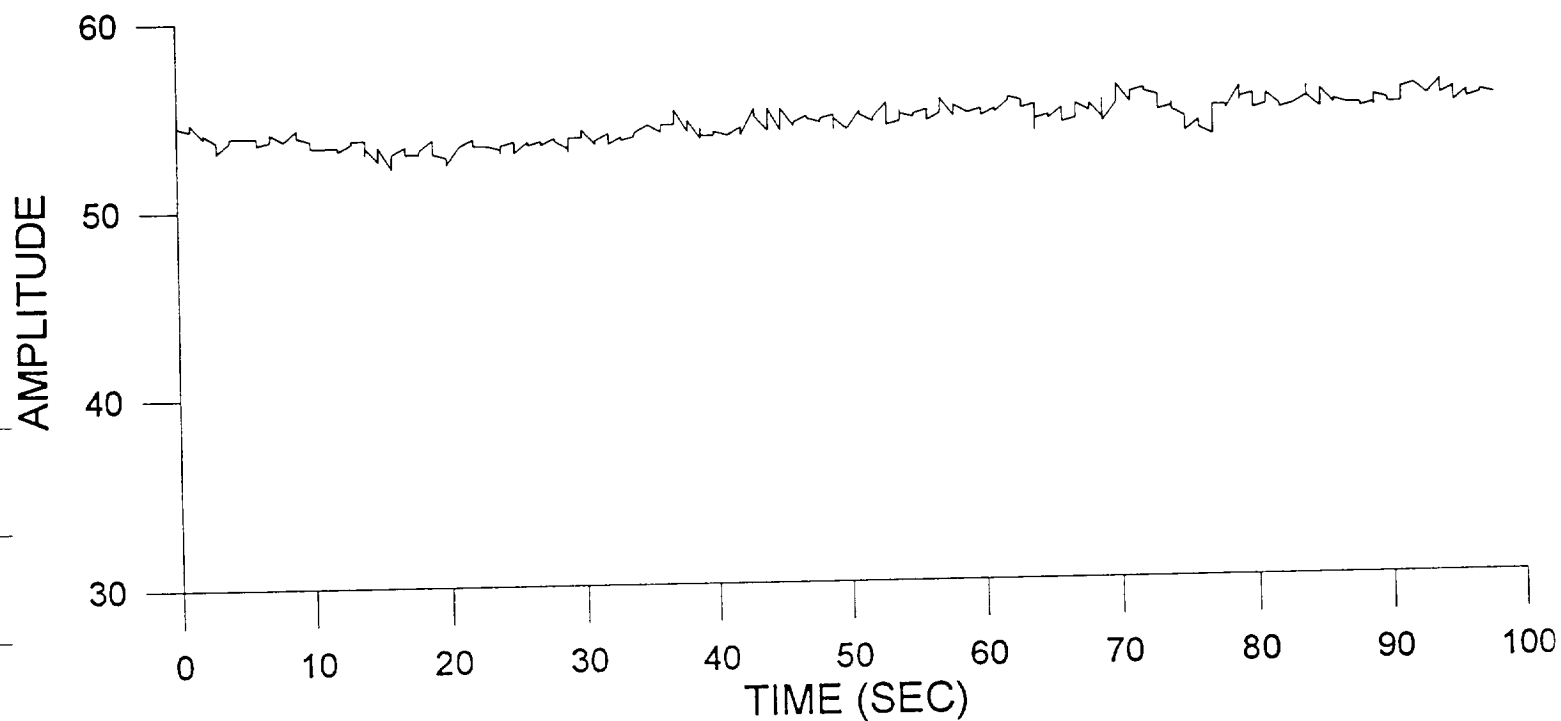


Figure D.44

AMPLITUDE AND LINE OF SIGHT WIND VELOCITY
AS A FUNCTION OF TIME
(POLYPULSE DATA)

SCAN PERIOD: FIXED
ELEVATION ANG.: 2.5 DEG

RANGE GATE: 10

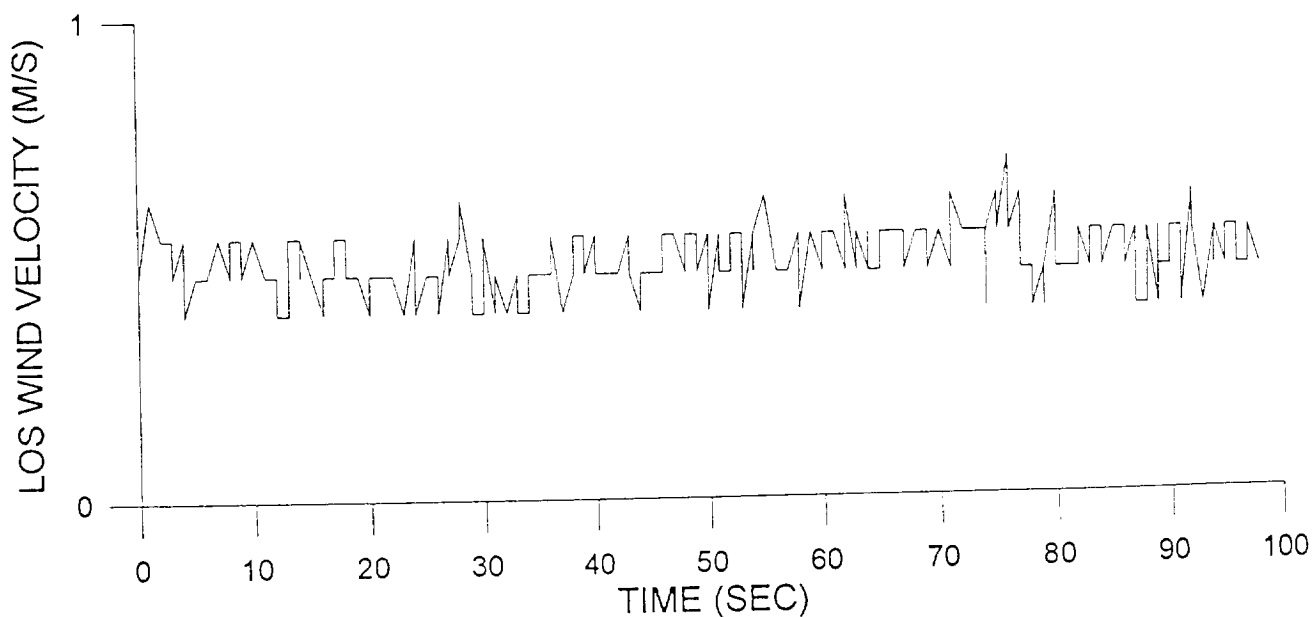
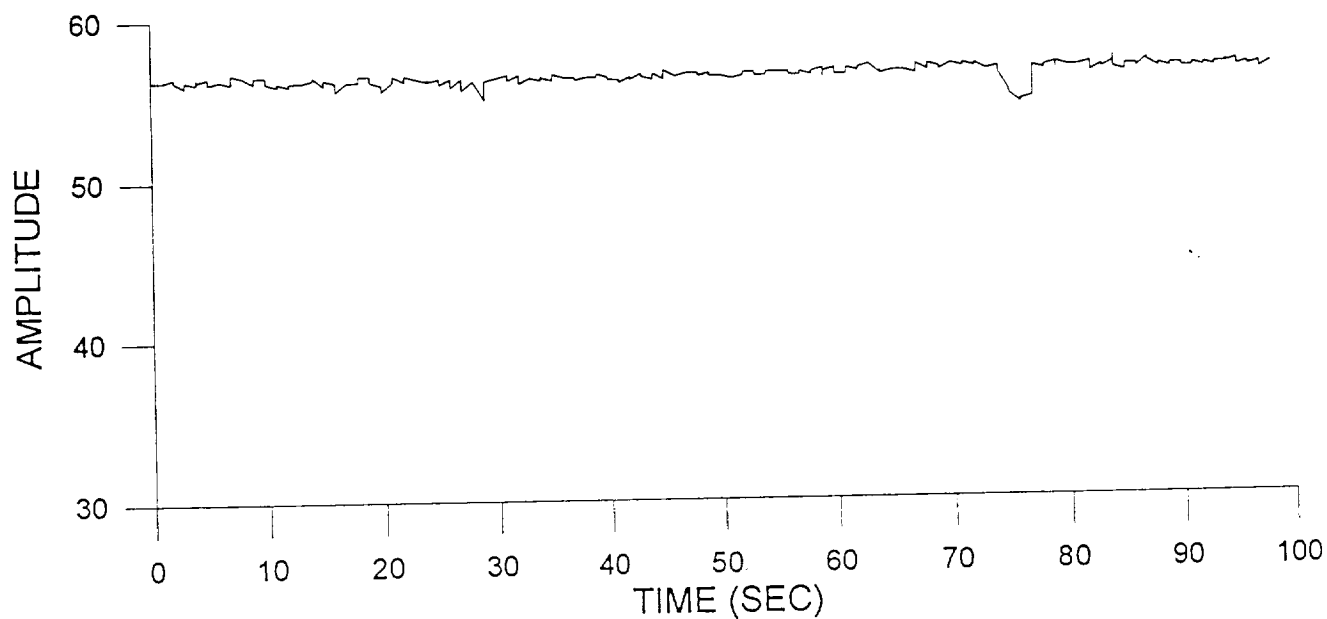


Figure D.45

AMPLITUDE AND LINE OF SIGHT WIND VELOCITY
AS A FUNCTION OF TIME
(POLYPULSE DATA)

SCAN PERIOD: FIXED
ELEVATION ANG.: 4.0 DEG

RANGE GATE: 8

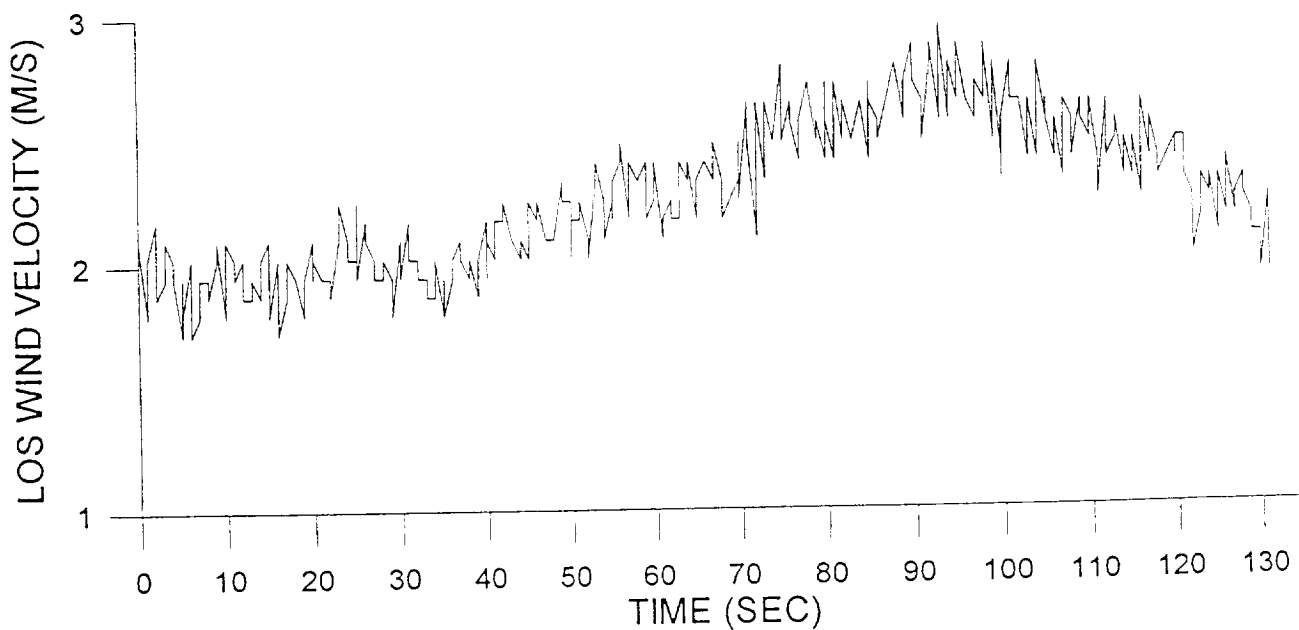
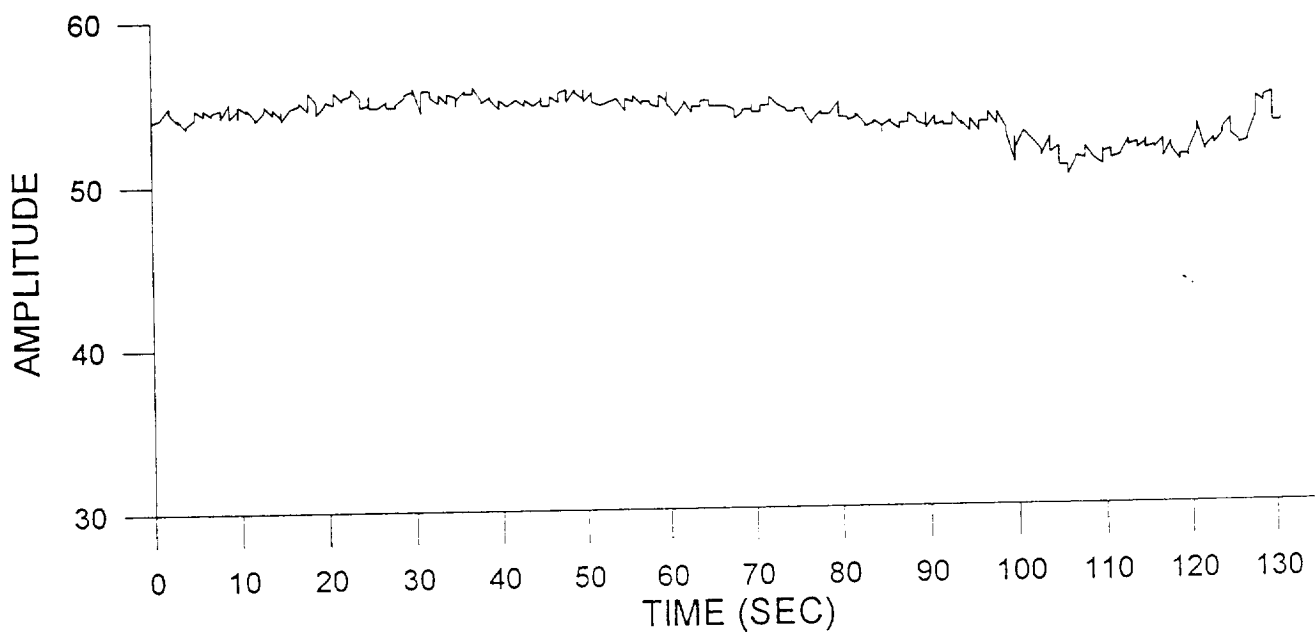


Figure D.46

AMPLITUDE AND LINE OF SIGHT WIND VELOCITY
AS A FUNCTION OF TIME
(POLYPULSE DATA)

SCAN PERIOD: FIXED
ELEVATION ANG.: 4.0 DEG

RANGE GATE: 11

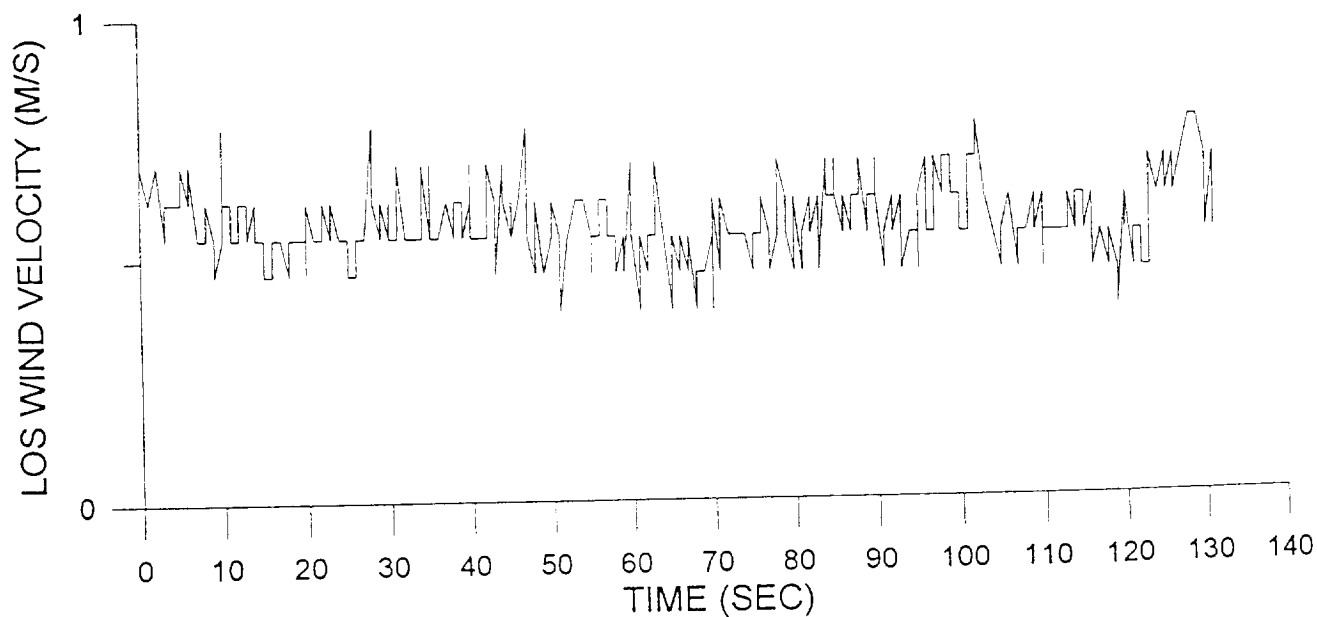
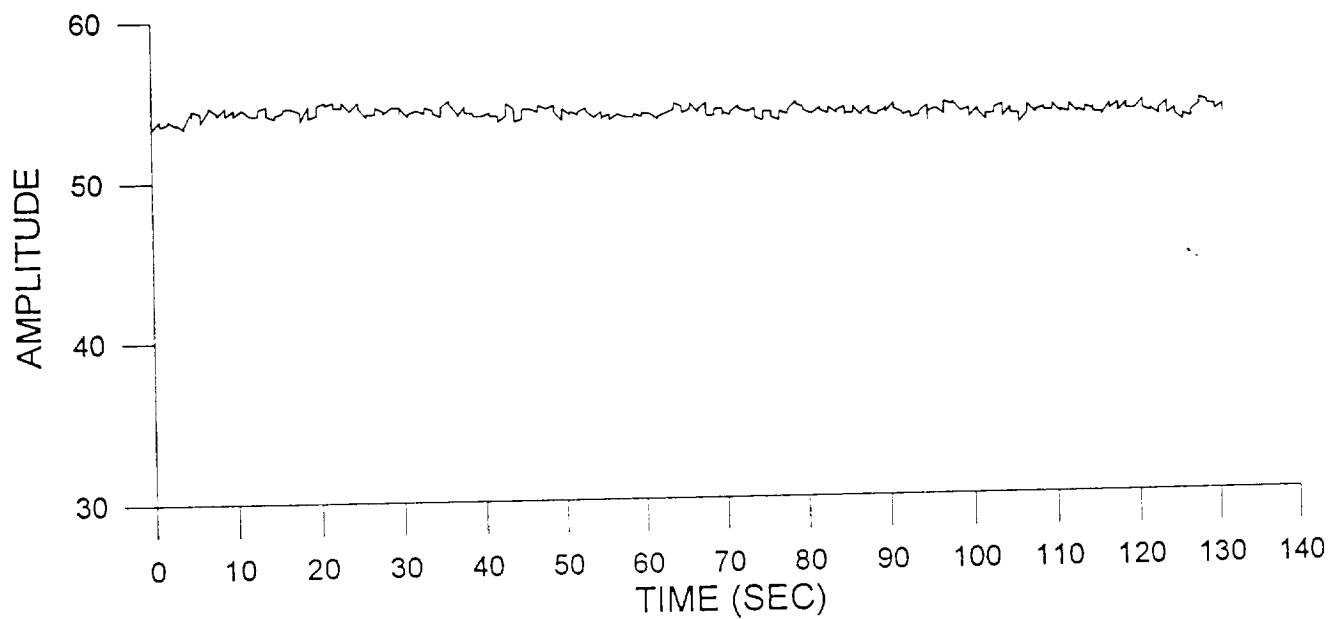


Figure D.47

APPENDIX E ADDITIONAL STUDIES

1.0 Backscatter Comparison Between the Wavelengths 9.11 and 2.1 μm

The presentation, "Integration of Lowtran Into Global Circulation Models for Observing System Simulation Experiments" by S.A. Wood and G.D. Emmitt, compared the global relative backscatter performance of a 9.11 μm system to a 2.1 μm system.

A LAWS Simulation Model (LSM) has been developed to assess the potential impact of a space-based lidar wind sounder on global and regional features (see Appendix A). The LSM provides simulated winds for use in the Observing System Simulation Experiments (OSSEs) as described in Appendices B and C. The LSM contains "streamlined" versions of AFGL's LOWTRAN and FASCODE models that, coupled with the ECMWF model's atmospheric profile data, provides $1^\circ \times 1^\circ$ estimates of global aerosol backscatter and molecular attenuation.

The LSM uses a unique $1^\circ \times 1^\circ$ global LOWTRAN input data base that, given a location on the earth, provides a latitudinal location profile, haze model, coastal influence parameter, stratospheric profile and upper atmosphere profile. These LOWTRAN inputs along with global GCM inputs such as winds, relative humidity, temperature, pressure and clouds are used to compute aerosol backscatter and molecular attenuation.

Given the baseline LAWS wideband Signal-to-Noise (SNR) equation (described in Appendix A, Eq. 6.3), we can rewrite the SNR_w equation as follows

$$\text{SNR}_w = \frac{K}{R^2} * \lambda^2 * \beta_r(\lambda) * 2 \alpha(\lambda) dr$$

where

K	=	system variables
λ	=	wavelength
$\beta_r(\lambda)$	=	aerosol backscatter
$\alpha(\lambda)$	=	attenuation
R	=	range

and grouping all system variables in the constant K, we simplify the equation to atmospheric variables and wavelength. For our discussion, we multiplied all optical properties by λ^2 , thus our performance comparison is in terms of the optical properties and wavelength and any additional enhancement of the SNR must come from the system (K) itself.

Figures E.1 and E.2 show the global unattenuated aerosol backscatter for 9.11 μm and 2.1 μm , respectively. Since our aerosol backscatter model is largely driven by relative humidity, Fig. E.3 gives the corresponding global relative humidity field to highlight the high relative humidity regions (i.e., high backscatter). This study shows that at high relative humidity regions, the 2.1 μm had distinct advantages over the 9.11 μm system. However, no advantage was evident at low relative humidities and in some dry regions the 2.1 μm system actually performed worse than the 9.11 μm . Figures E.4 and E.5 show the 9.11 μm and 2.1 μm attenuated aerosol backscatter for a given LAWS baseline configuration, respectively. Likewise, the performance of the 9.11 μm system is much better than the 2.1 μm system in most of the northern hemisphere. Whereas, in most of the "wetter" southern hemisphere, the 2.1 μm is better than 9.11 μm .

Since LSM cloud fields are also driven by the moisture fields, we looked at high β regions where total cloud cover did not exist. Figure E.6 shows all 9.11 μm attenuated backscatter greater than $2.5 \text{ e}^{-6} \text{ m}^{-1} \text{ sr}^{-1}$ for integrated cloud cover less than 90%. Figure E.7 shows all integrated cloud cover to the surface. Large areas of high backscatter regions are found in the northern hemisphere even though there is a large amount of cloudiness present. For most of the southern hemisphere, either the backscatter was weak or cloud cover was dominate.

In conclusion, any significant advantages of a 9.11 μm system over a 2 μm system, or visa versa, over the obvious wavelength considerations must come from lidar system parameters such as power, telescope diameter or system constants.

2.0 System Design Trade Studies

Throughout the design of the LAWS instrument, several optimization issues have been addressed. In most instances, the dependent parameters in the trades have been the LOS accuracy, shot density and global coverage.

2.1 Optimal Scan Angle

The angle from nadir for the telescope orientation is a critical design parameter from several perspectives (Emmitt, 1991). All of the following are functions of the scan angle:

- 1) Range to target - returned signal strength has $1/R^2$ dependence;
- 2) Molecular attenuation - attenuation is a function of the slant path through the atmosphere;
- 3) Vertical velocity contamination - the greater the

nadir angle the smaller the projection of the vertical motion onto the LOS;

- 4) Sample density - for a fixed prf the sample density decreases with increased nadir angle; and
- 5) Global coverage - decreases with decreasing nadir angle.

Relaxing global coverage, the LAWS simulation model indicates that a nadir angle of 28-32 degrees would be optimum - i.e., the horizontal wind components are estimated with the lowest errors (Fig. E.8). However, since the trade is fairly flat, global coverage considerations have led the LAWS Science Team to select a nadir angle of $\sim 45^\circ$ for most of the design studies.

2.2 Pulse Energy vs Pulse Repetition Frequency

The total observation error for a LAWS measurement within a specified grid area can be expressed as σ_o^2 and is a combination of accuracy along a line-of-sight and the representativeness of the samples taken by several shots. The following is an expression for σ_o^2 that can be used to examine trades between pulse energy and pulse repetition frequency:

$$\sigma_o^2 = \frac{\sigma_m^2 + \sigma_s^2}{P \cdot N}$$

where

σ_o	=	total observation error for given grid cell
σ_m	=	accuracy along a line-of-sight
σ_s	=	variance of actual winds on all wavelengths below the Nyquist
P	=	percent of shots into grid cell that are good
N	=	total number of shots attempted into grid cell.

The expression for the observational error (σ_o) within a specific size grid cell involved four primary terms, σ_m , σ_s , P and N. As explained above, trades need to be assessed between laser energy (E) (which is inversely related to σ_m and directly related to P) and pulse repetition frequency (prf).

The product of the energy per pulse and prf is limited by the available platform power. Thus, a doubling of the pulse energy may improve σ_m and P but the required halving of the prf reduces the number of shots available to reduce the overall observational error (σ_o). Since σ_s is usually larger than σ_m , and target volume, σ_s , is quite variable around the globe, trade studies are difficult to interpret. For example, if the mission

requirements favor the low backscatter low turbulent regions of the troposphere, then higher energy/pulse would be favored over higher shot density. However, if the higher backscatter situations (clouds, dust layers, PBL) are the primary mission objectives, then higher prfs are needed to reduce the σ_g/N in these regions (Fig. E.9). The energy/pulse vs. prf trades continue to be conducted as mission requirements evolve (Emmitt and Wood, 1991).

2.3 Optimal Scan Rate and Intra-Scan Shot Management

The present objectives of the LAWS instrument are to provide the greatest global coverage with the highest density of wind measurements having acceptable accuracy and representativeness constrained, of course, by available platform resources and mission costs. This translates into optimizing the placement of a fixed number (e.g., 25,000) of lidar shots per orbit.

The best scan rate is one that produces the most even distribution of shots in both the along track and cross track directions. The optional scan rate is a function of average prf and, for the LAWS instrument, was found to be 10-12 rpm; 12 rpm was used in the simulation shown in Fig. A.8.

The best wind information that can be provided to the global models is obtained where there are both forward and aft shots with angular separations near 90°. This means that shots taken directly forward, aft, port and starboard are not very "useful" since there is no second perspective to resolve the wind vector. Shot management has been designed to redistribute these less useful shots into angular perspectives that have lower potential error (Fig. A.8).

FIGURE CAPTIONS

- Figure E.1: Global $9.11 \mu\text{m}$ relative aerosol backscatter ($\mu\text{m}^2 \text{m}^{-1} \text{sr}^{-1}$) at the earth's surface for 1/16/79, 0600Z. The aerosol backscatter has been multiplied by the lidar wavelength squared.
- Figure E.2: As for Fig. E.1 but for $2.1 \mu\text{m}$.
- Figure E.3: Global relative humidity field at the earth's surface for 1/16/79, 0600Z.
- Figure E.4: Attenuated global $9.11 \mu\text{m}$ relative aerosol backscatter ($\mu\text{m}^2 \text{m}^{-1} \text{sr}^{-1}$) at the earth's surface for 1/16/79, 0600Z. The aerosol backscatter has been multiplied by the lidar wavelength squared.
- Figure E.5: As for Fig. E.4 but for $2.1 \mu\text{m}$.
- Figure E.6: Global $9.11 \mu\text{m}$ relative aerosol backscatter ($\mu\text{m}^2 \text{m}^{-1} \text{sr}^{-1}$) greater than 2.5×10^{-6} with integrated cloud cover less than 90% for 1/16/79, 0600Z. The aerosol backscatter has been multiplied by the lidar wavelength squared.
- Figure E.7: Global integrated cloud cover from the top of the atmosphere to the earth's surface for 1/16/79, 0600Z.
- Figure E.8: Results of a scan angle trade involving global coverage and grid volume wind observation accuracy. In the top panel, the % global coverage vs. nadir scan angle is shown for three (40° , 60° and 98°) orbit inclinations (orbit altitude is 525 km). In the lower panel, the σ_0 for a 100×100 km grid area where $\sigma_s = 2 \text{ m s}^{-1}$ is shown as a function of nadir scan angle for the upper troposphere and the PBL.
- Figure E.9: An example of the energy vs. prf trade for regions of high and low SNR defined by the 20 j system.

LOG AEROSOL BACKSCATTER ($\mu\text{m}^2 \text{ m}^{-1} \text{ sr}^{-1}$)



OVER -4.0
-4.2 TO -4.0
-4.3 TO -4.2
-4.6 TO -4.3
-5.0 TO -4.6
-5.2 TO -5.0
-5.3 TO -5.2

WAVELENGTH: 9.11 μm

-5.6 TO -5.3
-6.0 TO -5.6
-6.2 TO -6.0
-6.3 TO -6.2
-6.6 TO -6.3
-7.0 TO -6.6
BELOW -7.0

SURFACE

Figure E.1

LOG AEROSOL BACKSCATTER ($\mu\text{m}^2 \text{ m}^{-1} \text{ sr}^{-1}$)



OVER -4.0
-4.2 TO -4.0
-4.3 TO -4.2
-4.6 TO -4.3
-5.0 TO -4.6
-5.2 TO -5.0
-5.3 TO -5.2

WAVELENGTH: 2.1 μm

-5.6 TO -5.3
-6.0 TO -5.6
-6.2 TO -6.0
-6.3 TO -6.2
-6.6 TO -6.3
-7.0 TO -6.6
BELOW -7.0

SURFACE

Figure E.2

RELATIVE HUMIDITY AT THE SURFACE



21 -	< 28	56 -	< 63	91 -	- 100
14 -	< 21	49 -	< 56	84 -	< 91
07 -	< 14	42 -	< 49	77 -	< 84
00 < ■	< 07	35 -	< 42	70 - ■	< 77
00 - ■		28 -	< 35	63 -	< 70

0600Z

1/16/79

Figure E.3

LOG ATTENUATED BACKSCATTER ($\mu\text{m}^2 \text{ m}^{-1} \text{ sr}^{-1}$)



OVER -4.0
-4.2 TO -4.0
-4.3 TO -4.2
-4.6 TO -4.3
-5.0 TO -4.6
-5.2 TO -5.0
-5.3 TO -5.2

-5.6 TO -5.3
-6.0 TO -5.6
-6.2 TO -6.0
-6.3 TO -6.2
-6.6 TO -6.3
-7.0 TO -6.6
BELOW -7.0

WAVELENGTH: 2.1 μm

SAT. ALT. - 525 KM

NADIR ANG. - 45°

SURFACE

Figure E.4

LOG ATTENUATED BACKSCATTER ($\mu\text{m}^2 \text{ m}^{-1} \text{ sr}^{-1}$)



OVER -4.0
 -4.2 TO -4.0
 -4.3 TO -4.2
 -4.6 TO -4.3
 -5.0 TO -4.6
 -5.2 TO -5.0
 -5.3 TO -5.2

-5.6 TO -5.3
 -6.0 TO -5.6
 -6.2 TO -6.0
 -6.3 TO -6.2
 -6.6 TO -6.3
 -7.0 TO -6.6
 BELOW -7.0

WAVELENGTH: 9.11 μm

SAT. ALT. - 525 KM

NADIR ANG. - 45°

SURFACE

Figure E.5

LOG ATTENUATED BACKSCATTER ($\mu\text{m}^2 \text{ m}^{-1} \text{ sr}^{-1}$)

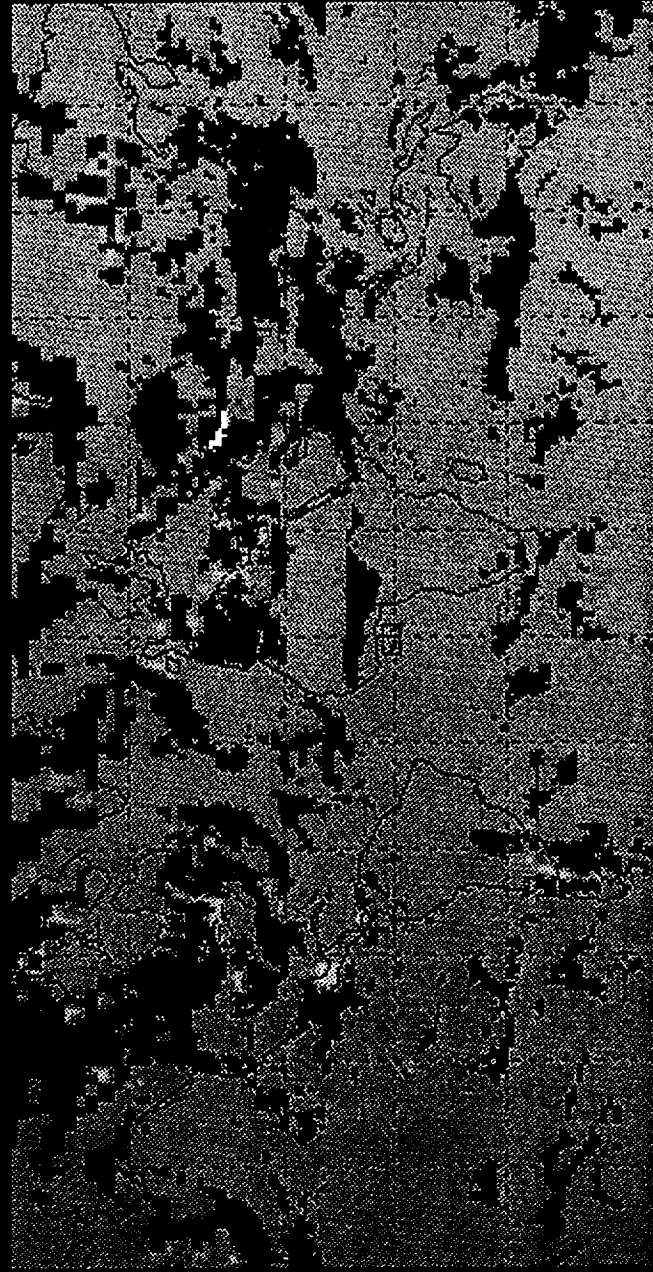


Figure E.6

INTEGRATED CLOUD COVER FROM THE TOP OF THE ATMOSPHERE TO THE SURFACE OF THE EARTH



91 -	- 100	56 -	< 63	21 -	< 28
84 -	< 91	49 -	< 56	14 -	< 21
77 -	< 84	42 -	< 49	07 -	< 14
70 -	■ < 77	35 -	< 42	00 < ■	< 07
63 -	< 70	28 -	< 35	00 -	■

Figure E.7

SCAN ANGLE VS ACCURACY AND GLOBAL COVERAGE RESOLUTION VOLUME

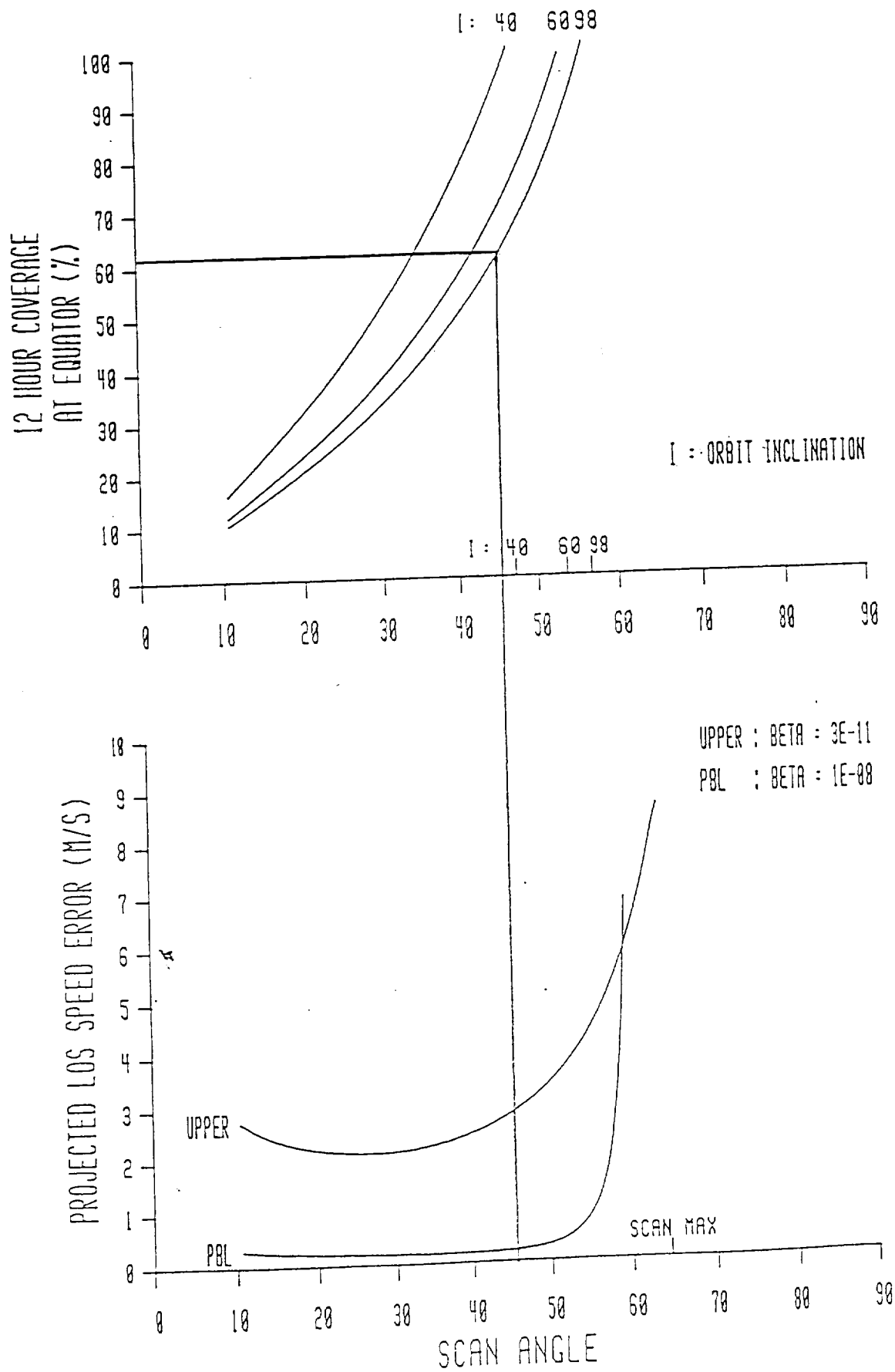


Figure E.8

ENERGY .VS. PRF TRADE

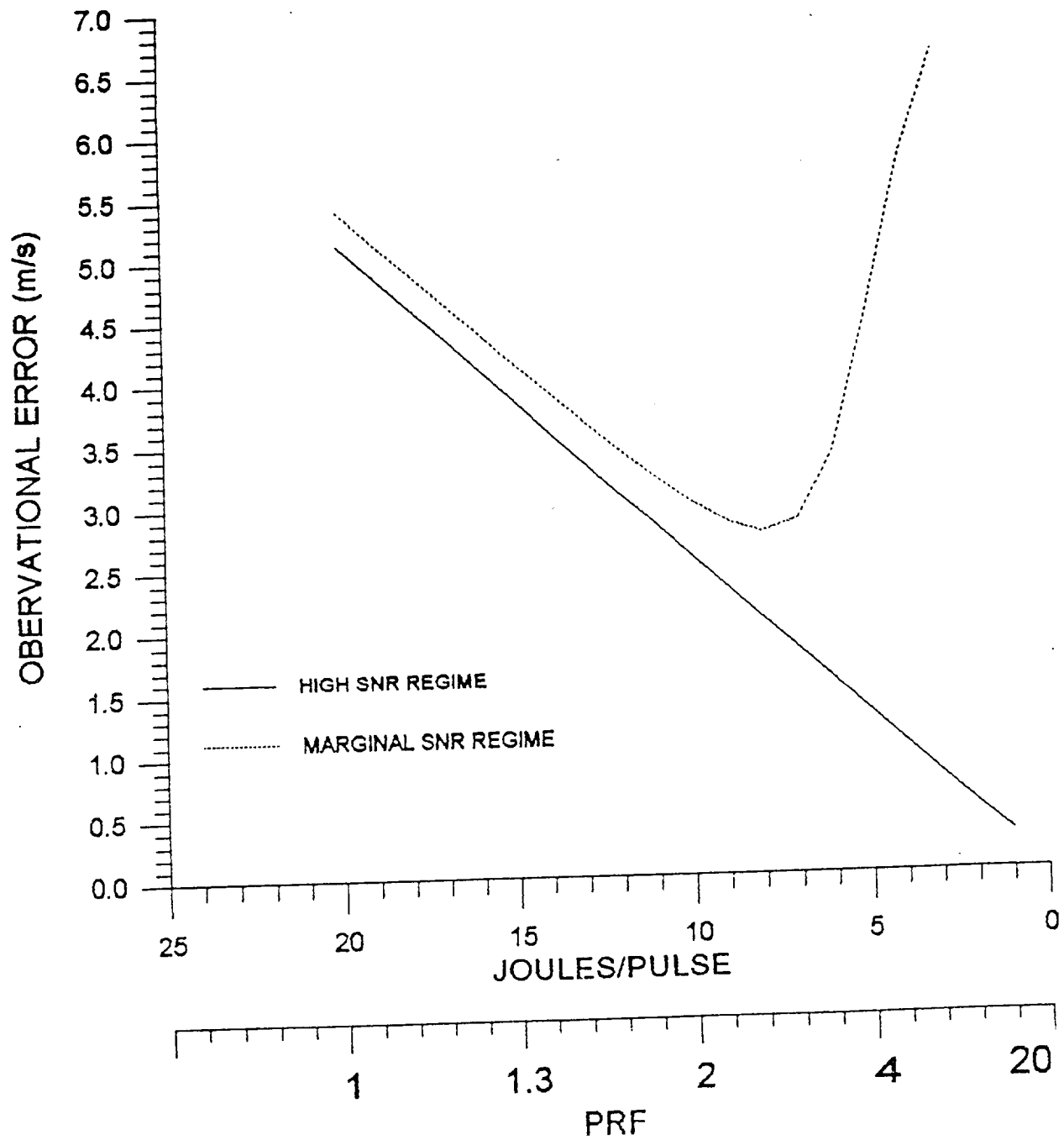


Figure E.9

APPENDIX F

HDF FORMAT FOR GLOBE DATA

The GLOBE database project involves the development of a system for archiving, distributing and retrieving aerosol data obtained from seven different sites. Over the past several months, we have worked on completing the archival strategy for one site (GSFC) with the goal of developing a storage format that will be useful for data from all of the sites. We focussed on several factors when creating the format for storing data from GSFC. First, data storage needed to be both efficient and consistent. Our goal was to maintain consistency in the format so that it could be used for all sites, while making the best possible use of disk space. Second, we developed a storage format from which data could easily be retrieved, both by internal project scientists and by external users. This involved using reliable and freely available database management tools and maintaining information about the data as part of the storage format.

The GLOBE database project scientists at MSFC had already begun to develop a system of data storage using the database management system known as the Hierarchical Data Format (HDF). HDF is distributed by the National Center for Supercomputing Applications (NCSA) and is freely available to users. We chose to continue using HDF to format the data because it met the criteria outlined above, and it is also the data format distributed by the DAACs.

HDF consists of a set of routines that are callable either from C or Fortran. These routines allow for the storage of many data blocks in one file. They also allow the user to store meta-data referring to either individual data blocks or the file as a whole. Thus, a wide range of meta-data can be saved, from information about variables themselves (e.g., their units of measure) to information about the creation of the dataset as a whole (e.g., the type of equipment used for data collection). Although the original computer programming for the storage of GLOBE data was done in Fortran, we agreed to re-write these programs in C as part of the project, so that all programs would be written in one language. C is the language of choice when using HDF because it allows for more flexibility in formatting and because some new HDF functions are not callable from Fortran.

The first phases of work on the GLOBE database project began in early March after we received and configured a Silicon Graphics workstation. HDF (version 3.2R3) was downloaded from NCSA and compiled on our computer. It was tested using examples provided by NCSA and with small sample datasets created at SWA. After this initial testing period, we downloaded two sample datasets which were provided by Dean Cutten of MSFC. These datasets contained similar information but were from two different sites (GSFC and JPL). They were representative of the

different formats in which the data are received. We focussed on the GSFC data as our test case for developing a complete system for formatting the data.

We continued our initial testing process by creating a small sample HDF data file from the GSFC data provided by MSFC. The practicality of creating data blocks and header information for those blocks was tested. Also, we checked to be certain that we could access the data files using HDF utilities such as XCollage (which creates screen images from HDF data files), and we tested the creation of histograms and raster images from other sample HDF files. This was done to ensure that HDF would suit our needs for reliability and usefulness to external users.

After completing this initial testing phase, we began work on re-writing the Fortran programs provided by Dean Cutten for formatting the GSFC data. Our goal was to create new C programs that would incorporate all of the information saved in the old programs while modifying the database structure and adding some information that was not previously saved. Toward this end, we began with a sample dataset that contained only one block of data collected at GSFC. This data block was used to test all aspects of data storage, and the program was expanded to store many data blocks only after the test block was successfully formatted in an HDF data file.

The HDF format that was developed for storing each data block consists of several components. First, the data are stored in an unmodified form as a matrix of data points. Second, information about the data block is stored as a separate matrix associated with the data matrix. This matrix contains the numeric header information, and it consists of the following variables:

- Number of layers in the data block
- Lidar pointing up (1) or down (2)
- Start Year (indicating the beginning of data collection)
- Start Month
- Start Gregorian Day
- Start Julian Day
- Start Hour
- Start Minute
- Start Second
- End Year (indicating the end of data collection)
- End Month
- End Gregorian Day
- End Julian Day
- End Hour
- End Minute
- End Second
- Start Latitude
- Start Longitude

Start Altitude
 End Latitude
 End Longitude
 End Altitude
 Maximum Latitude
 Maximum Longitude
 Maximum Altitude
 Minimum Latitude
 Minimum Longitude
 Minimum Altitude

Our program obtained some of this information directly from the raw data files provided by GSFC. For instance, the direction in which the lidar is pointing is available in the original data file. Other variables are created or modified by the program before being stored in HDF. For example, our program provides routines for converting Julian days to Gregorian days and vice versa. Also, the position information stored as part of the numeric header is interpolated by the program using data obtained from DADS data files provided by Dean Cutten at MSFC. This was done to maintain consistency between sites. Although position information is provided by GSFC in their data files, other sites do not provide this information. It was felt that the use of one source for latitude, longitude and altitude information would be more consistent than relying on multiple sources depending on the original site of data collection.

In addition to the numeric header, two other pieces of information are stored with each block of data in an HDF file. First, a short block label is assigned to each block. This label provides information about the start year, Julian day, hour, minute and second of data collection (formatted as yydddhhmmss). Although these data are already available in the numeric header matrix, the short label provides easy access for a user who might wish to retrieve a data block collected at a particular time. Second, a block descriptor is also associated with each block of data. This consists of numeric information that is specific to GSFC (that is, it does not generalize across sites) and thus was not included as part of the numeric header for the data block.

Several categories of meta-data stored in each HDF data file did not pertain to individual data blocks but were instead associated with all blocks of data stored in the file. These types of information were stored only once in each data file. They fall into four different classifications. First, every HDF data file contains a file label. This is a short text string that consists of the project name (GLOBE I or GLOBE II), the flight number, the institution from which the data were received, and the instrument that was used for data collection. Second, a longer file descriptor is saved with each HDF file. This contains information about whether the flight was transit or local, the start and end locations for the flight (saved as city

names rather than latitude and longitude coordinates), and any special comments regarding the flight (such as its purpose). The information stored in the file descriptor is obtained by user input during the archival procedure.

The third type of data stored at the file level consists of a number of text header fields that contain information about the flight and the scientists involved in the flight. The following fields are saved as part of the text header:

- Task Type
- Experiment Name
- Experiment Sub-Name
- Platform
- Instrument Type
- Instrument Name
- Processing Level
- PI Name
- PI Phone
- PI E-Mail Address
- PI Fax
- Other Researcher's Name
- Other Researcher's Phone
- Other Researcher's E-Mail Address
- Other Researcher's Fax
- Institution

These fields represent information that might be of use during data retrieval, when a user might want to search data files to find particular instruments or experiments or to contact the PI with questions about the data. All of the fields are obtained from user input during the archival process with the exception of the institution. This field refers to the site from which data are received. It is specific to the data being processed, and it is assigned by the program.

Finally, each HDF file contains documentation stored on the file level that describes the process by which the file was created so that the history of each dataset is preserved. This documentation consists of the following variables:

- HDF File Creation Date
- HDF File Creation Time
- Program Name and Version used for HDF File Creation
- Processing Steps
- Remarks

Information about 'processing steps' include details about when and in what form the data were received from the original source, the types of transformations that were performed on the data, and the process by which the data were stored in an HDF format. This differs from the 'remarks' section in which information about the

experiment itself is stored (e.g., details about instrument performance, weather problems, etc). This type of documentation was saved for two purposes. First, it provides a user with useful information about the condition and storage of the data. Second, it documents every transformation that has occurred in the data so that earlier versions of the data can be recreated if necessary.

The HDF format outlined above represents a departure from the format previously used by the GLOBE database project in several ways. First, this format allows all information (data and meta-data) to be stored in one HDF file. The previous format used two separate files to store these types of information. Second, the current format stores more meta-data than did the previous format. New storage objects include the file level header information and documentation. In November, Dina Bai travelled to MSFC to meet with David Bowdle and Dean Cutten regarding the status of the GLOBE database project. Further changes in the format were made at that meeting and are also reflected in the structure outlined above. Specifically, more detailed information was added to the text header and documentation sections of the meta-data, and the format for other sections, such as the short file and block labels and descriptors, was decided at that time.

Much of the discussion during the November meeting at MSFC centered on the method by which GLOBE data might later be distributed to and retrieved by interested scientists. We have developed a system for archiving data from GSFC to an HDF file format in such a way as to provide both the experimental data and information about that data in one package. Although we concentrated on data obtained from one site, the current format should be applicable to data from the other GLOBE database project sites with little modification. Some programming will be necessary to achieve this goal since raw data files from each site are formatted differently. As regards the distribution and retrieval of the data, the use of HDF is consistent with the data format distributed by the DAACS and the format that will eventually be distributed by EOSDIS. These systems appear to be the best avenue of distribution for GLOBE data because they allow scientists to search for variables of interest to them. If the GLOBE data is to reside on one of these systems in the future, several steps will need to be taken. It will be necessary to isolate relevant meta-data into separate files to be used by the DAAC to create searchable fields for the data files. Also, retrieval programs and documentation generally describing the data would need to be written. These would be provided to users when they retrieved GLOBE HDF data files so that the user could interpret and use the data. The creation of the archival system for GSFC data is the first step toward developing a more general system of archival and distribution for all of the GLOBE project data.

APPENDIX G
CONFERENCE PRESENTATIONS AND PAPERS

1991:

AMS 71st Annual Meeting, Seventh Symposium on Meteorological Observations and Instrumentation, Special Session on Laser Atmospheric Studies, New Orleans, LA, January

- a. "Optimal Nadir Scan Angle for a Space-Based Doppler Lidar Wind Sounder" (G.D. Emmitt)
- b. "Clear Line of Sight (CLOS) Statistics Within Cloudy Regions and Optimal Sampling Strategies for Space-Based Lidars" (G.D. Emmitt and G. Séze)
- c. "Simulating Thin Cirrus Clouds in Observing System Simulation Experiments (OSSE) for LAWS" (G.D. Emmitt and S.A. Wood)
- d. "A Reference Atmosphere for LAWS Trade Studies: An Update" (S.A. Wood and G.D. Emmitt)
- e. "Implications of Several Orbit Inclinations for the Impact of LAWS on Global Climate Studies" (R. Atlas and G.D. Emmitt)

AMS 71st Annual Meeting, Second Symposium on Global Change Studies, New Orleans, LA, January

- a. "Using a Global Spectral Model in an Observing System Simulation Experiment for LAWS - An EOS Wind Measuring System" (T.N. Krishnamurti, J. Xue, G. Rohaly, D. Fitzjarrald, G.D. Emmitt, S. Houston and S.A. Wood)

Optical Remote Sensing of the Atmosphere, Fifth Topical Meeting, Williamsburg, VA, November

- a. "Global Three-Dimensional Distribution of LAWS Observations Based Upon Aerosols, Water Vapor and Clouds" (S.A. Wood, G.D. Emmitt and L.S. Wood)

1992:

Sixteenth International Laser Radar Conference, Cambridge, MA, July

- a. "Identification of Critical Design Points for the EAP of a Space-Based Doppler Lidar Wind Sounder" (G.D. Emmitt and S.A. Wood)

1993:

Optical Remote Sensing of the Atmosphere, Sixth Topical Meeting,
Salt Lake City, UT, March

- a. "Simulation Space-Based Doppler Lidar Wind Measurements Using Ground-Based Single Shot Observations" (G.D. Emmitt, J. Dieudonné, S.A. Wood and L. Wood)

Atmospheric Transmission Models Annual Conference, Boston, MA,
June

- a. "Integration of Lowtran into Global Circulation Models for Observing System Simulation Experiments" (S.A. Wood and G.D. Emmitt)

7th Conference on Coherent Laser Radar Applications and Technology, Paris, France, July

- a. "Using Ground-Based Coherent Doppler Lidars to Evaluate Algorithms for Shot Management and Signal Processing of Proposed Space-Based Wind Sounders" (G.D. Emmitt)

1994:

AMS 7th Symposium on Global Climate Studies, Nashville, TN,
January

- a. "Resolving Ageostrophic Winds With a Space-Based Doppler Lidar Wind Sounder. To be presented.

OTHER PUBLICATIONS

1992:

"Lower atmospheric wind velocity estimates using single shot lidar", J.A. Dieudonné, Undergraduate degree paper, University of Virginia, December.

OPTIMAL NADIR SCAN ANGLE FOR A SPACE-BASED
DOPPLER LIDAR WIND SOUNDER

George D. Emmitt

Simpson Weather Associates, Inc.
Charlottesville, Virginia

1. INTRODUCTION

The choice of a nadir scan angle is critical to the overall performance of a space-based Doppler lidar wind sounder such as the LAWS (Laser Atmospheric Wind Sounder). The scan angle determines the average signal strength, performance in regions of marginal backscatter, global coverage (i.e., swath width), spatial resolution and accuracy. A LAWS computer simulation model has been used to conduct a series of trades between scan angle and accuracy/coverage to determine the optimal scan angle. The current "baseline" angle for LAWS is 45°. Factors included in this study were vertical backscatter profiles, advanced signal processing, pulse lengths, shot density, and vertical velocity variance.

2. MODEL DESCRIPTION

The LAWS Simulation Model (LSM) has been developed to provide simulated data to atmospheric models for evaluating both LAWS sampling patterns as well as providing data for model assimilation forecast impact studies. In this case we have used a subset of the model programs to look at the issue of optimal nadir angles for the LAWS telescope.

The following baseline data were used in the scan angle trade studies:

10 Joule laser	$\lambda = 9.11 \mu\text{m}$
1.5 meter mirror	705 km polar orbit
3 μs pulse	
10 pulses/second	
6 RPM scanner	

The atmosphere was assumed to be cloud-free tropical maritime. Turbulence on the scale of the lidar pulse ($\sim 450 \text{ m}$) was taken to be $\sigma_u = \sigma_v = \sigma_w = 1.0 \text{ m s}^{-1}$.

All computations were done for 1 km layers with averaging of the number of range gates (N_R) within the layer. For instance, at a scan angle of 45° the number of range gates that can be averaged is 4.

Since single lidar shots have such a small sample volume (a cylinder with diameter = 10 m and length = 450 m), in most applications there will be some averaging. We have defined a resolution volume as being $100 \times 100 \times 1 \text{ km}^3$. The number of shots (N_s) to average or be used in any wind vector computation algorithm will then vary with scan angle.

3. MODEL EXPERIMENT

Basically the following tendencies are traded against each other in a series of experiments to define an optimum scan angle - an optimum that has a different value in the mid and upper troposphere than in the planetary boundary layer.

As the nadir scan angle is increased:

SNR (Signal to Noise) decreases due to increased slant range and pathwise attenuation.

N_R increases as the slant depth of a 1 km layer increases.

N_s decreases as the slant depth of a 1 km layer increases.

Horizontal wind projection into LOS increases.

Vertical wind (shot scale) induced errors decrease.

4. RESULTS

In Fig. 1 we show the LOS speed uncertainty (m s^{-1}) projected into the horizontal plane as a function of nadir scan angle for a single laser shot into the upper troposphere and lowest 1 km of the earth's atmosphere for expected backscatter values. We expect β values near 10^{-8} in the boundary layer and therefore the LAWS baseline scan angle of 45° appears to be nearly optimum for this region.

In the mid to upper troposphere the expected backscatter is on the order of 10^{-11} . Using the value of 3×10^{-11} we get an optimum scan angle of 38-40°.

When we express our measurement uncertainties for the target resolution volume of $100 \times 100 \times 1 \text{ km}^3$, we find that the optimum scan angle moves toward smaller nadir angles since the number of shots (N_s) available per resolution volume increases as the scan angle decreases. In the boundary layer (Fig. 2) the performance sensitivity is rather weak for the expected 10^{-7} to 10^{-8} backscatter. In the mid-upper troposphere we find an optimum for 3×10^{-11} near a scan angle of 25°. Given that most of LAWS scan domain below 15 km will involve such low aerosol backscatter, we may want to reconsider the 45°

baseline angle.

The scan angle/accuracy trade cannot be done without regard to the scan angle/global coverage trades. In Figs. 1 and 2 we illustrate both trades for the single shot and resolution volume cases respectively. In Fig. 1 for single shot performance, the LAWS baseline case is noted with a line at 45° scan angle. At this angle we are nearly optimum in the PBL, slightly less than optimum in the upper troposphere and will achieve approximately 62% coverage at the equator in 12 h for a polar orbit. For comparison, we also show the equatorial cover for the inclined orbits of 40 and 60°. The additional tic marks labeled 40, 60, and 98 on the scan angle axis indicate the full coverage scan angle for those orbit inclinations. The same trades for the resolution volume are shown in Fig. 2.

5. CONCLUSIONS

We are continuing to explore ways to provide the most meaningful basis for selecting LAWS system design and configuration parameters. While we can do more of what is shown in the figures discussed above, the broader issue of science impact must be addressed from the global coverage perspective as well as the measurement accuracy viewpoint.

A coverage vs accuracy trade is difficult to make analytically. The importance of gaps in the coverage is best evaluated with a GCM. Perhaps more important than the gaps themselves is the persistence of their locations for sun synchronous and low inclination orbits.

6. ACKNOWLEDGEMENTS

This work has been supported in part by NASA Contract NAS8-38559.

SCAN ANGLE VS ACCURACY AND GLOBAL COVERAGE
SINGLE SHOT

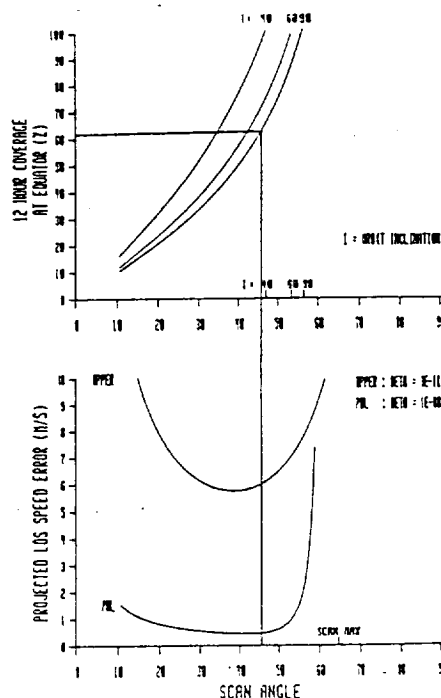


Fig. 1. LOS speed uncertainty ($m s^{-1}$) projected into the horizontal plane as a function of nadir scan angle for a single laser shot.

SCAN ANGLE VS ACCURACY AND GLOBAL COVERAGE
RESOLUTION VOLUME

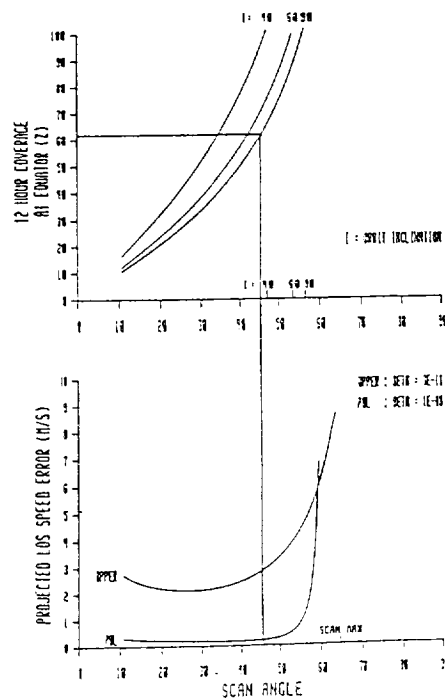


Fig. 2. Performance sensitivity in the boundary layer.

CLEAR LINE OF SIGHT (CLOS) STATISTICS WITHIN CLOUDY
REGIONS AND OPTIMAL SAMPLING STRATEGIES FOR SPACE-BASED LIDARS

G.D. Emmitt

Simpson Weather Associates, Inc.
Charlottesville, VA

and

G. Séze

Laboratoire de Météorologie Dynamique
Paris, France

1. INTRODUCTION

The ability of the LAWS (Laser Atmospheric Wind Sounder) or any other proposed space-based lidar system (e.g., GLARS, ATLID, BEST, ALADIN) to obtain profiles into the planetary boundary layer (PBL) will often depend upon the convolution of the instrument's sampling pattern and the size/space distribution of "holes" in partly cloudy regions. Partly cloudy refers to cloudy areas having subareas (or holes) with optical depths below some specified threshold determined by laser power and wavelength.

Simulated cloud/hole fields as well as LANDSAT imagery were used in a computer model to evaluate several proposed sampling patterns and shot management schemes for pulsed space-based Doppler lidars. In this paper we will limit our discussion to two proposed sampling strategies - one obtained from a conically scanned single telescope and the other from four fixed telescopes that are sequentially used by one laser.

2. DESCRIPTION OF THE PROBLEM

The impact that a direct, space-based measurement of tropospheric winds will have on our understanding of global circulations and climate change is expected to be significant. This is particularly true in the tropics. If the future laser wind sounders are going to provide important PBL measurements over the tropical oceans, they will do so as clouds permit.

We know from satellite cloud climatologies that, on the average, 50-55% of the globe is covered by cloud. The distribution of that coverage by latitude is shown in Fig. 1. Are we to assume then that we will get measurements into the PBL only 30% of the time in some tropical latitudinal bands? We expect that not to be the case since the lidars, with beam diameters of a few 10's of meters, will find holes in some of the cloud classified by the satellite cloud algorithm. We further expect that efforts within the International Satellite Cloud Climatology Program (ISCCP) will eventually provide better statistics on global cloud coverage at finer resolution.

However, at this point in time we would like to answer the question, "Given a target resolution area and the current technical limitations of the proposed space-based lidar wind sounders, are there any sampling patterns that maximize the number of resolution areas with vertical soundings to the PBL?"

The answer you get to the question posed above depends upon the choice of a resolution area. The choice of the resolution area depends upon the intended use (climate models, forecast models, mesoscale studies, etc.) and the desired accuracy. In this case accuracy includes measurement errors as well as errors of representativeness. In this study we have chosen to pose the question in terms of the lidar constraints and expected measurement accuracies. - "How does the number of accurate wind measurements obtained within the scan domain of the lidar systems vary as a function of sampling pattern?"

3. DESCRIPTION OF THE SAMPLING PATTERNS

Both the LAWS and ALADIN systems employ conical scanning of the laser beam with pulse repetition frequencies (PRF) of 2-10 Hz. The resulting pattern from a 500 km orbit altitude is shown in Fig. 2 for a PRF of 10 Hz and a nadir scan angle of 45°.

The average shot density is about 11 shots per 100x100 km² or (about 30 km between samples). The shot density will actually vary across the scan domain but here we assume it constant.

The BEST system, proposed by France, uses four telescopes pointed into the four quadrants of its scan domain. One of the arguments for this sampling approach is that the shots will be clustered into small regions (~ 50x50 km) and thus will provide sufficient sampling on the subgrid scales if tomorrow's GCMs to reduce the representativeness errors due to sparse sampling. The resulting pattern for a 2 Hz BEST system in a 500 km orbit is shown in Fig. 3.

4. EXPERIMENTAL SET UP

We have assumed that the line-of-sight (LOS) measurement accuracy of both lidar systems is equivalent. Since we are looking at the relative advantages of the two sampling patterns we have used the number of shots getting through a cloud scene in a 100x100 km area as the index of accuracy - more correctly, the square root of the number of shots. We call the 100x100 km area our "minimum resolution area".

The "scan domain" is defined by the lateral distance (from satellite ground truth) viewable from the satellite ground track for some specific nadir angle. Here we use 45° for the nadir angle. In our experiments the scan domain has the dimensions of approximately 1000x1000 km. The scan domain thus contains 100 minimum resolution areas.

The first series of experiments has assumed that the cloud cover statistics in each resolution area are the same. Thus, we can answer the question of performance over the domain in terms of two quantities:

P_{100} = percent of resolution areas sampled within scan domain

P_N = probability within a resolution area that (if sampled) N shots will get through to the PBL.

From simple geometry we can calculate that for the pattern in Fig. 2, $P_{100} = 1.00$ and for the pattern in Fig. 3, $P_{100} = .14$.

The probability, P_N , is the focus of our study and is a function of the following factors:

- 1) lidar sampling pattern
- 2) size distribution of holes (or extinction free line-of-sight: EFLOS)
- 3) spatial organization of the holes.

The first factor we can easily specify. The second factor we can simulate using some limited knowledge at the larger scales in our range of interest (100 km) and extend it down to the finer (10 m) scales. The third factor is addressed by the use of real images.

We first set up an experiment using simulated cloud coverage to develop an analysis methodology and to define the types of real cloud scenes we want to examine.

5. EXPERIMENT WITH SIMULATED CLOUD COVERAGE

For this experiment we used simple representations of the LAWS/ALADIN and BEST sample patterns (Fig. 4). While the patterns were fixed, their location and orientation within the 100x100 km area were varied randomly, usually 1000 times per cloud scene.

The cloud scenes were generated using a log-normal distribution of the side dimension of the "box holes". The ratio of the dimension of the largest hole to that of the smallest was kept constant at 100. The total amount of "cloud free"

area was varied from 2% to 50%.

After a cloud scene was constructed (Fig. 5), the two patterns were located at random within the area and a count made of how many shots from each pattern hit holes. This was repeated 1000 times and a histogram constructed (Table 1).

While some small variation did occur for various values of the slope of the log normal distribution, the results in Table 1 were typical.

6. EXPERIMENT WITH OBSERVED SATELLITE CLOUD RADIANCE FIELDS

In this experiment, LANDSAT and SPOT high resolution satellite cloud radiance fields have been used. The LANDSAT and SPOT data sets with a resolution comparable to the diameter of the lidar sample volume (10 m for SPOT, 30 m for LANDSAT), are well adapted to study the effects of the LAWS and BEST patterns. The LANDSAT scene used has been registered during the ICE experiment (International Cirrus Experiment) over North Sea and corresponds to a multi-layered cloud situation. From this scene of about 160 km by 160 km, several sub-scenes of 100 km by 100 km have been extracted (Fig. 6). The determination of the cloudy/clear parts of these sub-scenes used a simple threshold technique.

As in the simulated cloud case, the patterns of LAWS and BEST (Fig. 4) were fixed but their location and orientation within the LANDSAT sub-scene were located at random; the number of shots from each pattern that hits holes were then counted. This was repeated many times and a histogram constructed to test the effect of increasing percentage of clear sky. The reflectivity threshold was arbitrarily increased up to 80% of clear sky. This process was applied to several threshold scenes.

As in the simulated cloud experiments, while some small variations occur from one sub-scene to another, the results in Table 2 are typical. Applying the same treatment to a SPOT scene registered during the FIRE experiment on stratocumulus, we found also the same results in spite of the fact that a 20 km by 20 km scene was interpreted as a 100 km by 100 km scene.

7. CONCLUSIONS

From Tables 1 and 2 we conclude that LAWS, with 11 shots into a resolution area compared to 20 shots for BEST, is more likely to get 1 to 4 shots through the scene. However, as expected, when BEST hits a hole it places more shots into it than does LAWS. The implications of this result must be combined with the other quantity P_{100} (see Section 4).

If we ask the question "in what percent of the resolution areas within the scan domain is a profile based upon at least four samples obtained?" we must multiply P_4 by P_{100} to get the total probability, P_r . When we do that we get

the final result shown in Table 3.

8. ACKNOWLEDGEMENTS

This work has been supported in part by NASA Contract NAS8-38559 and by the Laboratoire de Météorologie Dynamique du CNRS, Ecole Normale Supérieure.

9. REFERENCE

Stowe, L.L., H.Y.M. Yeh, T.F. Eck, C.G. Wellemeyer, H.L. Kyle and The Nimbus-7 Cloud Data Processing Team, 1989: Nimbus-7 global cloud climatology. Part II: First year results. *J. Clim.*, 2, 671-709.

Table 1.

CPER	NHOLE	SIZE	BEST1	LAWS1	BEST4	LAWS4	BEST9	LAWS9
98.1	42	22.3	22.	20.	0.	0.	0.	0.
96.2	61	27.4	46.	35.	1.	0.	0.	0.
94.5	74	30.8	57.	46.	5.	0.	0.	0.
92.5	89	33.4	64.	60.	9.	0.	0.	0.
90.8	101	35.4	67.	61.	11.	2.	0.	0.
89.2	113	37.4	69.	70.	14.	3.	0.	0.
87.4	122	39.1	67.	69.	22.	7.	1.	0.
85.8	136	40.5	79.	83.	25.	6.	0.	0.
84.5	144	41.8	76.	80.	29.	10.	1.	0.
81.9	154	43.0	79.	87.	37.	13.	5.	0.
80.0	167	44.1	78.	90.	39.	16.	8.	0.
78.8	177	45.1	84.	90.	53.	17.	12.	0.
78.2	186	46.1	82.	91.	48.	21.	12.	0.
75.9	192	47.0	85.	98.	49.	24.	13.	0.
74.3	202	47.9	87.	95.	57.	32.	13.	0.
73.3	212	48.7	88.	96.	60.	32.	17.	0.
71.2	223	49.4	87.	97.	61.	46.	22.	0.
70.2	221	50.2	95.	98.	67.	37.	24.	0.
69.9	226	50.9	83.	96.	55.	44.	21.	0.
67.1	237	51.5	89.	99.	61.	50.	26.	0.
65.5	246	52.2	93.	99.	70.	52.	31.	0.
66.1	250	52.8	96.	99.	70.	53.	25.	0.
63.1	262	53.4	93.	99.	70.	40.	35.	2.
62.5	266	53.9	94.	99.	65.	56.	33.	3.
60.4	278	54.5	94.	100.	74.	65.	41.	1.
59.9	282	55.0	93.	100.	68.	61.	34.	3.
58.9	294	55.5	95.	100.	72.	75.	40.	2.
56.8	300	56.0	91.	100.	68.	74.	43.	1.
55.0	310	56.5	96.	100.	74.	75.	44.	2.
57.5	313	57.0	96.	99.	77.	68.	38.	4.

CPER = percent cloud cover
 NHOLE = number of holes in the scene
 SIZE = side dimension (km) of largest hole
 BESTN = percent of the total trials (e.g., 1000) when at least N shots got through a hole for a BEST type pattern
 LAWN = percent of the total trials when at least N shots got through a hole for a LAWS type pattern

Table 2.

CPER	BEST1	LAWS1	BEST4	LAWS4	BEST9	LAWS9
95.	28.	38.	0.	0.	0.	0.
89.	56.	86.	22.	0.	0.	0.
83.	64.	82.	22.	8.	10.	0.
76.	70.	100.	40.	30.	12.	0.
70.	80.	94.	44.	44.	20.	0.
63.	76.	100.	52.	66.	24.	0.
56.	74.	96.	50.	78.	34.	2.
50.	84.	100.	64.	90.	42.	6.
44.	92.	100.	70.	96.	40.	6.
36.	86.	100.	68.	100.	52.	22.
30.	94.	100.	80.	100.	52.	26.
24.	90.	100.	70.	100.	54.	36.

Table 3.

CPER	P4B	P4L	PrB	PrL
95	5	0	.7	0
90	12	3	1.7	3
80	39	16	5.5	16
70	67	37	9.4	37
60	74	65	10.4	65
50	76	78	10.6	78
40	77	90	10.7	90
30	80	100	11.2	100

PrB = total probability (see text) for BEST (in %)

PrL = total probability (see text) for LAWS (in %)

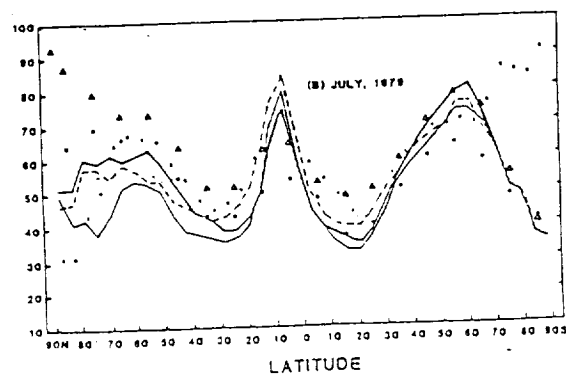


Fig. 1. Zonal averaged total cloud amount for the monthly means of July taken from Stowe et al. (1989).

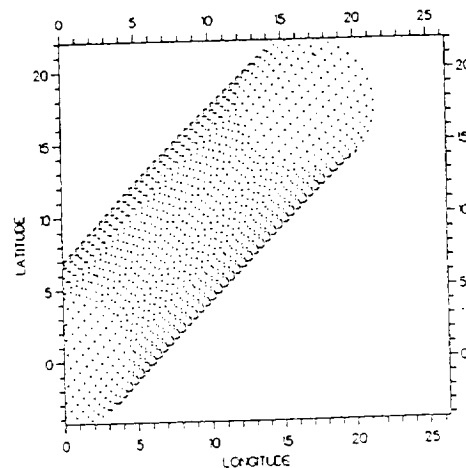


Fig. 2. Resulting pattern from a conical scanning lidar in a 500 km orbit.

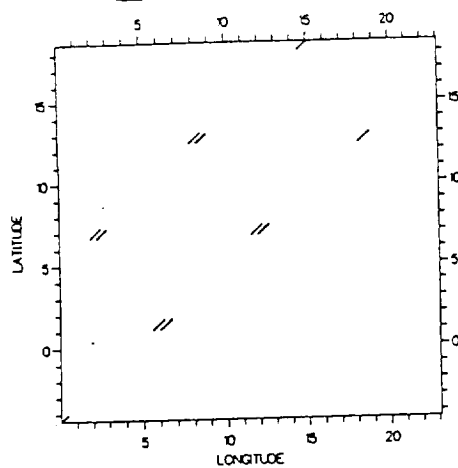


Fig. 3. Resulting pattern for a 2 Hz BEST system in a 500 km orbit.

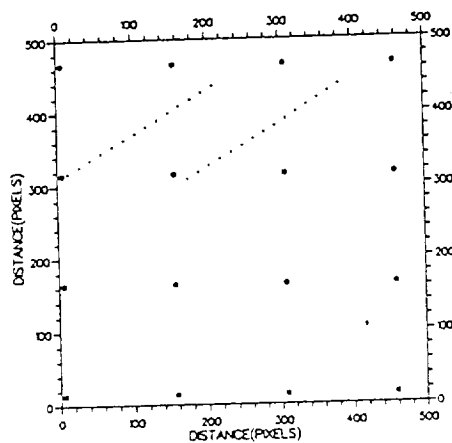


Fig. 4. Simple representations of the LAUS/ALADIN and BEST sample patterns.

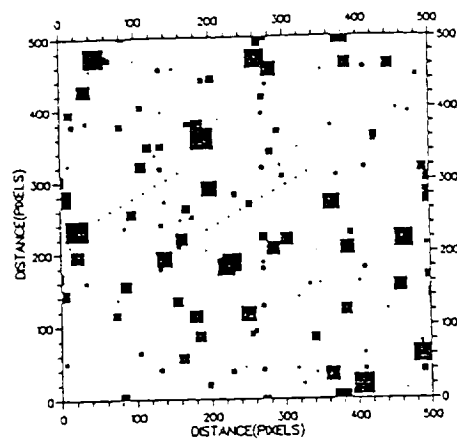


Fig. 5. Example of a simulated cloud scene where the holes (black areas) covers ~ 10% of the area.

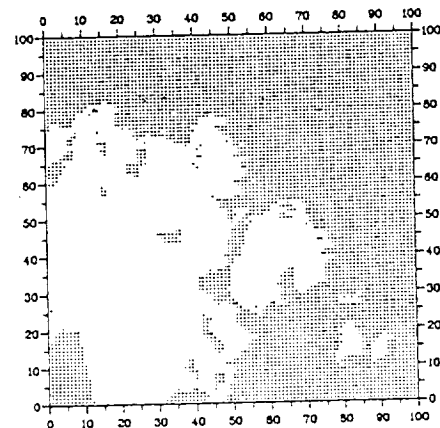


Fig. 6. An example of a SPOT image processed for use in the experiments. Cloud-free area is noted with black dots.

SIMULATING THIN CIRRUS CLOUDS IN OBSERVING SYSTEM
SIMULATION EXPERIMENTS (OSSE) FOR LAWS

G.D. Emmitt and S.A. Wood

Simpson Weather Associates, Inc.
Charlottesville, Virginia

ABSTRACT

Pulsed Doppler lidars can be designed primarily to detect and measure the motion of atmospheric aerosols along the cloud-free lines of sight. Available literature suggests that a space-based lidar system will encounter clouds more than 50% of the time. Since the presence of very thin cirrus clouds is underestimated with today's passive systems, we can expect that lidar cloud return will be even greater.

In addition to realistically simulating the accuracy of a space-based Doppler lidar system such as LAWS, it is important to realistically simulate where measurements will be made. Current simulation studies with Goddard Space Flight Center (GSFC) and Florida State University are attempting to include first order estimates of optically thin ($\tau < 1.0$) clouds based upon grid point data from General Circulation Models (GCMs).

1. INTRODUCTION

A space-based Doppler Lidar Atmospheric Wind Sounder (LAWS) has been proposed by NASA as a facility instrument for the NASA Earth Observing System. A LAWS Simulation Model (LSM) has been developed that, coupled with Global Circulation Models (GCMs), evaluates the potential impact on the predictive skills of current forecast models. Simpson Weather Associates (SWA) is currently participating in Observing System Simulation Experiments (OSSE) by providing realistic LAWS simulation winds and errors for assimilation into NASA/GSFC and Florida State's GCMs (Atlas and Emmitt, 1991; Krishnamurti et al., 1991). It is important to provide these experiments with winds at locations where LAWS measurements will be possible.

Previous studies have shown that, given current LAWS baseline orbital configuration and signal processing capabilities, obtaining mid-level wind information will be very difficult unless sub-visual cirrus is present (Wood and Emmitt, 1990, 1991). In fact, thin cirrus clouds will probably be the primary discriminator between marginal measurement accuracy and resolution in the upper troposphere and some of the best wind measurements made by LAWS.

2. GLOBAL CLOUD CLIMATOLOGIES

Most of our knowledge of global cloud coverage is derived from data obtained with space-based sensors. Climatologies such as those based upon Nimbus-7 data (Stowe et al., 1989) and, more

recently those being generated by the International Satellite Cloud Climatology Program (ISCCP) all find an average global cloud coverage of 50-55%. These climatologies must be considered as climatologies of basically visible cloud. They are suspected of severely underestimating the amount of very thin clouds - clouds with optical depth less than .1 or .2.

To get some idea of the extent of thin cirrus, data taken during the SAGE (Stratospheric Aerosol and Gas Experiment) was processed to get statistics on the frequency of occurrence of upper tropospheric cirrus (Woodbury and McCormick, 1983). That study indicated that in some latitudinal bands, very thin cirrus occurred more than 25% of the time.

We have concluded that any OSSE that omits the contribution of thin cirrus will severely misrepresent both the frequency and accuracy of wind observation in the upper troposphere. For this reason, we are attempting to estimate the presence of such cloud by using model soundings in a cirrus cloud model.

3. MODELING CIRRUS IN THE LAWS SIMULATION MODEL

The LAWS Simulation Model (LSM) simulates LAWS' scanning/sampling and computes line-of-sight radial wind velocities. The model includes the effects of aerosol backscatter, molecular attenuation, atmospheric turbulence, opaque clouds and terrain. The line-of-sight velocity information is used to compute the horizontal wind components. In previous studies, the LSM has been used to address some key LAWS issues and trades involving accuracy and interpretation of LAWS information, data density, signal strength, cloud obscuration and temporal data resolution (Emmitt, 1991; Emmitt and Wood, 1989; Emmitt and Wood, 1988). Currently, SWA is providing global LAWS simulated winds for five days to NASA/GSFC to address the impact of three proposed LAWS orbital configurations. To insure that LAWS winds are represented in the upper troposphere in these simulations, we attempt to simulate the global presence of optically thin cirrus clouds.

The LSM cirrus cloud model is based upon a model obtained from Heymsfield (NCAR). The Heymsfield model computes a profile of cirrus cloud ice water content, along with cloud base and top altitudes, based upon a vertical atmospheric sounding taken with a rawinsonde. The LSM version of the Heymsfield model uses European Center for Medium Range Weather Forecasting (ECMWF) profile data to supply atmospheric soundings as input to determine the presence of cirrus clouds. While the rawinsonde

profile may contain thin layers of near saturation, the ECMWF model rarely shows saturation because of the vertical averaging. Therefore, we have taken an approach which computes a probability of a cirrus layer from the (< 100%) relative humidity in the ECMWF layers above 500 mb. Currently we use a threshold of 70% RH for the probable occurrence of cirrus. As the RH increases so does the probability of a saturation layer. Figure 1 shows a typical ECMWF relative humidity profile depicting a high humidity aloft and thus the likely presence of a cirrus cloud.

Once a cirrus ice profile is determined, the LSM assigns a subvisible cirrus backscatter from the baseline atmosphere library (Wood and Emmitt, 1990, 1991) as a function of cirrus base altitude. The baseline median cirrus backscatter ranges from E^{-9} to $E^{-8} \text{ m}^{-1} \text{ sr}^{-1}$ for altitudes 7 to 14 km, respectively. The LSM uses the LOWTRAN 6 cirrus cloud model (Kneizy et. al., 1983) to approximate cirrus attenuation effects by utilizing the cirrus cloud thickness. The optically thin cirrus attenuation ranges from 0.0001 to 0.15 km^{-1} for cloud thicknesses 0.001 to 1 km, respectively. A future update of the cirrus model will provide thin cirrus optical properties using a radiative transfer model such as Liou et. al. (1990).

Figure 2 is an example showing the location of cirrus cloud profiles for 0000z 11/10/79 that the LSM generated over North America. Contours of the ECMWF 500 mb relative humidity inputs over North America are shown in Fig. 3.

4. CONCLUSIONS

It is too early in this study to conclude whether or not the simulated thin cirrus cloud is realistic. Without much "real" data we are left with primarily sensitivity studies. In the extremes we can assume no clouds other than those provided directly by the ECMWF model or we can generate 20-25% global coverage of additional thin cirrus. If larger differences in the model performance are found between these two extremes we will then be faced with developing a more rigorous algorithm.

5. ACKNOWLEDGEMENTS

This work was supported under NASA contracts NAS8-37779 and NAS8-38559.

6. REFERENCES

Atlas, R., and G.D. Emmitt, 1991: Implications of several orbit inclinations for the impact of LAWS on GCMs and global climate studies. Paper to be presented at the AMS 71st Annual Meeting's Special Session on Laser Atmospheric Studies, New Orleans, LA, January.

Emmitt, G.D., and S.A. Wood, 1988: Simulated space-based Doppler lidar performances in regions of backscatter inhomogeneities. Paper presented at the SPIE's Symposium on Lasers and Optics, Anaheim, CA, January.

_____, and _____, 1989: Simulation of a space-based Doppler lidar wind sounder - sampling errors in the vicinity of wind and aerosol inhomogeneities. Presented at the 5th Conference on Coherent Laser Radars, Munich, Germany, June.

Emmitt, G.D., 1991: Optimal nadir scan angle for a space-based Doppler lidar wind sounder. Paper to be presented at the AMS 71st Annual Meeting's Special Session on Laser Atmospheric Studies, New Orleans, LA, January.

Kneizy, F.X., E.P. Shettle, W.O. Gallery, J.H. Chetwynd, L.W. Abreu, J.E.A. Selby, S.A. Clough, and R.W. Fenn, 1983: Atmospheric Transmittance/Radiance: Computer Code LOWTRAN 6. AFGL-TR-83-0187.

Krishnamurti, G.D. Emmitt, S. Houston, and S.A. Wood, 1991: Using a global spectral model in an observing system simulation experiment (OSSE) for LAWS - An EOS wind measuring system. Paper to be presented at the AMS 71st Annual Meeting's Second Symposium on Global Change Studies, New Orleans, LA, January.

Liou, K.N., T. Takano, S.C. Ou, A. Heymsfield, and W. Kreiss, 1990: Infrared transmission through cirrus clouds: A radiative model for target detection. Appl. Opt., 29, 1886.

Stowe, L.L., H.Y.M. Yeh, T.F. Eck, C.G. Wellemeyer, H.L. Kyle, and the Nimbus-7 Cloud Data Processing Team, 1989: Nimbus-7 global cloud climatology. Part II: First year results. J. Clim., 2, 671-709.

Wood, S.A., and G.D. Emmitt, 1990: A reference atmosphere for LAWS trade studies. Paper presented at the 1990 Optical Remote Sensing of the Atmosphere Topical Meeting, Lake Tahoe, NV, February.

_____, and _____, 1991: A reference atmosphere for LAWS trade studies: An update. Paper to be presented at the AMS 71st Annual Meeting's Special Session on Laser Atmospheric Studies, New Orleans, LA, January.

Woodbury, G.E., and M.P. McCormick, 1983: Global distributions of cirrus clouds determined from SAGE data. Geophys. Res. Lett., 10, 1180-1183.

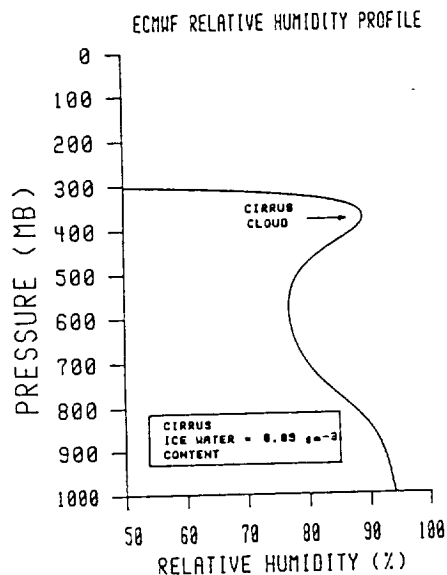


Fig. 1. A relative humidity profile from the ECMWF data set 11/10/79, 0000Z. The Heymsfield cirrus model was used to compute the cirrus ice water content at the higher relative humidities aloft.

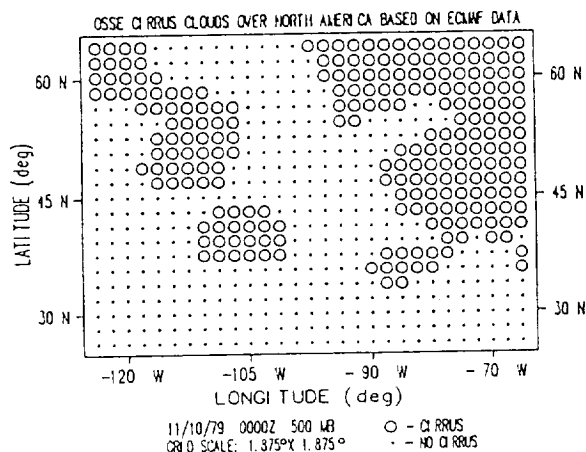


Fig. 2. Locations of cirrus cloud profiles over North America for 11/10/79, 0000Z. The profile locations were determined using the Heymsfield cirrus model and ECMWF gridded profile data.

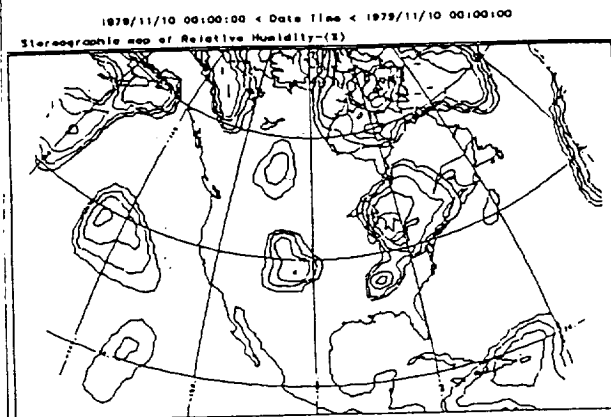


Fig. 3. 500 mb ECMWF relative humidity contour plot over North America for 11/10/79, 0000Z. The relative humidity contours are plotted from 70% to 100%.

A REFERENCE ATMOSPHERE FOR LAWS TRADE STUDIES:
AN UPDATE

S.A. Wood and G.D. Emmitt

Simpson Weather Associates, Inc.
Charlottesville, Virginia

ABSTRACT

A reference atmosphere from the LAWS Simulation Model is used to examine LAWS baseline signal-to-noise (SNR) and line-of-sight (LOS) velocity errors for two proposed LAWS satellite orbits.

1. INTRODUCTION

A space-based Doppler Lidar Atmospheric Wind Sounder (LAWS) has been proposed by NASA as a facility instrument for the NASA Earth Observing System. A LAWS Simulation Model (LSM) has been developed to assess the impact of a space-based Doppler lidar wind profiler on global and regional features. Hardware feasibility and data studies are on-going (Emmitt and Houston, 1987; Emmitt and Wood, 1988; Emmitt and Wood, 1989). The uniqueness of global lidar wind measurements from space raises many fundamental questions that may impact the design of such a system. The distribution of aerosols that provide backscatter, the molecular attenuation that reduces signal strength, the effects of wind shear and turbulence that effect measurement accuracy, and the presence of thin cirrus clouds that can enhance the performance are all issues that must be considered.

This paper describes a candidate reference atmosphere from the LSM's atmospheric library. The reference atmosphere is used to examine LAWS baseline signal-to-noise and line-of-sight velocity errors for two proposed LAWS orbital configurations.

2. REFERENCE ATMOSPHERE

The LSM atmospheric library provides a probabilistic aerosol backscatter profile, a probabilistic thin cirrus cloud backscatter profile, a molecular attenuation profile, a zig-zag wind shear profile, sub-pulse scale turbulence, and a correlated horizontal wind field within a $100 \times 100 \times 15 \text{ km}^3$ volume.

In a previous study (Wood and Emmitt, 1990), a probabilistic aerosol backscatter profile, shown in Fig. 1a, was constructed from ground-based lidar data taken at the Jet Propulsion Laboratory (JPL) and the Wave Propagation Laboratory (WPL). The circles indicate the median value (including data "dropouts") as a function of altitude. The number in the circles is the percentage of total observations associated with that particular

median. The ± 1 sigma error bars were computed from several hundred profiles. The model assumes that backscatter is log normal around the median at all levels. The JPL and WPL lidar data sets did not have any contributions of thin cirrus clouds to the upper tropospheric backscatter. Therefore, the cirrus mode from 7 to 15 km has been estimated based on general reports of high frequency of occurrence of thin subvisual cirrus clouds. The distribution of subvisual cirrus has been estimated as 30% at 7 km as seen from a ground perspective at JPL, Boulder and Hawaii and 50% at 14 km. This is believed to be underestimated for the tropics from a space perspective, where 70-80% may be the closer value. The cirrus relative backscatter is also assumed to be log normal.

In this study, the probabilistic aerosol profile was modified, based on the LAWS Science Team's suggestions, to attempt to better represent a maritime profile. The maritime aerosol backscatter profile is shown in Fig 1b. It is noted that the backscatter near the ocean surface is thought to be much higher than shown.

The molecular attenuation profile, shown in Fig. 2, was generated by a LOWTRAN 7 model and represents attenuation in a tropical maritime atmosphere, Earth's surface. No cirrus cloud attenuation is included. The atmospheric generator creates a "zig-zag" wind shear profile, as shown in Fig. 3. This shear profile allows the effects of wind shear to be considered at any level in the atmosphere. A very general sub-pulse scale turbulence due to wind shear is included. Using Von Karman (-5/3) turbulence spectra for wind shear (Rhyne et al., 1976), the LSM integrates the spectra over the pulse length scale, which is multiplied by an estimated total wind shear turbulence that is proportional to the "zig-zag" shear.

3. A REFERENCE ATMOSPHERE APPLIED TO SNR AND LOS UNCERTAINTY

The reference atmosphere's maritime median backscatter profile, a tropical maritime attenuation profile and a shear layer of 0.005 s^{-1} was used to examine baseline LAWS signal-to-noise and line-of-sight velocity error for satellite altitudes, 705 km and 500 km. The LOS velocity error was based upon pulse-pair autocorrelation processing of the Doppler signal. Figure 4 highlights that SNR for both satellite altitudes were well below 5 dB for the mid-levels and at extreme-scan-angles at the surface. If 5

dB is the threshold SNR for extracting useful line-of-sight wind measurements, then for a scan angle of 45° , a backscatter greater than $E^{-10} \text{ m}^{-1} \text{ sr}^{-1}$ is needed. Figure 5a shows that for an altitude of 705 km, the probability of getting the backscatter needed to obtain a 5 dB SNR is nearly 80% of the time at the surface, but quickly decreases to below 30% in the mid-level to less than 10% at upper levels. Sub-visual cirrus can increase the probability of getting 5 dB from 25% around the tropopause to 50% at 14 km. Figure 5b shows that for a satellite altitude of 500 km, the probability of getting the backscatter needed to obtain a 5 dB SNR is nearly 85% of the time at the surface, but decreases to below 45% in the mid-level to less than 10% at upper levels. Sub-visual cirrus increases the probability of getting 5 dB from 40% around the tropopause to 50% at 14 km.

If we could extract information at a lower threshold SNR, via some advance signal processing, the picture changes significantly. Figures 5a and 5b show that the probability of getting backscatter to obtain a -5 dB SNR is much higher at the upper levels, on the order of 80% and 90% for the satellite altitudes, 705 km and 500 km, respectively. Figure 6 shows the radial velocity uncertainty as a function of signal-to-noise. Errors on the order of $1-2 \text{ m s}^{-1}$ are expected at the surface layer, where SNR is 13 dB. At a SNR of 5 dB, errors on the order of 8 m s^{-1} should be expected. Again, if an advance signal processing scheme could relax the 5 dB threshold by 10 dB, then radial velocity errors at 5 dB could be on the order of 1 m s^{-1} .

4. CONCLUSIONS

We have defined one possible candidate reference atmosphere from the LAWS Simulation Model. We have looked at the baseline signal-to-noise and radial velocity errors at two proposed LAWS satellite orbits, 705 and 500 km, using the reference atmosphere. Based on a tropical maritime atmosphere, we have shown that obtaining wind information in the mid-levels will be difficult unless better signal processing is possible and/or sub-visual cirrus is present. This study does not consider cloud obscuration, particularly in the PBL. A current follow on study is including clear-line-of-sight cloud statistics for penetrating cloudy regions.

5. ACKNOWLEDGEMENTS

This work was supported under NASA Contracts NAS8-37779 and NAS8-38559.

6. REFERENCES

- Ermitt, G.D., and S.H. Houston, 1987: Impact of a space-based Doppler lidar wind profiler on our knowledge of hurricanes and tropical meteorology. American Meteorological Society's 17th Conference on Hurricanes and Tropical Meteorology, Miami, FL, April.
- Ermitt, G.D., and S.A. Wood, 1988: Simulated space-based Doppler lidar performances in regions of backscatter inhomogeneities. Presented at the SPIE's Symposium on Lasers and Optics, Anaheim, CA, January.
- Ermitt, G. D. and S. A. Wood, 1989; Simulation of a space-based Doppler lidar wind sounder - sampling errors in the vicinity of wind and aerosol inhomogeneities. Presented at the 5th Conference on Coherent Laser Radars, Munich, West Germany, June.
- Wood, S.A., and G.D. Ermitt, 1990: A reference atmosphere for LAWS trade studies. Presented at the 1990 Optical Remote Sensing of the Atmosphere Topical Meeting, Lake Tahoe, NV, February.
- Rhine, R.H., H. Murrow, and K. Sidwell, 1976: Atmospheric turbulence power spectral measurements to long wavelengths for several meteorological conditions, NASA Conference, Hampton, VA, pp. 271-286.

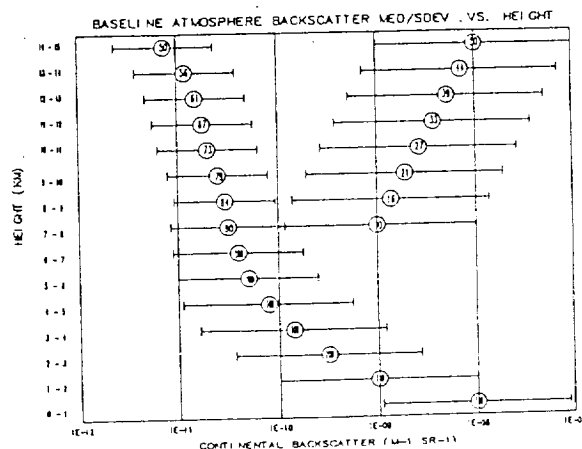


Fig. 1a. Probabilistic continental backscatter profile where locations at the circles indicates the median value including data "drop outs" in the original WPL and JPL profiles. The number in the circle is the percentage of total observations associated with that median. The error bars ± 1 sigma in the log backscatter is based upon several hundred profiles. The cirrus mode above 7 km has been estimated.

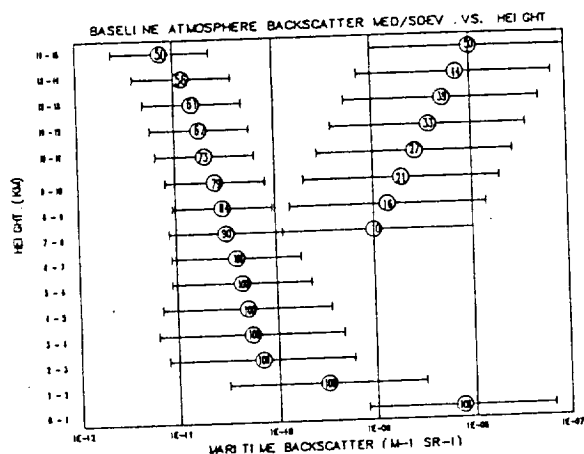


Fig. 1b. Probabilistic maritime backscatter profile where locations at the circles indicates the median value including data "drop outs" in the original WPL and JPL profiles. The number in the circle is the percentage of total observations associated with that median. The error bars ± 1 sigma in the log backscatter is based upon several hundred profiles. The cirrus mode above 7 km and the log tropospheric aerosol mode have been estimated.

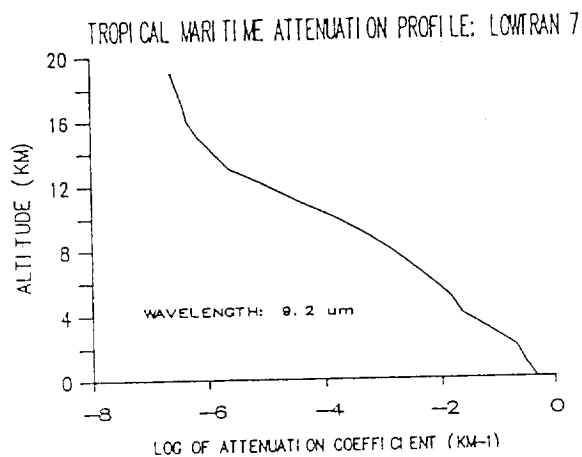


Fig. 2. Average tropical maritime attenuation profile based on LOWTRAN 7 code.

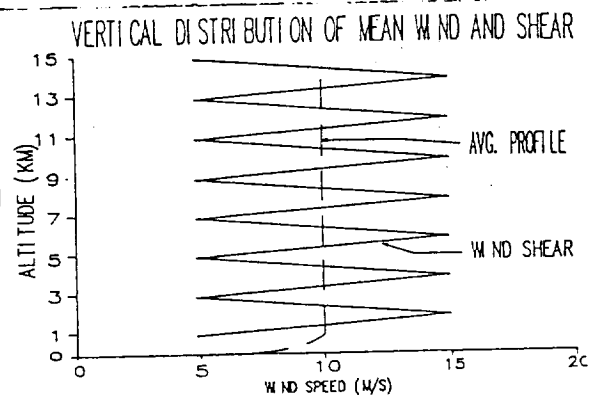


Fig. 3. Reference atmosphere's vertical distribution of mean horizontal wind and a "zig zag" wind shear.

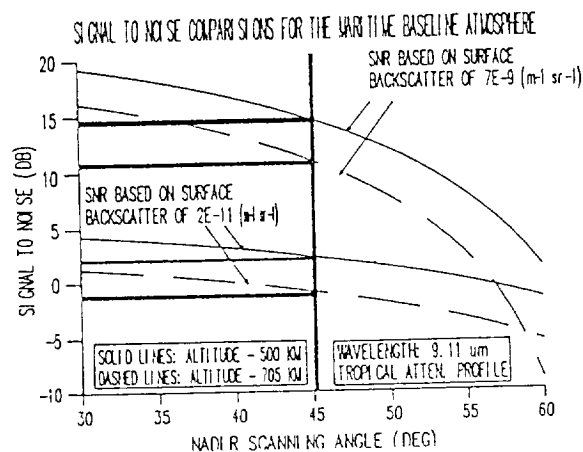


Fig. 4. Signal-to-noise comparison for a tropical maritime atmosphere as a function of nadir scan angle for satellite altitudes 705 and 500 km. A comparison at a scan angle of 45° is highlighted for the surface and mid-altitudes.

Fig. 5. Example of profile of resulting "successful shots" using 5 dB and -5 dB as a threshold for the reference atmosphere.

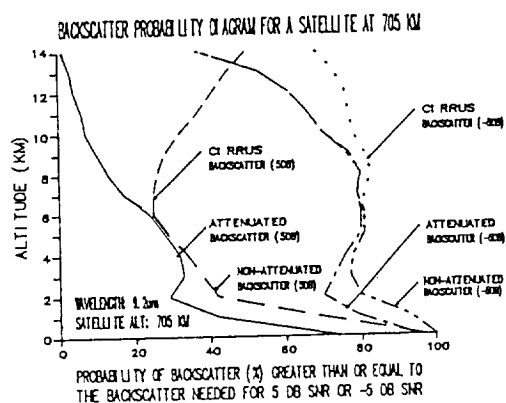


Fig. 5a. Profile is for a 705 km satellite altitude.

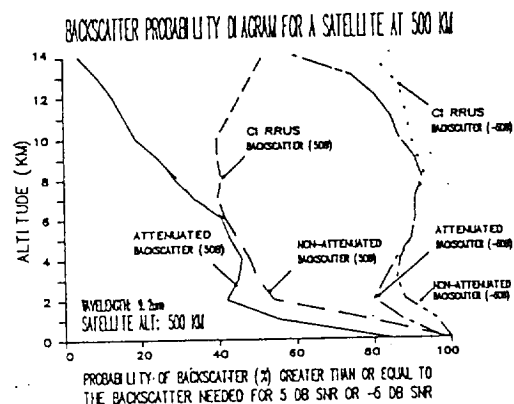


Fig. 5b. Profile is for a 705 km satellite altitude.

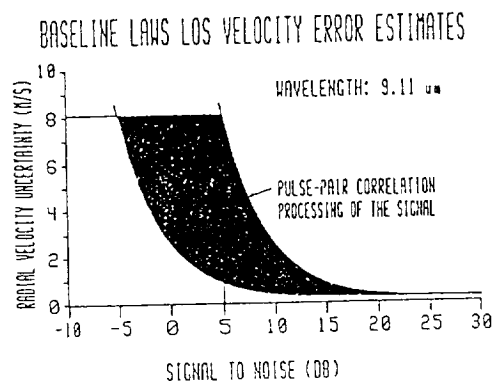


Fig. 6. Radial velocity uncertainty ($m s^{-1}$) as a function of signal-to-noise (dB). The right hand curve is for a pulse-pair correlation processing of the Doppler signal. The left hand curve represents the potential velocity error if the threshold SNR was -5 dB.

IMPLICATIONS OF SEVERAL ORBIT INCLINATIONS FOR THE IMPACT OF LAWS ON GLOBAL CLIMATE STUDIES

R. Atlas
Laboratory for Atmospheres
NASA/Goddard Space Flight Center
Greenbelt, MD 20771

G. D. Emmitt
Simpson Weather Associates
809 E. Jefferson St, Charlottesville, VA 22902

1. INTRODUCTION

Since the advent of meteorological satellites in the 1960's, a considerable research effort has been directed toward the design of space-borne meteorological sensors, the development of optimum methods for the utilization of satellite soundings and winds in global-scale models, and an assessment of the influence of existing satellite data and the potential influence of future satellite data on numerical weather prediction. Observing System Simulation Experiments (OSSE's) have played an important role in this research and in the planning of Data System Tests (DST) and the Global Weather Experiment (FGGE). Such studies have aided in the design of the global observing system, the testing of different methods of assimilating satellite data, and in assessing the potential impact of satellite data on weather forecasting (see Arnold and Dey, 1986 for a review of many of these experiments).

At the present time, OSSE's are being conducted to (1) provide a quantitative assessment of the potential impact of currently proposed space-based observing systems on data assimilation and global change research, (2) evaluate new methodology for the processing and assimilation of specific observing systems, and (3) evaluate tradeoffs in the design and configuration of these observing systems, involving coverage, resolution, accuracy, and data redundancy. Most of this research is concerned with Earth Observing System (EOS) facility instruments. In addition, OSSE's have been conducted to test new methodology for assimilating satellite derived surface wind data and to evaluate its impact on global analyses (Atlas and Bloom, 1989).

In this paper, we report on early results from experiments that are being conducted to evaluate critical issues related to the Laser Atmospheric Wind Sounder (LAWS). Previous simulation studies, conducted by Atlas *et al.* (1985) demonstrated tremendous potential for accurate wind profile observations from space to improve global analysis and prediction. Here we examine questions related to the orbit configuration for LAWS. Specifically, the objective of the current study is to determine the impact on data assimilation of changing the orbit for LAWS from polar to 55 degrees inclination and the impact of lowering the orbit from 705 km to 450 km. Lowering the inclination would benefit studies of diurnal processes and tropical and mid-latitude circulation but would result in the elimination of LAWS wind profile data poleward of about 63°.

2. THE SIMULATION SYSTEM

For these experiments, we make use of the analysis/forecast simulation system, previously employed by Atlas *et al.* (1985). This system consists of the following elements: (1) A long atmospheric model integration, referred to as the "reference atmosphere" or "nature". This integration is assumed to represent the complete record of the "true" state of the atmosphere and is used to fabricate observational reports and to evaluate analyses and forecasts. (2) A series of data assimilation cycles that differ with regard to the data used or the assimilation methodology employed. (3) Atmospheric or oceanic model forecasts using initial conditions provided by the data assimilation cycles.

As in Atlas *et al* (1985), we avoid the "identical twin" character of previous simulation studies by using different models to generate the nature run and for assimilation and forecasting. In the current study, a 1.875° latitude by 1.875° longitude European Centre for Medium Range Forecasts (ECMWF) model forecast from 0000 GMT 10 November 1979 is used as nature, while a 4° latitude by 5° longitude version of the GLA model is used for assimilation and forecasting.

All conventional observations were previously simulated at the National Meteorological Center (NMC) as described by Dey *et al.* (1985) and are identical to those used in the Atlas *et al* (1985) study. In essence, these data were simulated at the appropriate observational locations with random errors added. Satellite temperature soundings (satemps) were simulated at actual Tiros-N observational locations. But in the first few runs to be reported here, the satemps are perfect, i.e., no observational errors were added to the interpolated nature run values.

Simulated LAWS observations were obtained from the LAWS Simulation Model (LSM) developed by NASA (Emmitt and Wood, 1990). The LSM simulates a space-based, conically scanned, pulsed Doppler lidar wind sounder. The model includes: (1) platform motions and orbit parameters; (2) laser/optics parameters such as laser power, frequency stability, pulse length, mirror diameters, etc.; (3) LAWS sampling parameters (e.g., scan rates, scan angle, pulse repetition rates, etc.); (4) measurement accuracy estimation involving aerosols, signal attenuation and atmospheric turbulence; and (5) measurement termination by cloud or earth's surface. The results reported in this paper are based upon a simplified version of the LSM to isolate the sampling and global coverage issues from those related to measurement accuracies.

To generate input winds to the GLA analysis/forecast system, the LSM was applied to ECMWF nature fields. The LSM generated line-of-sight sample locations which were then used to extract both "true" winds and cloud coverage from the ECMWF gridded data. The cloud coverage is derived from the ECMWF temperature and moisture profiles using the AFGL cloud algorithm. A topographic data file was also checked for sample terminations for those shots not obscured by clouds.

In our initial experiments, the LAWS data were simulated without error. Realistic accuracies for LAWS will be simulated in subsequent experiments.

3. PRELIMINARY RESULTS

In this section, we report on results from our initial set of experiments, using the perfect satemps and LAWS winds. For all of the assimilation experiments, a 4° latitude by 5° longitude version of the new GLA general circulation model and a three-dimensional multivariate analysis scheme were used.

Initial conditions for the simulated data assimilations were provided by a four-day assimilation of "real" conventional data, which began at 0000 GMT 6 November 1979, and used the above GLA analysis/forecast system. At 0000 GMT 10 November, five assimilation cycles using simulated data began: (1) a "control," which utilized only conventional data, (2) "satemp," in which the perfect satellite temperature soundings were added to the control, (3) "LAWS," in which the simulated LAWS in a polar, 705 km orbit were added to the satemp experiment, (4) "LAWS 755," which is the same as (3) except that LAWS in a 55° orbit at 705 km are used, and (5) "LAWS 455," which is the same as (3) except that LAWS in a 55° orbit at 450 km are used.

As in earlier OSSE's, the impact of both perfect temperatures and wind profiles is small on the average for the Northern Hemisphere (although cases of significant regional impact occur) and large and beneficial for the Southern Hemisphere. As shown in Figure 1, satemps reduce wind analysis error significantly in the Southern Hemisphere. LAWS data in either orbit improve the analysis significantly further, although the 55° orbit is somewhat degraded relative to the polar orbit. The impact of orbit inclination is shown for both poles (where differences should be largest) in Figure 2. Lowering of the inclination gives a small (probably insignificant) degradation at the North Pole but a substantial degradation at the South Pole. This impact is illustrated in Figure 3, which shows 300 mb wind analysis errors near the South Pole for the satemp, LAWS, and LAWS 755 experiments after two days of assimilation.

The impact of orbit altitude (i.e. the difference between experiments 4 and 5) was found to be negligibly small and is not shown.

400 MB ZONAL WIND - SH. EXTRA TROPICS
LAT: 86S - 30S LONG: 0 - 35SE

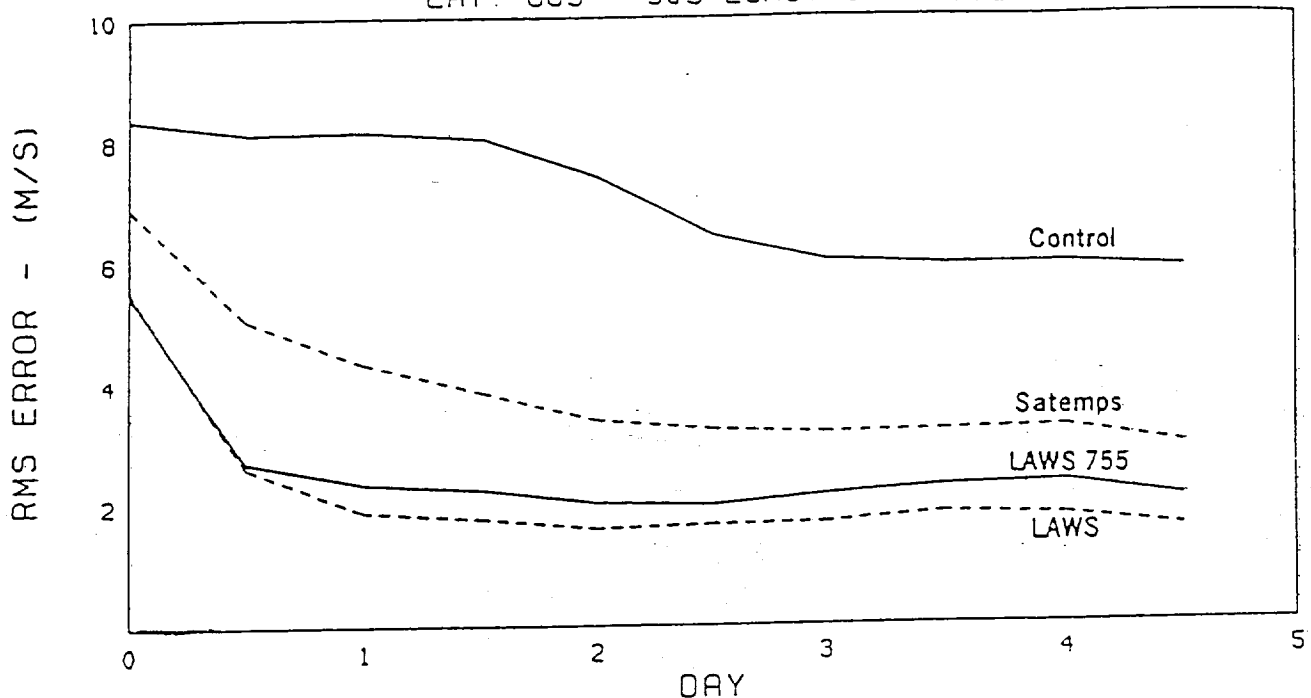


Fig.1 400mb zonal wind analysis error (RMS) for the Southern Hemisphere extratropics for the control, satemp, LAWS, and LAWS 755 experiments.

4. CONCLUSIONS

A preliminary set of experiments was conducted to quantitatively evaluate the impact of changing the orbit inclination and altitude for LAWS. The results to date agree with earlier OSSE's in showing a very large improvement in our ability to represent the global atmospheric circulation using LAWS. The effect of lowering the orbit altitude for LAWS appears to be small. However, the results indicate that lowering the orbit inclination would result in a substantial degradation over Antarctica. This degradation must be weighed against the potential improvements to the representation of the tropics and mid-latitudes. In addition, this result is dependent upon the aerosol distribution near the poles and the ability of LAWS to obtain accurate wind profiles in this region. This and other considerations will be evaluated in upcoming experiments.

ACKNOWLEDGMENTS

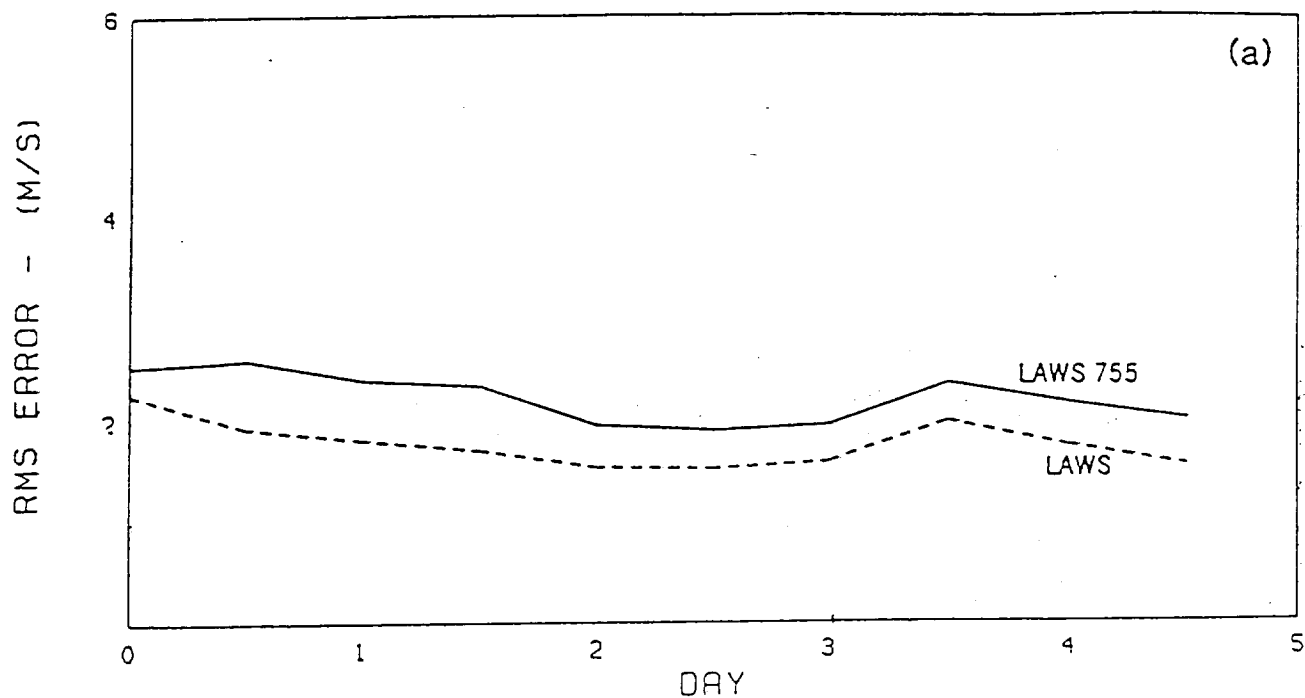
The authors wish to acknowledge G. Brin, J. Terry, J. Ardizzone, and S.A. Wood for their very significant contributions to this project. In addition, we would like to thank Dr. W.E. Baker, the LAWS Team Leader, and Dr. R. Kakar of NASA HQ. for their encouragement. We also would like to thank LAWS Team members for

their helpful comments. Q. Philpot and L. Rumburg prepared the manuscript. This work was supported by NASA Headquarters.

REFERENCES

- Arnold, C. P. and C. H. Dey, 1986: Observing system simulation experiments: Past, present, and future. Bull. Amer. Meteor. Soc., **67**, 687-695.
- Atlas, R., E. Kalnay, W. E. Baker, J. Susskind, D. Reuter, and M. Halem, 1985: Simulation studies of the impact of future observing systems on weather prediction. Preprints Seventh Conference on Numerical Weather Prediction, 145-151.
- Atlas, R. and S. C. Bloom, 1989: Global surface wind vectors resulting from the assimilation of satellite wind speed data in atmospheric general circulation models. Oceans, 260-265.
- Dey, C. H., W. J. Bostelman, and C. P. Arnold Jr, 1985: Design of a Windsat observing system simulation experiment. Proceedings of the NASA Symposium on Global Wind Measurements. Deepak Publishing, Hampton, Va., 73-80.
- Emmitt, G. D. and S. A. Wood, 1990: Space-based Doppler lidar sampling strategies algorithm development and simulated observation experiments. Monthly Progress Rept. under NASA Contract NAS8-38559, October.

400 MB ZONAL WIND - NORTH POLE 1
LAT: 63N - 86N LONG: 0 - 355E



400 MB ZONAL WIND - SOUTH POLE 1
LAT: 86S - 63S LONG: 0 - 355E

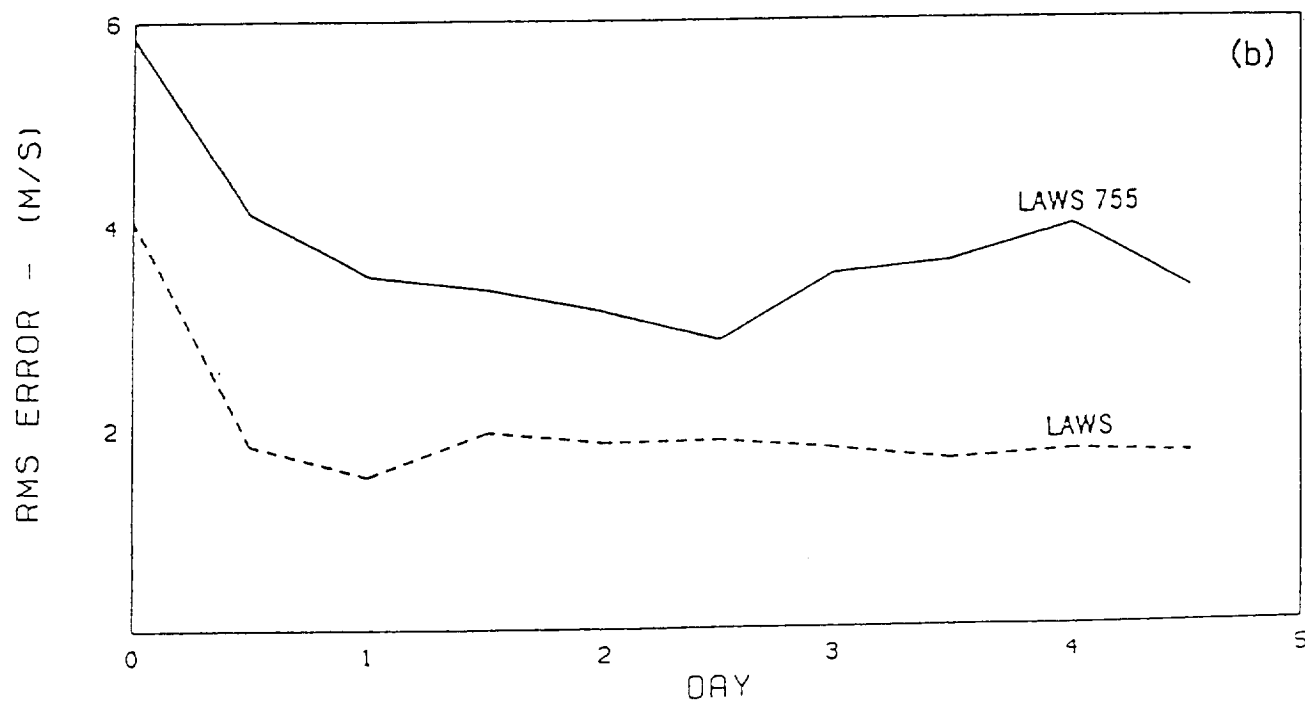


Fig.2 400 mb zonal wind analysis error (RMS) for the LAWS and LAWS 755 experiments (showing the effect of lowering the orbit inclination) for (a) 63-86N and (b) 63-86S.

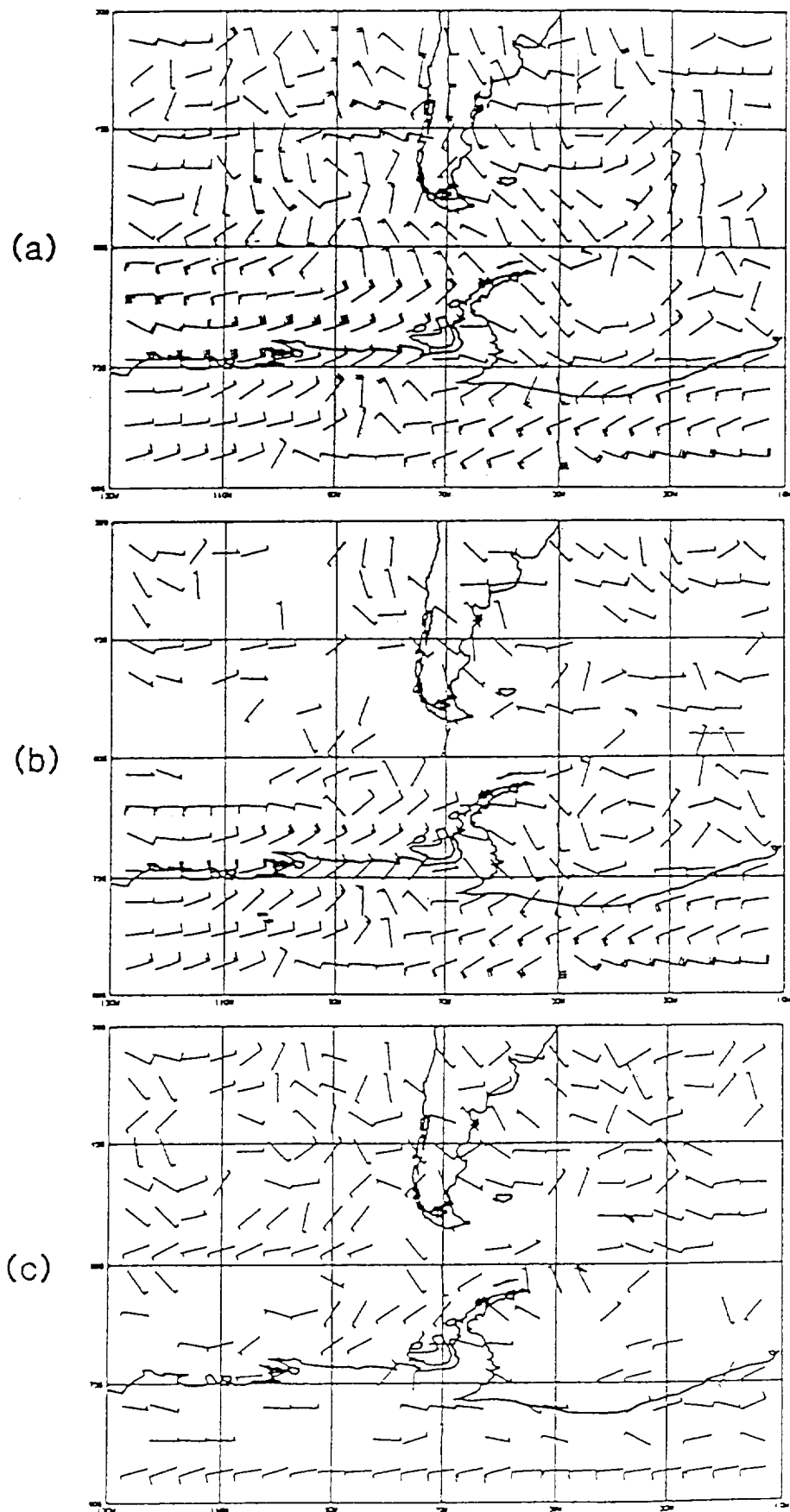


Fig.3 300 mb wind analysis errors (in knots) after two days of assimilation for (a) Satemp, (b) LAWS 755, and (c) LAWS experiments

USING A GLOBAL SPECTRAL MODEL
IN AN OBSERVING SYSTEM SIMULATION EXPERIMENT
FOR LAWS - AN EOS WIND MEASURING SYSTEM

T.N. Krishnamurti, J. Xue, G. Rohaly

¹Department of Meteorology
Florida State University
Tallahassee, FL 32306

²D. Fitzjarrald

²NASA ED42
Marshall Space Flight Center
Huntsville, AL 35812

³G.D. Emmitt, S. Houston, and A. Wood

³Simpson Weather Associates, Inc.
809 E. Jefferson St.
Charlottesville, VA 22902

In this study we present preliminary results of a few observing system simulation experiments for LAWS (Laser Atmospheric Wind Sounder of NASA). Table 1 lists the acronyms. These experiments were carried out with the FSU global spectral model, which is based on using spherical harmonics as basis functions; the spectral forms of the momentum, mass, continuity, thermodynamics, moisture conservation, and pressure tendency equations are expressed in terms of their coefficients. A semi-implicit time differencing scheme is used to enhance the time step for the gravitational modes. The vertical coordinate is based on an earth-following σ -surface at the lower boundary. The details of the FSU global spectral model are referenced in Krishnamurti et al. (1989). It is a multilevel model that includes a complete array of physical processes and envelope orography. The first of these was a control experiment which was a long run from the global model (at a horizontal resolution T42). This experiment was intended to produce the benchmark data sets for identical twin experiments. It is also called the Nature run experiment. The output on day 5 of this long run was interpolated to the locations of the different elements of the World Weather Watch (based on a typical day's operational coverage). Random errors based on the typical observational errors were introduced to each of the elements of the observing system which are shown in Table 2. Data for 12 vertical layers of the global model were generated by this process. The data were analyzed using a univariate optimal interpolation scheme; long term monthly mean data sets (for all vertical levels for all variables) were used as first guess fields in the analyses. These analyses were carried out within a 4D assimilation cycle where the interpolated data from the parent tape was inserted at the location of the WWW every 6 hours and subjected to an optimal interpolation. The use of climatology as a first guess was necessary since the alternative, i.e., the nature run everywhere, would be unacceptable. After a 24 hour assimilation, the prediction experiment was carried out. The experiment is labelled as the WWW identical twin experiment.

Table 1: A List of Useful Acronyms

ECMWF	European Centre for Medium-range Weather Forecasting
EOS	Earth Observing System
FSU	Florida State University
LAWS	Laser Atmospheric Wind Sounder
LSM	LAWS Simulation Model
NASA	National Aeronautic and Space Administration
TRMM	Tropical Rainfall Measuring Mission
WWW	World Weather Watch

Table 2: Observational Errors of the Different Observing Systems

Commercial Aircraft	
height	5.4 m.
u-component	3.5 ms ⁻¹
v-component	3.5 ms ⁻¹
Surface Ships (1000 mb)	
pressure	5.4 m.
u-component	3.5 ms ⁻¹
v-component	3.5 ms ⁻¹
Satellites	
height	13.8 m
u-component	3.5 ms ⁻¹
v-component	3.5 ms ⁻¹
temperature	1.0 °C
relative humidity	5.0%
Upper Air Stations*	
height	5.0, 5.4, 6.0, 9.4, 13.8, 13.8, 13.8 m.
u-component	2.2, 2.5, 2.6, 3.1, 3.1, 3.0, 2.4 ms ⁻¹
v-component	2.2, 2.5, 2.6, 3.1, 3.1, 3.0, 2.4 ms ⁻¹
temperature	1.0 °C
relative humidity	5.0%
LAWS Winds	
speed	2.0 ms ⁻¹
direction	5°
* listed for 1000, 850, 700, 500, 300, 200, 100 mb pressure levels.	

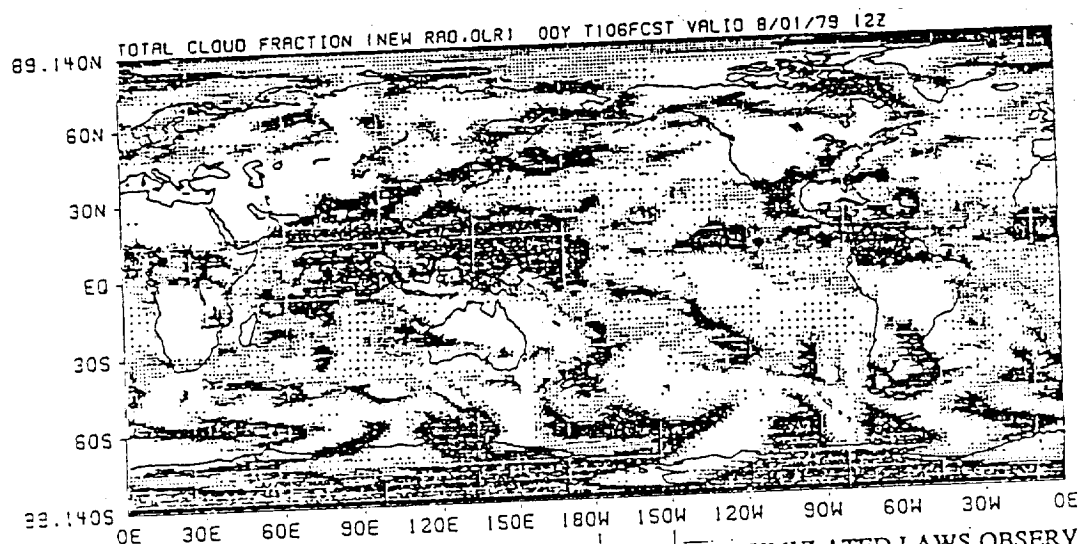
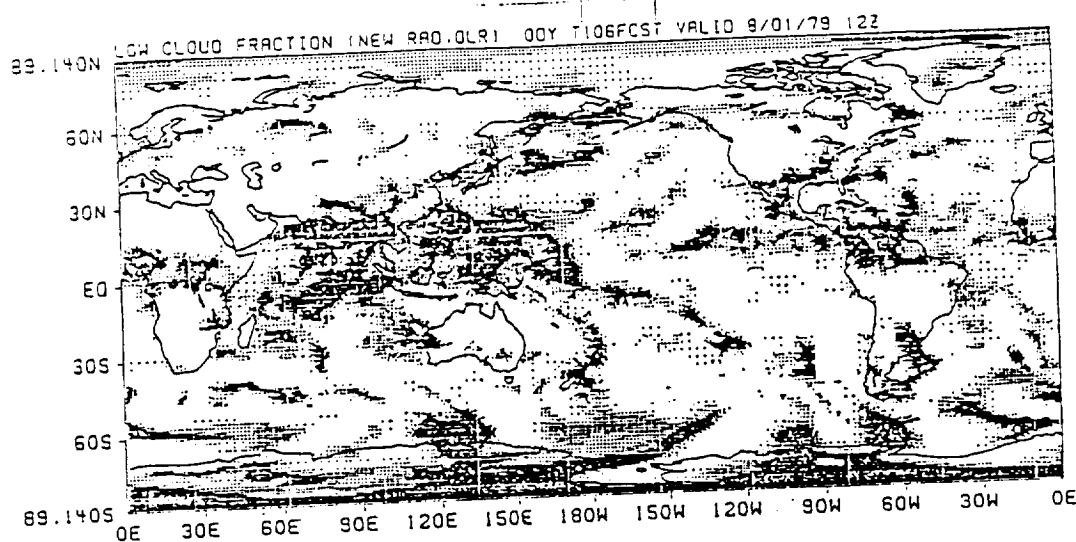


Fig 1a (top): Shows the fractional cloud cover for low clouds; three levels of shading are shown in this diagram. The least dense shading indicates percentages between 20% and 40%; the middle tone indicates fractions between 40% and 60% and the heavy dark areas denote percentages in excess of 60%. This describes the model based low cloud cover at the initial time. The case study involves an active phase of the monsoon on August 1, 1979. Heavy low clouds extend from the Arabian sea to the Western Pacific ocean where the LAWS vectors are suppressed below the low clouds.

Fig 1b (bottom): Shows the total fractional cloud cover. This includes the low, middle and high clouds. Roughly 50% of the globe is cloud covered; it shows the areas of cloud contamination for the LAWS vectors.

This was followed by experiments where simulated LAWS data were added to the WWW data. The simulated LAWS data were obtained as follows: the satellite's orbital height was assigned a value of 705 km and the inclination of the orbit was assumed to be either 90, 55, or 45°. These were based on the current plans for the joint launch of the TRMM instrument on the Japanese platform.

SIMULATED LAWS OBSERVATIONS

The input winds were obtained from the LAWS Simulation Model (LSM) developed by NASA (Emmitt et al., 1990). The LSM simulates a space-based, conically scanned, pulsed Doppler lidar wind sounder. The model includes:

- 1) platform motions and orbit parameters;
- 2) laser/optics parameters such as laser power, frequency stability, pulse length, mirror diameters, etc.;
- 3) LAWS sampling parameters such as scan rates, scan angle, pulse repetition rates, etc.;
- 4) measurement accuracy estimation involving aerosols, signal attenuation and atmospheric turbulence; and
- 5) measurement termination by cloud or earth's surface.

The results reported in this paper were based upon a simplified version of the LSM to isolate the sampling and global coverage issues from those related to measurement accuracies. To generate input winds to the FSU global spectral model, the LSM was used with wind data from the ECMWF analysis fields and cloud coverage data from the FSU model. The LSM generated shot locations, determined the sample termination level from the cloud and topography data, and produced a wind vector based upon the interpolated ECMWF gridded winds. A random error ($\sigma = 2 \text{ m s}^{-1}$) was added to each LAWS simulated wind measurement.

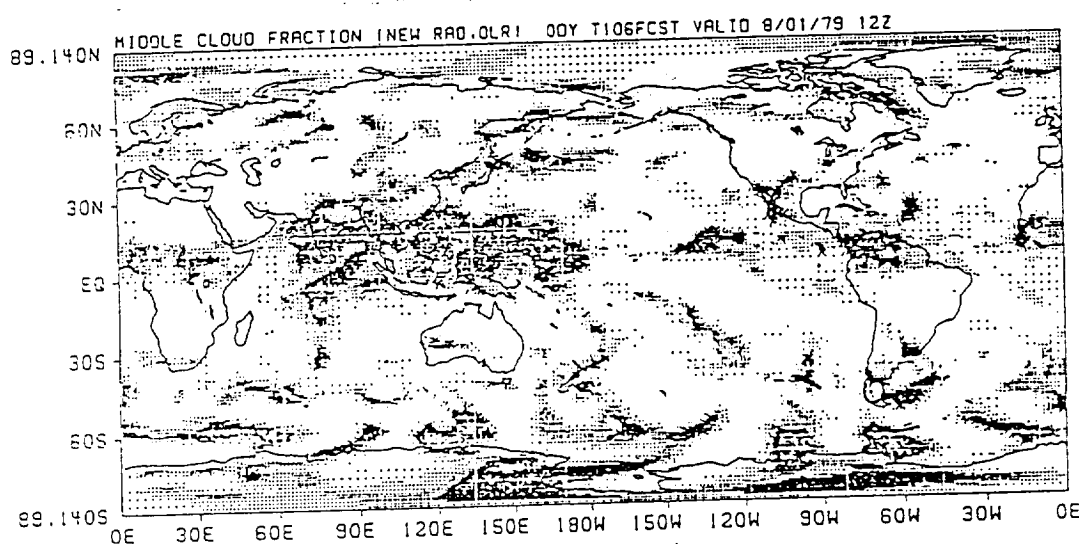
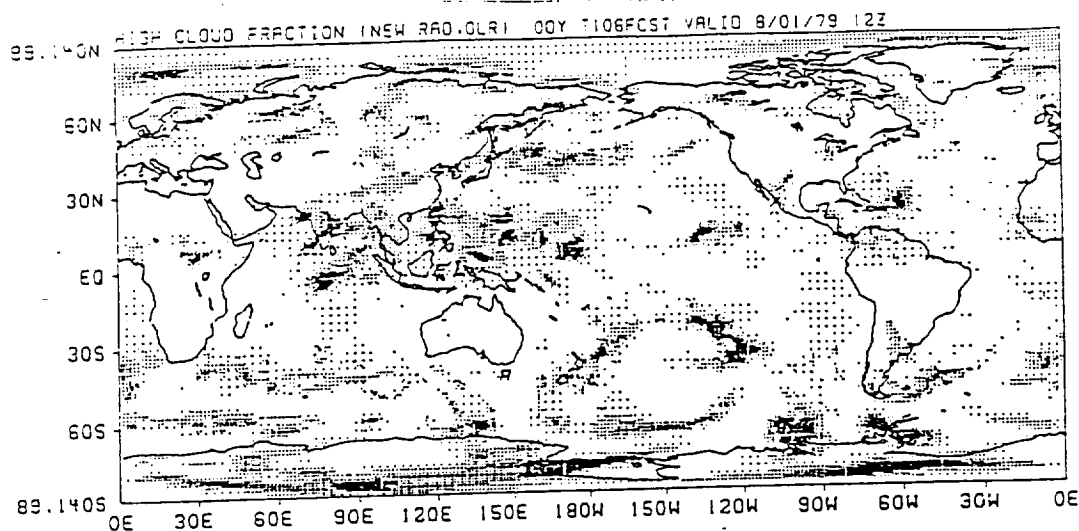


Fig 1c: Shows the fractional cloud cover for the high clouds.

Fig 1d: Shows the fractional cloud cover for the middle clouds.

The backscattered radiation does not penetrate clouds. Thus it was necessary to obtain fields of fractional clouds. The number of LAWS vectors were degraded to account for the presence of clouds in the field of view of the satellite. The fractional cloud cover for a Gaussian grid square was obtained from the radiation transfer algorithm of our spectral model. This is largely determined from a comparison of the model relative humidity with an assigned value of a threshold relative humidity. Figure (1. a,c,d) illustrates the low, high and middle cloud fractions determined by this procedure. The total cloud fraction is shown in figure 1b. Within a Gaussian grid square an equivalent fraction of LAWS vectors were terminated below that cloud level.

The lack of aerosols is another factor that is taken into consideration for prorating the number of LAWS vectors within a Gaussian grid square. For back scattering, the aerosols and even 'invisible' cirrus elements are considered important. This first phase of the study does not include a distribution of aerosols, and thus it overestimates the number of LAWS vectors.

Figure 2a shows that the rms height error for 500 mb is decreased by the addition of LAWS. As the inclination angle is increased, a reduction of the height error is noted. The polar orbiting satellite shows better results due to a more global coverage. The polar orbit would reduce the day 0 error by approximately 50%, but by day 5 the error approaches that of the satellite with an inclination angle of 55°. Figure 2b shows the largest reduction of error at 500 mb occurs in the southern hemisphere where typical WWW rms errors average around 75 m. LAWS would add a large amount of data over the southern hemisphere thereby reducing the rms error. The lack of WWW data over this hemisphere is the cause of such height errors and LAWS is able to help supplement in this regard. The northern hemisphere shows a smaller impact of LAWS although through day 5 one sees improved rms error values with the addition of these observations as illustrated by figure 2c.

Figures 3 a,b show the impact of LAWS at lower levels on the rms wind errors. The additional data decrease the day 0 rms 850 mb wind errors by at least 33% globally as can be seen in figure 3a. The polar orbit exemplifies the most improvement; however, the satellite with a 55° inclination angle performs notably as well. In the tropics, the orbit seems inconsequential although a definite improvement of the wind analysis can be seen at day 0 and continues through day 5 of the forecast as shown in figure 3b.

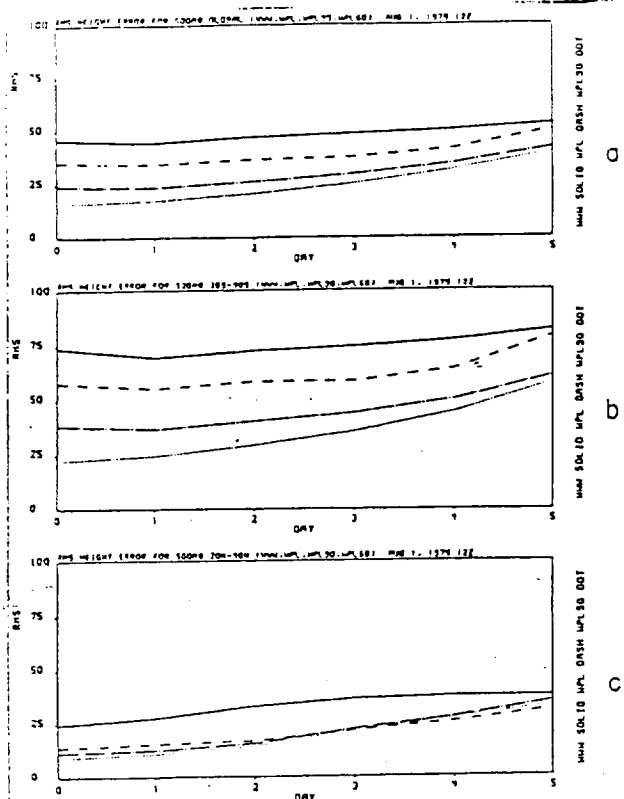


Fig. 2. 500 mb height rms errors as a function of days of forecast a) global; b) southern hemisphere and c) northern hemisphere. Solid line WWWW; dashed line 45° inclination angle LAWS; dot dashed line 55° inclination angle LAWS; polar LAWS is shown by dots.

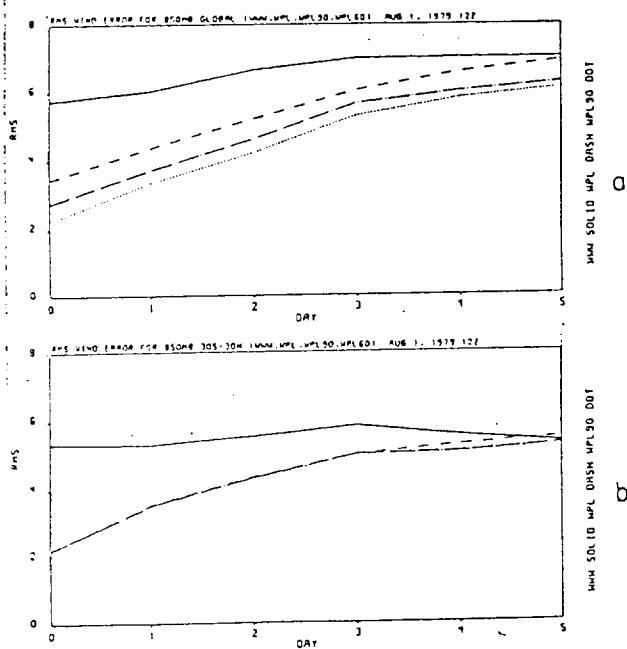


Fig. 3. 850 mb wind rms errors a) global and b) tropics (rest of legend same as fig. 2).

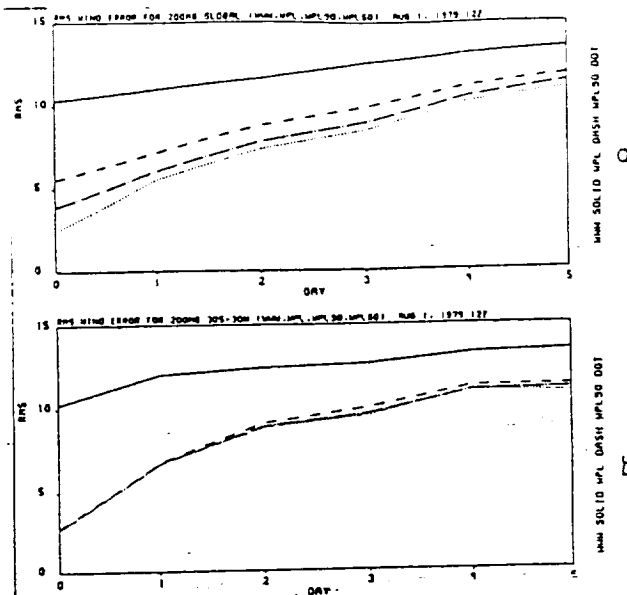


Fig. 4. 200 mb wind rms errors a) global and b) tropics (rest of legend same as fig. 2).

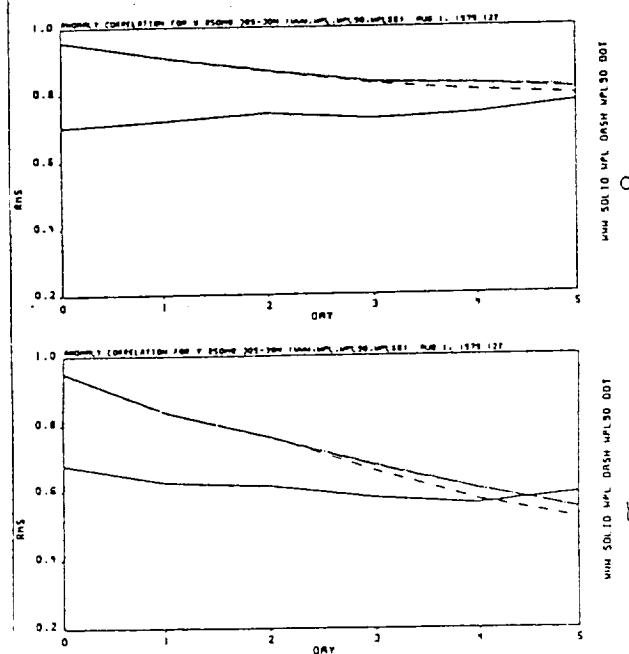


Fig. 5. 850 mb wind anomaly correlation for a) u-component and b) v-component in the tropics (rest of legend same as in fig. 2).

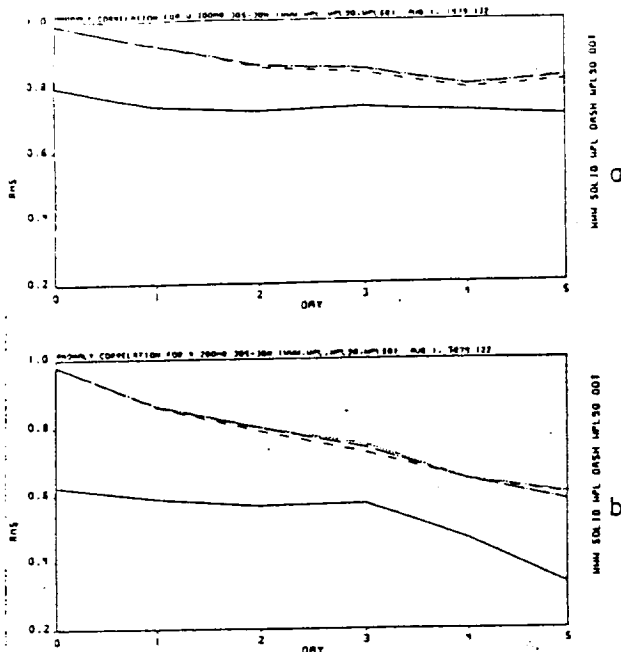


Fig. 6. 200 mb wind anomaly correlation for a) u-component and b) v-component (rest of legend same as in fig. 2).

In the upper atmosphere, the contamination resulting from clouds would be much less thus implying a large amount of the LAWS data would be incorporated into numerical models. Figures 4 a,b show the impact of this additional data upon the 200 mb rms wind errors. Over the globe at 200 mb the rms wind errors are reduced by approximately 50% at day 0. A large part of this improvement is due to much better wind observations over the tropics as seen from all orbits which had been experimented. By comparing figures 4 a,b, it is evident that the tropical winds are being better forecast with the addition of LAWS. This influences the global forecast rms errors as well. On day 5 the WWW plus LAWS forecast shows equivalent 200 mb rms wind errors with that of the initial analysis containing only the WWW observations which is a marked improvement.

Figures 5 a,b provide the anomaly correlations (AC) of the u and v wind components for respectively 850 mb. These again imply an improvement of the forecast when LAWS is included in the WWW data. From figures 5 a,b an improvement in not only the wind speed but also in direction is inferred by the high anomaly correlations at day 0. By day 5, the forecast with LAWS and the forecast with WWW data only show approximately the same AC. This illustrates a much improved short range forecast of the wind field in the tropics.

This improvement seems to be more evident at the 200 mb level as seen in figures 6 a,b. The AC for the u and v wind components again is greatly improved in the initial analysis (day 0). The impact of LAWS seems to be about equal for the 200 mb and 850 mb wind fields; therefore LAWS will aid in forecasting all levels of the atmosphere in clear air regions. The quality of the WWW observations in the tropics seems to have a larger impact at the 200 mb level than at the 850 mb level on a 5 day forecast as can be seen by the AC in figures 5 and 6. This is due in part to the small amount of mid and upper level observations that are collected in the tropics which comprise about half of the earth's surface. Alone, this would degrade upper level wind and height forecasts by global models.

In short, the impact of LAWS will be greatest in the tropics, especially over the oceans. This is seen from experiments run with satellite inclination angles of 45° and 55°. The impact in the mid latitudes and polar regions will be less for these satellite orbits versus a polar orbiting satellite which would gather data over the poles as well as the tropics. Even though LAWS provides solely wind direction and speed, a good multivariate optimal interpolation analysis would improve the geopotential height analysis thus better coupling the height and wind fields especially in the midlatitudes and near the poles, where the geostrophic approximation is a valid assumption.

Further work: This was a preliminary contribution on the impact of LAWS in identical twin experiments. We plan to extend this study in the following areas:

Over the oceans in the upper troposphere, aerosols are often less abundant. These and other low aerosol areas present a problem for LAWS to derive a wind. This must be approached to resolve its effect on LAWS as well as using high thin cirrus as a tracer to derive upper level winds in regions of thin cirrus.

It may be necessary to coordinate the LAWS planning with another NASA program, TRMM, possibly launched from the same satellite. Thus it may be necessary to optimize the inclination angle for the best use of both instruments. It would also be beneficial to increase model resolution to see how LAWS affects the forecasting of sub-synoptic scale features. These and other areas must be viewed so as to better realize a broader impact of LAWS.

Acknowledgements: This work is supported by NASA grant nos, NAG8-761 and NAS5-30932.

REFERENCES

- Emmit, G.D. and S.A. Wood, 1990: Space-based Doppler lidar sampling strategies - algorithm development and simulated observation experiments. Monthly Progress Rept. under NASA Contract NAS8-38559, October.
- Krishnamurti, T.N., D. Oosterhof and N. Dignon, 1989: Hurricane prediction with a high resolution global model. *Mon. Wea. Rev.*, 117, 631-669.

Global Three-Dimensional Distribution of LAWS
Observations Based Upon Aerosols, Water Vapor and Clouds

S. A. Wood, G. D. Emmitt and L. S. Wood

Simpson Weather Assoc., Inc., 809 E. Jefferson St., Charlottesville, Va 22902
(804) 979 - 3571 or FAX (804) 979 - 5599

1.0 Introduction

A space-based Doppler Lidar Atmospheric Wind Sounder (LAWS) has been proposed by NASA as a facility instrument for the NASA Earth Observing System. Simpson Weather Associates, Inc. has developed LAWS Simulation Models (LSM) that are coupled with Global Circulation Models (GCM) to evaluate the potential impact of global wind observations on the basic understanding of the earth's atmosphere and on the predictive skills of current forecast models (GCM and regional scale). This paper uses the LSM to examine the three dimensional distribution of LAWS' observations over the globe. Such a study must consider the effects of atmospheric aerosols, molecular attenuation of the lidar signal, opaque clouds, and the presence of thin cirrus clouds.

2.0 LAWS Simulation Model

The LSM is a fully integrated simulation model that provides global three-dimensional simulated lidar winds. The major model components are for satellite location, laser scanner, atmospheric library, line of sight velocity, and the horizontal wind components. The atmospheric library model incorporates the effects of atmospheric aerosols, water vapor, opaque clouds and transparent cirrus clouds.

The LSM provides global aerosol backscatter via two methods; either tailored versions of the AFGL's FASCODE and LOWTRAN models or from probabilistic backscatter profiles based upon GLOBE data (LAWS baseline profiles). In our study we used the baseline maritime and continental aerosol backscatter profiles (Wood and Emmitt, 1991), as shown in Figure 1, in conjunction with European Center for Medium Range Weather Forecasting (ECMWF) relative humidity profiles to provide expected aerosol backscatter with natural variability.

The LSM uses the AFGWC Automated Cloud Analysis Model in conjunction with ECMWF data to infer global cloud cover. We find that the cloud model exaggerates the cloud coverage when compared to various satellite-derived cloud climatologies (Figure 2). We have taken several steps to empirically adjust the AFGL model so that the zonal distribution of total cloud coverage approximates that in Figure 3. The results are shown in Figure 4.

The LSM cirrus cloud model (Emmitt and Wood, 1991) is based upon a model obtained from Heymsfield (NCAR). The Heymsfield model computes a profile of cirrus cloud ice water content, along with cloud base and top altitudes, based upon a vertical atmospheric sounding taken with a rawinsonde. The LSM version of the Heymsfield model uses ECMWF profile data to supply atmospheric soundings as input to determine the presence of cirrus clouds.

3.0 Global Three-Dimensional LAWS Observations

Currently participation in the Observing System Simulation Experiments (OSSE) involves providing realistic LAWS simulation winds and observational errors for assimilation into NASA/GSFC and Florida State's GCMs (Atlas and Emmitt, 1991, Krishnamurti et. al., 1991). These OSSEs are addressing LAWS coverage issues. It is important to simulate in these experiments, both data quality and the data distribution (horizontal and vertical).

We have chosen to examine the global three-dimensional distribution of LAWS observations from the first day of our OSSE runs. Figures 5-7 depict the global averages of the number of LAWS shots in a 208X208 km target area as a function of altitude. The figures consider the effects of aerosols, aerosols and opaque clouds, and aerosols, opaque clouds and cirrus clouds, respectively.

4.0 References

- Atlas, R. and G. D. Emmitt, 1991; Implications of Several Orbit Inclinations for the Impact of LAWS in Global Climate Studies. Paper presented at the AMS 71st Annual Meeting, Special Session on Laser Atmospheric Studies, New Orleans, LA, January.
- Emmitt, G. D. and S. A. Wood, 1991; Simulating Thin Cirrus Clouds in Observing System Simulation Experiments (OSSE) for LAWS. Paper presented at the AMS 71st Annual Meeting, Special Session on Laser Atmospheric Studies, New Orleans, LA, January.
- Krishnamurti, T., Xue, G. Rohallo, G. D. Emmitt, S. H. Houston and S. A. Wood, 1991; Using a Global Spectral Model in an Observing System Simulation Experiment (OSSE) for LAWS - An EOS Wind Measuring System. Paper presented at the AMS 71st Annual Meeting, Second Symposium on Global Change Studies, New Orleans, LA, January.
- Wood, S. A. and G. D. Emmitt, 1991; A Reference Atmosphere for LAWS Trade Studies: An Update. Paper presented at the AMS 71st Annual Meeting, Special Session on Laser Atmospheric Studies, New Orleans, LA, January.

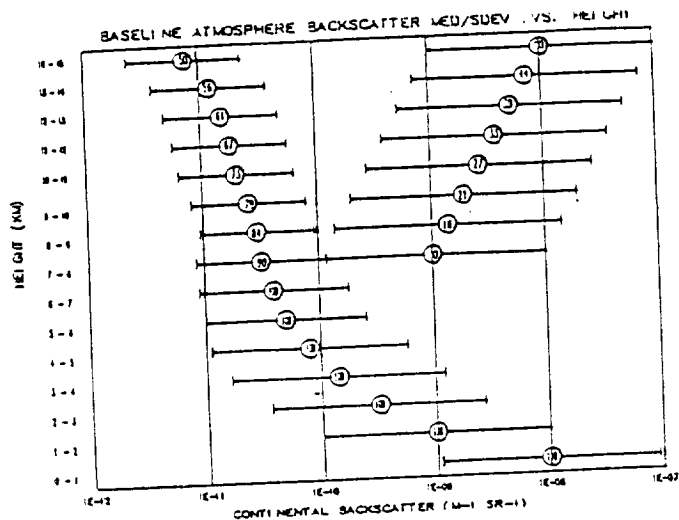


Figure 1a.

Probabilistic continental backscatter profile where locations at the circles indicates the median value including data "drop outs" in the original WPL and JPL profiles. The number in the circle is the percentage of total observations associated with that median. The error bars ± 1 sigma in the log backscatter is based upon several hundred profiles. The cirrus mode above 7 km has been estimated.

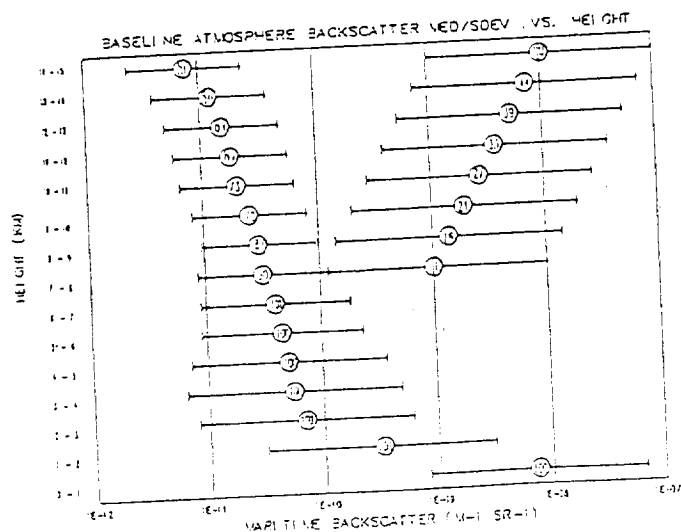


Figure 1b.

Probabilistic maritime backscatter profile where locations at the circles indicates the median value including data "drop outs" in the original WPL and JPL profiles. The number in the circle is the percentage of total observations associated with that median. The error bars ± 1 sigma in the log backscatter is based upon several hundred profiles. The cirrus mode above 7 km and the low tropospheric aerosol mode have been estimated.

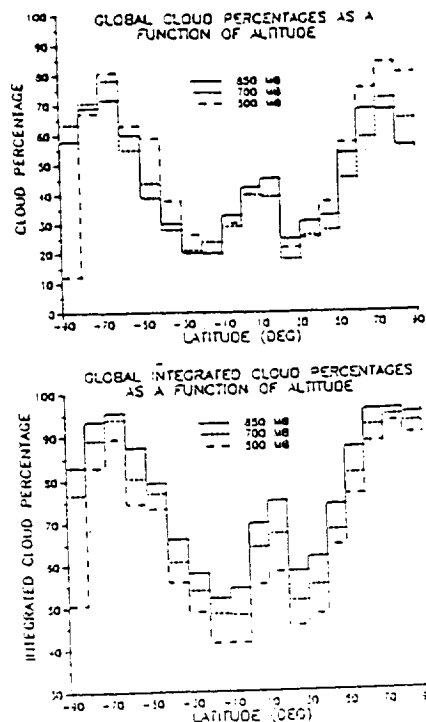


Figure 2. A) Global cloud percentages computed from the AFGL cloud model with ECMWF profile data from 11/10/79. Cloud percentages computed at 500, 700 and 1000 mb levels. B) Cloud percentages integrated top-down to the 500, 700 and 1000 mb levels.

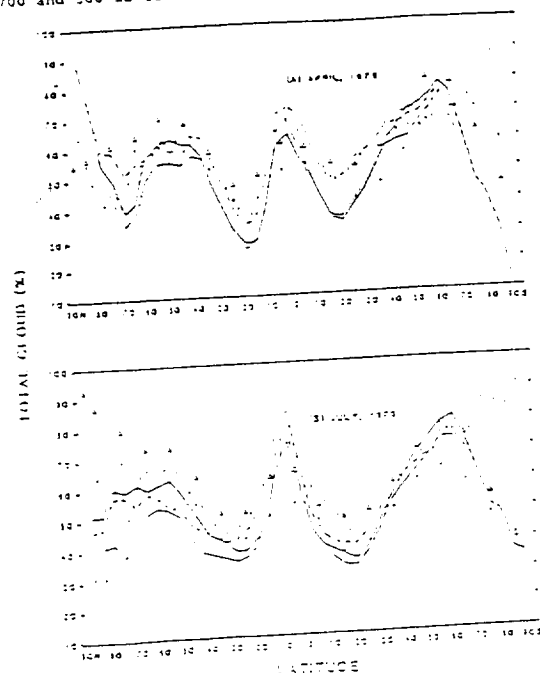


Figure 3. Global averaged total cloud amount for the monthly means of (a) April, (b) July, (c) October, and (d) January. The various cloud data are shown by a heavy solid line for ascending node (local noon) with TOMS data, a thin solid line for ascending node without TOMS data, a dashed line for descending node, and a dotted line for Bejvand and Strickland's (1980) 10 year cloud climatology (O); the Air Force 10 year cloud climatology (X); compiled by Hughes and Henderson-Sellers, 1985; and London's (1957) multiyear averaged cloud climatologies (O).

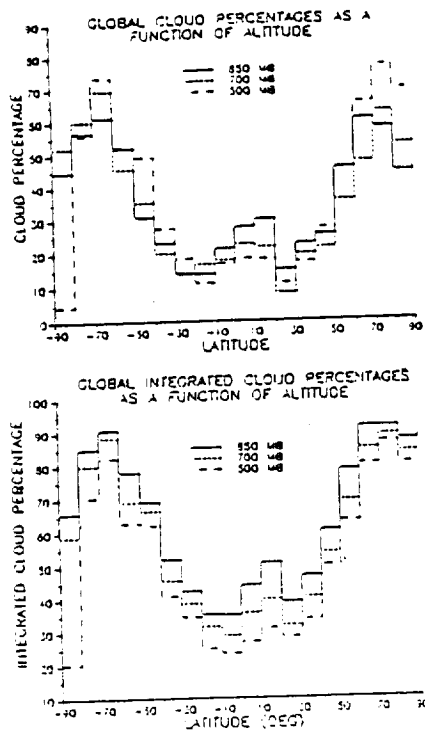


Figure 4. A) As for Fig 2(a) except empirically adjusted.
B) As for Fig 2(b) except empirically adjusted.

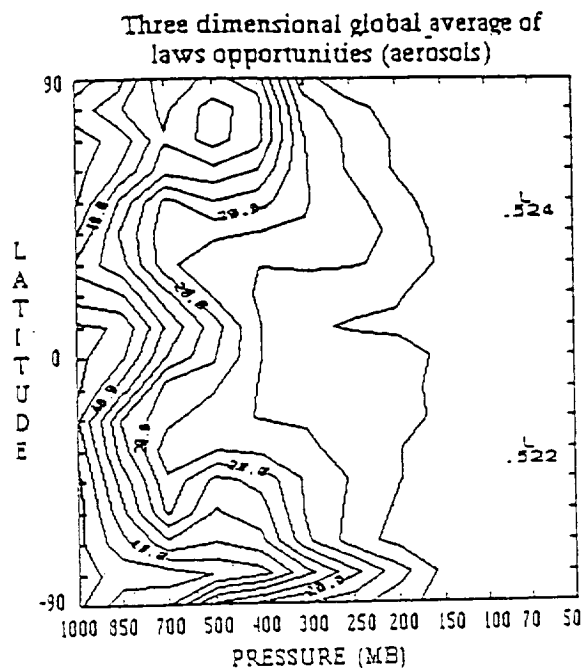


Figure 5. Global average of the number of LWS opportunities in a 108 X 108 km area as a function of altitude. Only aerosol effects are considered.

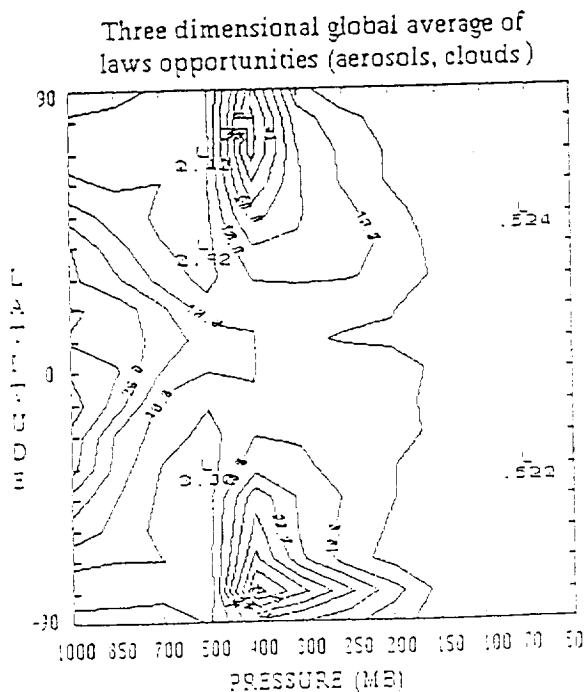


Figure 6. Global average of the number of LWS opportunities in a 108 X 108 km area as a function of altitude. Only aerosol and opaque cloud effects are considered.

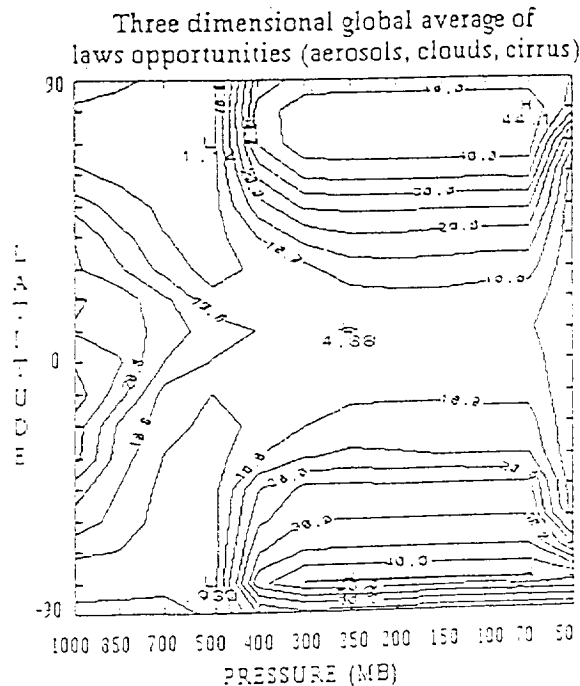


Figure 7. Global average of the number of LWS opportunities in a 108 X 108 km area as a function of altitude. Aerosol, opaque cloud and cirrus effects are considered.

**IDENTIFICATION OF CRITICAL DESIGN POINTS
FOR THE EAP OF A SPACE-BASED DOPPLER LIDAR
WIND SOUNDER**

G.D. Emmitt and S.A. Wood
Simpson Weather Associates, Inc.
Charlottesville, VA 22902

The feasibility of making tropospheric wind measurements with a space-based Doppler lidar has been studied by a number of agencies over the past 10-15 years. Currently NASA has a plan to launch such an instrument, the Laser Atmospheric Wind Sounder (LAWS), within the next decade.

The design of the LAWS continues to undergo a series of interactions common to most instruments targeted for a space platform. In general, the constraints of available platform power, weight allowance and project funds continue to change. With these changes the performance and design specifications also must change.

One of the most basic design considerations is the Energy Aperture Product (EAP) which is directly related to the weight and power constraints. The power requirements are scaled to the energy of the laser pulse and its average pulse repetition frequency (prf). The weight of the instrument is determined in part by the energy of the laser and its prf and in part by the size (aperture) of the optics. While not linearly, costs also scale to both the laser energy and telescope diameter.

One of the more critical trades being performed is that of the observations (number and accuracy) returned as a function of EAP. Lidar returns are obtained from aerosols, transparent cirrus, and the tops of opaque clouds. The accuracy of the line-of-sight (LOS) measurement is dependent upon the signal-to-noise ratio (SNR). The accuracy or representativeness of the wind information within a specific volume containing several LOS samples depends upon both the SNR and the number of samples.

The distribution of the observational opportunities can be described in terms of a log normal distribution of aerosol backscatter with a median near $3\text{-}5 \times 10^{-11} \text{ m}^{-1} \text{ sr}^{-1}$ for $9.11 \mu\text{m}$ plus a broad distribution of high backscatter from clouds, desert dusts and

PBL aerosols with a median around $10^{-7} \text{ m}^{-1} \text{ sr}^{-1}$ (see Figure 1).

Our ability to detect useful information (sufficient SNR and number of samples) can be expressed in terms of a consensus algorithm which is shown schematically in Figure 1b. Note that approximately 8 dB spans the gap between $< 5\%$ useful returns to $> 95\%$ useful returns. Overlaying Figure 1b on Figure 1a presents a clear picture of several of the critical regions for performance - one in the region less than 10^{-10} and the other greater than 10^{-8} .

In our presentation we will explore the sensitivity of the performance of a space-based Doppler lidar to a range of EAPs given a realistic distribution of observation opportunities around the globe. A GCM will be used in a simulation experiment to produce performance profiles in terms of the source of backscattered information (see Figures 2 and 3 for examples). Critical design points for the EAP vs backscatter will be identified in terms of marginal performance.

Acknowledgement

This work has been supported under NASA contract NAS8-38559.

Figure Captions

Figure 1: (a) Schematic distribution of backscatter opportunities for a space-based lidar wind sounder. (b) Schematic of a signal processing algorithm based upon the consensus of 8 independent observations along the LOS.

Figure 2: Summary plot of the distribution of backscatter returns from the equator to 10°N band for a 20 joule laser with a 1.45 meter diameter telescope and in a 500 km orbit during a 12 hour period simulated with a global general circulation model (GCM). This summary indicates the percentage of time the lidar system can make a useful wind measurement in terms of the backscatter conditions - clouds, thin cirrus, aerosols or no returns due to obscuration by higher clouds.

In the GCM based simulation experiment opaque cloud returns are derived from Nimbus 7 climatology and the GCM. Upper tropospheric thin cirrus are obtained from SAGE statistics. The aerosol returns are based upon a $9.11 \mu\text{m}$

backscatter profile derived from recent GLOBE data and the LAWS baseline 9.11 μm backscatter profile. The usefulness of a measurement is judged in terms of the SNR, the number of shots into a 200x200 km area and the resulting observational uncertainty, σ_0 . A threshold value of $\sigma_0 = 5 \text{ m s}^{-1}$ is used above 300 mb while a value between 1 and 5 m s^{-1} is used below that level. Fractional cloud coverage is used to calculate the number of shots (out of 26) that succeed in passing through to lower layers.

Figure 3: Same as Figure 2 except for a 4 joule .75 meter telescope system.

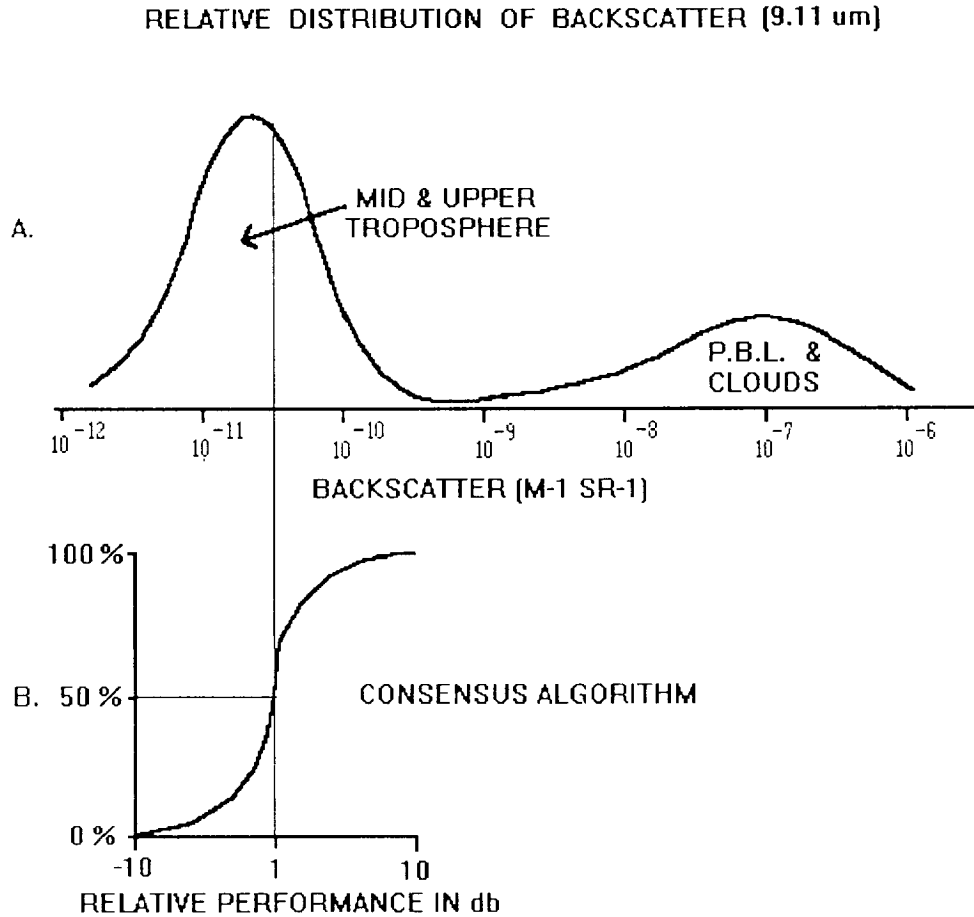


FIGURE 1

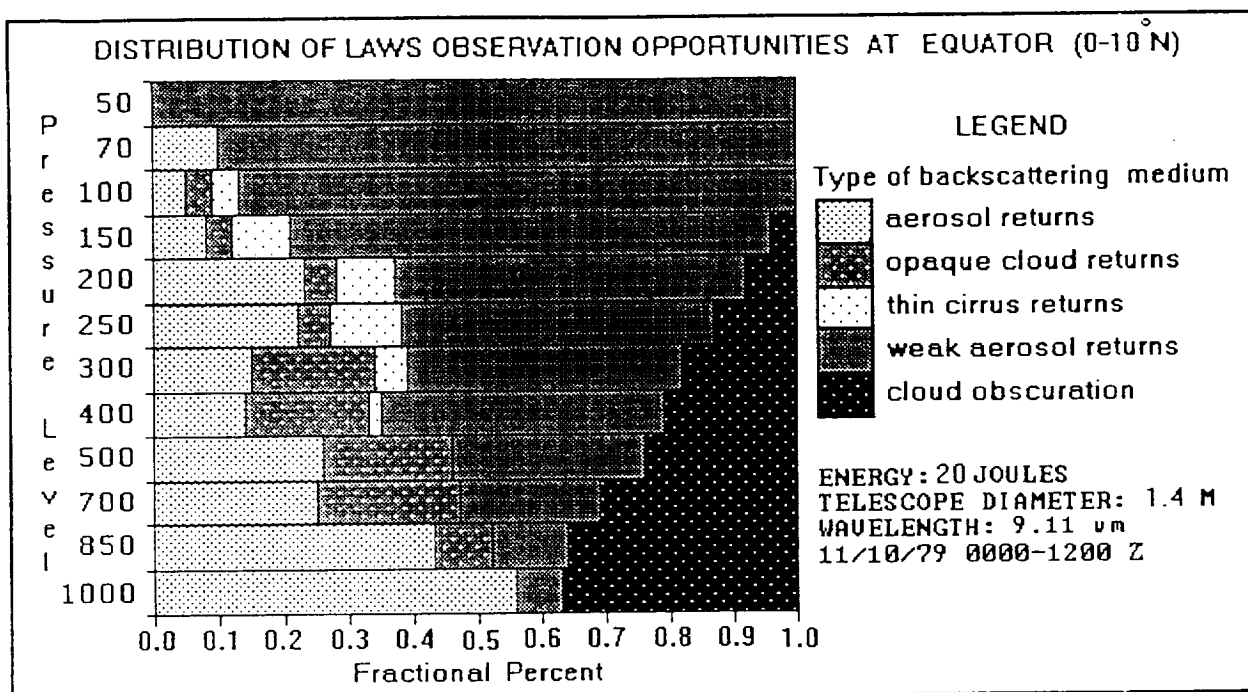


FIGURE 2

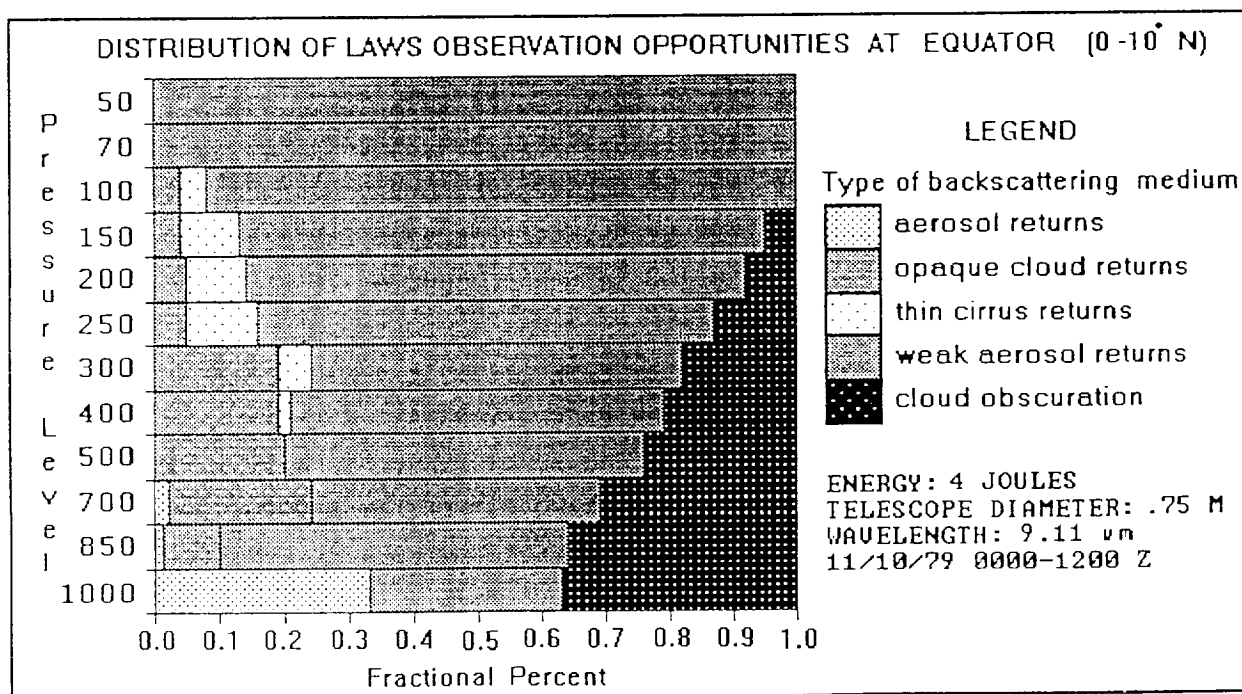


FIGURE 3

Simulation Space-Based Doppler Lidar Wind Measurements Using
Ground-Based Single Shot Observations

G. D. Emmitt, J. Dieudonné, S.A. Wood
and L. Wood

Simpson Weather Associates, Inc.
809 E. Jefferson Street
Charlottesville, VA 22902
Telephone: (804)979-3571

Both single-agency and multi-agency efforts are currently underway to put a Doppler lidar wind sounder into space within the next decade. Justification for this ambitious project rests mainly in the universally recognized need to provide direct measurements of the winds as input to both climate studies and forecast models. Expectations of success are based heavily upon ground-based observations as well as a few airborne observations. While the space-based observations will be taken at 5-10 Hz providing samples with a spatial separation of 50 to 70 kilometers within the earth's atmosphere, both the ground-based and airborne observations have been acquired primarily at 20 to 100 hertz providing a shot density of many samples per square meter resolution. Furthermore, many of the wind velocity estimates derived from these ground-based and airborne instruments have been acquired by using a poly-pulse pair technique involving 20 to sometimes 100 pulses. Currently there is very little in the way of data that is acquired in a single shot mode and processed to achieve resolution, both in space and time, that will approximate that which is achievable with a space-based system.

Over the past year data have been collected at the Marshall Space Flight Center's (MSFC) Ground-Based Doppler Lidar facility. These data have been collected both in the single shot mode as well as in the poly-pulse pair processor mode. These observations were taken with the following objectives:

- 1) to obtain single shot data that could be used to simulate a space-based observing perspective and inter-shot spacing;
- 2) to examine the velocity fields at the cloud boundaries, particularly at the lower boundary of cirrus clouds; and
- 3) to examine single shot statistics in comparison to those derived from the poly-pulse pair statistics.

The MSFC's lidar is a 20 mJ, 10.6 μ m pulsed incoherent Doppler system. During most of our observations, the laser was operated at 110 Hz with the scanner rotating at 3-4 degrees per second. The data was processed by the poly-pulse pair processor

every 50 shots providing line-of-sight (LOS) measurements every .5 sec. Twice per second, a single set of in-phase and quadrature data was recorded - i.e., every 50th shot. The single shot data was then processed with a complex FFT to obtain LOS wind measurements. Figures 1 and 2 are examples of poly-pulse (pp) pair and single shot (ss) observations taken during the same 360° scan.

Construction of vertical soundings was accomplished using a sine-fitting program to the velocity azimuth display (VAD) data for each range gate between 1 and 10 km in slant range. Figures 3 and 4 are examples of sine wave fitting to the 15th range gate of the VADS shown in Figures 1 and 2. The goodness of fit estimates provide a first order expression of the representativeness of LOS observations.

For the presentation we expect to show the results of a study using multiple VADS where the poly-pulse pair product is considered "truth" for the simulation of space-based observations using the single shot data. The effects of spatial separation of space-based observations will be accounted for by combining single shots from ground-based VADS separated in time.

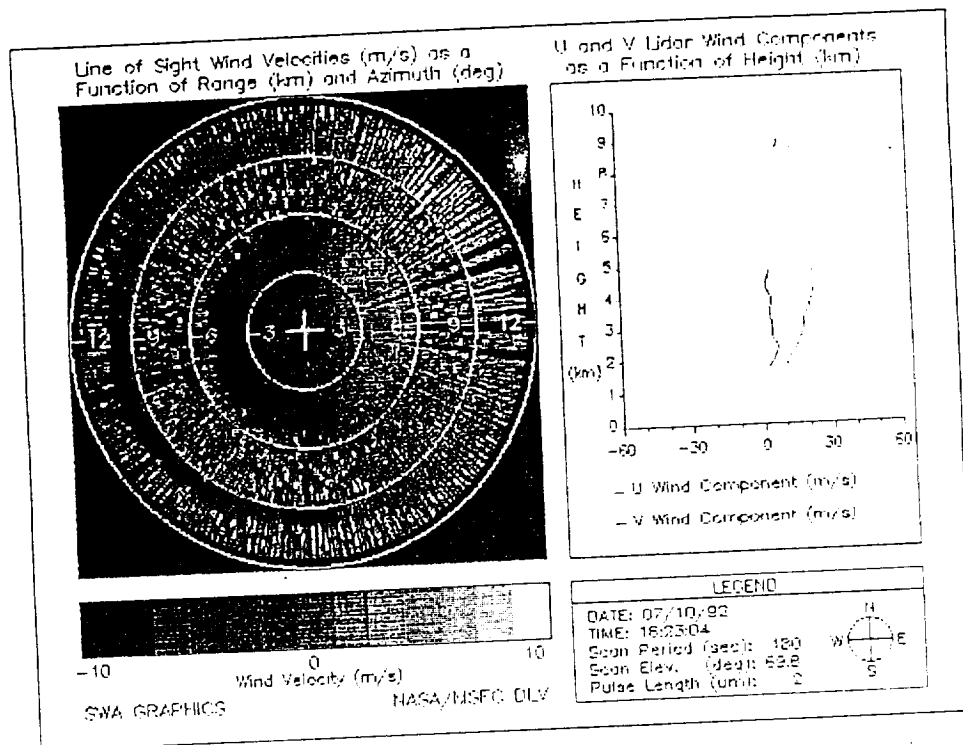


Fig. 1. Display of Doppler lidar data processed with a poly-pulse pair algorithm using 50 sequential shots. Vertical profile is obtained with sine fitting of individual range gates. The lidar was operated at 110 Hz.

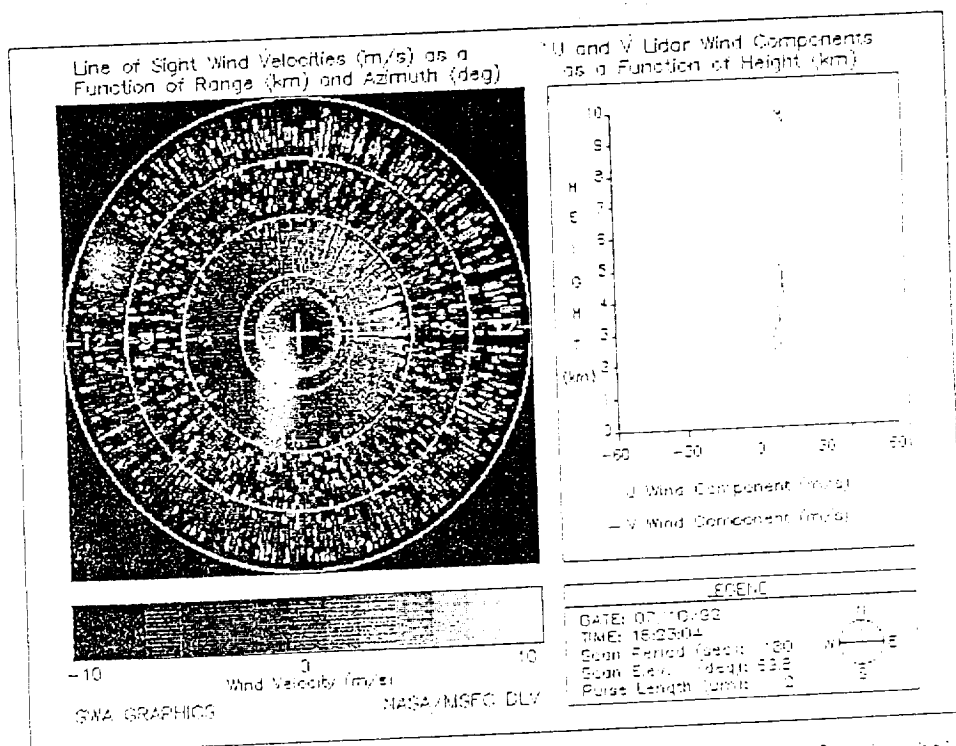


Fig. 2. Display of single shot Doppler lidar data taken at 1.50 azimuthal increments. These data were taken at the same time as those shown in Fig. 1.

SINE FIT TO NASA/MSFC GBDL DATA POLY-PULSE PAIR

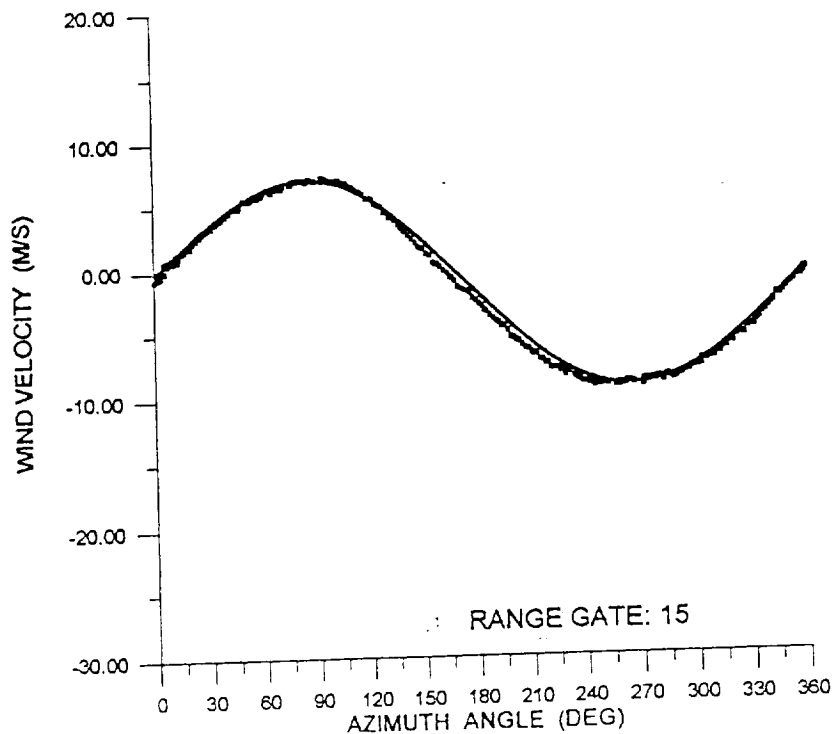


Fig. 3. Velocity Azimuth Display (VAD) for the 15th range gate of the data displayed in Fig. 1. Each data point is derived from a 50 shot poly-pulse pair processing.

SINE FIT TO NASA/MSFC GBDL DATA SINGLE SHOT

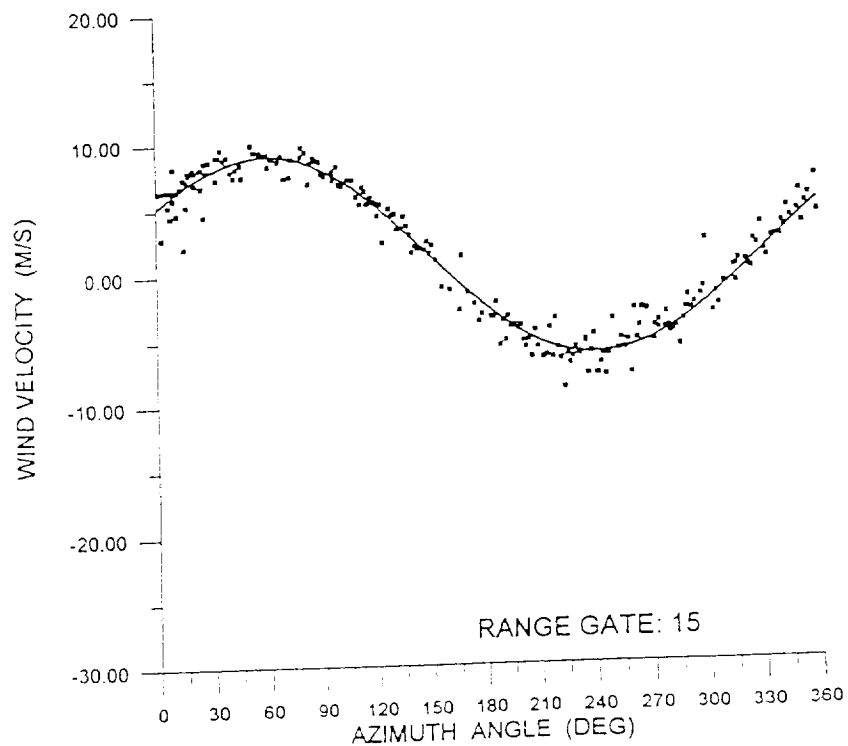


Fig. 4. VAD for the 15th range gate of the single shot data displayed in Fig. 2.

Atmospheric Transmission Models
Annual Conference
June, 1993
Boston, MA

INTEGRATION OF LOWTRAN INTO GLOBAL
CIRCULATION MODELS FOR
OBSERVING SYSTEM SIMULATION EXPERIMENTS

S.A. Wood and G.D. Emmitt
Simpson Weather Associates, Inc.
809 E. Jefferson Street
Charlottesville, VA 22902

The LAWS Simulation Model (LSM) simulates observations from a space-based Doppler lidar wind sounder. A main component of the LSM is its atmosphere generator model that produces global estimates of aerosol optical properties, opaque clouds and subgrid scale turbulence using output from the European Center Medium Range Weather Forecast (ECMWF) global circulation model. A major issue that will be discussed is the reasonableness of the β backscatter fields resulting from the integration of LOWTRAN into the Global Circulation Models (GCMs).

USING GROUND-BASED COHERENT DOPPLER LIDARS
TO EVALUATE ALGORITHMS FOR SHOT MANAGEMENT AND
SIGNAL PROCESSING OF PROPOSED SPACE-BASED WIND SOUNDERS

G.D. Emmitt
Simpson Weather Associates, Inc.
Charlottesville, VA 22902

Introduction

Programs to launch a space-based Doppler lidar wind sounder must rely on computer simulations and data obtained from ground-based and airborne lidar systems. To date, there have been no pulsed Doppler lidar wind measurements made with a space-based perspective on the atmosphere. Although there are plans to obtain such observations with an airborne facility (WIND-DLR & CNRS and MCCAWS-NASA & NOAA), we have begun using a ground-based system to explore issues related to signal processing and data interpretation:

- 1) measurement and sounding errors in single shot mode (as compared to the usual poly-pulsed mode);
- 2) velocity observations near cloud boundaries;
- 3) vertical speeds within cloud gaps; and
- 4) effects of chirp on observations.

In this paper we address only the first issue.

A series of experiments are being conducted using a 10.6 μm lidar at MSFC in Huntsville, AL. While the pulse energy is rather low (10-15 mJ), the frequency stability make this lidar ideal for making single shot velocity measurements.

Lidar System Characterization

For our experiments there are two characteristics of the lidar system that are of primary concern:

- 1) frequency stability, and
- 2) whiteness of total system noise.

Hard targets were used to evaluate the stability of the velocity estimates at high SNRs. In Figure 1, 100 seconds of poly-pulse pair (PPP) LOS estimates demonstrate that the stability for a 50 shot

based estimate is on the order of $.05 \text{ m s}^{-1}$. This implies that single shot estimates should have a $\sigma \approx \sqrt{50} \cdot .05 \approx .35 \text{ m s}^{-1}$.

The noise floor for the system was determined by plotting the distribution of velocity estimates for SNR's (NB) less than -3 dB (Figure 2). The band width of the signal processor was $\pm 28 \text{ m s}^{-1}$. Clearly the sensitivity of the system is not independent of frequency. This narrow noise band presents a problem to some of our analyses and is undergoing corrections at this time.

All of our experiments involve recording data in two modes. The lidar is operated at 110 Hz and all returns are processed through the Lassen PPP processor using 50 pulses per estimate. For every 50th pulse both the in-phase and quadrature spectra are recorded and processed off line using a complex FFT and a simple peak detector. Figure 3 illustrates a matched PPP and SS VAD.

Sine Fitting Algorithm

To achieve the best estimate of the wind vector at each range gate, a recursive sine fitting routine was developed. In Figure 4 the performance of this algorithm is shown with a range of high and low SNR situations. Fitting sine waves to both the PPP and SS data allows for justifying the two data streams before performing shot pair calculations.

Simulating LAWS Observations

Velocity estimates from a space-based platform will be derived from single shots distributed with a spatial density of 6-10/10000 km^2 . Bi-perspective samples will be combined using single shot assimilation by general circulation models. Many questions arise regarding the accuracy and representativeness of such velocity data. The MSFC lidar was operated

in the VAD mode (45° elevation angle) to collect more than 20 hours of data that could then be used to evaluate the quality of the expected data from a space-based system.

LAWS observations were simulated by matching single shots in angular pairs approximating that for a space-based conically scanned system. Figure 5 shows the distribution of speed estimates using the sine fit from the PPP as the true wind. To convert these results to the case, for example, of six shots per estimate, the errors in Figure 5 would be divided by the $\sqrt{6/2} = 1.73$.

Presently, a consensus algorithm is being used to obtain "acceptable" estimates of the line-of-sight component. Six or seven contiguous range gates are processed separately for a velocity estimate. If four or more of those estimates cluster within 1-2 m s⁻¹ of each other, a consensus is declared and the average of their estimates is considered a good measurement. There have been computer simulations of the behavior of the consensus algorithm as a function of SNR (Figure 5). The ground-based data were used to evaluate the general features of the theoretical curves. Preliminary results shown in Figure 6 will be updated with the oral presentation.

LINE OF SIGHT VELOCITY FROM A STATIONARY TARGET

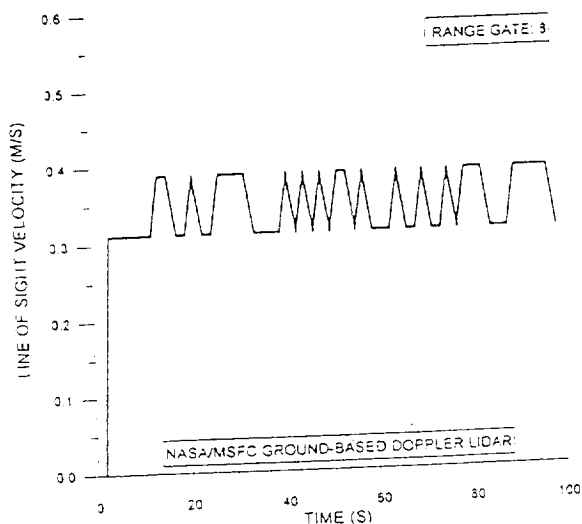


Fig. 1. A one hundred second sample of the velocity estimate for a return from a hard target located 2.6 km from the lidar.

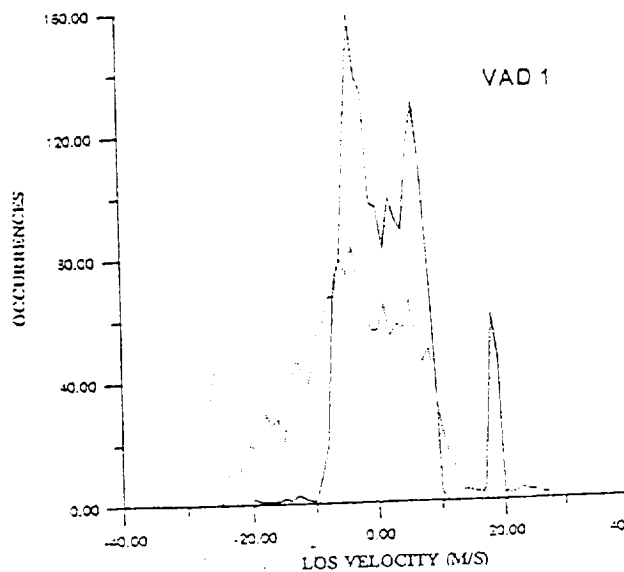


Fig. 2. Solid line is the distribution of LOS estimates during one 360° scan for range gates having SNRs greater than 5 dB. The dashed line is for LOS estimates where the SNR is less than -3 dB. Receiver bandwidth is ± 28 m s⁻¹.

NASA/MSFC GEOL DATA

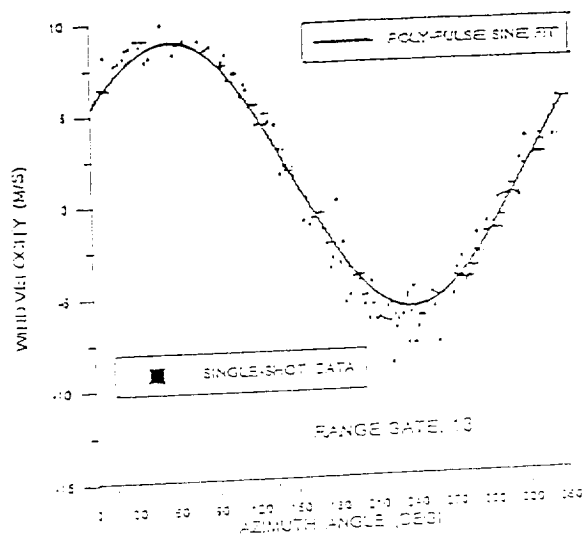


Fig. 3. Comparison of a poly-pulsed pair signal with the single shot data retrieved at the same time.

SINE FIT TO NASA/MSFC GBOL DATA 1823-VA01

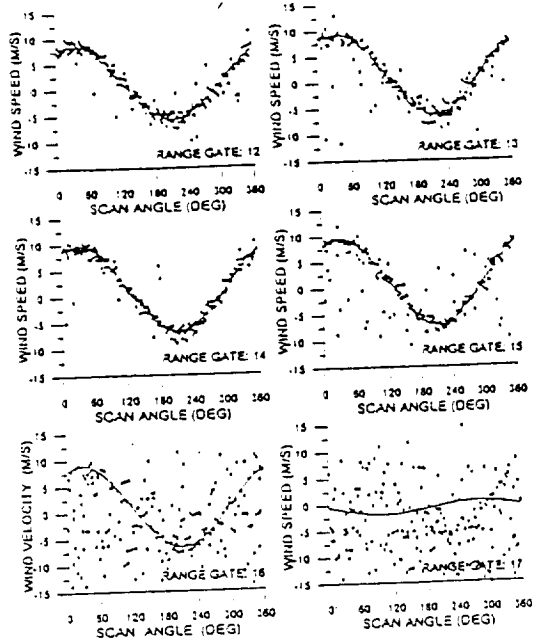


Fig. 4. Example of sine fits to a range of SNR conditions. The data are filtered by amplitude prior to sine fitting.

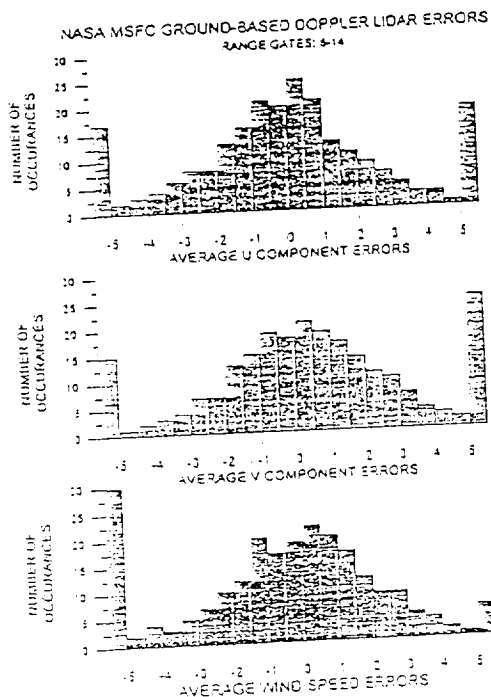


Fig. 5. Distribution of U, V and total wind speed estimates resulting from observation pairing as discussed in text. The lowest and highest bins in the histogram include all values $<$ or $>$ respectively.

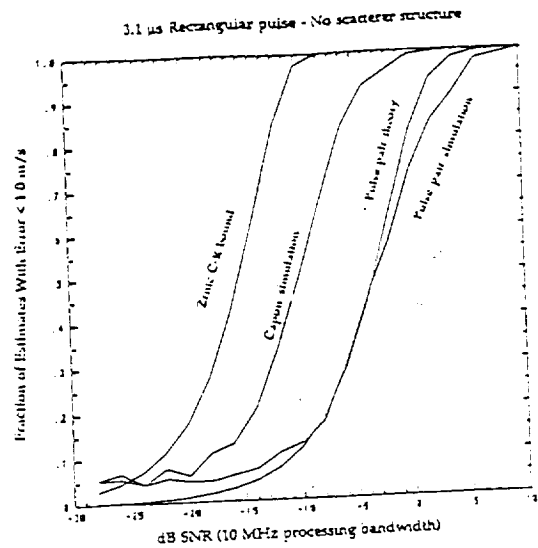


Fig. 6. Plot of several estimators as functions of SNR (courtesy of John Anderson, Univ. of Wisconsin). Capon simulation is approximately that being used in current LAWS simulations.

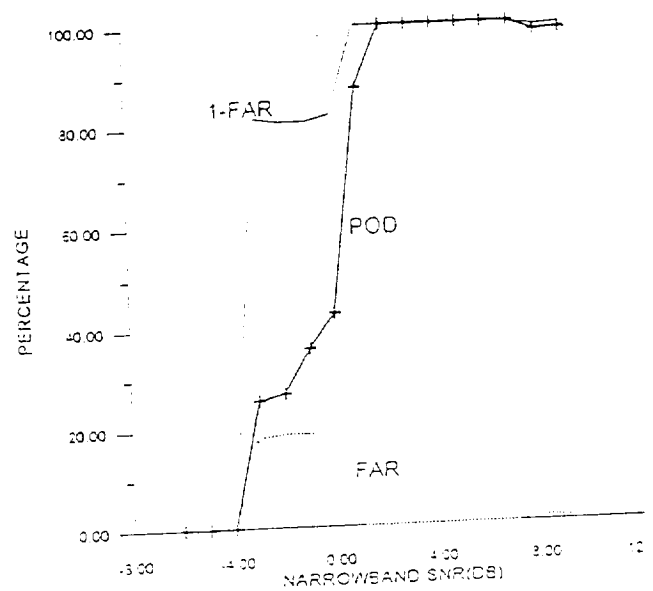


Fig. 7. Plot of consensus results derived from nearly 600 estimates. POD = probability of detection (4 out of 9 consensus within 2 m s^{-1}); FAR = false alarm ratio (consensus on bad estimate); 1-FAR = percentage of consensus estimates that were correct (within 2 m s^{-1} of true wind).

Lower Atmospheric Wind Velocity Estimates
using Single Shot Lidar

Jennifer A. Dieudonné
December, 1992

ABSTRACT

The benefits in developing accurate instrumentation to measure global wind patterns are multifold impacting many sectors of the scientific community. Out of this existing need emerged NASA's LAWS (Laser Atmospheric Wind Sounder) project to develop a space-based, conically scanning Doppler lidar system to measure global wind patterns. The proposed design makes use of single line-of-sight scans (one forward and one aft per measurement volume), and, thus, from this proposal emerged the need to test and characterize the accuracy of wind velocity measurements using single shot lidar. Much theoretical work has been done to postulate the capabilities and limitations of a single shot system. Yet, up until this point little actual experimentation has been done to test these theories. This study is one such effort.

In this study data from a ground-based Doppler lidar system was collected, processed, and analyzed in an attempt to provide a qualitative basis of understanding of single shot lidar returns in the lower atmosphere. That is, on a qualitative level are general wind patterns in the lower atmosphere obtained through single shot estimates using Doppler lidar as it backscatters from the dense concentration of aerosols in the lower atmosphere. Additionally, on a more quantitative level this study was an attempt to determine a critical signal-to-noise ratio (SNR) value below which it is unlikely to obtain reasonable single shot measurements. The proposed, theoretical value for such an SNR is somewhat unclear due to the relative nature of the classification of "good" estimates. However, for narrow band signals the general postulate is that an SNR of 0 dB is the point below which "good" estimates are unobtainable. Additionally, there is a theoretical notion that 5 dB is the point after which there is a consistent breakdown in measurement capabilities.

Due to the relative notion of a "good" estimate as this term takes on a range of meaning when applied to different scientific applications, this study sought to create a flexible scale of single shot accuracy. Obtaining single shot wind velocity estimates that were within designated threshold values (5 m/s, 4 m/s, 3 m/s, 2 m/s, 1 m/s) 50% of the time was used to designate a "beneficial" SNR value for obtaining "quality" measurements within these ranges of error. Thus, this study has potential applicability to a variety of applications.

The results of this study show that on a qualitative level expected lower atmospheric wind patterns are observable using single shot estimates. This focus of the study reveals some qualitative errors but asserts a belief that these errors result from correctable instrumentation problems. The results of the second aspect of the study clearly support the theoretical notion of critical SNR values in that it is shown that to obtain single shot wind measurements to within 1 m/s of truth 50% of the time an SNR value of 2.5 dB is needed. Additionally, to obtain accurate measurements to within 5 m/s 50% of the time an SNR of -2 dB is needed. Finally, it is shown that 5 dB is an obvious point at which accurate measurement capabilities clearly break down.

BACKGROUND

A Doppler lidar system in basic form consists of a frequency controlled laser transmitter, a heterodyne detector, a local oscillator, and a signal processing system. A laser pulse is transmitted at an initial frequency, f_0 . The pulse backscatters from atmospheric aerosols moving at the desired line-of-sight (LOS) wind velocity, v_{LOS} , thereby resulting in a return signal Doppler shifted in frequency, $f_r = f_0 + \Delta f_D$. The heterodyne detector, then, detects the beat frequency f_r produced by the summed combination of the initial and Doppler shifted frequency components. This return signal is then beaten against the local oscillator in order that the magnitude of the frequency return is in an acceptable range for processing by the signal processing system. Thus, the frequency of the local oscillator is such that the heterodyned electrical frequency output is on the order of 30 to 75 MHz (Werner, 1991). The end result is the determination of the line-of-sight wind velocity which is obtained through knowledge of the Doppler frequency shift, Δf_D :

$$\Delta f_D = 2 \left(\frac{v_{LOS}}{c} \right) f_0 \quad (1)$$

where f_0 is simply,

$$f_0 = \frac{c}{\lambda}$$

and λ is the wavelength of the laser

$$\lambda = 10.6 \text{ } \mu m$$

(A CO₂ laser was used in this study).

Determination of Δf_D requires demodulation of the electrical signal. In order that high precision is obtained a method of complex demodulation is employed such that a one arm signal return path is instead split into two paths: the Inphase and Quadrature paths. These two components represent the original signal in the form of a complex vector. The phase inherent in this complex vector representation aids in the determination of the relative sense of wind direction (positive or negative, forward blowing or aft blowing), and the magnitude corresponds to instantaneous signal amplitude used in the determination of the relative quality of the results (strong return or sketchy return). The Inphase and Quadrature components of the signal return are digitized at a rate at least twice as large as the highest possible frequency return in order to avoid signal aliasing.

A ground-based Doppler lidar system is designed to perform 360-degree scans in which data is collected repeatedly for returns from individual line-of-sight firings of the laser. Each 360-degree scan is known as a Velocity Azimuth Display (VAD) scan. The number of line-of-sight firings which make up a full VAD is determined by the scan rate of the system. Further, each line-of-sight firing includes returns for several range gates along that line-of-sight. The importance here is that for a perfect, noise-free instrument, the radial component of wind (v_{LOS}) as a function of azimuth for a particular range gate is sinusoidal in nature. Thus, sine-fits applied to a full VAD per each range gate provide a way to average out the effects of instrument noise and obtain radial wind velocity estimates.

DATA DESCRIPTION AND ANALYSIS

The data used in this study was collected by the ground-based Doppler lidar system at Marshall Space Flight Center (MSFC) on July 17, 1992. A CO₂ laser pulse 2 μ s in width was used, and Inphase and Quadrature data points were collected at a digitization rate of 15 MHz. This rate was chosen so as to avoid signal aliasing by making it twice as large as the largest possible Doppler frequency shift of 7.5 MHz corresponding to a line-of-sight wind velocity of 40 m/s. A poly pulse pair processor (Lassen Processor) collected and analyzed data simultaneous to this single shot data collection. These poly pulse pair results provided true wind velocity measurements, and, thus, was used to test and analyze the results obtained from the single-shot system.

The data collected per shot consisted of ancillary data including azimuth angle, pitch, elevation, time (hours, minutes, seconds) and a series of time domain Inphase and Quadrature data points all converted from electrical impulse to ascii integer values by the computer driven signal processing device. A full collection of single shot data consisted of four complete VADs collected at a scan rate of approximately 4-degrees per second. The full collection of single shot data was then parsed into individual shots, and those shots corresponding directly in time to full VADs of poly pulse pair data were grouped and separated. In this way, analysis could be done on a full single shot VAD and compared directly to poly pulse pair truth.

1024 Inphase and 1024 Quadrature data points were collected for each single shot. Range gates were determined by the pulse width of the signal, and, thus, at a digitization rate of 15 MHz with a pulse width of 2 μ s,

$$(15 \times 10^6 \text{ Hz}) (2 \times 10^{-6} \text{ s}) = 30 \text{ cycles}$$

thirty data points corresponded to all frequency information contained within a single range gate. However, Fast Fourier Transforms (FFTs) were used in the analysis of the data and required input in divisions of powers of two. Thus, range gates were extended by two data points, and throughout this study thirty-two data points corresponded to a single range gate. Thus, with 1024 total data points only thirty-two range gates were possible from which to obtain single shot wind velocity estimates. In terms of distance, this corresponds to 10.24 km.

$$32 \text{ data points} = 2.13 \times 10^{-6} \text{ s}$$

One way distance is then,

$$\frac{1}{2}d = \frac{1}{2}ct = \frac{1}{2}(3 \times 10^8)(2.13 \times 10^{-6}) = .32 \text{ km}$$

$$(.32 \text{ km})(32 \text{ gates}) = 10.24 \text{ km}$$

In an initial attempt to filter out random noise variations both the Inphase and Quadrature data points were corrected by estimating that the signal return from the far range gates would consist largely of noise. Thus, a mean value of the data in range gates twenty-one through thirty-two was obtained, and this mean was subtracted from all data points (Inphase and Quadrature were treated separately). A second correction was performed in an effort to normalize the Inphase and Quadrature signals to insure that the amplitude response of each taken concurrently denoted equivalent information. Thus, a correction factor was determined by taking the ratio of the value of the root means square (rms) of all Inphase data points to the value of the rms of all Quadrature data points. All Quadrature data points were then multiplied by this

correction factor in order to equalize the signals.

$$\frac{\sqrt{\frac{1}{N} \sum I^2}}{\sqrt{\frac{1}{N} \sum Q^2}} = \alpha$$

$$Q_{COR} = \alpha Q$$

An anomaly in the data resulted in the omission of the first Inphase data point and the replacement of this data by the first Quadrature point. This was corrected by eliminating the first Quadrature data point all together and pairing the last recorded Quadrature data point with a repetition of the last recorded Inphase data point (e.g., only 1023 Inphase data points were recorded by the instrumentation. The last Inphase data point was repeated in an effort to make up for the error.)

The next step was to divide the data for each single shot into range gate divisions and to determine the dominant frequency value characterizing each range gate. The procedure was the same for each range gate and consisted of vectorizing the thirty-two Inphase and corresponding thirty-two Quadrature data points.

$$z = I + iQ$$

This set of thirty-two complex vectors was then padded with trailing zeros out to a final set length of 1024. This data set was then submitted to a FFT routine which returned an array of 1024 frequency values associated with this range gate and an amplitude associated with each frequency value. The rationale behind the zero padding resulted from the desire to obtain the best possible frequency resolution. With 1024 values digitized at 15 MHz a resolution of about

15 kHz is obtained

$$\frac{15 \times 10^6 \text{ Hz}}{1024} = 14648 \text{ Hz}$$

This is about four times better resolution than that which is obtained by using a thirty-two point FFT, and, in fact, corresponds to better than 1 m/s in velocity knowledge by Equation 1.

$$V_{Los} = \frac{\lambda f_D}{2}$$

$$V_{Los} = \frac{(10.6 \times 10^{-6}) (14648 \text{ Hz})}{2} = .08 \text{ m/s}$$

Much experimentation was done to determine the effects in terms of the accuracy of final results obtained by zero-padding the signal and, further, to determine the best possible resolution that could be obtained using different zero padding scenarios (front padding, rear padding, varying the length of the padding). Most sources indicated that zero-padding would have a strong negative effect on the accuracy of results. However, on trial after trial on data with known frequency component values full accuracy was obtained using rear zero-padded signals up to the desired length of 1024 points. Thus, as 1024 was the closest power of two which provided fine resolution this method of zero-padding was chosen with no reservations. A power spectrum corresponding to the 1024 frequency values returned by the FFT routine was then obtained using the relation

$$P = f \cdot f^*$$

where f is the amplitude associated with a particular frequency, f^* is the conjugate of f , and P is the power corresponding to that frequency value. The dominant frequency value of the range gate was then determined by selecting that frequency value corresponding to the most dominant

power. By virtue of the use of a complex FFT both positive and negative frequency values were obtained. Thus, the corresponding line-of-sight wind velocity could be obtained from this frequency value by the relation

$$v_{LOS} = \frac{\lambda f_D}{2}$$

where λ is the wavelength of the CO₂ laser equal to 10.6 μ m, and direction is determined by the sign of the velocity (forward or aft blowing). (It should be noted here that the power associated with this velocity (frequency) was retained for use in determining an SNR value for the signal return which provided this velocity estimate.) In this way, velocity estimates were obtained for all range gates of each shot and for all shots in an entire VAD.

The next step was to plot the velocity estimates for all range gates for a full VAD of single shot data and compare these estimates with the corresponding poly pulse pair VAD (Figure 1 and Figure 2). This stage proved quite illuminating in that it was discovered that the above procedure indeed provided accurate, yet less intense results.

The wind pattern for lower atmospheric winds is evident in Figure 1. In fact, the thin line of cirrus clouds which exhibits itself as a ring in the distant range gates in the poly pulse pair returns of Figure 2 is faintly detectable as a similarly positioned ring in Figure 1. Notice, however, the slight variation in the color schemes from the single shot VAD (Figure 1) to the poly pulse pair VAD (Figure 2). The trend displayed in the single shot returns is correct, i.e., positive to negative blowing winds incremented or decremented in band widths quite similar to the poly pulse pair display. However, there is an offset associated with the single shot returns in that the maximum positive wind velocity represented in the single shot display is greater than

Start & End Times
18:23: 6 - 18:24:50
89 EL. DEG
23 AZ. DEG

re1823.ss
VELOCITY
PLOT
DAY OF YEAR
199
RUN=> 6

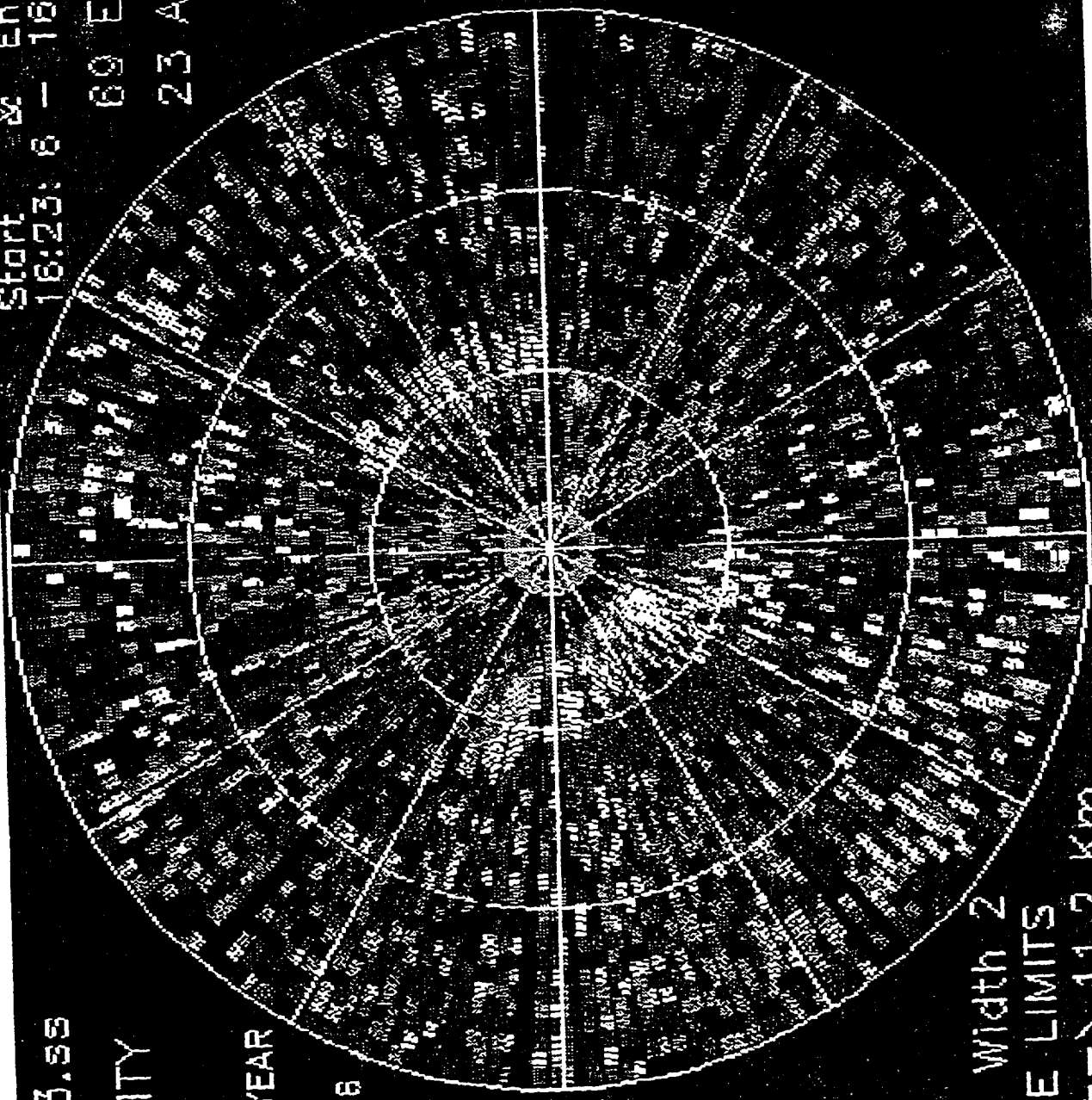


Figure 1

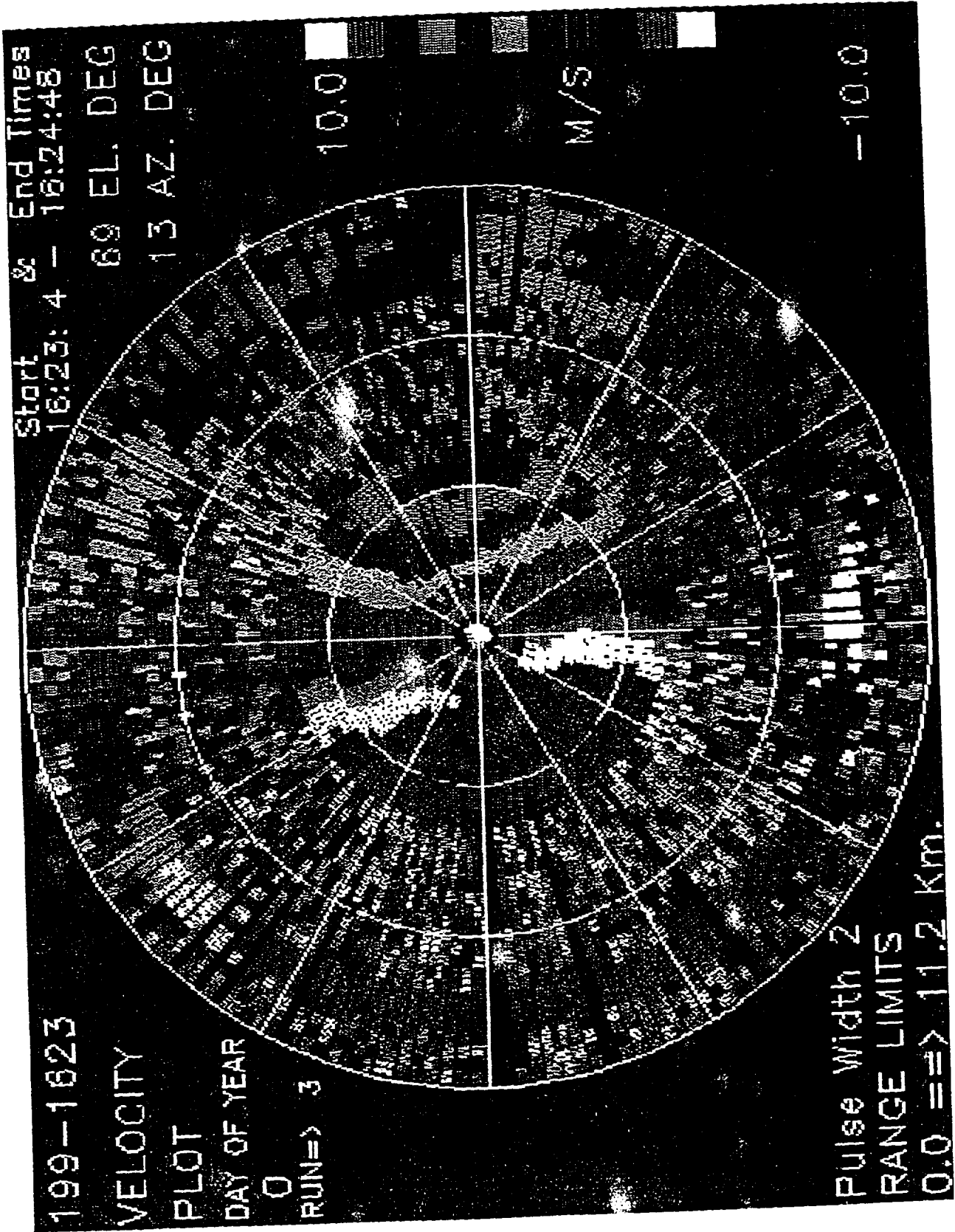


Figure 2

the maximum positive wind velocity represented in the poly pulse pair display. Further, the maximum negative wind in the single shot display is less than the maximum negative wind in the poly pulse pair display. It is as if there is a shifting across the origin. It should be stated here that at this stage of analysis it was found that it was necessary to "dummy" in two additional range gates at the beginning of each single shot to correct for the lag time effects of signal returns. This lag time, it is assumed, was already corrected for by the poly pulse pair processor. (Figure 1 is a display created after this correction had been made.) Notice also, though, that there is approximately a 20-degree rotation in wind direction between Figure 1 and Figure 2. It is postulated that both of these anomalies are results of correctable hardware problems that exist with the system at MSFC. I believe that the ancillary data (azimuth angle, time, etc.) which is associated with each shot in a sort of labeling procedure in the processing of returns is associated, in fact, with the wrong shot. That is, there exists some lag in associating ancillary data with shots so that an improper time and azimuth angle is being associated with each shot in a consistently incorrect manner. This would account for the 20-degree rotation in wind direction. The offset is a bit more perplexing. However, at the stage in data collection at which this data was taken a good case exists for the improper mounting of the laser. The laser, in fact, may not be level which could skew the returns and upset the maximum and minimum detectable wind velocity values in just this fashion. What is important in this study, however, is that relatively clear and accurate results are obtainable with single shot Doppler lidar in the lower atmosphere as clearly illustrated by Figures 1 and 2.

In the next stage of analysis data for all azimuth angles in each particular range gate was grouped together in an effort to quantitatively study the accuracy of the single shot estimates.

It was noted that gates eight through fifteen in this particular data set contained strong single shot returns. Thus, a least squares sine fit routine was applied to each of these gates of poly pulse pair data so that eight resultant sine fits were obtained for the wind velocity in each of these gates (i.e., one sine fit for gate eight, one for gate nine, etc.). Then all single shot estimates in gates eight through fifteen were processed in such a way that an SNR value was obtained and associated with each estimate, and the difference between the estimate and the truth of the corresponding poly pulse sine fit at that particular azimuth angle was obtained (Figure 4). This stage requires much elaboration. From the FFT processing each estimate had associated with it a representation of signal strength in the form of a power value (described previously). Taking into account the cirrus cloud layer that was detectable in gates thirty through thirty-two, the power associated with all estimates in gates twenty-one through twenty-nine were averaged. This average value provided an estimate of system noise

$$N = 5.4$$

Then, the SNR for all analyzed wind velocity estimates was obtained using the relationship

$$SNR \text{ (dB)} = 10 \log \left(\frac{S}{N} \right)$$

where S is the power associated with the given estimate. The final SNR values in decibels ranged from -5 dB to 20 dB for this data set. As described earlier a problem existed with the offset and phase of single shot returns. Thus, in order to make this analysis of single shot accuracy possible, the sine fits to the poly pulse pair data were corrected in offset and phase to correspond to the single shot returns. (This correction was relative in that single shot data could have been shifted to correspond to the poly pulse pair sine fit.) The amplitude of the poly pulse pair sine fit remained untouched, however, as it was this information that was used to compute

the differences in poly pulse pair truth and single shot returns for each estimate. Then, for each SNR value the number of these differences which were less than or equal to threshold values of 5 m/s, 4 m/s, 3 m/s, 2 m/s, 1 m/s were tabulated. Additionally, for each SNR value these differences were summed, and the number of estimates at each particular SNR value was tabulated. From this information the percentage of total estimates at each particular SNR value which fell within the desired thresholds was calculated as was the variance and standard deviation of estimates at each SNR value. Figure 3 resulted from a portion of this information. The percentage of total estimates per SNR which were less than each threshold value was plotted as a function of SNR.

Figure 3 shows that to obtain wind velocity estimates from single shot Doppler lidar which are within 1 m/s of truth 50% of the time an SNR value of about 2.5 dB is necessary. Likewise, to obtain results that are within all other threshold values of reality 50% of the time an SNR of about -2 dB is needed. Interestingly enough, the SNR for obtaining results within all thresholds excluding 1 m/s clusters at -2 dB. Also worth noting is the fact that a fall off from 100% accuracy occurs quite evidently at 5 dB, and the decay in accuracy from that point on is quite steep and rapid.

Figure 5 was also created in the hopes of completing an analysis to characterize the variance in single-shot wind velocity estimates for cases of low SNR. It was expected that as more estimates were added the improvement trend in this curve would not be that of \sqrt{n} . However, time constraints made completion of this part of the study impossible. Figure 5 remains, though, for future study.

Accuracy versus SNR

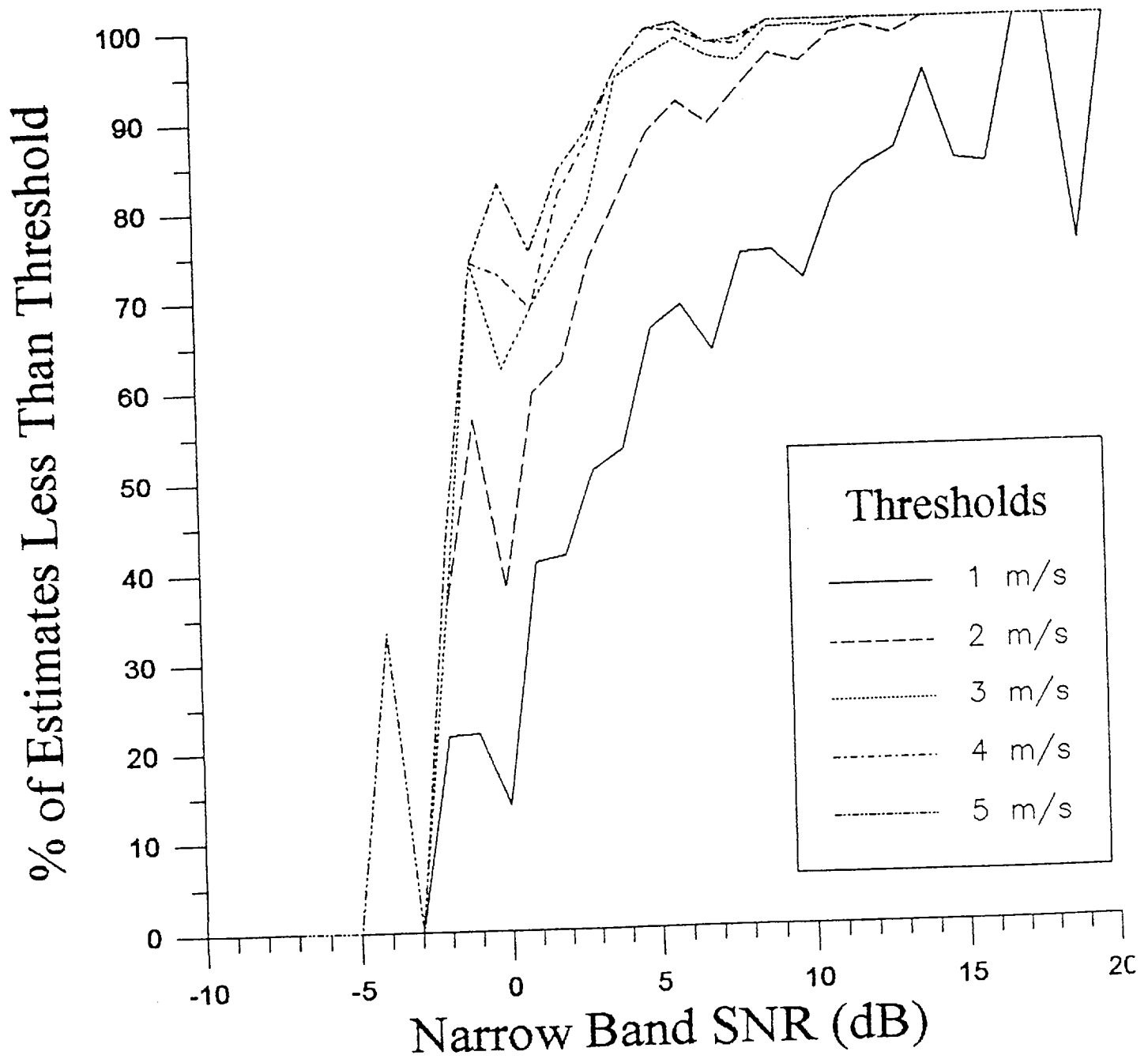


Figure 3

NASA/MSFC GBDL DATA

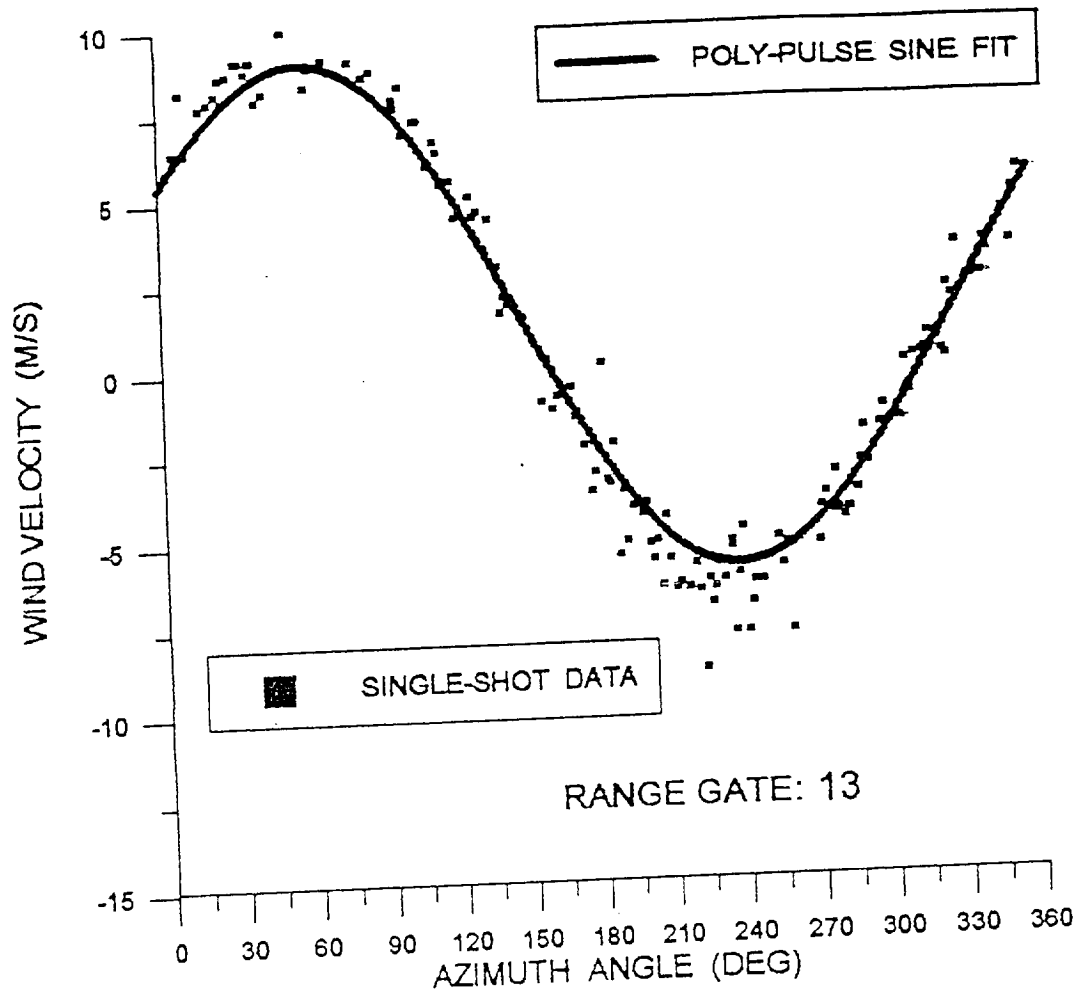


Figure 4

Standard Deviation versus SNR

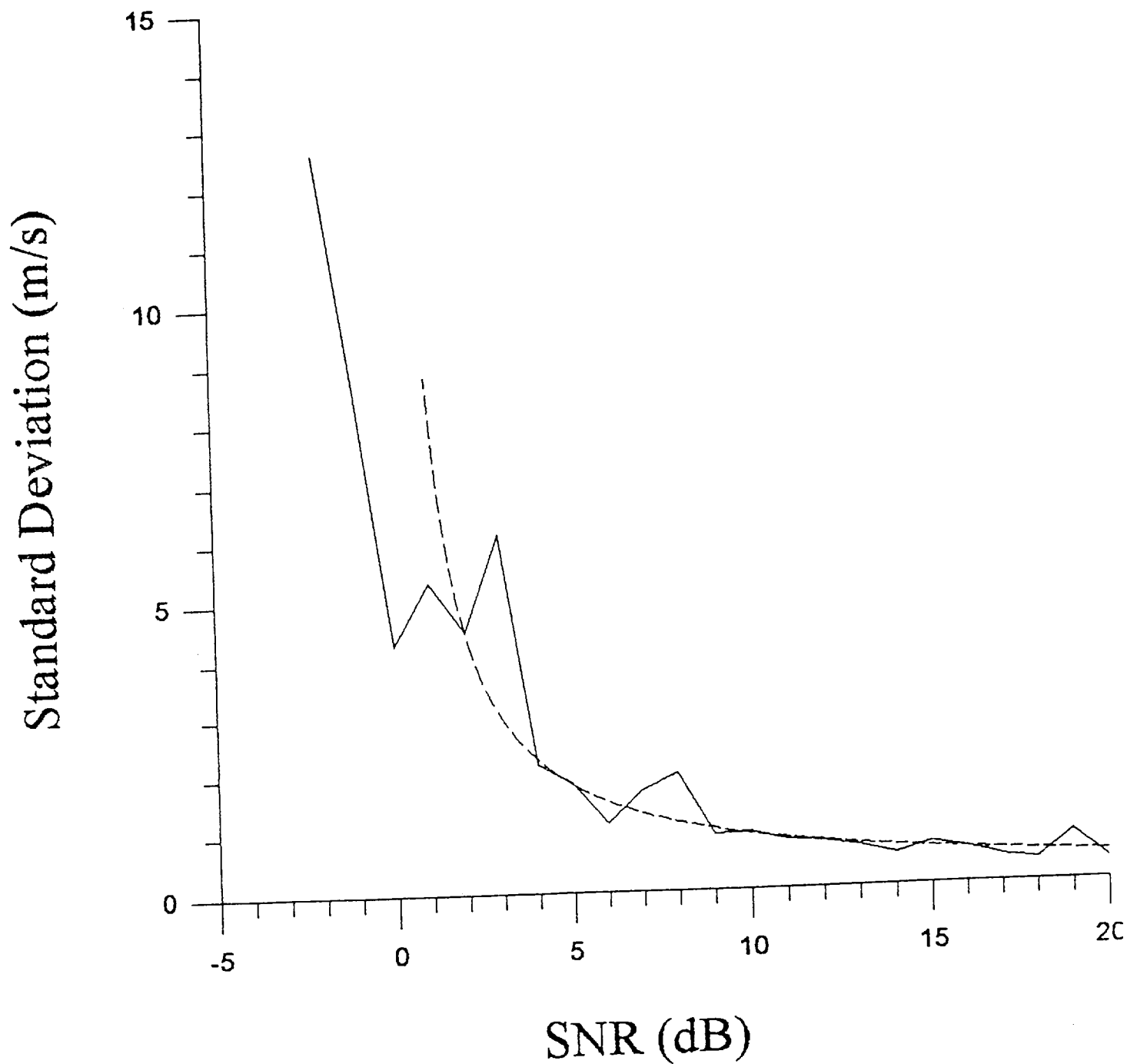


Figure 5

CONCLUSION

The results of this study show that reasonable wind velocity estimates using single shot Doppler lidar can be obtained in the lower atmosphere. In addition, this study experimentally established a scale of accuracy as a function of SNR that can be used to determine "critical" SNR values for which results beneficial to particular scientific applications can be obtained. In doing so, the theoretical notions regarding these critical SNR values were supported in that it was found that to obtain accuracy in wind velocity estimates to within 1 m/s of truth 50% of the time using single shot Doppler lidar in the lower atmosphere an SNR of 2.5 dB is needed. Likewise, to obtain estimates which are within a range of 2 m/s to 5 m/s of reality 50% of the time an SNR value of -2 dB is necessary. In addition, the theoretical SNR value for which a breakdown in obtaining wholly accurate results occurs was verified by this experiment to be 5 dB.

Several aspects are left open-ended at the conclusion of this study. First, it would be desirable to repeat this process on a larger number and wider spatial array of single shot VADs in order to unquestionably verify the reliability of the results. Additionally, it might be tempting to apply the conclusions of this study which established a quantitative representation of single shot accuracy to problems for which these results simply do not apply. For example, obtaining wind velocity estimates in the upper atmosphere to within 5 m/s of truth would be to attain excellent results. Thus, it might seem obvious to apply the results of this experiment and to assume, then, that results in wind velocity measurements which fell within 5 m/s of reality could be acquired 50% of the time using a single shot Doppler lidar system and a SNR value of -2 dB. However, this would be a gross misinterpretation of the conclusions. This study applies only

to lower atmosphere scenarios and does not pretend to provide information regarding obtaining wind velocity estimates using single shot Doppler lidar in higher atmospheric regions in which a less dense concentration of aerosols is present. Finally, the characterization of the variance in single shot wind velocity estimates for cases of low SNR is still left to be determined.

BIBLIOGRAPHY

- Chatfield, C. The Analysis of Time Series: An Introduction. London: Chapman and Hall, 1975.
- Ramirez, Robert W. The FFT: Fundamentals and Concepts. Englewood Cliffs: Prentice-Hall, Inc., 1985.
- Werner, Ch., G. Wildgruber, and J. Streicher. Representativity of Wind Measurement from Space: Final Report. Munich: DLR - Institute of Optoelectronics Sensorlab, 1991.

REFERENCES

- Atlas, R. and G.D. Emmitt, 1991: Implications of several orbit inclinations for the impact of LAWS on global climate studies. Proc. AMS Second Symp. on Global Change Studies, New Orleans, LA, January, pp. 28-32.
- Del Guasta, M., M. Morandi and L. Stefanutti, 1993: One year of cloud lidar data from Dumont d'Urville (Antarctica), 1. General overview of geometrical and optical properties. J. Geophys. Rev., 98, 18575-18587.
- Doviak, R.J. and D.S. Zrnic, 1984: Doppler radar and weather observations, Academic Press, New York, 458 pp.
- Emmitt, G.D. and S.A. Wood, 1988: Influence of coherent meso-scale structures on satellite-based Doppler lidar wind measurements II. Report under NASA Contract NAS8-36902.
- _____, _____ and M. Morris, 1990: Space-based Doppler lidar sampling strategies -- algorithm development and simulated observation experiments. Report under NASA Contract NAS8-37779.
- Gallery, W.O., F.X. Kneizys and S.A. Clough, 1983: Air mass computer program for atmospheric transmittance/radiance calculation: FSCATM. Report to the Air Force Geophysical Laboratory, Hanscom AFB, MA, Rept. AFGL-TR-83-0065.
- Hanel, G., 1972a: Computation of the extinction of visible radiation by atmospheric aerosol particles as a function of the relative humidity based upon measured properties. Aerosol Sci., 3, 377-386.
- _____, 1972b: The ratio of the extinction coefficient of the mass of atmospheric aerosol particles as a function of the relative humidity. Aerosol Sci., 3, 455-460.
- Kells, L.M., W.F. Kern and J.R. Bland, 1940: Plane and Spherical Trigonometry, McGraw-Hill Book Company, New York, 2nd Ed., 309-321.
- Kneizys, F.X., E.P. Shettle, L.W. Abreu, G.P. Anderson, J.H. Chetwynd, W.O. Gallery, J.E.A. Selby and S.A. Clough, 1983: Users guide to LOWTRAN 7. Air Force Geophysical Laboratory, Hanscom AFB, MA, Contract AFGL-TR-88-0177 (Rept. ADA206773).
- Krishnamurti, T.N., J. Xue, G. Rohaly, D. Fitzjarrald, G.D. Emmitt, S. Houston and S.A. Wood, 1991: Using a global spectral model in an observing system simulation experiment for LAWS - An EOS wind measuring system. Proc. AMS Second Symp. on Global Change Studies, New Orleans, LA, January, pp. 23-27.

- Menzel, W.P., D.P. Wylie and K.L. Strabala, 1992: Seasonal and diurnal changes in cirrus cloud as seen in four years of observations with the VAS. Submitted to J. Appl. Meteor.
- Press, W.H., B.P. Flannery, S.A. Teukolsky, W.T. Vetterling, 1986: Numerical Recipes: The Art of Scientific Computing, Chap. 14, Cambridge, Press, New York.
- Rohaly, G.D. and T.N. Krishnamurti, 1993: An observing system simulation experiment for the Laser Atmospheric Wind Sounder (LAWS). J. Appl. Meteor., 32, 1453-1471.
- Slingo, A., R.C. Wilderspin and S.J. Brentnall, 1987: Simulation of the diurnal cycle of outgoing longwave radiation with an atmospheric GCM. Mon. Wea. Rev., 1451-1457.
- Stowe, L.L., H.Y. Michael Yeh, T.F. Eck, C.G. Wellemeyer, H.L. Kyle and The Nimbus-7 Cloud Data Processing Team, 1989: Nimbus-7 global cloud climatology, Part II: First year results. J. Clim., 2, 671-709.
- Wood, S.A. and G.D. Emmitt, 1990: A reference atmosphere for LAWS trade studies. Paper presented at the 1990 Optical Remote Sensing of the Atmosphere Topical Meeting, Lake Tahoe, NV.
- _____ and _____, 1991: A reference atmosphere for LAWS trade studies: An update. Proc. AMS 71st Annual Meeting Seventh Symp. Meteor. Obs. and Instru., Spec. Sess. Laser Atmos. Stud., New Orleans, LA, January.
- Woodbury, G.E. and M.P. McCormick, 1986: Zonal and geographical distributions of cirrus clouds determined from SAGE data. J. Geophys. Res., 91, 2775-2785.

REPORT DOCUMENTATION PAGE			Form Approved OMB No. 0704-0188	
<small>Public reporting burden for this collection of information is estimated to average 1 hour per response, including the time for reviewing instructions, searching existing data sources, gathering and maintaining the data needed, and completing and reviewing the collection of information. Send comments regarding this burden estimate or any other aspect of this collection of information, including suggestions for reducing this burden to Washington Headquarters Services, Directorate for Information Operations and Reports, 1215 Jefferson Davis Highway, Suite 1204, Arlington, VA 22202-4302, and to the Office of Management and Budget, Paperwork Reduction Project (0704-0188), Washington, DC 20503.</small>				
1. AGENCY USE ONLY (Leave blank)	2. REPORT DATE 12/1/93	3. REPORT TYPE AND DATES COVERED Final - 6/27/90-12/1/93		
4. TITLE AND SUBTITLE Space-based Doppler lidar sampling strategies -- algorithm development and simulated observation experiments		5. FUNDING NUMBERS NAS8-38559		
6. AUTHOR(S) S.A. Wood, G.D. Emmitt, M. Morris, L. Wood and D. Bai		8. PERFORMING ORGANIZATION REPORT NUMBER		
7. PERFORMING ORGANIZATION NAME(S) AND ADDRESS(ES) Simpson Weather Associates, Inc. 809 E. Jefferson Street Charlottesville, VA 22902		10. SPONSORING / MONITORING AGENCY REPORT NUMBER		
9. SPONSORING / MONITORING AGENCY NAME(S) AND ADDRESS(ES) NASA/Marshall Space Flight Center Marshall Space Flight Center, AL 35812		11. SUPPLEMENTARY NOTES		
12a. DISTRIBUTION / AVAILABILITY STATEMENT		12b. DISTRIBUTION CODE		
13. ABSTRACT (Maximum 200 words) This report covers work performed under NAS8-38559 for the period of June 27, 1990 through December 1, 1993. A summary provides a brief overview of efforts with appendices attached containing more detailed reporting.				
14. SUBJECT TERMS Space-based Doppler lidar, LAWS Simulation Model, OSSEs		15. NUMBER OF PAGES 266		16. PRICE CODE n/a
17. SECURITY CLASSIFICATION OF REPORT n/a	18. SECURITY CLASSIFICATION OF THIS PAGE n/a	19. SECURITY CLASSIFICATION OF ABSTRACT n/a	20. LIMITATION OF ABSTRACT n/a	